Block Copolymer Micelles as Efficient Templates for Mesostructured Hybrid Materials

DISSERTATION

zur Erlangung des akademischen Grades einer Doktorin/eines

Doktors der Naturwissenschaften (Dr. rer. nat.)

in der Bayreuther Graduiertenschule für Mathematik und Naturwissenschaften

(BayNAT)

der Universität Bayreuth

vorgelegt von

Judith Schöbel

aus *Halberstadt*

Bayreuth, 2017

Die vorliegende Arbeit wurde in der Zeit von Februar 2014 bis September 2017 in Bayreuth am Lehrstuhl Makromolekulare Chemie II unter Betreuung von Herrn Professor Dr. Andreas Greiner angefertigt.

Vollständiger Abdruck der von der Bayreuther Graduiertenschule für Mathematik und Naturwissenschaften (BayNAT) der Universität Bayreuth genehmigten Dissertation zur Erlangung des akademischen Grades einer Doktorin/eines Doktors der Naturwissenschaften (Dr. rer. nat.).

Dissertation eingereicht am: 27.11.2017

Zulassung durch das Leitungsgremium: 07.12.2017

Wissenschaftliches Kolloquium: 02.05.2018

Amtierender Direktor: Prof. Dr. Dirk Schüler

Prüfungsausschuss:

Prof. Dr. Andreas Greiner (Gutachter/in)
Prof. Dr. Birgit Weber (Gutachter/in)
Jun.-Prof. Dr. Anna Schenk (Vorsitz)
Prof. Dr. Peter Strohriegl

All truths are easy to understand once they are discovered; the point is to discover them.

Galileo Galilei

Dedicated to my family and my grandmother Christa Schöbel (†)

Table of Contents

Summary

The improvement of catalyst performance is an omnipresent issue in science. The discovery of the excellent catalytic activity of nanoparticles (NPs) paved the way to the development of a myriad of different catalyst materials. The main advantage of NP containing catalysts represents simultaneously their main drawback: the high surface activity. To prevent a loss of activity by agglomeration and aggregation, efficient stabilization of the NPs is needed. However, the efficient stabilization by ligands results in catalysts, which are hardly separable from the reaction medium, thus limiting their reusability. To solve this problem, this thesis is focused on two concepts for the synthesis of mesostructured catalyst materials, which simultaneously provide resuablity and high activity: one concept is based on the use of polymeric supports for stabilization of the NPs and the other concept deals with a controlled aggregation of NPs to form highly porous, mesostructured hybrid materials.

For the preparation of supported NP hybrid materials, worm-like crystalline-core micelles (wCCMs) with a patchy-like microphase-separated corona as functional templates were used. The wCCMs were formed by crystallization-driven self-assembly of polystyrene-*block*-polyethylene-*block*-poly(methyl methacrylate) triblock terpolymers in solution. To provide appropriate anchor groups for the stabilization of NPs, first, an efficient synthetic strategy to functionalize the poly(methyl methacrylate) block was developed. To this end, an amidation was chosen for the introduction of amide and amine groups. The morphology of the resulting functionalized patchy wCCMs was studied in detail allowing for a precise control over the patch size and shape. However, for a high degree of functionalization, the amidation decreased the solubility of the patches, thus, leading to ill-defined wCCMs.

Therefore, the amidation was optimized yielding in well-defined highly functionalized patchy wCCMs, which were selectively loaded with different types of NPs, i.e. noble metal and transition metal NPs. The *in situ* reduction of the corresponding noble metal salt proved to be a robust and versatile method for the incorporation of noble metal NPs like gold (Au), silver and platinum and was successfully transferred from a batch process to a continuous loading process via microfluidics. The average diameter of the formed NPs was 2-5 nm, which is comparable small and therefore interesting for an application in catalysis. However, a rather broad size distribution of the NPs was obtained. Therefore, a ligand exchange method was used to incorporate preformed acetate-stabilized zinc oxide (ZnO) and copper oxide NPs showing a narrow size distribution. For binary loading of the patchy wCCMs with

two types of NPs, the ligand exchange route for loading of the functionalized poly(methyl methacrylate) patch was combined with the loading of the polystyrene patch with polystyrene-stabilized AuNPs through selective solvent interactions. All used methods provided successful fixation of the NPs within the patchy corona without showing agglomeration or aggregation.

To provide the excellent stabilization ability of the wCCMs for heterogeneous catalysis, the wCCMs were coated on the surface of polystyrene nanofibers by coaxial electrospinning resulting in a nonwoven with a patch-like surface. A facile dipping method, based on a ligand exchange process, allows for incorporation of preformed aqueous citrate-stabilized AuNPs showing a homogeneous distribution over the whole nonwoven without agglomeration and aggregation. The hybrid nonwoven exhibited an excellent catalytic activity in the alcoholysis of dimethylphenylsilane at mild reaction conditions. It was easily separable from the reaction medium and even after ten cylces of reuse, no limitation in the activity was observed, which could be attributed to the absence of leaching effects.

The second concept for preparation of mesostructured hybrid materials is based on the use of cylindrical polymer brushes (CPBs) consisting of a crosslinked polybutadiene core and a quaternized poly(2-vinylpyridine) shell. The quaternization resulted in a stable positive charge, which enables the loading with acetate-stabilized ZnONPs. Pyrolysis of the polymeric template led to a controlled aggregation of the ZnONPs and the formation of highly porous nanotubes, which showed a higher catalytic activity in the photocatalytic degradation of ciprofloxacin, a common antibiotic found in hospital wastewater, than Degussa P25, a commercially available titanium dioxide catalyst.

The performance of the ZnO nanotubes was even enhanced by a combination of the ZnONPs with AuNPs, which is attributed to synergistic effects. A study of different ZnO/Au compositions revealed an optimum composition of 12 wt-% Au and 88 wt-% ZnO. In addition to the photocatalytic degradation of ciprofloxacin, this material also showed an increased activity in the degradation of a second common antibiotic, levofloxacin, which shows the versatility of this mesostructured catalyst.

In summary, this thesis demonstrates the superior perfomance of mesostructured materials in heterogeneous catalysis. A tailor-made polymeric support provides efficient stabilization and guarantees a precise arrangement of the NPs. With and without pyrolysis of the

polymeric template, highly efficient and reusable heterogeneous catalysts for organic reactions as well as wastewater purification were developed.

Zusammenfassung

Die Leistungssteigerung von Katalysatoren ist ein allgegenwärtiges Thema in der Wissenschaft. Die Entdeckung der exzellenten katalytischen Aktivität von Nanopartikeln (NP) ebnete den Weg zur Entwicklung unzähliger unterschiedlicher Katalysatormaterialien. Der Hauptvorteil von NP-haltigen Katalysatoren ist hierbei gleichzeitig ihr größter Nachteil: die hohe Oberflächenaktivität. Um eine Minderung dieser Oberflächenaktivität durch Agglomeration und Aggregation zu verhindern, wird eine effiziente Stabilisierung der NP benötigt. Diese effiziente Stabilisierung bewirkt allerdings, dass die Katalysatoren schwer vom Reaktionsmedium zu entfernen sind und ihre Wiederverwendbarkeit eingeschränkt ist. Um dieses Problem zu lösen, bedient sich diese Dissertation zweier Konzepte zur Synthese von mesostrukturierten Katalysatoren, die gleichzeitig Wiederverwendbarkeit und eine hohe Aktivität bereitstellen. Ein Konzept basiert auf der Verwendung von Polymerträgern für die Stabilisierung von NP und das andere Konzept stützt sich auf die kontrollierte Aggregation von NP um hochporöse, mesostrukturierte Hybridmaterialien herzustellen.

Für die Herstellung von geträgerten NP-Hybridmaterialien wurden wurmartige Mizellen mit kristallinem Kern und einer patchartig mikrophasenseparierten Korona (engl. worm-like crystalline-core micelles, wCCMs) als funktionale Template verwendet. Die wCCMs wurden durch kristallisationsinduzierte Selbstassemblierung von Polystyrol-*block*-Polyethylen-*block*-Polymethylmethacrylat-Blockcopolymeren in Lösung erhalten. Um geeignete Ankergruppen für die Stabilisierung von NP zu erhalten, wurde zuerst eine effiziente Synthesestrategie entwickelt, um den Polymethylmethacrylat-Block zu funktionalisieren. Dazu wurde eine Amidierungsreaktion für die Einführung von Amid- und Amingruppen gewählt. Die Morphologie der erhaltenen gepatchten wCCMs wurde im Detail analysiert, was eine präzise Kontrolle über die Patchgröße und –form ermöglichte. Für höhere Funktionalisierungsgrade wurde jedoch eine schlechtere Löslichkeit der Amidpatches erhalten, was zur Bildung von undefinierten wCCMs führte.

Daher wurde die Amidierung optimiert, was in der Bildung von definierten funktionalisierten wCCMs resultierte. Diese wurden selektiv mit verschiedenen Typen von NP, hier Edelmetall- und Übergangsmetalloxid-NP, beladen. Eine robuste und vielseitige Methode war hier die *in situ*-Reduktion der korrespondierenden Metallsalze zu den Edelmetall-NP wie Gold (Au), Silber oder Platin. Diese Methode konnte erfolgreich von einem Batch-Prozess zu einer kontinuierlichen Beladung via Mikrofluidik ausgebaut

werden. Die durchschnittliche Größe der erhaltenen NP war zwischen 2 und 5 nm, was vergleichsweise klein und daher interessant für die Katalyse ist. Allerdings wurde hier eine relativ breite Verteilung der NP-Größe erhalten. Daher wurde die Ligandenaustausch-methode verwendet, um vorgeformte Acetat-stabilisierte Zinkoxid- (ZnO) und Kupferoxid-NP mit einer engen Größenverteilung einzulagern. Um die gepatchten wCCMs gleichzeitig mit zwei NP-Sorten zu beladen, wurde die Ligandenaustauschmethode zur Beladung der funktionalisierten Polymethylmethacrylat-Patches kombiniert mit der Beladung der Polystyrol-Patches mit Polystyrol-stabilisierten AuNP durch lösungsmittelselektive Wechselwirkungen. Alle hier gezeigten Methoden führten zur erfolgreichen Einlagerung der NP in die gepatchte Korona ohne einen Hinweis auf Agglomeration oder Aggregation.

Um die exzellente NP-Stabilisierung der wCCMs für die heterogene Katalyse zugänglich zu machen, wurden die wCCMs über koaxiales Elektrospinnen auf die Oberfläche von Polystyrol-Nanofasern aufgebracht. Dies resultierte in Faservliesen mit einer patch-artigen Oberfläche. Eine einfache Eintauch-Prozedur, die auf einem Ligandenaustausch basiert, erlaubt die Einlagerung von vorgeformten Zitrat-stabilisierten AuNP. Diese zeigen eine homogene Verteilung über das gesamte Faservlies ohne Agglomeration oder Aggregation. Das Hybrid-Faservlies zeigte eine exzellente katalytische Aktivität in der Alkoholyse von Dimethylphenylsilan unter milden Reaktionsbedingungen. Es konnte einfach aus der Reaktionslösung entfernt werden und auch nach zehn Katalysezyklen konnte kein Verlust der Aktivität festgestellt werden. Dies wurde auf das Fehlen von sogenannten Leaching-Effekten zurückgeführt.

Das zweite Konzept für die Herstellung von mesostrukturierten Hybridmaterialien basiert auf der Verwendung von zylindrischen Polymerbürsten (engl. cylindrical polymer brushes, CPBs), die aus einem vernetzten Polybutadien-Kern und einer quaternisierten Poly-2-vinylpyridin-Korona bestehen. Die Quaternisierung resultierte in einer stabilen positiven Ladung, was die Einlagerung von Acetat-stabilisierten ZnONP ermöglichte. Die Pyrolyse des Polymertemplats führte zu einer kontrollierten Aggregation der ZnONP und damit zur Bildung von hochporösen Nanoröhren. Diese Nanoröhren zeigten eine höhere katalytische Aktivität für den photokatalytischen Abbau von Ciprofloxacin, einem bekannten Antibiotikum, das sich in Krankenhausabwässern befindet, als Degussa P25, ein kommerziell erhältlicher Titandioxid-Katalysator.

Die Leistung der ZnO-Nanoröhren konnte durch die Kombination mit AuNP noch gesteigert werden. Dies ist auf synergistische Effekte zurückzuführen. Ein Vergleich verschiedener

ZnO/Au-Zusammensetzungen ergab eine optimale Zusammensetzung von 12 gew-% Au und 88 gew-% ZnO. Dieses Material zeigte zusätzlich zur hohen Aktivität beim photokatalytischen Abbau von Ciprofloxacin auch eine hohe Aktivität beim Abbau eines zweiten bekannten Antibiotikums, Levofloxacin. Dies untermauert die Vielseitigkeit des Katalysators.

Zusammenfassend zeigt diese Dissertation die ausgezeichnete Leistung von meso-strukturierten Materialien für die heterogene Katalyse. Ein maßgeschneiderter Polymerträger bietet eine effiziente Stabilisierung und garantiert eine präzise Anordnung von NP. Sowohl mit als auch ohne Pyrolyse des Polymertemplats konnten hocheffiziente, wiederverwendbare heterogene Katalysatoren für die organische Synthese und die Krankenhausabwasserreinigung entwickelt werden.

1 Introduction

1.1 Self-Assembly of Block Copolymers

1.1.1 Amorphous Block Copolymers

An important issue in polymer science is to mimick natural nano- and mesostructures, which gives access to different applications for example in medicine, nanooptics or nanoelectronics.[1,2] One of the most common methods to reach this aim is the self-assembly of block copolymers (BCPs). The microphase separation of BCPs is based on long range repulsive (incompatibility of the blocks) and short range attractive (covalent bond between the blocks) forces.[3] The covalent bond between the blocks excludes a macrophase separation.

The self-assembly of BCPs offers a variety of accessible structures in bulk as well as in solution. Here, the number, miscibility (given by the Flory-Huggins parameter χ) and volume fraction of the blocks as well as the overall degree of polymerization of the BCPs play a vital role.[4,5] For the self-assembly of diblock copolymers (AB-type) in bulk, phase diagrams are reported.[6] These phase diagrams describe the evolution of the formed bulk morphologies in dependence of the composition of the block copolymer. For AB diblock copolymers, where *B* is the major fraction, *A* forms spheres in a matrix of *B* (Figure 1-1, S).[7] With increasing volume fraction of *A*, hexagonally packed cylinders (C), gyroids (G) and finally lamellea (L) are formed. If the fraction of *A* is further increased, the corresponding inverse morphologies of the diblock copolymer result.
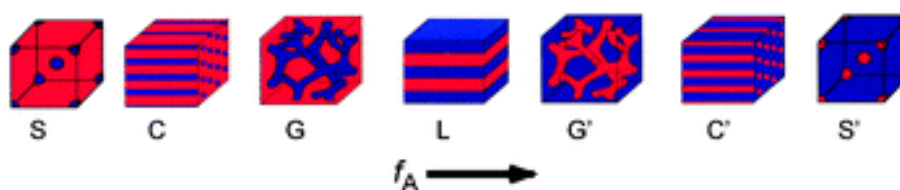
Figure 1-1. Morphologies of a diblock copolymer in bulk (block *A*: blue, block *B*: red) in dependence of the volume fraction of block A (f_A). Reproduced from Ref. 7 with permission of The Royal Society of Chemistry.

In case of ABC triblock terpolymers even more complex morphologies result.[8]

However, an application of self-assembled structures in the medical sector (in particular drug release or imaging) or as surfactants demands self-assembled structures in solution.[5,9–14] Here, diblock and triblock copolymers with an amphiphilic character are used. The simplest

morphology of a micelle, formed in a selective solvent for one of the blocks, is a spherical micelle and consists of an insoluble core (collapsed block of the BCP) and a soluble corona. Two types of these spherical micelles can be distinguished: star-like micelles, for which the corona shows a larger size than the core, and crew-cut micelles showing a large core and a small corona.[15] A variation of the BCP composition and the solvent quality can lead to the formation of cylindrical micelles or vesicles. This was already reported by Eisenberg et al. who synthesized polystyrene-*block*-poly(acrylic acid) (PS-*b*-PAA) diblock copolymers and observed crew-cut micelles, cylindrical micelles and vesicles in dioxane dependent on the fraction of PAA present in the diblock copolymer.[16] However, regarding the cylindrical micelles no length control was achieved, which led to a broad length distribution.

One possibility to overcome a broad length distribution is the formation of cylindrical polymer brushes (CPBs), which was the focus of different studies since the late 1980's.[17] In contrast to the cylindrical micelles of self-assembled diblock copolymers, these CPBs exhibit a "frozen" backbone, i.e. the core is either formed by a linear polymer backbone on which corona-forming side chains are grafted or by a core-crosslinked self-assembled linear BCP. The CPBs can be used as template for the formation of hybrid materials or as nanocarriers[17,18] and are accessible by four different approaches: grafting-to, grafting-from, grafting-through and selective crosslinking of BCPs in bulk or in micelles.[18,19] The first three methods can be realized by a combination of different controlled polymerization techniques like anionic polymerization and atom transfer radical polymerization (ATRP).[20] Müller et al. showed the formation of CPBs with poly(*t*-butyl acrylate)-*b*-poly(*n*-butyl acrylate) side chains.[21–23] Hydrolysis of the poly(*t*-butyl acrylate) block resulted in PAA, which is accessible for further chemical modification or for the stabilization of nanoparticles (NPs). The amphiphilic CPBs showed a length of 180 nm and a narrow length distribution.

The use of linear BCPs requires the fourth method for CPB formation. The selective crosslinking of a diblock copolymer consisting of PS and poly(2-cinnamoylethyl methacrylate) in bulk resulted in such CPBs.[24] These CPBs showed a core width of 25 nm and a length in the micrometer range. Another study uses diblock copolymers of poly(3-(triethoxysilyl)propyl methacrylate) and PS.[25] By self-assembly and crosslinking of the poly(3-(triethoxysilyl)propyl methacrylate) block in bulk, sheets, cylinders and spheres were obtained. To form cylinders, the morphology in bulk was tuned by addition of oligo-styrene. Further addition of oligo-3-(triethoxysilyl)propyl methacrylate yielded in the formation of

cylinders with varying core diameter. Dissolution of the crosslinked bulk morphology resulted in CPBs with controllable core diameter.

More complex morphologies than spheres, cylinders or sheets can be achieved by the step-wise self-assembly of triblock terpolymers or mixtures of diblock copolymers in solution. Here, a compartmentalization of the core and the corona are possible (Figure 1-2).[1,2,4,26,27] Two morphologies of a compartmentalized core are observable: Janus micelles (Figure 1-2, no. 2, 3 and 5) and multicompartment micelles (Figure 1-2, no. 4, 6 and 7). Janus micelles exhibit a core, which is divided in two hemispheres with different chemistry and/or physical properties. Multicompartment micelles (MCMs) possess at least two components forming a multiple segmented core. Both types of core-segmented micelles can be observed with different corona morphologies: a Janus-corona (Figure 1-2, no. 1-4) and a patchy corona (Figure 1-2, no. 5, 7 and 8), in which more than two segments are formed in an alternating or random fashion.
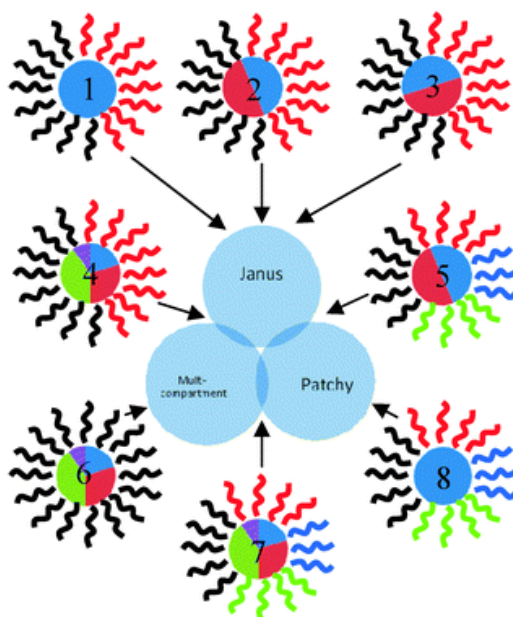
Figure 1-2. Schematic representation of Janus, patchy and multicompartment micelles. Reproduced from Ref. 2 with permission from The Royal Society of Chemistry.

Müller et al. described the formation of Janus particles, patchy particles and MCMs, using different triblock terpolymers.[28–30] The self-assembly of Polystyrene-*block*-polybutadiene-*block*-poly(methyl methacrylate) (SBM) yields in MCMs with different morphologies, for example "hamburger", "clover" or "football"-like structures. Crosslinking of the polybutadiene (PB) middle block results in Janus particles with a controllable Janus balance depending on the block length ratio of the corona-forming blocks.[29] A systematic study of

the influence of the block lengths and the solvent conditions opened the way to cylinders and vesicles with a tailor-made multicompartment structure.[31,32] A controlled co-assembly of patchy and Janus particles creates hierarchical multicompartment cylinders with a size in the micrometer range (Figure 1-3).[27]
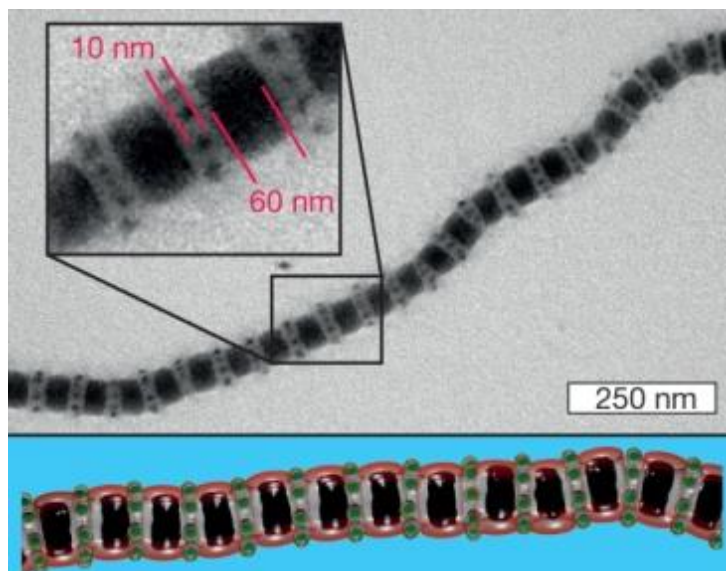
Figure 1-3. Hierarchical co-assembly of MCMs results in cylindrical superstructures. The different copolymer blocks are selectively stained with OsO_4 to provide contrast. Reprinted by permission from Macmillan Publishers Ltd: Nature (Ref. 27), copyright (2017).

In summary, the self-assembly of amorphous BCPs provides numerous different morphologies, but regarding cylindrical micelles, a length control is hardly accessible and demands a complex preparation procedure. The use of BCPs bearing a crystalline block facilitates the production of cylindrical micelles with a well-defined length distribution.

1.1.2 Crystalline Block Copolymers

In contrast to the self-assembly processes of amorphous BCPs, the self-assembly of crystalline BCPs is less discussed in literature. The mechanism for self-assembly of crystalline BCPs is more complex because of the additional parameters for structure formation, which is not limited to microphase separation and solvent quality but also includes crystallization processes. The first theoretical model for the crystallization of diblock copolymers was described by Vilgis and Halperin in 1991.[33] The model is based on the assumption that the crystalline block is insoluble in the used solvent and therefore forms the core of a micelle. Within this core, the chains undergo chain folding, i.e. the chains

are multiply folded, to form a polymer crystal. The folding of chains results in two surface tensions, one in the fold plane and one in the lateral plane. The amorphous blocks of the diblock copolymer are grafted to the fold surface of the crystals, while the grafting density of the amorphous blocks is influenced by the number of chain folds in the crystalline core (Figure 1-4).
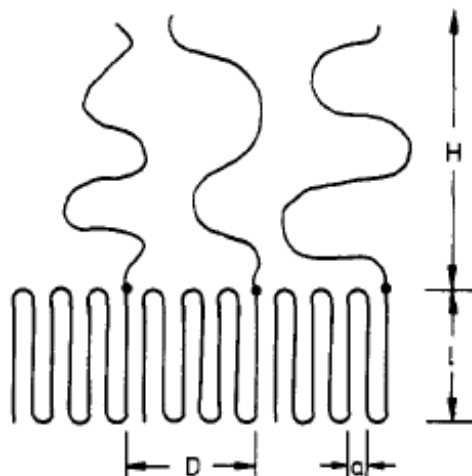

Figure 1-4. Chain folding of a crystalline-coil block copolymer with H: thickness of corona, l: thickness of the crystalline core, a: monomer size and D: dimension of the folded chain. Reprinted with permission from Ref. 33. Copyright (2017) American Chemical Society.

The final morphology of the polymer crystal is therefore affected by three competing factors: the number of chain folds, the grafting density and the surface energy of the polymer crystal. To lower the total free energy, the formation of anisotropic morphologies, i.e. lamellae or cylinders, was predicted.

1.1.2.1 PFS-Containing Block Copolymers

In 1998, first reports of Manners and Winnik et al. showed the formation of crystalline-core micelles (CCMs) with a cylindrical shape.[34] They used diblock copolymers of poly(ferrocenyl dimethylsilane)-*block*-polydimethylsiloxane (PFS-*b*-PDMS) for inducing a crystallization-driven self-assembly (CDSA) in a hot hexane solution. The PFS block forms the core of the cylindrical micelles and the corona is formed by the PDMS block (Figure 1-5). The cylindrical micelles showed an average length up to 440 nm and a width of 20 nm.
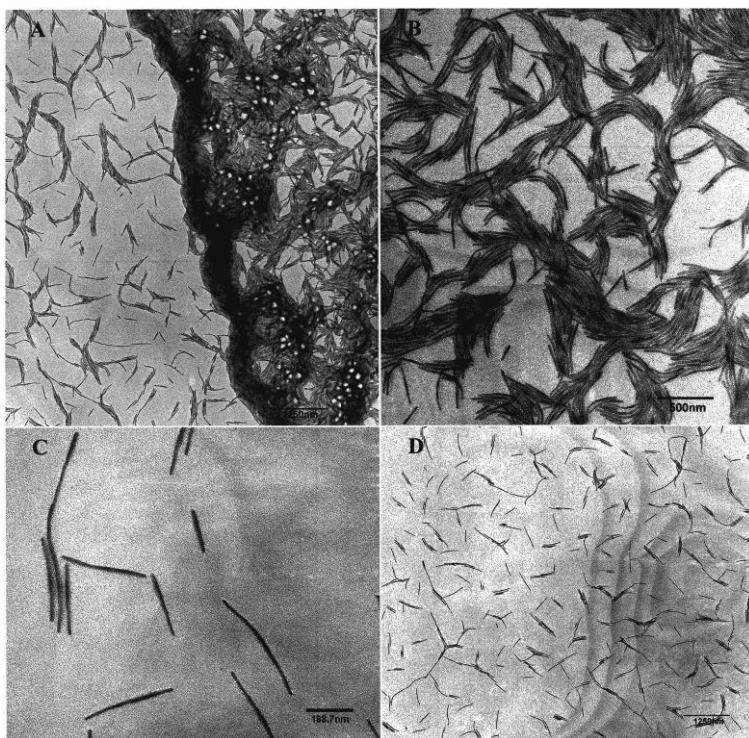
Figure 1-5. Cylindrical micelles with a crystalline PFS core. The corona is formed by PDMS and is not observable on the TEM micrographs. Reprinted with permission from Ref. 34. Copyright (2017) American Chemical Society.

The fabrication of diblock copolymers with a crystalline PFS core and a polyisoprene (PI) corona opened the way for tailoring the width of the crystalline core by varying the block length ratio in the BCP. For long PI blocks, cylindrical micelles were formed whereas short PI blocks result in the formation of tape-like micelles.[35]

The development of a seeded-growth process paved the way to cylindrical micelles with defined length and narrow length distribution.[36] The seeded growth is based on a defined amount of seeds, prepared by ultrasonification of existing cylindrical micelles (stub micelles), on which unimers (molecularly dissolved BCP chains) add in a controlled manner (Figure 1-6 A-D). This guarantees a slow and homogeneous growth. The length of the cylindrical micelles increases linear with the unimer/seed ratio (Figure 1-6 E), which is similar to living anionic polymerization, showing a linear increase in molecular weight with increasing conversion. The ends of the cylindrical micelles remain active for further addition of unimers. With respect to the living polymerization, this kind of crystallization is named living CDSA and enables the formation of block comicelles (analogous to BCPs) with PFS containing diblock copolymers.[36,37]
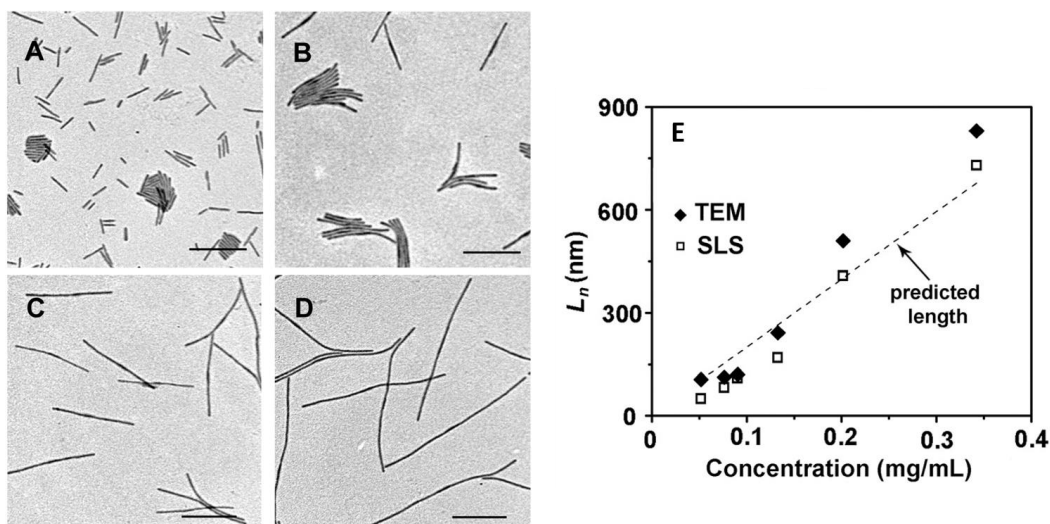
Figure 1-6. TEM micrographs of the PFS-*b*-PI stub micelles (A) and after addition of different amounts of PFS-*b*-PI unimers (B-D). The number-average length L_n shows a nearly linear increase with increasing unimer concentration. The concentration of seed micelles was kept constant. From Ref. 36. Adapted with permission from AAAS.

The living CDSA is a simple but precise way for the formation of cylindrical CCMs with a defined length and morphology control. This is an important advantage with respect to amorphous cylindrical micelles because the length control is still a remaining problem.

The seeded growth of cylindrical micelles is not limited to PFS-*b*-PI diblock copolymers. Further investigations show that the corona-forming block can be changed with preservation of the living CDSA character. One example are diblock copolymers of PFS and a fluorescent block which were self-assembled in fluorinated solvents.[38] For the preparation of these micelles, a self-seeding protocol was applied. The self-seeding procedure is based on the rather broad melting point ranges of polymer crystals, which are caused by different degrees of crystallinity within the polymer crystals. If the polymer chains with lower degree of crystallinity are dissolved, unimers are formed, which can grow to the remaining seed crystals with higher crystallinity. This results in cylindrical micelles with a narrow length distribution. The additional fact of a color-tunable fluorescent corona gives rise to applications in sensing and diagnostics.

The concept of living CDSA for the formation of block comicelles paved the way for different applications and accessible morphologies. With the use of diblock copolymers bearing hydrophilic corona forming blocks consisting of poly(ethylene oxide)-*graft*-triethylene glycol (PEO-*g*-TEG) and quaternized poly(2-vinylpyridine) (P2VP), the block

comicelles were transferred to an aqueous medium, which is of great importance for medicinal applications (Figure 1-7).[39]
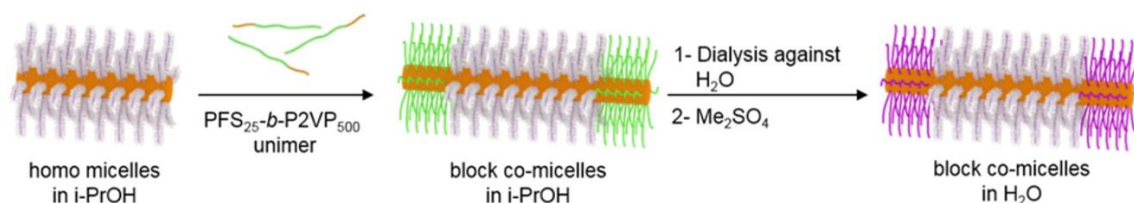
Figure 1-7. Schematic preparation of block comicelles starting from PFS-*b*-(PEO-g-TEG) seed micelles. Reprinted with permission from 39. Copyright (2017) American Chemical Society.

The concept of fluorescent cylindrical micelles was enhanced to the production of block comicelles through living CDSA. Here, fluorescent barcode micelles with alternating blocks of fluorescent PFS containing triblock copolymers and non-fluorescent PFS-*b*-P2VP diblock copolymers were formed.[40] In addition to the barcode micelles, color-tunable centrosymmetric multiblock comicelles were produced.[41] These micelles showed a distinct emission of up to three different wavelengths. Using seed micelles with only one end available for CDSA, a unidirectional growth of the fluorescent unimers to triblock comicelles with different emission wavelengths was achieved (Figure 1-8).
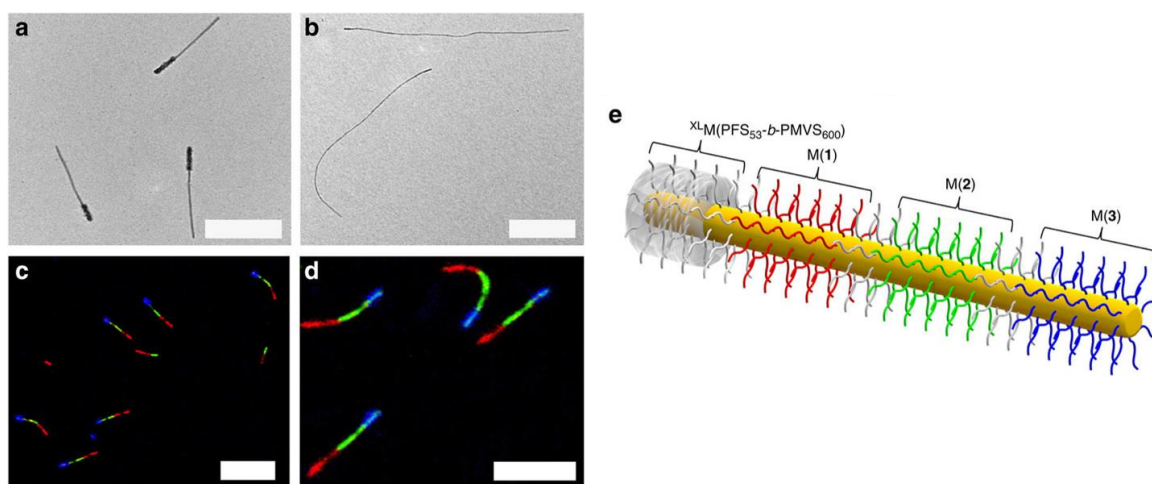
Figure 1-8. TEM micrographs (a,b), confocal fluorescence micrographs (c,d) and schematic representation (e) of fluorescent triblock comicelles obtained by unidirectional living CDSA of different PFS-containing diblock copolymers. Adapted from Ref. 41, open access journal, no permission required.

The unidirectional growth of seed micelles enabled the formation of non-centrosymmetric cylindrical micelles which represents a milestone for accessible structures by CDSA.[42] For

the non-centrosymmetric growth, seed micelles have to be prepared in a slightly more complex route than normal seed micelles. First, centrosymmetric triblock comicelles are prepared. The coronal chains of the outer two blocks have to be crosslinked to block the ends of the triblock comicelles. Dissolution of the middle block yields the "daughter micelles", which can be used as seeds. As one end of the seed micelles is blocked by the crosslinked corona, only a unidirectional growth is possible.

Further attempts of Manners et al. lead to a gradient self-assembly of diblock copolymers with PFS core. Using different corona blocks, the gradient comicelles showed a patchy corona which was, at that time, only reported by Schmalz et al. for triblock terpolymers with a polyethylene (PE) core (see chapter 1.1.2.2 PE-Containing Block Copolymers).[43,44] The gradient self-assembly process was used for a cocrystallization of linear and brush-like BCPs in a living manner. The steric repulsion of the brush-like BCPs resulted in a gradual integration. Therefore, a patchy corona, formed by the brush-like BCPs, was observable (Figure 1-9).
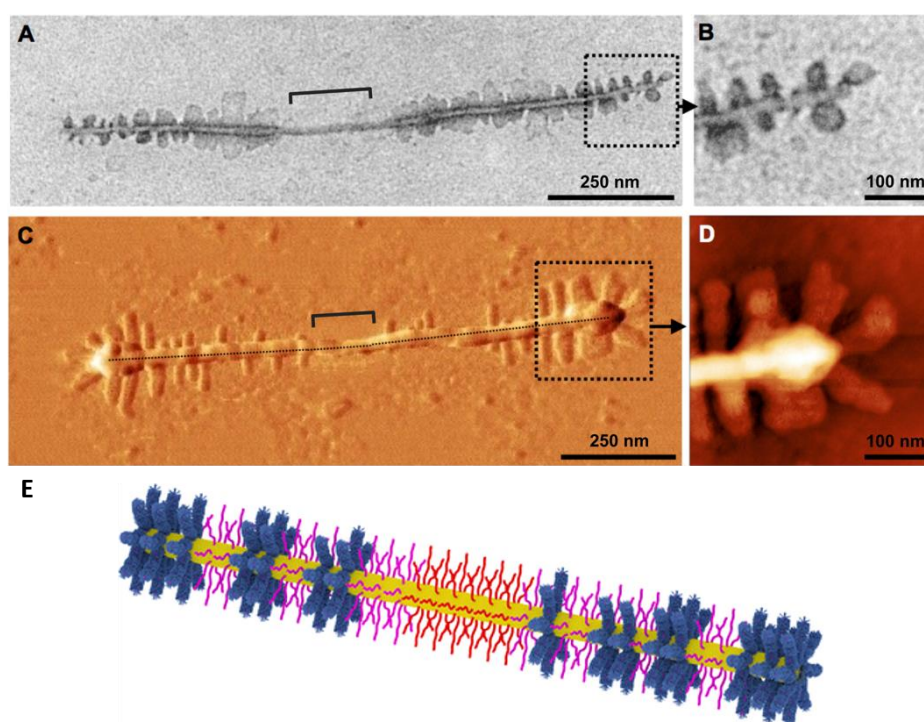
Figure 1-9. TEM micrographs (A, B), AFM height images (C, D) and schematic representation of cylindrical micelles with a patchy corona obtained by gradient self-assembly of linear and brush-like BCPs. Adapted with permission from 43. Copyright (2017) American Chemical Society.

The CDSA is not limited to diblock copolymers. ABA triblock copolymers with two crystallizable PFS blocks were synthesized and self-assembled. The CDSA resulted in flower-like micelles, which were formed by the aggregation of single cylindrical micelles.[45] In following studies, the hierarchical self-assembly of cylindrical micelles was analyzed in detail. It was possible to use platelet-like micelles as nucleating seeds for living CDSA. Here, the cylindrical micelles cocrystallize on the ends of the platelets and scarf-like micelles were obtained (Figure 1-10). These scarf-like micelles were prepared by homo- as well as heteroepitaxial growth, which means that a BCP with a second crystallizable block is added to the PFS seed crystal. This second crystallizable block needs similar lattice parameters to enable the heteroepitaxial growth. For the growth on PFS crystals, one example is poly(ferrocenyl dimethylgermane). The heteroepitaxial growth was transferred to the formation of pentablock comicelles.[46] Similar structures were observed through blending of a PFS homopolymer with a PFS-containing diblock copolymer. Here, the platelet-like micelles were formed by both, the PFS homopolymer and the diblock copolymer.[47]
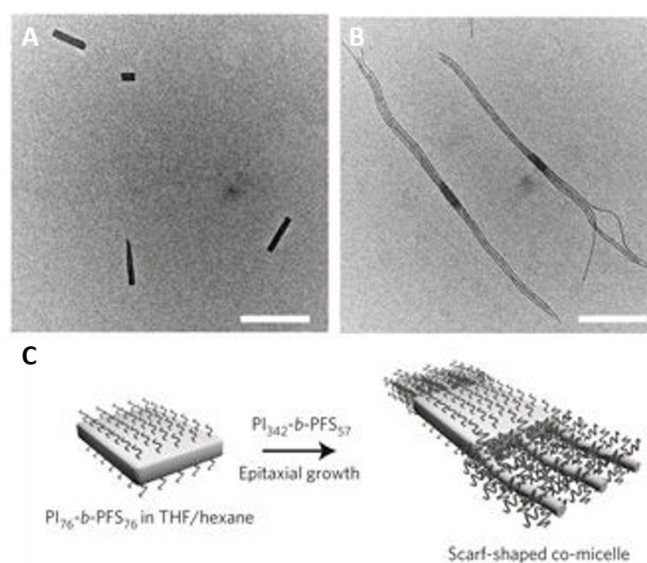
Figure 1-10. TEM micrographs of the platelet-like seed micelles (A) and the scarf-shaped micelles after epitaxial growth of a second PFS containing diblock copolymer on the seed micelles (B). Schematic representation of the epitaxial growth (C). Adapted by permission from Macmillan Publishers Ltd: Nature Materials (Ref. 46), copyright (2017).

The development of the hierarchical self-assembly gave rise to numerous morphologies, also expanding the scope to two dimensional and three dimensional superstructures.[48–59] As the focus of this thesis is laid on cylindrical micelles, these hierarchical superstructures are only highlighted by two examples. Both examples are based on selective interactions between block comicelles by hydrogen bonds. The block comicelles bear a hydrogen donor block and

a hydrogen acceptor block. If these blocks are located at the block comicelle ends, linear hierarchical assemblies are formed. If the middle blocks of the block comicelles bear the hydrogen donor or acceptor groups, more complex two dimensional assemblies, e.g. dumbbell or cross micelles, are observed. The combination of hydrogen bonds and solvophobic interactions results in cross supermicelles, which are still accessible for CDSA. Further growth of unimers to the cross supermicelles forms windmill structures (Figure 1-11). [60]
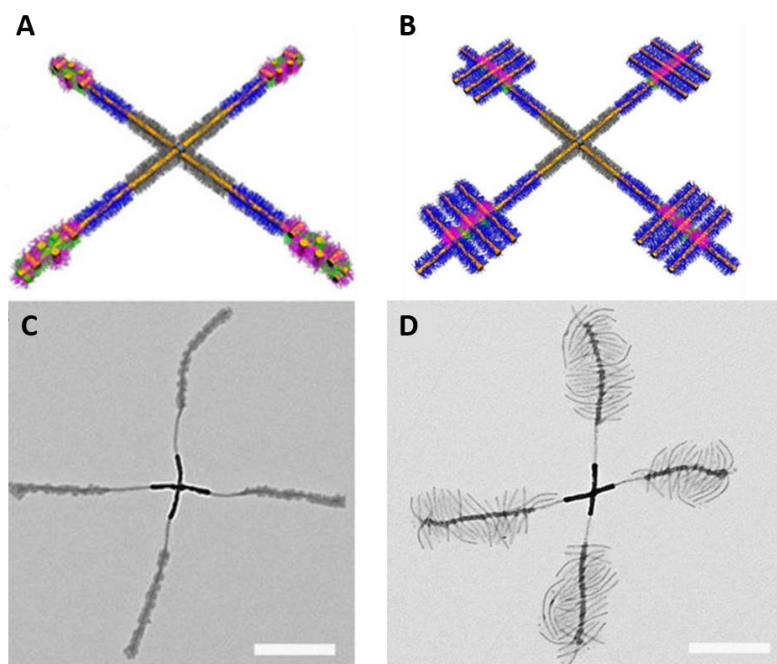
Figure 1-11. Schematic representation (A, B) and TEM micrographs (C, D) of a cross supermicelle and a windmill supermicelle formed by hierarchical self-assembly through hydrogen bonds. Adapted from Ref. 60, open access journal, no permission required.

The concept of hydrogen bonds was extended with the use of hydrogen acceptor seed micelles. These seed micelles were attached to the hydrogen acceptor blocks and formed a shish-kebab structure. Furthermore, the addition of hydrogen donor homopolymer to triblock comicelles with a hydrogen acceptor middle block resulted in three dimensional supermicelles.[61]

The PFS containing polymers are the most investigated BCPs for CDSA. One example for other crystalline-core forming micelles are PE containing di- and triblock copolymers, which can also undergo CDSA and, depending on the corona blocks, are able to form a patchy corona.

1.1.2.2 PE-Containing Block Copolymers

The PE containing BCPs are known for CDSA since 1996 when Gast et al. used a combination of theoretical calculations and experimental data to expand the theory of Vilgis and Halperin.[33] Gast et al. used diblock copolymers of PE and polyethylpropylene (PEP) and self-assembled these BCP in *n*-decane. They compared the thickness of the resulting platelet micelles (ca. 6 - 9 nm) with theoretical calculations and found that these calculations matched in a certain range well with the experimental observations.[62]

A similar work of Richter et al. obtained a platelet thickness of 4-8 nm using the same diblock copolymer. In addition to the platelet structure of the micelles, needle-like aggregates of the diblock copolymer were found. These aggregates were attributed to the interactions of the amorphous corona blocks.[63] Instead of linear diblock copolymers with PE and PEP, also miktoarm star polymers were used for self-assembly. Here, the PE forms the core of the miktoarm star polymers and PEP forms the arms. After self-assembly of these BCPs, disk like micelles were observed. The size and width of these disks were dependent on the molecular weight of the PEP arms. A theoretical model for the calculation of the disk size was not applicable.[64] The miktoarm star polymers as well as the linear diblock copolymers of PE and PEP were used as nucleation agent for paraffin. This leads to a potential application in diesel fuel because the nucleated paraffin crystals are small enough to pass the diesel particle filter. Without any nucleation agent, the paraffin crystals are too big and clog the filters.[65,66]

Triblock terpolymers with two outer crystalline polyethylene blocks and an amorphous PDMS middle block were self-assembled to nanoplatelets. To this end, the block copolymer was dissolved in hot toluene and cooled down to room temperature, which induced the self-assembly. The resulting nanoplatelets were analyzed and manipulated with AFM. The manipulation led to a donut structure.[67]

Different PE-containing linear and star-shaped block copolymers were self-assembled in aqueous medium to obtain cylinders, platelets or disks. To guarantee the dispersion of these micelles in water, a hydrophilic second or third block was needed. Examples for these hydrophilic blocks are polyoxazoline, poly(ethylene glycol), poly(isopropyl acryalamide), poly(2-vinyl pyridine) and poly(dimethyl acrylamide).[68–74] These hydrophilic BCPs can be used for targeted drug delivery in medicinal applications.[75,76] The self-assembly of amphiphilic PE-containing BCPs is not restricted to water. In organic solvents, for example

dimethylformamide (DMF) and trichlorobenzene, the self-assembly of the BCPs leads to rhombic, disk-like and spherical micelles.[77,78] Other cylindrical micelles were observed for diblock copolymers of PE and poly(dimethyl acrylamide) and poly(*tert*-butyl acrylate). However, the self-assembly of these BCPs was not studied in detail.[79,80]

The first cylindrical or worm-like crystalline-core micelles (wCCMs) with PE core and a patch-like microphase-separated corona were reported by Schmalz et al. The wCCMs were self-assembled from PS-*b*-PE-*b*-PMMA (SEM) triblock terpolymers in toluene and tetrahydrofuran (THF) by using CDSA. These wCCMs showed a corona with alternating nanometer sized patches of PS and PMMA as revealed by TEM (Figure 1-12).[44]
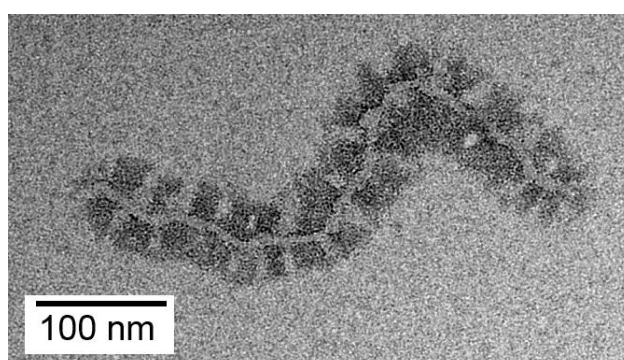
Figure 1-12. SEM wCCM with a patchy corona. The sample is selectively stained with RuO$_4$. PS appears dark; PE and PMMA appear bright.

The self-assembly of the PE containing triblock terpolymers was studied in detail in dependence of the solvent quality for the PE core and the concentration of the BCP in the corresponding solvent. These parameters influence the morphology of the micelles and the patchy corona. In particular, the solvent quality is crucial for the formation of wCCMs (Figure 1-13). In a good solvent for the PE core (THF, toluene), the unimers are molecularly dissolved above the melting temperature of the PE core. Cooling to room temperature induces homogeneous nucleation and the unimers further grow onto the formed nuclei to form wCCMs. A bad solvent for the PE core (dioxane) results in the formation of spherical micelles with a patchy corona. This is attributed to the insolubility of the PE core even in the hot solvent. Therefore, confined crystallization in preformed spherical micelles leads to the final spherical crystalline-core micelles (sCCMs).[81]
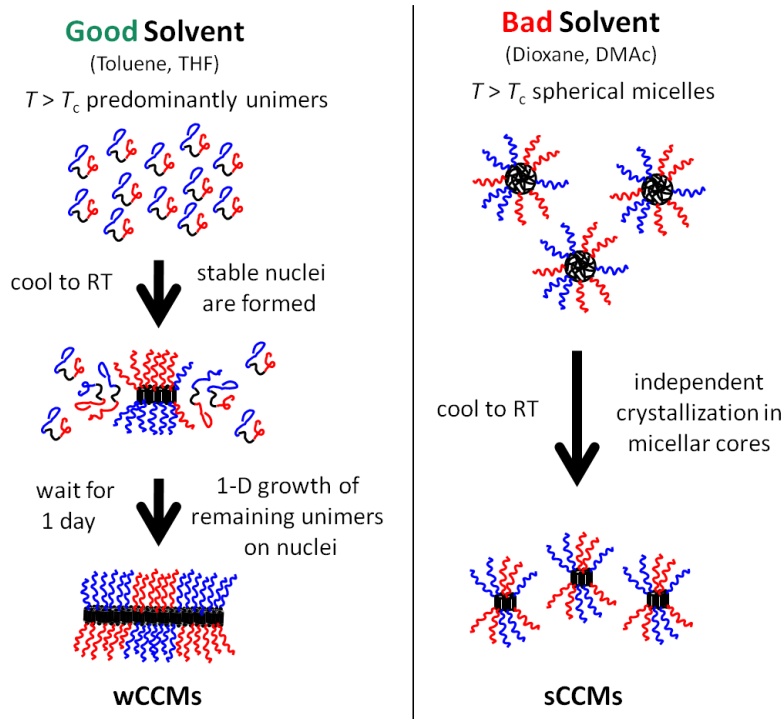
Figure 1-13. CDSA of SEM triblock terpolymers in good and bad solvents for the PE core (black: PE, blue: PS, red: PMMA). Adapted with permission from 81. Copyright (2017) American Chemical Society.

To verify the patchy morphology of the wCCM corona, small angle neutron scattering (SANS) experiments were conducted. In general, the SEM triblock terpolymers are able to form two different corona morphologies, which is attributed to the immiscible corona blocks. The first morphology is a Janus structure, which is characterized by two equally sized hemi-cylinders of the corona blocks. The patchy morphology, which was also observed by TEM measurements, is the second possibility. To proof the patchy morphology, theoretical calculations were compared to the SANS experiments and supported the TEM observations of a patchy corona.[82] The size of the corona patches can be tuned by cocrystallization of a SEM and a PS-*b*-PE-*b*-PS (SES) triblock copolymer. To this end, both BCPs are mixed before crystallization, heated above the melting temperature and crystallized at room temperature. With increasing amount of SES in this mixture, the size of the PMMA patches decreases. The advantage of this method is to avoid the complex synthesis of SEM triblock terpolymers with different compositions of the blocks, because every composition can be tailor-made by blending of both, SES and SEM.[83]

The concept of living CDSA was also transferred to the SEM triblock terpolymer wCCMs. Here, a precise length control of the patchy wCCMs with a length dispersity down to 1.1 is

realizable. The patchy corona is not influenced by the living character of this crystallization method. The length of the resulting wCCMs ranges up to 500 nm. Furthermore, the preparation of block comicelles was observed by sequential addition of unimers to seed micelles. If SES seed micelles are used, primarily ABA triblock comicelles were obtained, whereas SEM seed micelles favor the formation of AB diblock comicelles and only a small fraction of ABA triblock comicelles were observed (Figure 1-14).[84] The living character opens the way for creation of complex structures as reported by Winnik and Manners et al.[54,85]
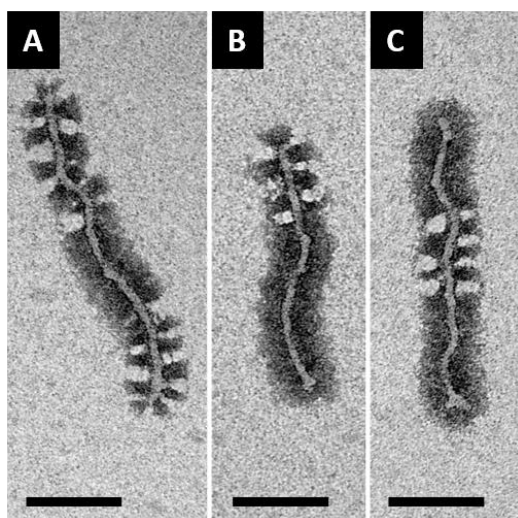
Figure 1-14. TEM micrographs of ABA triblock comicelles formed from SES seeds (A). AB diblock comicelles (B) and ABA triblock comicelles (C) formed from SEM seeds. The samples are selectively stained with RuO_4. Adapted with permission from 84. Copyright (2017) American Chemical Society.

The SEM wCCMs offer an excellent surface activity, which was tested by pendant-drop measurements. The patchy corona compatibilizes the toluene-water interface as the PS patch is hydrophobic and the PMMA patch shows an increased hydrophilicity in comparison with PS. The surface activity measured in this experiment was similar to that obtained by Janus particles. Here, an application as pickering emulsifier or compatibilizer in polymer blends is possible.[86] To enhance the stability of the patchy micelles, SEM triblock terpolymers were non-covalently grafted onto the surface of CNTs by the use of ultrasonification and heteroepitaxial growth. The patchy corona was preserved on the CNTs, which promises a high surface activity and an application as blend compatibilizer.[87] Studies for the compatibilization PS/PMMA blends (80/20 wt-%) proofed the high surface activity (Figure 1-15). With increasing amount of patchy CNTs, the PMMA domains within the PS matrix

decreased in size. As CNTs are known for mechanical enhancement of polymers, these composite materials offer a high technical relevance in industrial scale.[88]
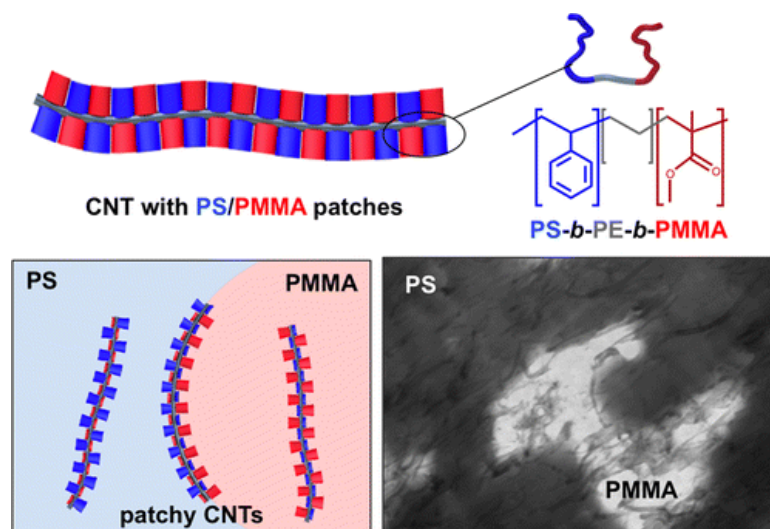
Figure 1-15. Concept of heteroepitaxial growth of SEM triblock terpolymers onto CNTs (upper row) and application as blend compatibilizer (lower row). Reprinted with permission from 88. Copyright (2017) American Chemical Society.

1.1.2.3 Other Crystalline-Coil Block Copolymers

In addition to PFS- and PE-containing block copolymers, some other BCPs with crystallizable blocks have been used in the past. As these BCPs and their self-assembly are not investigated as detailed as PFS- and PE-containing BCPs, they are only shortly mentioned in this chapter.

Different groups used diblock copolymers of poly(ε-caprolactone)-*block*-poly(ethylene oxide) (PCL-*b*-PEO) for self-assembly in water. The obtained morphologies were dependent on the composition of the diblock copolymer[89] and the pH of the aqueous medium.[90] The crystalline core of the micelles was formed by PCL and the water-soluble corona was formed by PEO. The morphologies ranged from spherical[91] and cylindrical micelles[92] to platelets.[93] The growth and the fragmentation of the cylindrical micelles was studied intensively. Here, the affinity for hydrolytic degradation of the PCL core in an aqueous medium was proven.[94] However, these biodegradable micelles were used as drug delivery agent for an anti-cancer drug. The tests were done with mice and showed that the cylindrical micelles exhibit an increased life time in blood circulation in comparison to spherical micelles.[95]

The fragmentation of the cylindrical PCL-*b*-PEO micelles was also shown to be reversible, as hydrogen bond forming agents induced an elongation of the wCCMs.[96] Furthermore, studies on the growth of PCL-*b*-PEO wCCMs under different conditions revealed two different growing mechanisms: the first is a fast crystallization process, in which the micelles grow by the addition of unimers; the second is a crystallization process, in which only the short cylindrical micelles grow with each other by end-to-end coupling.[97] A cocrystallization of PCL diblock copolymers bearing different second blocks, and PCL homopolymer yielded in platelet like micelles.[98,99] PCL nanocylinders were formed by PCL-*b*-PS diblock copolymers with photocleavable junctions. UV light exposure cleaved the PS corona from the cylindrical core and yields the before mentioned PCL cylinders.[100]

The PEO block was also used as crystalline core. To this end, PB or PS formed the corona blocks. These BCPs enable the fabrication of platelets with microchannels[101] and hybrid materials with silica NPs.[102] Furthermore, a phase map for the self-assembly of PB-*b*-PEO diblock copolymers resulting in different morphologies ranging from spheres, worms and rods to platelets and dendrites was generated.[103]

Cylindrical micelles can be obtained by CDSA of poly(*L*-lactide) (PLLA) containing diblock copolymers.[104] These BCPs can be prepared by living CDSA or by stereocomplex formation with poly(*D*-lactide) (PDLA).[105] In a mixture of PLLA- and PDLA-containing cylindrical micelles, respectively, a reorganization of the crystalline cores leads to a stereocomplexation of PLLA and PDLA, which yields spherical micelles with a mixed PLLA/PDLA core (Figure 1-16).[106] The morphology control was also achieved for enantiomeric pure PLLA-containing diblock copolymers, so spherical and cylindrical micelles can be tailor-made.[107] Using PLLA-*b*-PAA diblock copolymers, hollow tubes were prepared.[108] The variation of the corona forming block (for example PEO) increased the accessible repertoire of cylindrical micelles.[109] With the use of triblock terpolymers, the applicability of these cylindrical micelles was increased as a functionalization of a segment, which is in close proximity to the crystalline core leads to a successful incorporation of hydrophobic drugs.[110]
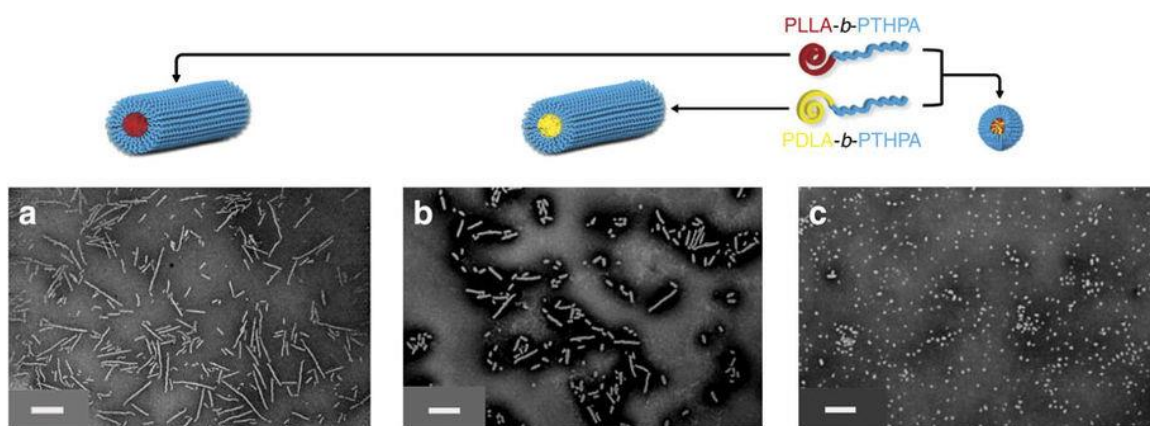
Figure 1-16. WCCMs of a PLLA-containing diblock copolymer (a) and a PDLA-containing diblock copolymer (b). Stereocomplex formation of a mixture of both diblock copolymers yields in spherical micelles (c). Scale bars = 500 nm. Adapted from Ref. 106, open access journal, no permission required.

Some further BCPs, which are less examined, are able for CDSA. These BCPs contain crystallizable blocks of poly(3-hexylthiophene) (P3HT),[111–113] poly(3-heptyl seleno-phene),[114] polyacrylonitrile (PAN),[115,116] polyoxazoline,[117] isotactic PS, syndiotactic polypropylene (PP) or poly(ether amine).[118–120] P3HT could find an application in solar cells and using PAN as crystalline core, CNTs can be observed by thermal treatment.

1.2 Nanoparticles

Nanoparticles (NPs) are of great interest for nowadays science. The versatile and unique properties offer a wide range of applications, for example in photonics, catalysis or medicine.[121–123] The high surface-to-volume ratio exhibits a remarkable enhancement for catalytic reactions, as for example bulk gold shows no catalytic activity in contrast to AuNPs.[124] This enhanced reactivity of NPs, caused by an increased surface energy, leads to a melting point depression in comparison to the bulk material.[125,126] Furthermore, NPs are prone to agglomeration and aggregation already at room temperature, which needs to be prevented by stabilizing ligands. These ligands possess different functional groups, which are able to bind to the NP surface because of selective interactions. The synthesis of ligand-stabilized NPs is described in the Chapters 1.2.1 Syntheses of Nanoparticles and 1.2.2 Polymer-Nanoparticle Hybrid Materials.

Another special property is the localized surface plasmon resonance (LSPR) of noble metal NPs, which is based on light interaction with these NPs. The model, which is used to describe the plasmon resonance, assumes that the positively charged metal atoms are fixed in their location whereas the free valence electrons are able to move around these fixed metal atoms. An electromagnetic field, which is caused by incident light, interacts with these valence eletrons and induces an oscillation if the diameter of the metal NPs is smaller than the wavelength of the incident light. This oscillation is called plasmon.[127] The described model is suitable for surfaces of thin metal films (surface plasmon resonance) (Figure 1-17 a) and for metal NPs showing a LSPR (Figure 1-17 b).[128] If the electric field is assumed to be continuous, the static polarizability α is given by:[127]

$$\alpha = 4\pi R^3 \frac{\varepsilon - \varepsilon_m}{\varepsilon + 2\varepsilon_m}$$

with R = radius of the sphere, ε = complex dielectric function of the metal and ε_m = dielectric constant of the surrounding medium. This leads to the conclusion that the LSPR is dependent on the size of the metal NPs, the type of metal and the type of surrounding medium. In addition, the shape of metal NPs influences the LSPR as the oscillation of the electrons is non-isotropic for non-spherical NPs. Here, a localization of the oscillation along the edges, corners or principal axes can be observed.[127] The LSPR of NPs is used in different applications like optoelectronics and sensors.[129–131]
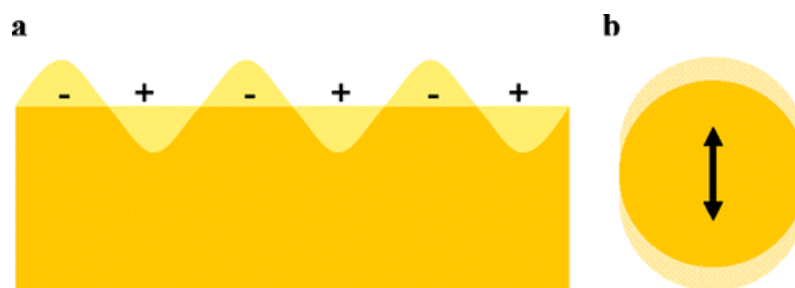
Figure 1-17. Schematic surface plasmon resonance (a) and localized surface plasmon resonance (b). Reprinted with permission from 130. Copyright (2017) American Chemical Society.

For magnetic materials, NP can exhibit superparamagnetic behavior. If the NPs are smaller than a critical diameter, they are considered as an assembly of individual magnetic moments. These individual magnetic moments are fluctuating at low thermal energies like room temperature. If a magnetic field is applied to the NP, an orientation of the magnetic moments is observable. If the magnetic field is released, the NP show a paramagnetic behavior. This

switching of magnetic behavior is faster than the detection limit, which leads to a magnetization curve without hysteresis.[132]

1.2.1 Syntheses of Nanoparticles

For the synthesis of NP, a lot of different methods ranging from reduction of a metal salt, seeded growth, ligand exchange, (reversed) micelles, sol-gel process, UV light reduction, sonochemical or heat treatment to radiolysis and vapor deposition were established until now.[126,129,133–135] As this work focusses on AuNP, the most common synthetic routes for the synthesis of AuNP are described in this chapter.

A well-known method for the synthesis of citrate-stabilized AuNP was reported by Turkevich in 1951.[136] Tetrachloroauric acid trihydrate ($HAuCl_4 \cdot 3\,H_2O$) is reduced in boiling water with a 1% sodium citrate solution. The color change from yellow to colorless, greyish blue and wine red usually proceeds within the first 5 min. These colors are characteristic for the different reduction and nucleation steps within this synthesis. First, Au^{3+} (yellow color originating from $HAuCl_4 \cdot 3\,H_2O$) is reduced to Au^+ (colorless) which is complexed by the oxidation product of citrate, a dicarboxy acetone species (Figure 1-18). Further reduction leads to the formation of Au^0 nuclei (greyish blue color) which grow to the AuNP (wine red color).[137]
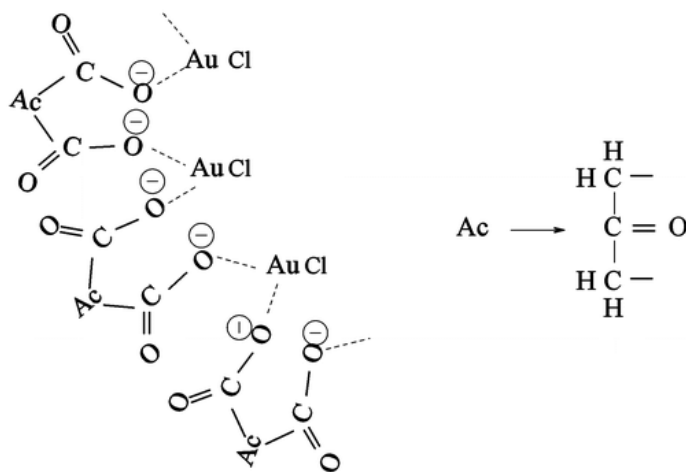
Figure 1-18. Complex formed by gold(I) chloride (AuCl) and dicarboxy acetone. Reprinted with permission from 137. Copyright (2017) American Chemical Society.

Turkevich obtained AuNPs with spherical shape and a rather narrow size distribution. This method was further optimized by Frens, who investigated systematically the influence of the citrate-to-gold ratio.[138] This led to spherical AuNPs with controllable diameter. As citrate

acts as reducing and stabilization agent, the nucleation is dependent on the amount of citrate. The more citrate is added to a boiling $HAuCl_4$ solution, the more nuclei are formed and the diameter of the NPs decreases. This synthesis route for AuNPs was picked up by a lot of scientists. Different variations in reaction time, temperature, reducing agent, pH and starting concentration of $HAuCl_4$ showed the versatility of this route.[139–145] Spherical AuNPs in the size range of 5-150 nm were realized, but the dispersity of AuNPs with sizes above 20 nm was comparably broad.[139] In contrast, very small AuNPs (~ 5 nm) showed a small dispersity. Therefore, these AuNPs were used for seeded growth methods. There are different approaches for seeded growth, but in general, seed particles in the size range of 3.5-5 nm are formed first by a strong reducing agent like sodium borohydride or tannic acid. Then, sodium citrate is added for stabilization and in different cycles of addition, more tetrachloroauric acid and a weaker reducing agent is added. This leads to a homogeneous growth of the AuNPs and the dispersity is significantly reduced.[146–149] The seeded growth method was also transferred to the synthesis of gold nanorods (Figure 1-19). Here, a tenside, like cetyltrimethylammonium bromide (CTAB), is used to ensure unidirectional growth of the spherical seed particles.[150–152]
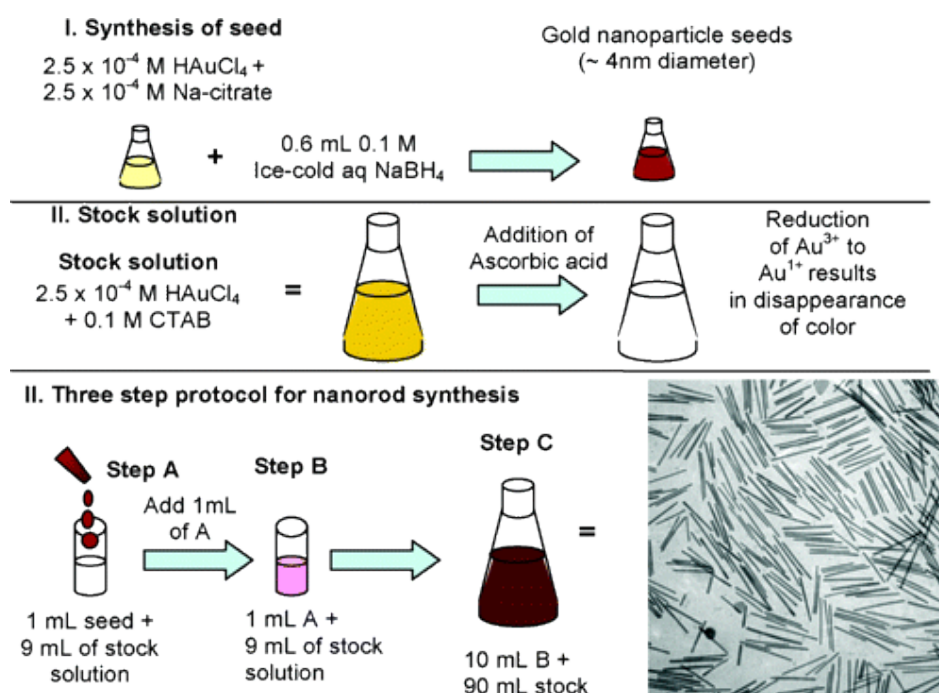
Figure 1-19. Synthesis procedure for gold nanorods according to a seeded-growth protocol. Reprinted with permission from 151. Copyright (2017) American Chemical Society.

With the use of other reducing agents than sodium citrate, the need for other ligands for AuNP stabilization arose. The first reports about thiol-stabilized AuNPs were published in

1993 by Giersig and Mulvaney.[153] They used alkanethiols with different alkyl chain length to produce a monolayer of AuNPs on carbon-coated copper grids. For preparation of the alkanethiol-stabilized AuNPs, a one-phase ligand exchange was applied. The ligand exchange method was improved by Brust and Schiffrin, who used a two-phase ligand exchange with tetraoctylammonium bromide (TOAB) as phase transfer agent (Figure 1-20 A).[154] The purification step was simplified as the organic phase was easily separable from the aqueous phase and could be precipitated. The resulting powder was dissolved in toluene and the particle size ranged from 1-3 nm. In 1995, the two-phase ligand exchange method was improved to a one-phase *in situ* method in methanol (Figure 1-20 B).[155] The AuNPs were formed by direct reduction of $HAuCl_4 \cdot 3\,H_2O$ with aqueous sodium borohydride ($NaBH_4$) in presence of a thiol ligand. The AuNPs prepared by this method showed a rather broad size distribution ranging from 2.4 to 7.6 nm. However, the use of TOAB was avoided and any thiol soluble in the same solvent like $HAuCl_4 \cdot 3\,H_2O$ was suitable for this synthesis.
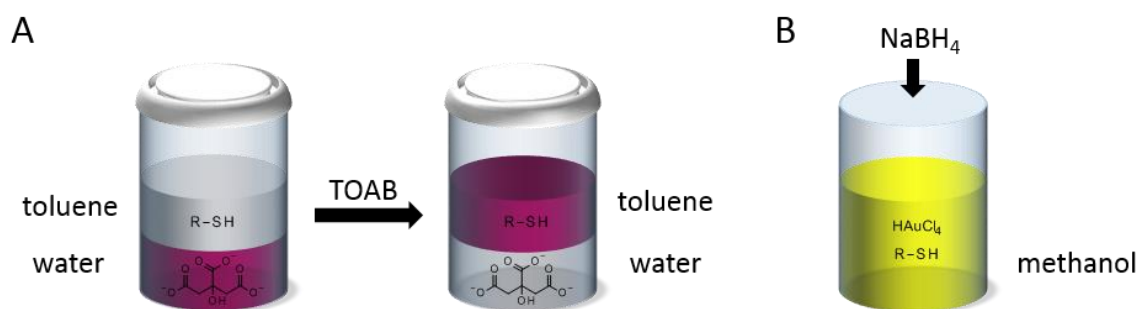
Figure 1-20. Synthesis of thiol-stabilized AuNP (purple color) by a two-phase ligand exchange (A) and the *in situ* reduction of $HAuCl_4 \cdot 3\,H_2O$ (B).

Both, the two-phase ligand exchange and the one-phase *in situ* method paved the way for very different approaches of AuNP stabilization, as the limitations of an aqueous system were eliminated. Furthermore, a variety of different ligands bearing different functional groups including disulfides,[156–158] trithiolates,[159] amines,[160–162] and carboxyls[163] were investigated. In addition to these monomeric stabilizing ligands, a variety of end-functionalized homopolymers and BCPs were employed to prevent agglomeration and aggregation of AuNPs very effectively, which will be dicussed in detail in the next section.

1.2.2 Polymer-Nanoparticle Hybrid Materials

Polymers as stabilizers for NPs provide different advantages in comparison to monomeric stabilizers. The higher molecular weight of polymers causes an increased steric repulsion, which effectively prevents agglomeration of the NPs in both, dissolved and dry state. Furthermore, the processibility of NPs is enhanced since they feature similar properties as the polymeric stabilizer. Thus, the hydrophilicity, the elasticity and the biocompatibility can be precisely tuned.[164–174] For example, Agarwal et al. produced thermoplastic elastomers by physically crosslinking of α,ω-thiol-terminated polyisoprene with AgNP.[169] In another work, high-molecular weight thiol-terminated PS was grafted onto AgNP by ligand exchange. The crucial parameter for successful stabilization was the use of ultrasonification, which enabled the formation of droplets. The AgNP-stabilizing thiol-groups were found at the interface of these droplets, thus, resulting in a high accessibility for the AgNP.[172] Greiner et al. reported the synthesis of tailor-made polymeric cages which can be used for size-selective fishing of AuNP.[173] The cages were prepared by a grafting-around technique, which gives rise to precise size-tuning of the cages. Different polymerization steps, crosslinking and etching of the used template-AuNP led to the final stable cages bearing Au-coordinating thiol groups (Figure 1-21). The cages were applied for the bottom-up synthesis of different metal NPs like AgNPs, PdNPs and PtNPs with a narrow size distribution., showing the versatility of these systems.[175]
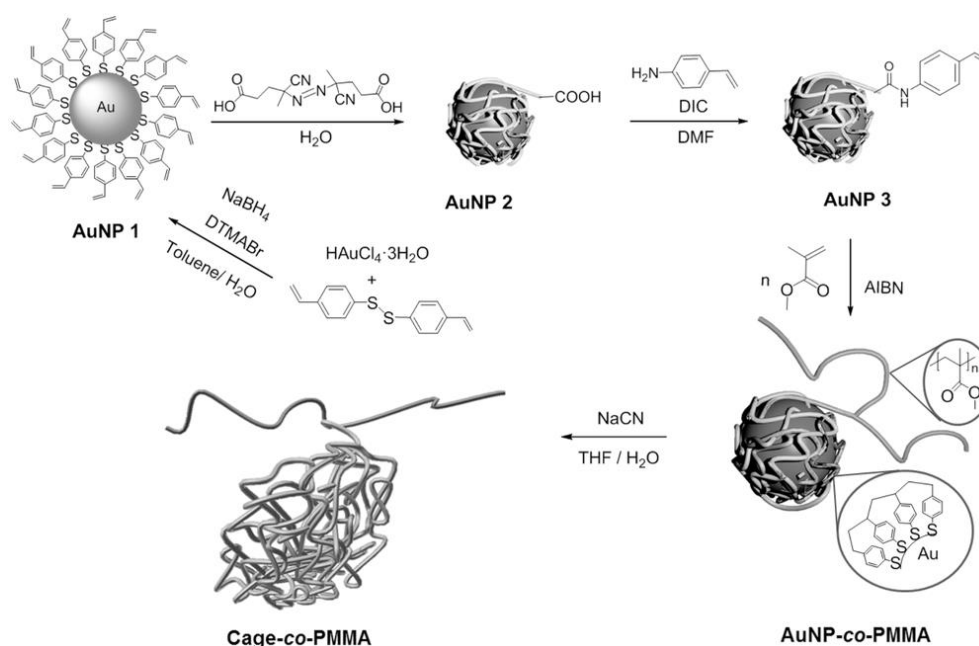

Figure 1-21. Synthesis route for the preparation of polymeric cages for AuNP-stabilization. Adapted from Ref. 173, open access journal, no permission required.

For stabilization of NPs, not only homopolymers but also BCPs are of great interest. The combination of different material properties and the possibility for compartmentalized structures provide a defined spatial control and therefore enhanced stability against aggregation and tailor-made optical properties. The most common used polymers for stabilization of different noble metal NPs in compartmentalized micelles are P2VP, P4VP, PAA and poly(methacrylic acid) (PMAA), as these polymers provide an easy access via controlled polymerization methods.

P2VP was used by Pochan et al. in core-shell-corona micelles prepared from PS-*b*-P2VP-*b*-PEO.[176] They succeeded in selectively loading AuNPs in the P2VP-shell by *in situ* reduction of $HAuCl_4$ with sodium borohydride in presence of the micelles. Lee et al. prepared hybrid materials of hollow flower-like micelles from a P2VP-*b*-poly(2-(4-vinylphenyl)pyridine), in which AuNPs were synthesized within the cavity of the micelles.[177] The stabilization was attributed to the P2VP moieties forming the cavity. Additional reduction of a platinum (Pt) salt resulted in dendritic PtNP growing from the AuNP surface. Cylindrical hybrid micelles were obtained by Walter and Müller et al., who self-assembled miktoarm star polymers with a PS-, a PB- and a P2VP-arm in bulk and crosslinked the PB moiety.[178] Dissolution by ultrasonification yielded in cylindrical micelles with a PB core and a corona with PS and P2VP compartments. The P2VP moieties were selectively loaded with AuNPs, AgNPs and cadmium selenide NPs (CdSe NPs), which was proven by a tilt series using TEM measurements.

Zhang et al. used a polymerization induced self-assembly process to form PS particles, on which poly(chloromethylstyrene)-*graft*-P4VP chains are bound.[179] These chains collapse onto the PS particles upon addition of water. Nevertheless, AuNPs can be selectively incorporated in the P4VP domains by *in situ* reduction of $HAuCl_4$ with $NaBH_4$. Depending on the size of the PS particles, the grafting density of the poly(chloromethylstyrene)-*graft*-P4VP can be controlled. This influences the loading density of AuNPs on the surface of the PS particles. Kim and Hawker et al. presented different studies on hybrid materials of multicompartment micelles and PS-stabilized AuNPs using PS-*b*-P2VP and PS-*b*-P4VP for coordination of the AuNPs.[180–182] The hybrid micelles were prepared in an oil-in-water emulsion of the BCPs and AuNPs in water by inducing the self-assembly via evaporation of the organic solvent phase. The presence of the AuNPs led to different multicompartment structures like raspberries, striped ellipsoidal particles or convex lens shaped particles (Figure 1-22). All these particles showed a highly precise arrangement of the AuNPs within

the P2VP or P4VP segments. Zhu and Jiang et al. used a similar method for preparing clover-like micelles and ellipsoids through emulsification of PS-*b*-P4VP diblock copolymers.[183] They incorporated PS-stabilized AuNPs selectively in the PS domains of the particles and P4VP-stabilized AuNP in the P4VP domains. They succeeded in preparing Janus particles with one AuNP domain, which were cooperatively self-assembled to clover-like micelles.
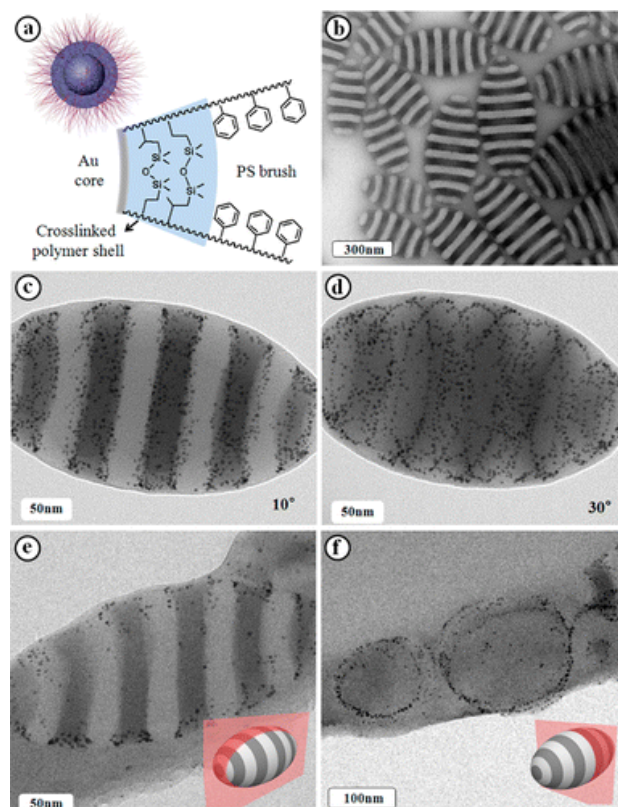
Figure 1-22. Striped ellipsoidal micelles formed by a PS-*b*-P2VP diblock copolymer. The micelles were decorated with PS-stabilized AuNP. Reprinted with permission from 181 Copyright (2017) American Chemical Society.

PAA and PMAA were used in different approaches for the preparation of metal NP-polymer hybrid materials. Pochan et al. showed the selective incorporation of AuNPs in the PAA domains of multicompartment micelles composed of PAA-*b*-poly(meth acrylate)-*b*-PS.[184] They created a homogeneous alternating distribution of AuNP loaded segments and pure polymer segments over a micrometer length scale. In 2011, they published a different protocol for the incorporation of AuNPs in PS domains of blend particles of PAA-*b*-PS and PAA-*b*-PB.[185] Blending of the two diblock copolymers yields in spherical micelles with a compartmentalized core of PS and PB and a homogeneous PAA corona. The composition of the core was controlled by the diblock copolymer ratio. The AuNPs were stabilized by PS

and mixed with the diblock copolymers before addition of a selective solvent, which ensures the incorporation of the AuNPs in the PS domains.

Another kind of NP-polymer hybrid materials is based on the formation of interpolyelectrolyte complexes (IPECs). Schacher and Müller et al. reported two different morphologies of the IPECs, in which they incorporated AuNPs, PtNPs and PdNPs to study the selectivity of NP incorporation. The first system consisted of core-shell-shell-corona micelles built by PB-*b*-P2VP$_q$-*b*-PMAA and P2VP$_q$-*b*-PEO.[186] In both BCPs, the P2VP block was quaternized (P2VP$_q$) to obtain a pH-independent positive charge. At high pH values, the pure PB-*b*-P2VP$_q$-*b*-PMAA triblock copolymer formed dynamic MCMs with a PB core, an IPEC shell of P2VP$_q$ and parts of the PMAA chains, and a corona consisting of excess PMAA. Addition of P2VP$_q$-*b*-PEO resulted in a second IPEC. The micelles were loaded with AuNPs before and after formation of the second IPEC, showing that in the pure PB-*b*-P2VP$_q$-*b*-PMAA micelles the AuNPs are found in the corona, whereas in the IPEC with additional P2VP$_q$-*b*-PEO, the AuNPs are located within the PMAA and P2VP$_q$ phase (Figure 1-23). The second system was self-assembled from polybutadiene-*block*-poly(2-vinyl pyridine-*block*-poly(*tert*-butyl methacrylate) (BVT) in bulk.[187] Crosslinking of the PB block, quaternization of the P2VP block and hydrolysis of the poly(*tert*-butyl methacrylate) block led to compartmentalized cylinders, which were used for IPEC formation. AuNPs, PtNPs and PdNPs were loaded into the micelles, showing a selective loading of the PdNPs within the intramicellar IPEC domains whereas AuNPs and PtNPs were loaded in both, the intramicellar IPEC domains and the PMAA corona.
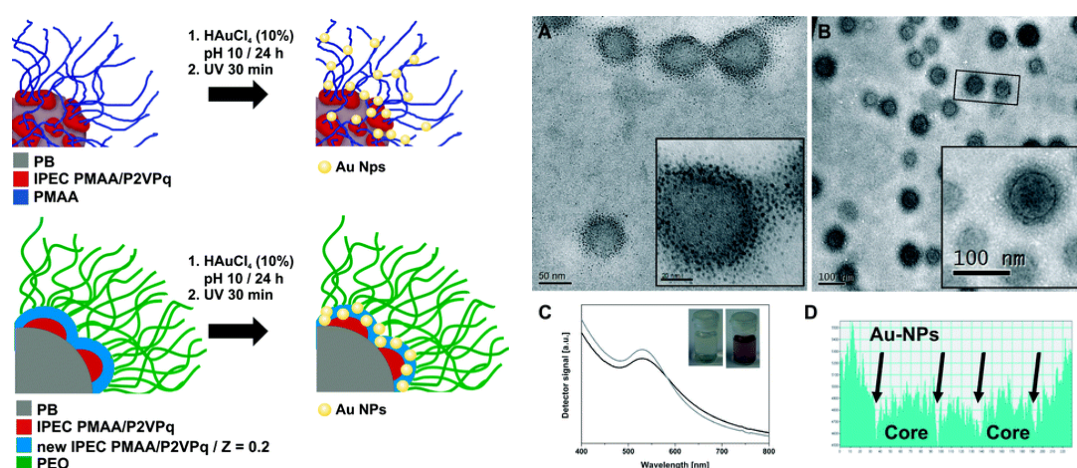
Figure 1-23. Incorporation of AuNPs in PB-*b*-P2VP$_q$-*b*-PMAA micelles (upper scheme, A) and in IPECs formed by addition of P2VP$_q$-*b*-PEO (lower scheme, B). The UV-Vis spectra prove the presence of AuNPs in both micellar species (C). The grey scale analysis of the black rectangle in B clearly shows AuNP formation around the core of the IPEC (D). Reprinted with permission from 186. Copyright (2017) American Chemical Society.

Moffitt et al. used PS-*b*-PAA-*b*-PMMA stabilized cadmium sulfide NPs (CdSNPs) as building blocks for the self-assembly of supermicelles.[188] Here, the PAA block binds to the CdSNP surface and crosslinking of this block generated stable micelles. Hydrolysis of the PMMA corona block leads to PMAA. Depending on the solvent quality for both corona blocks, the micelles were aggregated to form spherical or worm-like supermicelles containing the CdSNPs in different compartments. In another approach, AuNPs and two different diblock copolymers were assembled simultaneously.[189] The AuNP were stabilized by 11-mercapto-1-undecanol. In presence of a PS-*b*-PAA diblock copolymer, the solvent quality was changed and stable polymersomes were obtained. The same behavior was observed in presence of a PEO-*b*-PLA diblock copolymer. By changing the conditions of the self-assembly process even multicompartment polymersomes were obtained.

Except the different examples for NPs stabilized by P2VP, P4VP, PAA and PMAA blocks, there are some other carbonyl- or nitrogen-containing polymers, which were used for formation of compartmentalized micelles. A triblock terpolymer with a lipoic acid functionalized middle block was self-assembled to form spherical micelles, rods and vesicles with AuNPs in the interfaces of the micellar structures.[190] Davis and Boyer used a poly(dimethylaminoethyl methacrylate) (PDMAEMA) containing triblock terpolymer to form worm-like micelles and vesicles containing AuNPs in the PDMAEMA segments.[191] Polyvinyl formal, poly(dodecyl methacrylate) and titanium dioxide (TiO_2) NPs were self-assembled to tricompartment submicron particles in which the TiO_2 NPs were selectively found at the interface of both polymers or in the poly(dodecyl methacrylate) compartment depending on the pH.[192] Priestley et al. co-assembled PI, amine-terminated PS and citrate-stabilized AuNPs to prepare Janus structures with one half of the particles decorated with AuNPs.[193]

Using amorphous micelles to incorporate metal NP gives rise to a vast amount of morphologies. In contrast, there are limited reports about hybrid materials of semi-crystalline compartmentalized micelles with metal NPs. Manners and Winnik et al. used PFS-*b*-P2VP seed micelles and quaternized the P2VP block to incorporate different metal and metal oxide NPs. Co-crystallization with non-quaternized PFS-*b*-P2VP leads to cylindrical crystalline-core micelles with a functionalized middle part. AuNPs and PbS quantum dots were selectively loaded into this functionalized part.[37] Another possibility is the incorporation of dextran-magnetite NPs or of TiO_2 NPs by a sol-gel-process.[194] The PFS-*b*-P2VP seed micelles can also be crystallized onto the surface of silica (SiO_2) particles by hydrogen bonds

with the P2VP block. Further CDSA with PFS-*b*-P2VP unimers leads to a sunflower-like morphology.[51] Using PFS-*b*-PI wCCMs, the PI corona was crosslinked and the PFS block itself is able to reduce silver ions (Ag$^+$) to form AgNPs.[195] Here, the AgNPs are located closely to the crystalline PFS core (Figure 1-24). The loading density of AgNPs can be controlled by the amount of silver salt. Additionally to AgNPs, AgINPs can be prepared by addition of iodine (I$_2$). The AgINPs were shown to serve as seeds for further growth of AgINPs, so the size of the NPs can be precisely tuned.
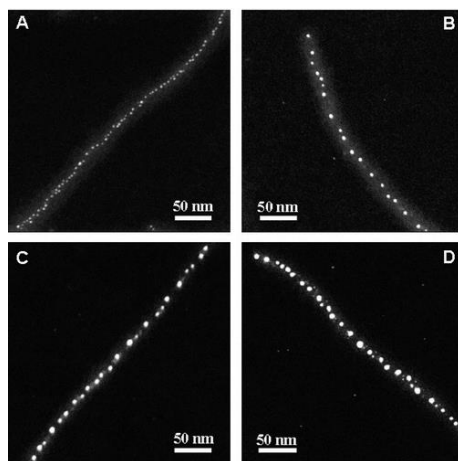
Figure 1-24. PFS-*b*-PI wCCMs loaded with different amounts of AgNPs: 12.5% (A), 25% (B), 50% (C) and 75% (D) with reference to the PFS units. Reprinted with permission from 195. Copyright (2017) American Chemical Society.

1.2.3 Catalysis with Nanoparticles

The unique properties of noble metal NPs enable them for a variety of applications.[196,197] One emerging field of applications is catalysis. The high surface-to-volume ratio leads to a high activity. In particular for Au, the bulk material is inert, but the NPs show a high catalytic activity in different reactions, for example CO oxidation or propylene epoxidation.[124] However, the NPs have a strong tendency for agglomeration because of this high surface-to-volume ratio. Therefore, stabilization of the NPs is indispensable, which is discussed in the preceding two chapters. Polymer-stabilized NPs exhibit different advantages regarding the solubility and, therefore, the activity of the NPs as the stabilizing ligand can be tailored to meet the demands of the catalytic reaction. For AuNPs, one of the most famous catalytic application is the reduction of 4-nitrophenol (4-NiP) with sodium borohydride.[198] This reaction proceeds in aqueous medium, which limits the stabilizing polymer ligands to hydrophilic polymers. The reaction can be easily followed *in situ* by UV-Vis spectroscopy

(Figure 1-25). The characteristic absorption maximum at $\lambda = 400$ nm derives from the nitrophenolate ions and decreases with time. Simultaneously, a smaller peak at $\lambda = 300$ nm, which is ascribed to the formed aminophenol, is increasing with time.
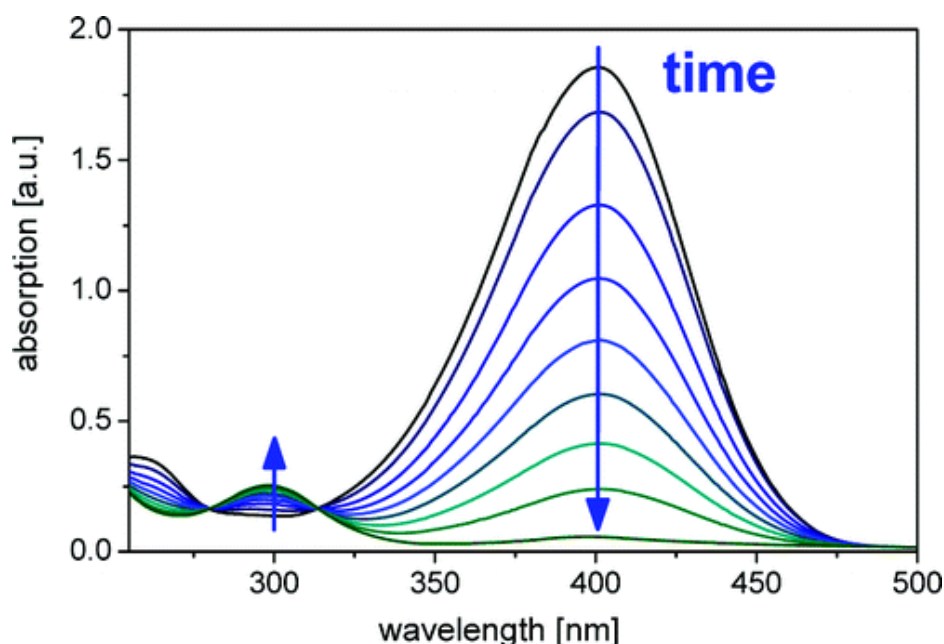
Figure 1-25. Typical UV-Vis spectra of 4-NiP (peak at 400 nm) reduction with $NaBH_4$. Adapted with permission from 198. Copyright (2017) American Chemical Society.

The reduction of 4-NiP was tested with different AuNP-stabilizing polymers, for example PEO-*b*-PAA, PVP or polyethyleneimine (PEI).[199] The disadvantage of these catalysts is the limited reusability of the catalyst material. To overcome this disadvantage, a CO_2-switchable polymer, poly(diethylaminoethyl methacrylate) (PDEAMA) was grafted onto the AuNP surface.[200] In a CO_2 saturated aqueous medium, the AuNPs are dissolved and catalytically active whereas in a N_2 saturated aqueous medium, the PDEAMA collapses and the AuNPs are insoluble. This leads to an easier separation of the catalyst material from the reaction medium.

Supported NP catalysts show a similar advantage, as the catalyst is insoluble in the reaction medium and can be easily separated by filtration. To this end, Ballauff et al. used spherical polyelectrolyte brushes with a solid PS core to incorporate AuNPs in the poly[(2-aminoethyl) methacrylate hydrochloride] corona.[201] The hybrid materials showed high activity in the reduction of 4-NiP, but less stability against agglomeration than alloys of AuNP and PtNP or PdNP.[202,203] Other approaches cover the use of AuNP dispersed on inorganic supports and also show a high catalytic activity.[204–206]

Beneath the catalysis in aqueous medium, for which the reduction of 4-NiP is the most common model reaction, there are several important catalytic reactions in organic media.[207] One example is the alcoholysis of dimethylphenylsilane with *n*-butanol (Figure 1-26).
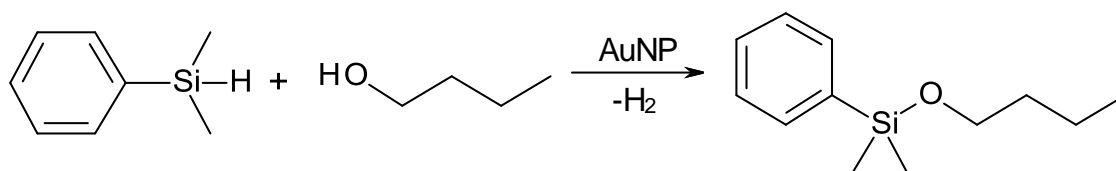
Figure 1-26. Alcoholysis of dimethylphenylsilane with *n*-butanol with an AuNP catalyst.

First reports showed that small AuNPs (3-5 nm) dispersed on aluminum oxide need harsh conditions (100 °C, 3h) for the conversion of the silane.[208] With ultrasmall AuNPs (d < 1 nm) supported on SiO_2, the temperature to yield quantitative conversion was decreased to 50 °C, but the reaction time increased to 5 h. However, the alcoholysis was conducted in THF as solvent, which could have an impact on the reaction time.[209] 3 nm-AuNP were supported on nanosized hydroxyapatite and showed a superior catalytic activity for small amounts of educts (2 mmol dimethylphenylsilane). The alcoholysis was conducted at room temperature and quantitative yield was observed after 20 min. Upscaling of the silane amount to 50 mmol demands for harsh reaction conditions (110 °C) and an increased reaction time of 15 h.[210] The alcoholysis of dimethylphenylsilane with *n*-butanol was further examined by self-assembled monolayer capped AuNP. These AuNP were immobilized on Au-coated substrates and yield a conversion of 82.8 % after 1 h at room temperature.[211] All of these examples cover the use of AuNP fixed on inorganic supports. The first example of polymer-supported AuNP were reported by Greiner et al. who used a nonwoven of poly(*p*-xylylene) tubes to immobilize AuNP at the inner wall of these tubes.[171] This catalyst was used in a teabag-like manner, which means, the nonwoven was dipped into the reaction medium and after full conversion, this nonwoven could be simply removed without the need of filtration or other purification steps. The polymer-supported AuNP catalyst showed quantitative conversion of dimethylphenylsilane with *n*-butanol after 26 h at room temperature and was reused in 18 cycles of catalysis without loss of activity.

AuNPs are not only able to catalyze organic reactions, they are also able to enhance the catalytic activity of transition metal oxides, for example TiO_2 or zinc oxide (ZnO).[212–215]

These hybrid catalyst materials can be applied in photocatalytic advanced oxidation processes (AOPs). The photocatalytic AOPs are based on the formation of highly reactive hydroxyl radicals, which are able to oxidize organic pollutants from wastewater. The role of the AuNPs in the hybrid catalyst materials is to enhance the light absorption range from UV to visible light. Therefore, only the solar spectrum and the hybrid catalysts are needed for purification of wastewater. Hybrid catalysts of AuNPs and TiO_2 were tested in the oxidation of thiocyanates[216] and 1-phenylethanol[217] as well as the degradation of 4-chlorophenol[218], oxalic acid[219] and formic acid[213] and showed higher activity than the pure TiO_2 catalysts. However, the enhancement of photocatalytic activity is not restricted to TiO_2 catalysts. Also hybrid materials of AuNP and ZnO were successfully used for the photocatalytic degradation of methyl blue[220] and methyl orange.[215] Another example describes AuNP doped silica and zirconium oxide. Both materials showed a clearly enhanced catalytic activity in the degradation of sulforhodamine-B in comparison to the pure transition metal oxides.[221]

1.3 Objective of the Thesis

In general, the activity of the catalyst in homogeneous catalysis is higher than for heterogeneous catalysts. However, a complex purification of the products and the expensive regeneration of the catalyst limit the applicability of homogeneous catalysts. Hence, there is a demand for heterogenous catalysts featuring an easy reusability in combination with a high activity. Mesostructured catalysts combine both advantages, as they exhibit a high active surface area while providing easy reusability through the mesostructure. Micellar polymeric templates are promising candidates for the construction of mesostructured catalysts, as they offer the possibility for efficient stabilization of nanoparticles (NPs) without losing the active surface area. Until now, different organic-inorganic hybrid materials bearing one or even two types of NPs have been described. However, the regio-selective incorporation of these NPs in specific compartments of micelles is still challenging. A synthetic route for the production of well-defined hybrid materials, decorated with two different types of NPs in specific regions of the polymeric templates would offer the opportunity to observe synergistic effects for an application in catalysis. Therefore, the main objective of this thesis was the synthesis of such binary regio-selectively loaded mesostructured catalysts, which

provide high activity and easy reusability in catalysis. To achieve this aim, two concepts were considered.

The first concept deals with worm-like crystalline-core micelles (wCCMs) with a microphase-separated corona made of alternating polystyrene and poly(methyl methacrylate) patches which offer structural advantages with regard to the production of mesostructured catalysts. In former studies, these patchy wCCMs were successfully obtained by crystallization-driven self-assembly (CDSA) in solution. The alternating nanometer-sized patches are ideal templates for the regio-selective incorporation of different catalytically active metal and metal oxide NPs. However, the corona patches do not bear suitable anchor groups for the stabilization of NPs. Therefore, the first challenge of this thesis was to introduce such anchor groups in the patchy corona of the wCCMs and to develop different strategies for hybrid material formation with the NPs. For an application of the hybrid wCCMs as mesostructured catalysts, a key question was to develop a strategy to support the hybrid wCCMs on a polymeric support, which should guarantee easy reusability without loss of activity. Finally, a route for binary loading of the patchy wCCMs with two types of NPs was a major aspect.

The second concept aims in the development of highly porous, self-supported transition metal oxide catalysts for the photocatalytic purification of clinical wastewater, which is highly contaminated with antibiotics, like ciprofloxacin. To enhance the water solubility of these antibiotics, carboxylate groups are generated, i.e. a catalyst with a positive surface charge favors electrostatically adsorption of the antibiotics. Here, zinc oxide is a promising candidate. A major issue of this thesis was to develop a synthetic strategy using cylindrical polymer brushes (CPBs) with a polyelectrolyte corona and a crosslinked core to incorporate zinc oxide NPs by electrostatic interactions. The CPBs offer the advantage of an increased temperature stability and a higher aspect ratio than the patchy wCCMs. This is inevitable for the pyrolytic template removal and the formation of stable self-supporting mesostructured catalysts. The combination of zinc oxide with noble metal NPs, which show a localized surface plasmon resonance, promises an increase in catalytic activity as the absorption of light is shifted to the visible spectrum. This concept should result in catalysts with improved catalytic activity and reusability in comparison to commercially available catalysts like Degussa P25, a titanium dioxide catalyst.

1.4 References

[1]   A. H. Gröschel, A. H. E. Müller, *Nanoscale* **2015**, *7*, 11841–11876.

[2]   J. Du, R. K. O'Reilly, *Chem. Soc. Rev.* **2011**, *40*, 2402–2416.

[3]   S. Förster, T. Plantenberg, *Angew. Chem. Int. Ed. Engl.* **2002**, *41*, 689–714.

[4]   J.-F. Gohy, *Adv. Polym. Sci.* **2005**, *190*, 65–136.

[5]   T. H. Epps, III, R. K. O'Reilly, *Chem. Sci.* **2016**, *7*, 1674–1689.

[6]   Y. Mai, A. Eisenberg, *Chem. Soc. Rev.* **2012**, *41*, 5969–5985.

[7]   M. D. Ward, M. J. Horner, *CrystEngComm* **2004**, *6*, 401–407.

[8]   F. S. Bates, *MRS Bull.* **2005**, *30*, 525–532.

[9]   F. H. Schacher, P. A. Rupar, I. Manners, *Angew. Chem. Int. Ed.* **2012**, *51*, 7898–7921.

[10]   M. Antonietti, S. Förster, *Adv. Mater.* **2003**, *15*, 1323–1333.

[11]   K. Kataoka, A. Harada, Y. Nagasaki, *Adv. Drug Deliv. Rev.* **2001**, *47*, 113–131.

[12]   G. Gaucher, M. H. Dufresne, V. P. Sant, N. Kang, D. Maysinger, J. C. Leroux, *J. Control. Release* **2005**, *109*, 169–188.

[13]   R. K. O'Reilly, C. J. Hawker, K. L. Wooley, *Chem. Soc. Rev.* **2006**, *35*, 1068–1083.

[14]   A. Blanazs, S. P. Armes, A. J. Ryan, *Macromol. Rapid Commun.* **2009**, *30*, 267–277.

[15]   J. Rodríguez-Hernández, F. Chécot, Y. Gnanou, S. Lecommandoux, *Prog. Polym. Sci.* **2005**, *30*, 691–724.

[16]   Y. Yu, L. Zhang, A. Eisenberg, *Macromolecules* **1998**, *31*, 1144–1154.

[17]   M. Müllner, A. H. E. Müller, *Polymer* **2016**, *98*, 389–401.

[18]   M. Zhang, A. H. E. Müller, *J. Polym. Sci. Part A Polym. Chem.* **2005**, *43*, 3461–3481.

[19]   S. S. Sheiko, B. S. Sumerlin, K. Matyjaszewski, *Prog. Polym. Sci.* **2008**, *33*, 759–785.

[20]   M. Müllner, J. Yuan, S. Weiss, A. Walther, M. Förtsch, M. Drechsler, A. H. E. Müller, *J. Am. Chem. Soc.* **2010**, *132*, 16587–16592.

[21]   M. Zhang, T. Breiner, H. Mori, A. H. E. Müller, *Polymer* **2003**, *44*, 1449–1458.

[22]   M. Zhang, M. Drechsler, A. H. E. Müller, *Chem. Mater.* **2004**, *16*, 537–543.

[23]   J. Yuan, M. Drechsler, Y. Xu, M. Zhang, A. H. E. Müller, *Polymer* **2008**, *49*, 1547–1554.

[24]   G. Liu, L. Qiao, A. Guo, *Macromolecules* **1996**, *29*, 5508–5510.

[25]   Y. Ruan, L. Gao, D. Yao, K. Zhang, B. Zhang, Y. Chen, C. Y. Liu, *ACS Macro Lett.* **2015**, *4*, 1067–1071.

[26] A. O. Moughton, M. A. Hillmyer, T. P. Lodge, *Macromolecules* **2012**, *45*, 2–19.

[27] A. H. Gröschel, A. Walther, T. I. Löbling, F. H. Schacher, H. Schmalz, A. H. E. Müller, *Nature* **2013**, *503*, 247–251.

[28] B. Fang, A. Walther, A. Wolf, Y. Xu, J. Yuan, A. H. E. Müller, *Angew. Chem. Int. Ed.* **2009**, *48*, 2877–2880.

[29] A. H. Gröschel, A. Walther, T. I. Löbling, J. Schmelz, A. Hanisch, H. Schmalz, A. H. E. Müller, *J. Am. Chem. Soc.* **2012**, *134*, 13850–13860.

[30] A. Walther, A. H. E. Müller, *Chem. Rev.* **2013**, *113*, 5194–5261.

[31] T. I. Löbling, O. Borisov, J. S. Haataja, O. Ikkala, A. H. Gröschel, A. H. E. Müller, *Nat. Commun.* **2016**, *7*, 12097–12106.

[32] T. I. Löbling, O. Ikkala, A. H. Gröschel, A. H. E. Müller, *ACS Macro Lett.* **2016**, *5*, 1044–1048.

[33] T. Vilgis, A. Halperin, *Macromolecules* **1991**, *24*, 2090–2095.

[34] J. Massey, K. N. Power, I. Manners, M. A. Winnik, *J. Am. Chem. Soc.* **1998**, *120*, 9533–9540.

[35] L. Cao, I. Manners, M. A. Winnik, *Macromolecules* **2002**, *35*, 8258–8260.

[36] X. Wang, G. Guerin, H. Wang, Y. Wang, I. Manners, M. A. Winnik, *Science* **2007**, *317*, 644–647.

[37] H. Wang, W. Lin, K. P. Fritz, G. D. Scholes, M. A. Winnik, I. Manners, *J. Am. Chem. Soc.* **2007**, *129*, 12924–12925.

[38] Z. M. Hudson, J. Qian, C. E. Boott, M. A. Winnik, I. Manners, *ACS Macro Lett.* **2015**, *4*, 187–191.

[39] A. Nazemi, C. E. Boott, D. J. Lunn, J. Gwyther, D. W. Hayward, R. M. Richardson, M. A. Winnik, I. Manners, *J. Am. Chem. Soc.* **2016**, *138*, 4484–4493.

[40] F. He, T. Gädt, I. Manners, M. A. Winnik, *J. Am. Chem. Soc.* **2011**, *133*, 9095–9103.

[41] Z. M. Hudson, D. J. Lunn, M. A. Winnik, I. Manners, *Nat. Commun.* **2014**, *5*, 3372–3379.

[42] P. A. Rupar, L. Chabanne, M. A. Winnik, I. Manners, *Science* **2012**, *337*, 559–562.

[43] J. R. Finnegan, D. J. Lunn, O. E. C. Gould, Z. M. Hudson, G. R. Whittell, M. A. Winnik, I. Manners, *J. Am. Chem. Soc.* **2014**, *136*, 13835–13844.

[44] H. Schmalz, J. Schmelz, M. Drechsler, J. Yuan, A. Walther, K. Schweimer, A. M. Mihut, *Macromolecules* **2008**, *41*, 3235–3242.

[45] R. Resendes, J. A. Massey, K. Temple, L. Cao, K. N. Power-Billard, M. A. Winnik, I. Manners, *Chem. - A Eur. J.* **2001**, *7*, 2414–2424.

[46] T. Gädt, N. S. Ieong, G. Cambridge, M. A. Winnik, I. Manners, *Nat. Mater.* **2009**, *8*, 144–150.

[47] G. Cambridge, M. J. Gonzalez-Alvarez, G. Guerin, I. Manners, M. A. Winnik,

Macromolecules **2015**, *48*, 707–716.

[48] H. Qiu, G. Cambridge, M. A. Winnik, I. Manners, *J. Am. Chem. Soc.* **2013**, *135*, 12180–12183.

[49] Z. M. Hudson, C. E. Boott, M. E. Robinson, P. A. Rupar, M. A. Winnik, I. Manners, *Nat. Chem.* **2014**, *6*, 893–898.

[50] L. Jia, L. Tong, Y. Liang, A. Petretic, G. Guerin, I. Manners, M. A. Winnik, *J. Am. Chem. Soc.* **2014**, *136*, 16676–16682.

[51] L. Jia, G. Zhao, W. Shi, N. Coombs, I. Gourevich, G. C. Walker, G. Guerin, I. Manners, M. A. Winnik, *Nat. Commun.* **2014**, *5*, 3882–3889.

[52] Y. Gao, H. Qiu, H. Zhou, X. Li, R. Harniman, M. A. Winnik, I. Manners, *J. Am. Chem. Soc.* **2015**, *137*, 2203–2206.

[53] H. Qiu, Y. Gao, V. A. Du, R. Harniman, M. A. Winnik, I. Manners, *J. Am. Chem. Soc.* **2015**, *137*, 2375–2385.

[54] H. Qiu, Z. M. Hudson, M. A. Winnik, I. Manners, *Science* **2015**, *347*, 1329–1332.

[55] O. E. C. Gould, H. Qiu, D. J. Lunn, J. Rowden, R. L. Harniman, Z. M. Hudson, M. A. Winnik, M. J. Miles, I. Manners, *Nat. Commun.* **2015**, *6*, 10009–10015.

[56] H. Qiu, Y. Gao, C. E. Boott, O. E. C. Gould, R. L. Harniman, M. J. Miles, S. E. D. Webb, M. A. Winnik, I. Manners, *Science* **2016**, *352*, 697–701.

[57] D. J. Lunn, O. E. C. Gould, G. R. Whittell, D. P. Armstrong, K. P. Mineart, M. A. Winnik, R. J. Spontak, P. G. Pringle, I. Manners, *Nat. Commun.* **2016**, *7*, 12371–12380.

[58] L. Jia, A. Petretic, G. Molev, G. Guerin, I. Manners, M. A. Winnik, *ACS Nano* **2015**, *9*, 10673–10685.

[59] X. Li, Y. Gao, C. E. Boott, D. W. Hayward, R. Harniman, G. R. Whittell, R. M. Richardson, M. A. Winnik, I. Manners, *J. Am. Chem. Soc.* **2016**, *138*, 4087–4095.

[60] X. Li, Y. Gao, C. E. Boott, M. A. Winnik, I. Manners, *Nat. Commun.* **2015**, *6*, 8127–8134.

[61] X. Li, Y. Gao, R. Harniman, M. Winnik, I. Manners, *J. Am. Chem. Soc.* **2016**, *138*, 12902–12912.

[62] E. K. Lin, A. P. Gast, *Macromolecules* **1996**, *29*, 4432–4441.

[63] D. Richter, D. Schneiders, M. Monkenbusch, L. Willner, L. J. Fetters, J. S. Huang, M. Lin, K. Mortensen, B. Farago, *Macromolecules* **1997**, *30*, 1053–1068.

[64] A. Ramzi, M. Prager, D. Richter, V. Efstratiadis, N. Hadjichristidis, R. N. Young, J. B. Allgaier, *Macromolecules* **1997**, *30*, 7171–7182.

[65] M. Monkenbusch, D. Schneiders, D. Richter, L. Willner, W. Leube, L. J. Fetters, J. S. Huang, M. Lin, *Phys. B Condens. Matter* **2000**, *276–278*, 941–943.

[66] D. Schwahn, D. Richter, P. J. Wright, C. Symon, L. J. Fetters, M. Lin, *Macromolecules* **2002**, *35*, 861–870.

[67]   J. Wang, J. H. Horton, G. Liu, S.-Y. Lee, K. J. Shea, *Polymer* **2007**, *48*, 4123–4129.

[68]   T. Rudolph, M. Von Der Lühe, M. Hartlieb, S. Norsic, U. S. Schubert, C. Boisson, F. D'Agosto, F. H. Schacher, *ACS Nano* **2015**, *9*, 10085–10098.

[69]   T. Li, W. J. Wang, R. Liu, W. H. Liang, G. F. Zhao, Z. Li, Q. Wu, F. M. Zhu, *Macromolecules* **2009**, *42*, 3804–3810.

[70]   W. Wang, R. Liu, Z. Li, C. Meng, Q. Wu, F. Zhu, *Macromol. Chem. Phys.* **2010**, *211*, 1452–1459.

[71]   L. Yin, M. A. Hillmyer, *Macromolecules* **2011**, *44*, 3021–3028.

[72]   Y. Zhao, X. Shi, H. Gao, L. Zhang, F. Zhu, Q. Wu, *J. Mater. Chem.* **2012**, *22*, 5737–5745.

[73]   R. Liu, Z. Y. Li, W. J. Wang, D. Yuan, C. F. Meng, Q. Wu, F. M. Zhu, *J. Appl. Polym. Sci.* **2013**, *129*, 2216–2223.

[74]   N. Alkayal, G. Zapsas, P. Bilalis, N. Hadjichristidis, *Polymer* **2016**, *107*, 415–421.

[75]   H. Gao, G. Li, Z. Hu, Z. Xiao, G. Liang, Q. Wu, *Polymer* **2014**, *55*, 4593–4600.

[76]   H. Gao, Y. Tan, Q. Guan, T. Cai, G. Liang, Q. Wu, *RSC Adv.* **2015**, *5*, 49376–49384.

[77]   H. Wang, C. Wu, G. Xia, Z. Ma, G. Mo, R. Song, *Soft Matter* **2015**, *11*, 1778–1787.

[78]   Z. Li, R. Liu, B. Mai, W. Wang, Q. Wu, G. Liang, H. Gao, F. Zhu, *Polymer* **2013**, *54*, 1663–1670.

[79]   L. Yin, T. P. Lodge, M. A. Hillmyer, *Macromolecules* **2012**, *45*, 9460–9467.

[80]   B. Fan, L. Liu, J.-H. Li, X.-X. Ke, J.-T. Xu, B.-Y. Du, Z.-Q. Fan, *Soft Matter* **2016**, *12*, 67–76.

[81]   J. Schmelz, M. Karg, T. Hellweg, H. Schmalz, *ACS Nano* **2011**, *5*, 9523–9534.

[82]   S. Rosenfeldt, F. Lüdel, C. Schulreich, T. Hellweg, A. Radulescu, J. Schmelz, H. Schmalz, L. Harnau, *Phys. Chem. Chem. Phys.* **2012**, *14*, 12750–12756.

[83]   J. Schmelz, H. Schmalz, *Polymer* **2012**, *53*, 4333–4337.

[84]   J. Schmelz, A. E. Schedl, C. Steinlein, I. Manners, H. Schmalz, *J. Am. Chem. Soc.* **2012**, *134*, 14217–14225.

[85]   J. Schmelz, F. H. Schacher, H. Schmalz, *Soft Matter* **2013**, *9*, 2101–2107.

[86]   J. Schmelz, D. Pirner, M. Krekhova, T. M. Ruhland, H. Schmalz, *Soft Matter* **2013**, *9*, 11173–11177.

[87]   T. Gegenhuber, A. H. Gröschel, T. I. Löbling, M. Drechsler, S. Ehlert, S. Förster, H. Schmalz, *Macromolecules* **2015**, *48*, 1767–1776.

[88]   T. Gegenhuber, M. Krekhova, J. Schöbel, A. H. Gröschel, H. Schmalz, *ACS Macro Lett.* **2016**, *5*, 306–310.

[89]   Z.-X. Du, J.-T. Xu, Z.-Q. Fan, *Macromolecules* **2007**, *40*, 7633–7637.

[90] W.-N. He, J.-T. Xu, B.-Y. Du, Z.-Q. Fan, F.-L. Sun, *Macromol. Chem. Phys.* **2012**, *213*, 952–964.

[91] B. Mai, Z. Li, R. Liu, S. Feng, Q. Wu, G. Liang, H. Gao, F. Zhu, *J. Polym. Res.* **2013**, *20*, 299–236.

[92] G. Rizis, T. G. M. van de Ven, A. Eisenberg, *Soft Matter* **2014**, *10*, 2825–2835.

[93] G. Rizis, T. G. M. van de Ven, A. Eisenberg, *Angew. Chem. Int. Ed.* **2014**, *53*, 9000–9003.

[94] Y. Geng, D. E. Discher, *J. Am. Chem. Soc.* **2005**, *127*, 12780–12781.

[95] Y. Geng, P. Dalhaimer, S. Cai, R. Tsai, M. Tewari, T. Minko, D. E. Discher, *Nat. Nanotechnol.* **2007**, *2*, 249–255.

[96] J.-X. Yang, B. Fan, J.-H. Li, J.-T. Xu, B.-Y. Du, Z.-Q. Fan, *Macromolecules* **2016**, *49*, 367–372.

[97] W.-N. He, B. Zhou, J.-T. Xu, B.-Y. Du, Z.-Q. Fan, *Macromolecules* **2012**, *45*, 9768–9778.

[98] G. Rizis, T. G. M. van de Ven, A. Eisenberg, *ACS Nano* **2015**, *9*, 3627–3640.

[99] J. Wang, W. Zhu, B. Peng, Y. Chen, *Polymer* **2013**, *54*, 6760–6767.

[100] S. Nakagawa, K. Kadena, T. Ishizone, S. Nojima, T. Shimizu, K. Yamaguchi, S. Nakahama, *Macromolecules* **2012**, *45*, 1892–1900.

[101] W. Y. Chen, C. Y. Li, J. X. Zheng, P. Huang, L. Zhu, Q. Ge, R. P. Quirk, B. Lotz, L. Deng, C. Wu, et al., *Macromolecules* **2004**, *37*, 5292–5299.

[102] A. M. Mihut, J. J. Crassous, J.-F. Dechézelles, S. Lages, A. Menzel, H. Dietsch, P. Schurtenberger, *Polymer* **2013**, *54*, 3874–3881.

[103] A. M. Mihut, J. J. Crassous, H. Schmalz, M. Drechsler, M. Ballauff, *Soft Matter* **2012**, *8*, 3163–3173.

[104] N. Petzetakis, A. P. Dove, R. K. O'Reilly, *Chem. Sci.* **2011**, *2*, 955–960.

[105] D. Portinha, F. Boué, L. Bouteiller, G. Carrot, C. Chassenieux, S. Pensec, G. Reiter, *Macromolecules* **2007**, *40*, 4037–4042.

[106] L. Sun, A. Pitto-Barry, N. Kirby, T. L. Schiller, A. M. Sanchez, M. A. Dyson, J. Sloan, N. R. Wilson, R. K. O'Reilly, A. P. Dove, *Nat. Commun.* **2014**, *5*, 5746–5754.

[107] N. Petzetakis, D. Walker, A. P. Dove, R. K. O'Reilly, *Soft Matter* **2012**, *8*, 7408–7414.

[108] N. Petzetakis, M. P. Robin, J. P. Patterson, E. G. Kelley, P. Cotanda, P. H. H. Bomans, N. A. J. M. Sommerdijk, A. P. Dove, T. H. Epps, R. K. O'Reilly, *ACS Nano* **2013**, *7*, 1120–1128.

[109] A. Pitto-Barry, N. Kirby, A. P. Dove, R. K. O'Reilly, *Polym. Chem.* **2014**, *5*, 1427–1436.

[110] L. Sun, A. Pitto-Barry, A. W. Thomas, M. Inam, K. Doncom, A. P. Dove, R. K.

O'Reilly, *Polym. Chem.* **2016**, *7*, 2337–2341.

[111] S. K. Patra, R. Ahmed, G. R. Whittell, D. J. Lunn, E. L. Dunphy, M. A. Winnik, I. Manners, *J. Am. Chem. Soc.* **2011**, *133*, 8842–8845.

[112] J. Qian, X. Li, D. J. Lunn, J. Gwyther, Z. M. Hudson, E. Kynaston, P. A. Rupar, M. A. Winnik, I. Manners, *J. Am. Chem. Soc.* **2014**, *136*, 4121–4124.

[113] J. Li, X. Li, D. Ni, J. Wang, G. Tu, J. Zhu, *J. Appl. Polym. Sci.* **2014**, *131*, 41186–41196.

[114] E. L. Kynaston, O. E. C. Gould, J. Gwyther, G. R. Whittell, M. A. Winnik, I. Manners, *Macromol. Chem. Phys.* **2015**, *216*, 685–695.

[115] M. Lazzari, D. Scalarone, C. E. Hoppe, C. Vazquez-Vazquez, M. A. Lòpez-Quintela, *Chem. Mater.* **2007**, *19*, 5818–5820.

[116] M. Lazzari, D. Scalarone, C. Vazquez-Vazquez, M. A. López-Quintela, *Macromol. Rapid Commun.* **2008**, *29*, 352–357.

[117] C. Legros, M.-C. De Pauw-Gillet, K. C. Tam, D. Taton, S. Lecommandoux, *Soft Matter* **2015**, *11*, 3354–3359.

[118] Z. Li, R. Liu, B. Mai, S. Feng, Q. Wu, G. Liang, H. Gao, F. Zhu, *Polym. Chem.* **2013**, *4*, 954–960.

[119] R. Liu, Z.-Y. Li, B.-Y. Mai, Q. Wu, G.-D. Liang, H.-Y. Gao, F.-M. Zhu, *J. Polym. Res.* **2013**, *20*, 64–74.

[120] B. Yu, X. Jiang, J. Yin, *Macromolecules* **2014**, *47*, 4761–4768.

[121] Y. Xia, Y. Xiong, B. Lim, S. E. Skrabalak, *Angew. Chemie - Int. Ed.* **2009**, *48*, 60–103.

[122] D. A. Giljohann, D. S. Seferos, W. L. Daniel, M. D. Massich, P. C. Patel, C. A. Mirkin, *Angew. Chemie - Int. Ed.* **2010**, *49*, 3280–3294.

[123] T. K. Sau, A. L. Rogach, F. Jäckel, T. A. Klar, J. Feldmann, *Adv. Mater.* **2010**, *22*, 1805–1825.

[124] M. Haruta, *Chem. Rec.* **2003**, *3*, 75–87.

[125] A. Cao, R. Lu, G. Veser, *Phys. Chem. Chem. Phys.* **2010**, *12*, 13499–13510.

[126] C. Burda, X. Chen, R. Narayanan, M. A. El-Sayed, *Chem. Rev.* **2005**, *105*, 1025–1102.

[127] S. Lal, S. Link, N. J. Halas, *Nat. Photonics* **2007**, *1*, 641–648.

[128] K. A. Willets, R. P. Van Duyne, *Annu. Rev. Phys. Chem.* **2007**, *58*, 267–297.

[129] M. Rycenga, C. M. Cobley, J. Zeng, W. Li, C. H. Moran, Q. Zhang, D. Qin, Y. Xia, *Chem. Rev.* **2011**, *111*, 3669–3712.

[130] K. M. Mayer, J. H. Hafner, *Chem. Rev.* **2011**, *111*, 3828–3857.

[131] N. J. Halas, S. Lal, W. S. Chang, S. Link, P. Nordlander, *Chem. Rev.* **2011**, *111*, 3913–3961.

[132] A. H. Lu, E. L. Salabas, F. Schüth, *Angew. Chemie - Int. Ed.* **2007**, *46*, 1222–1244.

[133] A. Chen, P. Holt-Hindle, *Chem. Rev.* **2010**, *110*, 3767–3804.

[134] S. Kango, S. Kalia, A. Celli, J. Njuguna, Y. Habibi, R. Kumar, *Prog. Polym. Sci.* **2013**, *38*, 1232–1261.

[135] M. C. M. Daniel, D. Astruc, *Chem. Rev.* **2004**, *104*, 293–346.

[136] J. Turkevich, P. C. Stevenson, J. Hillier, *Discuss. Faraday Soc.* **1951**, *11*, 55–75.

[137] S. Kumar, K. S. Gandhi, R. Kumar, *Ind. Eng. Chem. Res.* **2007**, *46*, 3128–3136.

[138] G. Frens, *Nat. Phys. Sci.* **1973**, *241*, 20–22.

[139] P. Zhao, N. Li, D. Astruc, *Coord. Chem. Rev.* **2013**, *257*, 638–665.

[140] B. V. Enüstün, J. Turkevich, *J. Am. Chem. Soc.* **1963**, *85*, 3317–3328.

[141] J. Kimling, M. Maier, B. Okenve, V. Kotaidis, H. Ballot, A. Plech, *J. Phys. Chem. B* **2006**, *110*, 15700–15707.

[142] C. Li, D. Li, G. Wan, J. Xu, W. Hou, *Nanoscale Res. Lett.* **2011**, *6*, 440–449.

[143] I. Ojea-Jiménez, N. G. Bastús, V. Puntes, *J. Phys. Chem. C* **2011**, *115*, 15752–15757.

[144] F. Schulz, T. Homolka, N. G. Bastús, V. Puntes, H. Weller, T. Vossmeyer, *Langmuir* **2014**, *30*, 10779–10784.

[145] H. Xia, S. Bai, J. Hartmann, D. Wang, *Langmuir* **2010**, *26*, 3585–3589.

[146] T. K. Sau, A. Pal, N. R. Jana, Z. L. Wang, T. Pal, *J. Nanoparticle Res.* **2001**, *3*, 257–261.

[147] N. G. Bastús, J. Comenge, V. Puntes, *Langmuir* **2011**, *27*, 11098–11105.

[148] C. Ziegler, A. Eychmüller, *J. Phys. Chem. C* **2011**, *115*, 4502–4506.

[149] J. Piella, N. G. Bastús, V. Puntes, *Chem. Mater.* **2016**, *28*, 1066–1075.

[150] B. Nikoobakht, M. A. El-Sayed, *Chem. Mater.* **2003**, *15*, 1957–1962.

[151] C. J. Murphy, T. K. Sau, A. M. Gole, C. J. Orendorff, J. Gao, L. Gou, S. E. Hunyadi, T. Li, *J. Phys. Chem. B* **2005**, *109*, 13857–13870.

[152] N. R. Jana, L. Gearheart, C. J. Murphy, *J. Phys. Chem. B* **2001**, *105*, 4065–4067.

[153] M. Giersig, P. Mulvaney, *Langmuir* **1993**, *9*, 3408–3413.

[154] M. Brust, M. Walker, D. Bethell, D. J. Schiffrin, R. Whyman, *J. Chem. Soc., Chem. Commun.* **1994**, *0*, 801–802.

[155] M. Brust, J. Fink, D. Bethell, D. J. Schiffrin, C. Kiely, *J. Chem. Soc. Chem. Commun.* **1995**, *0*, 1655–1656.

[156] J. R. G. Navarro, M. Plugge, M. Loumaigne, A. Sanchez-Gonzalez, B. Mennucci, A. Débarre, A. M. Brouwer, M. H. V Werts, *Photochem. Photobiol. Sci.* **2010**, *9*, 1042–1054.

[157] A. Manna, P.-L. Chen, H. Akiyama, T.-X. Wei, K. Tamada, W. Knoll, *Chem. Mater.* **2003**, *15*, 20–28.

[158] Z. Tang, B. Xu, B. Wu, M. W. Germann, G. Wang, *J. Am. Chem. Soc.* **2010**, *132*, 3367–3374.

[159] K. Wojczykowski, D. Meißner, P. Jutzi, I. Ennen, A. Hütten, M. Fricke, D. Volkmer, *Chem. Commun.* **2006**, *0*, 3693–3695.

[160] A. Kumar, S. Mandal, P. R. Selvakannan, R. Pasricha, A. B. Mandale, M. Sastry, *Langmuir* **2003**, *19*, 6277–6282.

[161] N. Wangoo, K. K. Bhasin, R. Boro, C. R. Suri, *Anal. Chim. Acta* **2008**, *610*, 142–148.

[162] D. I. Gittins, F. Caruso, *Angew. Chem. Int. Ed.* **2001**, *40*, 3001–3004.

[163] G. Li, D. Li, L. Zhang, J. Zhai, E. Wang, *Chem. - A Eur. J.* **2009**, *15*, 9868–9873.

[164] M. K. Corbierre, N. S. Cameron, R. B. Lennox, *Langmuir* **2004**, *20*, 2867–2873.

[165] Y. Kang, T. A. Taton, *Angew. Chem. Int. Ed.* **2005**, *44*, 409–412.

[166] Y. Lu, Y. Mei, M. Drechsler, M. Ballauff, *Angew. Chem. Int. Ed.* **2006**, *45*, 813–816.

[167] T. Niidome, M. Yamagata, Y. Okamoto, Y. Akiyama, H. Takahashi, T. Kawano, Y. Katayama, Y. Niidome, *J. Control. Release* **2006**, *114*, 343–347.

[168] S. Bokern, J. Getze, S. Agarwal, A. Greiner, *Polymer* **2011**, *52*, 912–920.

[169] S. Bokern, Z. Fan, C. Mattheis, A. Greiner, S. Agarwal, *Macromolecules* **2011**, *44*, 5036–5042.

[170] K. Gries, M. El Helou, G. Witte, S. Agarwal, A. Greiner, *Polymer* **2012**, *53*, 1632–1639.

[171] F. Mitschang, H. Schmalz, S. Agarwal, A. Greiner, *Angew. Chem. Int. Ed.* **2014**, *53*, 4972–4975.

[172] H. Pletsch, L. Peng, F. Mitschang, A. Schaper, M. Hellwig, D. Nette, A. Seubert, A. Greiner, S. Agarwal, *Small* **2014**, *10*, 201–208.

[173] Z. Fan, M. K. Serrano, A. Schaper, S. Agarwal, A. Greiner, *Adv. Mater.* **2015**, *27*, 3888–3893.

[174] M. S. Köhn Serrano, T. A. F. König, J. S. Haataja, T. I. Löbling, H. Schmalz, S. Agarwal, A. Fery, A. Greiner, *Macromol. Rapid Commun.* **2016**, *37*, 215–220.

[175] Z. Fan, X. Chen, M. Köhn Serrano, H. Schmalz, S. Rosenfeldt, S. Förster, S. Agarwal, A. Greiner, *Angew. Chem. Int. Ed.* **2015**, *54*, 14539–14544.

[176] J. Gohy, N. Willet, S. Varshney, J. Zhang, R. Jérôme, *Angew. Chemie* **2001**, *113*, 3314–3316.

[177] M. Changez, N.-G. Kang, D. W. Kim, J.-S. Lee, *Nanoscale* **2013**, *5*, 11554–11560.

[178] A. Walther, J. Yuan, V. Abetz, A. H. E. Müller, *Nano Lett.* **2009**, *9*, 2026–2030.

[179] P. Shi, C. Gao, X. He, P. Sun, W. Zhang, *Macromolecules* **2015**, *48*, 1380–1389.

[180] K. H. Ku, J. M. Shin, M. P. Kim, C. H. Lee, M. K. Seo, G. R. Yi, S. G. Jang, B. J. Kim, *J. Am. Chem. Soc.* **2014**, *136*, 9982–9989.

[181] S. G. Jang, D. J. Audus, D. Klinger, D. V. Krogstad, B. J. Kim, A. Cameron, S. W. Kim, K. T. Delaney, S. M. Hur, K. L. Killops, et al., *J. Am. Chem. Soc.* **2013**, *135*, 6649–6657.

[182] M. P. Kim, K. H. Ku, H. J. Kim, S. G. Jang, G. R. Yi, B. J. Kim, *Chem. Mater.* **2013**, *25*, 4416–4422.

[183] N. Yan, H. Liu, Y. Zhu, W. Jiang, Z. Dong, *Macromolecules* **2015**, *48*, 5980–5987.

[184] H. Cui, Z. Chen, S. Zhong, K. L. Wooley, D. J. Pochan, *Science* **2007**, *317*, 647–650.

[185] D. J. Pochan, J. Zhu, K. Zhang, K. L. Wooley, C. Miesch, T. Emrick, *Soft Matter* **2011**, *7*, 2500–2506.

[186] F. Schacher, E. Betthausen, A. Walther, H. Schmalz, D. V. Pergushov, A. H. E. Müller, *ACS Nano* **2009**, *3*, 2095–2102.

[187] F. H. Schacher, T. Rudolph, M. Drechsler, A. H. E. Müller, *Nanoscale* **2011**, *3*, 288–297.

[188] Y. Guo, S. Harirchian-Saei, C. M. S. Izumi, M. G. Moffitt, *ACS Nano* **2011**, *5*, 3309–3318.

[189] R. J. Hickey, Q. Luo, S. J. Park, *ACS Macro Lett.* **2013**, *2*, 805–808.

[190] J. Hu, T. Wu, G. Zhang, S. Liu, *J. Am. Chem. Soc.* **2012**, *134*, 7624–7627.

[191] R. Bleach, B. Karagoz, S. M. Prakash, T. P. Davis, C. Boyer, *ACS Macro Lett.* **2014**, *3*, 591–596.

[192] L.-P. Lv, Y. Zhao, H.-X. Zhou, K. Landfester, D. Crespy, *Polymer* **2014**, *55*, 715–720.

[193] V. E. Lee, C. Sosa, R. Liu, R. K. Prud'homme, R. D. Priestley, *Langmuir* **2017**, *33*, 3444–3449.

[194] H. Wang, A. J. Patil, K. Liu, S. Petrov, S. Mann, M. A. Winnik, I. Manners, *Adv. Mater.* **2009**, *21*, 1805–1808.

[195] H. Wang, X. Wang, M. A. Winnik, I. Manners, *J. Am. Chem. Soc.* **2008**, *130*, 12921–12930.

[196] C. Sanchez, P. Belleville, M. Popall, L. Nicole, *Chem. Soc. Rev.* **2011**, *40*, 696–753.

[197] E. C. Dreaden, A. M. Alkilany, X. Huang, C. J. Murphy, M. A. El-Sayed, *Chem. Soc. Rev.* **2012**, *41*, 2740–2779.

[198] P. Hervés, M. Pérez-Lorenzo, L. M. Liz-Marzán, J. Dzubiella, Y. Lu, M. Ballauff, *Chem. Soc. Rev.* **2012**, *41*, 5577–5587.

[199] P. Zhao, X. Feng, D. Huang, G. Yang, D. Astruc, *Coord. Chem. Rev.* **2015**, *287*, 114–136.

[200] J. Zhang, D. Han, H. Zhang, M. Chaker, Y. Zhao, D. Ma, *Chem. Commun.* **2012**, *48*, 11510–11512.

[201] S. Wunder, F. Polzer, Y. Lu, Y. Mei, M. Ballauff, *J. Phys. Chem. C* **2010**, *114*, 8814–8820.

[202] Y. Lu, A. Wittemann, M. Ballauff, *Macromol. Rapid Commun.* **2009**, *30*, 806–815.

[203] S. Gu, Y. Lu, J. Kaiser, M. Albrecht, M. Ballauff, *Phys. Chem. Chem. Phys.* **2015**, *17*, 28137–28143.

[204] Z. Zhang, C. Shao, P. Zou, P. Zhang, M. Zhang, J. Mu, Z. Guo, X. Li, C. Wang, Y. Liu, *Chem. Commun.* **2011**, *47*, 3906–3908.

[205] X. Huang, X. Liao, B. Shi, *Green Chem.* **2011**, *13*, 2801–2805.

[206] J. Zhang, G. Chen, M. Chaker, F. Rosei, D. Ma, *Appl. Catal. B Environ.* **2013**, *132–133*, 107–115.

[207] Y. Zhang, X. Cui, F. Shi, Y. Deng, *Chem. Rev.* **2012**, *112*, 2467–2505.

[208] P. Raffa, C. Evangelisti, G. Vitulli, P. Salvadori, *Tetrahedron Lett.* **2008**, *49*, 3221–3224.

[209] C. Wang, X. Lin, Y. Ge, Z. H. Shah, R. Lu, S. Zhang, *RSC Adv.* **2016**, *6*, 102102–102108.

[210] T. Mitsudome, Y. Yamamoto, A. Noujima, T. Mizugaki, K. Jitsukawa, K. Kaneda, *Chem. - A Eur. J.* **2013**, *19*, 14398–14402.

[211] T. Taguchi, K. Isozaki, K. Miki, *Adv. Mater.* **2012**, *24*, 6462–6467.

[212] V. Subramanian, E. E. Wolf, P. V. Kamat, *J. Am. Chem. Soc.* **2004**, *126*, 4943–4950.

[213] A. Primo, A. Corma, H. García, *Phys. Chem. Chem. Phys.* **2011**, *13*, 886–910.

[214] L. Sun, D. Zhao, Z. Song, C. Shan, Z. Zhang, B. Li, D. Shen, *J. Colloid Interface Sci.* **2011**, *363*, 175–181.

[215] F. Xiao, F. Wang, X. Fu, Y. Zheng, *J. Mater. Chem.* **2012**, *22*, 2868–2877.

[216] A. Dawson, P. V. Kamat, *J. Phys. Chem. B* **2001**, *105*, 960–966.

[217] D. Tsukamoto, Y. Shiraishi, Y. Sugano, S. Ichikawa, S. Tanaka, T. Hirai, *J. Am. Chem. Soc.* **2012**, *134*, 6309–6315.

[218] A. Orlov, D. A. Jefferson, N. Macleod, R. M. Lambert, *Catal. Letters* **2004**, *92*, 41–47.

[219] V. Iliev, D. Tomova, L. Bilyarska, G. Tyuliev, *J. Mol. Catal. A Chem.* **2007**, *263*, 32–38.

[220] L. Sun, D. Zhao, Z. Song, C. Shan, Z. Zhang, B. Li, D. Shen, *J. Colloid Interface Sci.* **2011**, *363*, 175–181.

[221] H. Zhu, X. Chen, Z. Zheng, X. Ke, E. Jaatinen, J. Zhao, C. Guo, T. Xie, D. Wang, *Chem. Commun.* **2009**, 7524–7526.

2 Thesis Overview

This thesis focuses on the development of highly active mesostructured catalysts. Therefore, two different concepts were established. The first deals with worm-like crystalline-core micelles (wCCMs) exhibiting a corona with alternating patches as template materials for the incorporation of metal and metal oxide nanoparticles (NPs). The second concept is based on the controlled aggregation of NPs yielding highly porous catalysts.

Polystyrene-*block*-polyethylene-*block*-poly(methyl methacrylate) (SEM) triblock ter-polymers are able to undergo crystallization-driven self-assembly (CDSA). This results in wCCMs with a corona showing alternating nanometer-sized patches of polystyrene (PS) and poly(methyl meth-acrylate) (PMMA). As both corona patches exhibit no functional groups for stabilization of NPs, **Chapter 3** deals with the post-polymerization modification of the PMMA block. Therefore, different *N,N*-dialkylethylenediamines were used for amidation. The effect of the amidation on the solubility of the resulting modified PMMA, the patch morphology and the CDSA was studied. The solubility of the amidated patches was found to be a crucial parameter for successful wCCM formation limiting this method to low degrees of amidation. However, a first test for stabilization of gold NPs was conducted.

As the amidation of Chapter 3 showed disadvantages regarding the reaction conditions, **Chapter 4** starts with the optimization of this reaction by activation of the *N,N*-dialkylethylenediamine before amidation. CDSA resulted in defined wCCMs showing highly functionalized patches without limitations in solubility. Different approaches for the formation of hybrid materials with noble metal and transition metal oxide NPs were investigated allowing for selective loading of both, the amidated patch and the PS patch. Combination of two loading techniques enabled binary loading of the wCCMs with two types of NPs.

For an application of the hybrid materials of Chapter 3 and 4 in catalysis, a support for the wCCMs was needed. **Chapter 5** deals with the coating of wCCMs on a PS nonwoven by coaxial electrospinning. The patchy nonwovens observed by this technique were loaded with preformed citrate-stabilized gold NPs by a simple dipping process based on a ligand exchange. No agglomeration or aggregation of the NPs was observed. The hybrid nonwovens showed high activity in the alcoholysis of dimethylphenylsilane at room temperature and were tested for reusability. In ten subsequent cycles of catalysis, no loss of activity was detected, which is attributed to the absence of leaching effects.

In cooperation with the department of inorganic chemistry of the University of Bayreuth, a second concept for the formation of mesostructured catalysts was developed. To this end, cylindrical polymer brushes (CPBs), obtained by crosslinking of the cylindrical bulk morphology of a polybutadiene-*block*-poly(2-vinylpyridine) (BV) diblock copolymer, were used as template materials. The aim was to simultaneously load these CPBs with zinc oxide (ZnO) and gold (Au) NPs.

To reach this aim, first, the loading of the CPBs with ZnONP was investigated (**Chapter 6**). To this end, the corona of the CPBs was quaternized to observe a stable positive charge. Acetate-stabilized ZnONPs were incorporated by electrostatic interactions. In a next step, the polymeric template was pyrolyzed to obtain a controlled aggregation of the ZnONP. This yielded in highly porous mesostructured catalysts, which were successfully tested for the photocatalytic degradation of ciprofloxacin, a common antibiotic found in hospital wastewater, under irradiation of visible light. This was attributed to the positive charge of ZnO at a typical $pH = 8$ of hospital wastewater, which supports the adsorption of the negatively charged ciprofloxacin.

Chapter 7 concentrates on the enhancement of the catalyst material of Chapter 6 by synergistic effects. Therefore, the CBPs were simultaneously loaded with ZnONPs and AuNPs. Pyrolysis again resulted in the mesostructured catalyst. To determine the effect of Au concentration on the photocatalytic degradation of ciprofloxacin, different compositions for the hybrid catalysts were synthesized and resulted in an optimum ratio of 88 wt-% ZnO and 12 wt-% Au. Furthermore, the degradation of a second common antibiotic, levofloxacin, was tested to show the versatility of this catalyst.

In the following, an overview of the main results presented in this thesis is given.

2.1 Patchy Worm-Like Micelles with Tailored Functionality by Crystallization-Driven Self-Assembly: A Versatile Platform for Mesostructured Hybrid Materials

SEM triblock terpolymers exhibit a worm-like morphology with a crystalline core and a patchy corona after CDSA in solution. To utilize this unique structure for NP incorporation, we developed a synthetic strategy for selective functionalization of the PMMA block of a $S_{40}E_{21}M_{39}{}^{108}$ triblock terpolymer, where subscripts correspond to the mass fraction of the blocks in wt % and the superscript denotes the overall molecular weight in kg mol^{-1}. An amidation reaction (Fig. 2.1-1 A) with different *N,N*-dialkylethylenediamines creates the required NP-stabilizing amide and amine groups within the corona patches, which was proven by the increasing amide I and II vibrations (1666 cm^{-1}, 1526 cm^{-1}) and the decreasing C=O ester (1728 cm^{-1}) vibration in the corresponding FT-IR spectra (Fig. 2.1-1 B). The desired degree of functionalization can be easily adjusted by the employed reaction time, as exemplarily shown in Fig. 2.1-1 C for a SEM amidation with *N,N*-dimethylethylenediamine.
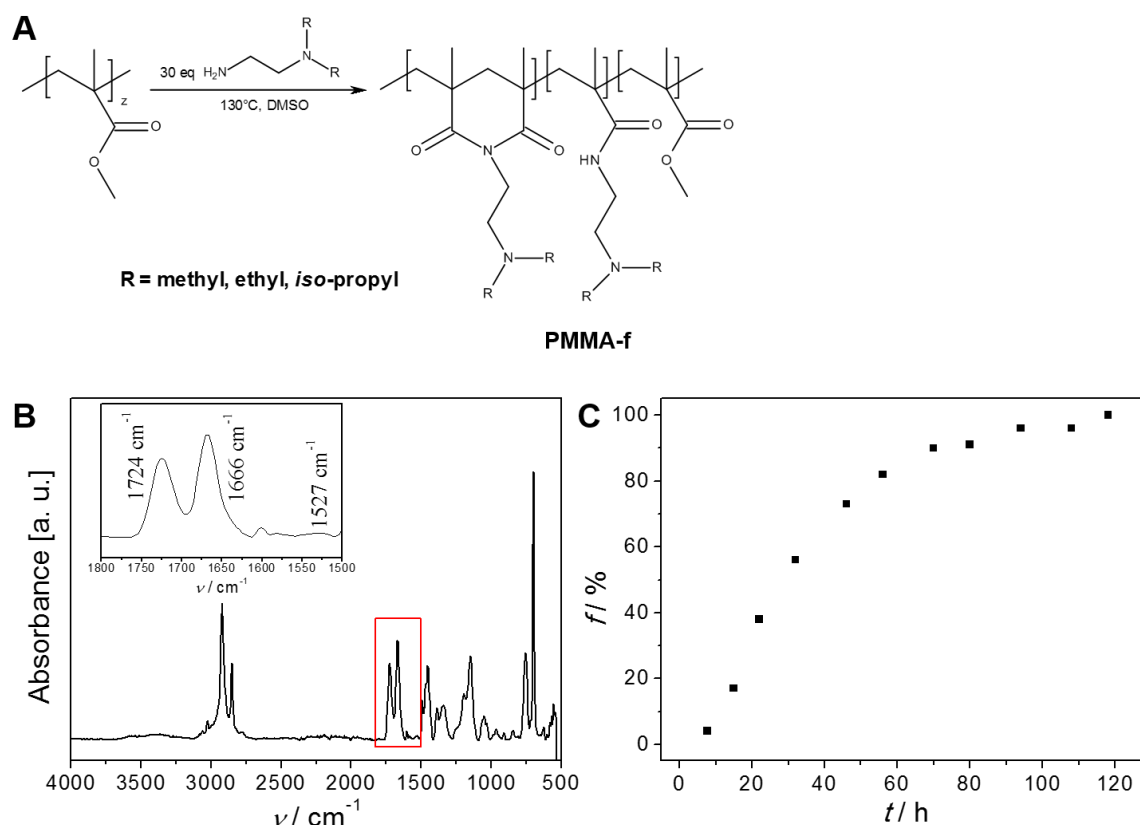
Figure 2.1-1. Amidation of the PMMA block with different *N,N*-dialkylethylenediamines (A). FT-IR spectrum of a 73 % amidated SEM triblock terpolymer (R = methyl) (B) and kinetics of the amidation of SEM with *N,N*-dimethylethylenediamine (C).

During the amidation, a side reaction causes imide formation of about 40-60 % (depending on the alkyl substituent R, Fig. 2.1-1 A) with respect to the converted ester units. This imide formation, observable in the IR spectrum by a vibration at 1716 cm^{-1}, impacts the polarity, the solubility and in turn the CDSA of the functionalized triblock terpolymers in organic solvents. With increasing polarity of the triblock terpolymer, the amidated block is insoluble in THF even above the melting temperature (T_m) of the PE core. This led to the formation of micelles, which caused nucleation of the PE at higher temperatures. CDSA resulted in a highly irregular structure and µm-sized aggregates were observed. Therefore, the CDSA of triblock terpolymers bearing different alkyl substituents R (= methyl, ethyl, *iso*-propyl) in the amidated block was investigated. Depending on the polarity of the used alkyl substituents, the maximum possible degree of amidation, which is suitable for the formation of well-defined patchy wCCMs, was increased of up to 60 % (*iso*-propyl substituents). The morphology of the amidated corona patch was found to change with increasing solubility in organic solvents. Polar patches, bearing R = methyl substituents, showed a collapsed spherical shape located in close proximity to the polyethylene (PE) core, whereas nonpolar patches, bearing R = *iso*-propyl groups, showed a rectangular morphology and span from the PE core to the outer rim of the corona (Fig. 2.1-2).
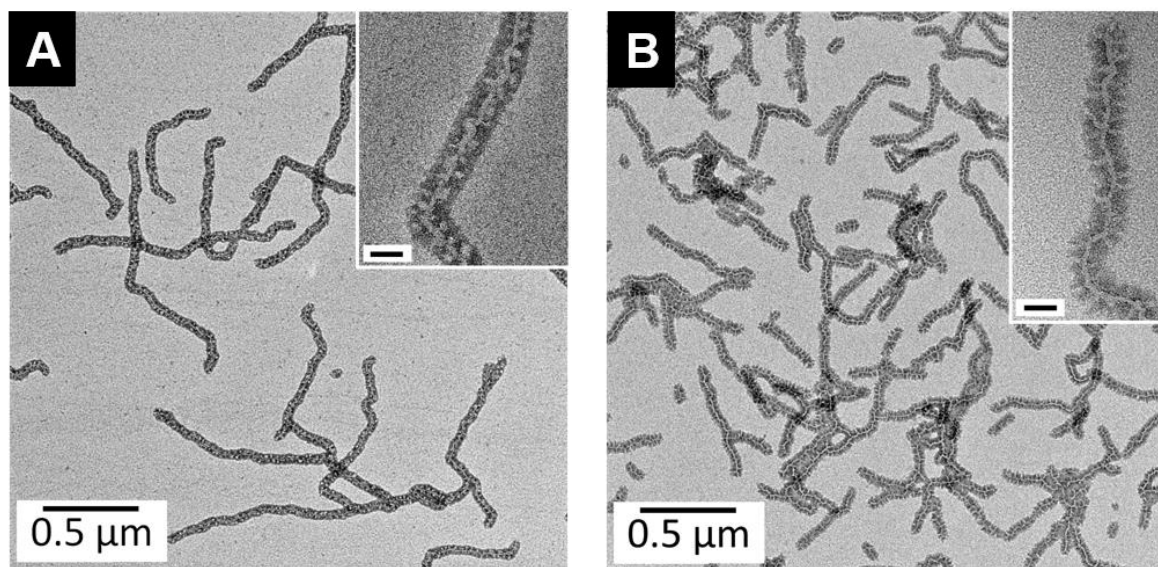
Figure 2.1-2. TEM micrographs of (A) a 17 % amidated SEM triblock terpolymer (R = methyl) and (B) a 58 % amidated SEM triblock terpolymer (R = *iso*-propyl). The scale bars in the insets are 50 nm. The polystyrene patches were selectively stained with RuO₄.

The functionalized wCCMs were tested for the stabilization of AuNPs. Therefore, tetrachloroauric (III) acid trihydrate was reduced *in situ* by Superhydride. The resulting

AuNPs ($d = 8.2 \pm 3.1$ nm) were selectively loaded into the functionalized patches as revealed by transmission electron microscopy (TEM) (Fig. 2.1-3). The hybrid material showed a narrow localized surface plasmon resonance (LSPR) at 533 nm, which is characteristic for AuNP and hints at the absence of agglomeration or aggregation.
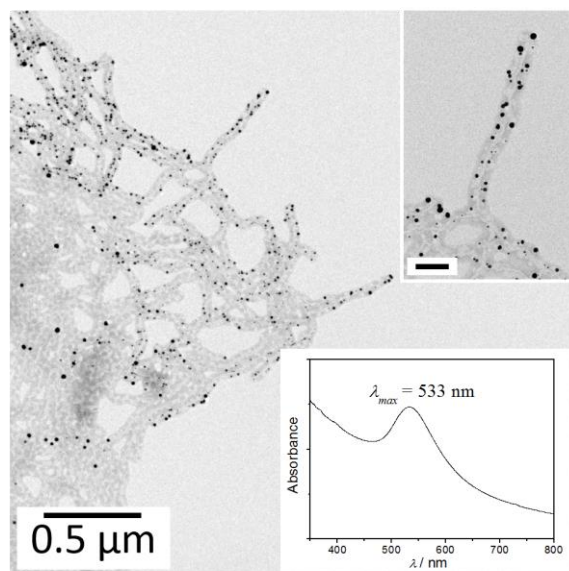

Figure 2.1-3. TEM micrograph and UV-Vis absorbance spectrum of AuNP-loaded functionalized wCCMs. The scale bar in the inset is 50 nm. Polystyrene is selectively stained with RuO_4.

2.2 Strategies for the Selective Loading of Patchy Worm-Like Micelles with Functional Nanoparticles

WCCMs with a patchy functional corona provide the possibility for a selective and controlled incorporation of different types of NPs within the corona patches. However, until now, only AuNPs were selectively incorporated into the functional corona patches (see Chapter 3). The morphology of the hybrid wCCMs shows limitations with regard to the AuNP distribution and loading capacity. Furthermore, for the CDSA of defined wCCMs, only low degrees of functionalization were possible because a side reaction, the imide formation, caused insolubility of the amidated patches.

In this publications, we developed a synthetic strategy for the production of defined wCCMs with high degrees of functionalization. The versatility of these wCCMs as NP template is shown by the incorporation of different types of NPs as well as binary loading with two types of NPs.

To overcome the limitations in loading capacity, the $S_{40}E_{21}M_{39}$[108] triblock terpolymer was functionalized by an optimized amidation reaction (Fig. 2.2-1), leading to 95 % functionalization of the PMMA block without imide formation. The resulting functionalized triblock terpolymer was completely soluble in organic solvents like THF. The crucial parameter for obtaining these high degrees of functionalization was the activation of the used amine by n-BuLi. TEM micrographs of the functionalized wCCMs show well-defined amidated patches (Fig. 2.2-1), which are comparable in size with the PS patches.
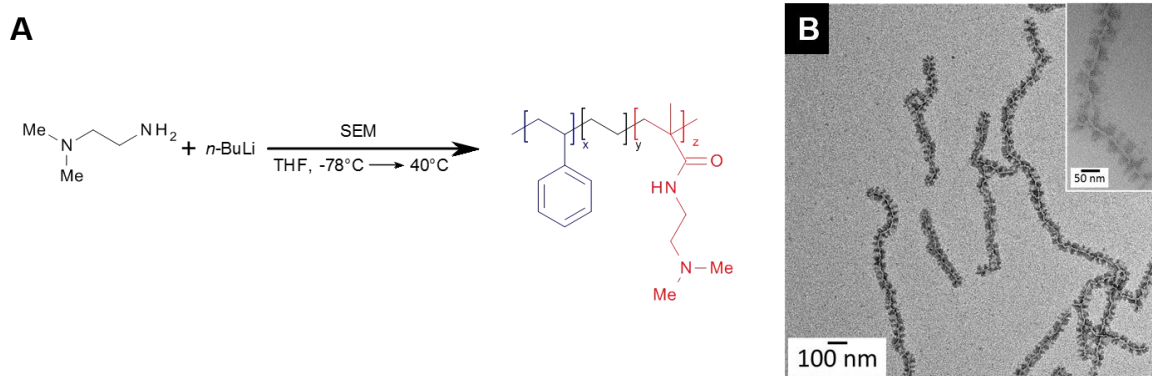

Figure 2.2-1. Amidation of the PMMA block of an $S_{40}E_{21}M_{39}$[108] triblock terpolymer with *N,N*-dimethylethylenediamine with prior activation of the amine by n-BuLi (A). TEM micrograph of the amidated SEM wCCMs (B). The sample is selectively stained with RuO_4.

The highly amidated PMMA patches provide functional groups for the incorporation of metal and metal oxide NPs. In a ligand exchange process, we loaded preformed acetate-stabilized zinc oxide (ZnO) and copper oxide (CuO) NPs in the amidated patches (Fig. 2.2-2 A-D). The wCCMs are still well dispersed and the NPs are incorporated selectively into the functionalized patches, which are observable without staining of the sample. As the size of the NPs was 2.7 ± 0.4 nm and 3.8 ± 0.6 nm for ZnO and CuO, respectively, more than one NP were incorporated per patch (width = 17 ± 5 nm). The key advantage of this loading method is the controllable size and size distribution of the preformed NPs.

In addition to the ligand exchange, we investigated the *in situ* reduction for the loading of wCCMs with metal NPs. Therefore, tetrachloroauric acid trihydrate, silver trifluoroacetate and hexachloroplatinic acid hydrate were reduced in the presence of the amidated wCCMs with a strong reduction agent. The fast reduction process leads to the formation of small NPs, which was confirmed by TEM (Fig. 2.2-2 A, E-G). The obtained NPs showed an average diameter below 5 nm for all three noble metals which promises a high active surface area for an application in catalysis. For a high loading capacity with AuNP, the patches are

observable without staining of the sample. In contrast, lower loading capacities (Ag and Pt) lead to hardly observable patches. We were furthermore able to transfer the *in situ* reduction to a continuous and controllable loading process via microfluidics. The results are similar to the batch process, which exhibits a high potential for easy upscaling, screening of reaction parameters and tailor-made hybrid materials.
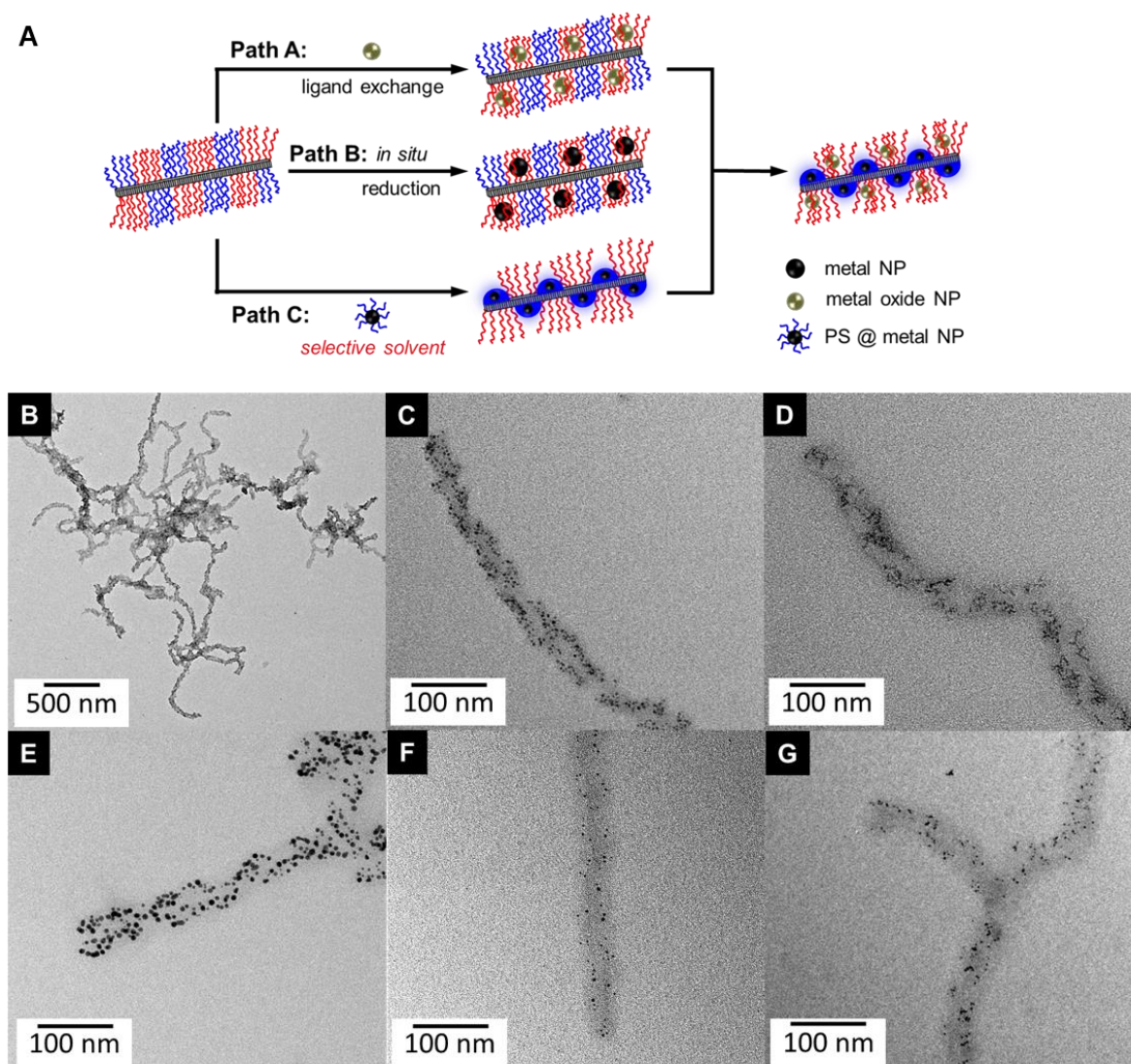
Figure 2.2-2. Strategies for NP incorporation in wCCMs (A). Hybrid wCCMs with different types of NPs: ZnO (B, C), CuO (D), Au (E), Ag (F) and Pt (G).

For binary loading of the wCCMs with two different types of NPs, a third method for NP incorporation in the PS patches is needed. To this end, co-precipitation, which is based on selective polymer-polymer and polymer-solvent interactions, is used. PS-stabilized AuNPs were first synthesized and then mixed with the wCCMs. Successive addition of acetone until a volume fraction of 90 vol % leads to a collapse of the PS patch which incorporates the PS-stabilized AuNPs (Fig. 2.2-2 A, Fig. 2.2-3 A). If ZnO NP are added before the co-

precipitation process, binary loaded hybrid wCCMs can be observed (Fig 2.2-2 A, Fig. 2.2-3 B). These hybrid wCCMs possess a high potential for photocatalytic applications as synergistic effects of ZnO and AuNP are known to enhance the catalytic activity (see Chapter 7).
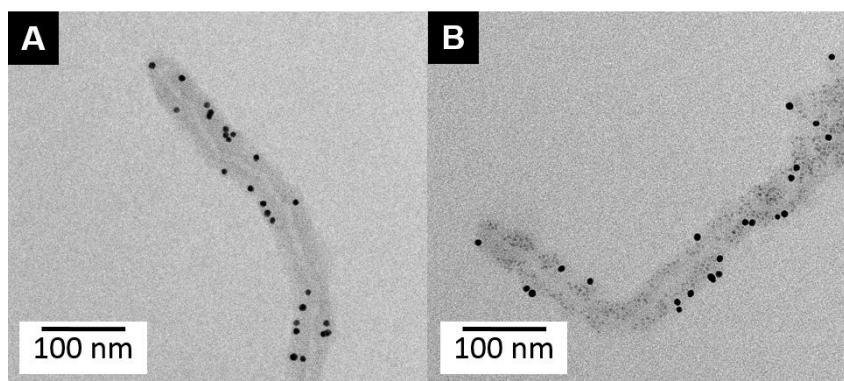

Figure 2.2-3. Stained hybrid wCCM obtained by co-precipitation with PS-stabilized AuNP (A) and binary loaded hybrid wCCM (B). The binary loaded hybrid wCCM is shown without staining to observe both, the ZnO NP (light grey spots) and the AuNP (black spots).

2.3 Bottom-Up Meets Top-Down: Patchy Hybrid Nonwovens as an Efficient Catalysis Platform

Based on the successful functionalization of the patchy wCCMs for incorporation of NPs, these materials should find an application as catalyst. Here, heterogeneous catalysis provides several advantages with respect to the purification of the reaction products and the reusability of the catalyst material. The major drawback of heterogeneous catalysts is their decreased activity compared to homogenous catalysts. To provide a sustainable catalyst, all these criteria must be taken into account.

The highly loaded hybrid wCCMs of the first two publications promised a great potential as heterogeneous catalyst. But as these hybrid materials sediment, a solution had to be found for fixation of the wCCMs on a polymeric support, which guarantees a high surface area for preservation of the good accessibility. Therefore, we designed an efficient and reusable catalyst material by the combination of coaxial electrospinning, which is a technically relevant processing method, and CDSA for the formation of functional patchy wCCMs. For coaxial electrospinning high molecular weight polystyrene (PS) was used as core material to enable the electrospinning process at low voltages (~ 10 kV) (Fig. 2.3-1 A). This low voltage was the crucial parameter for the successful coating of the supporting PS nonwoven

with the patchy wCCMs. The amino groups on the surface of the resulting patchy nonwoven are able to stabilize AuNP, which were loaded into the patches by dipping them into an aqueous dispersion of citrate-stabilized AuNPs for 24 h (Fig. 2.3-1 B).
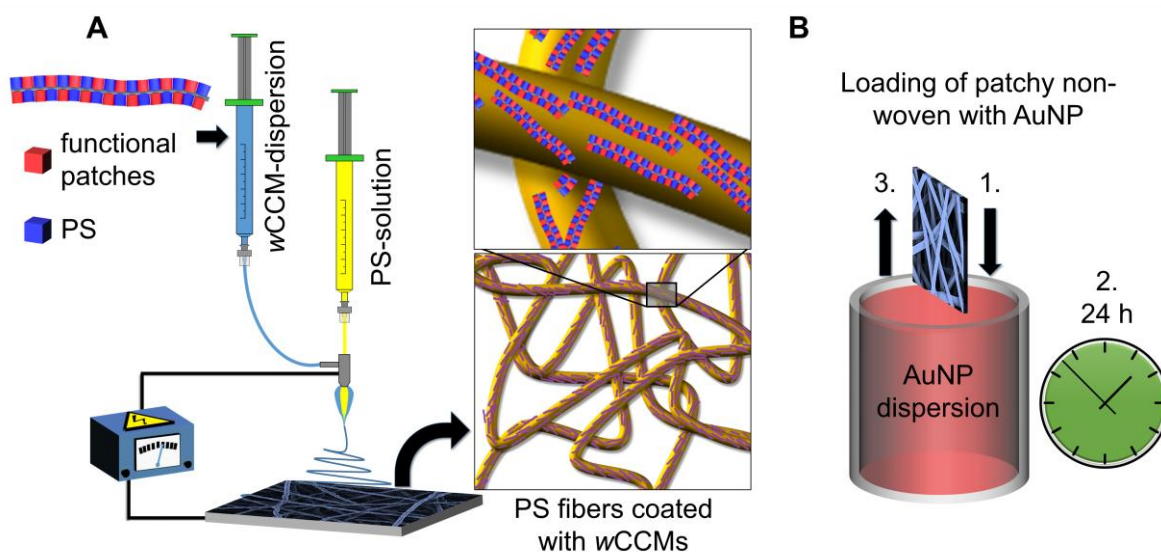
Figure 2.3-1. Schematic preparation process of patchy hybrid nonwovens through coaxial electrospinning (A) and loading of the resulting nonwovens with AuNP by dipping (B).

The obtained purple hybrid nonwovens were analyzed by scanning electron microscopy employing a backscattered electron (BSE) detector (Fig. S2.3-2 A), reflective UV-Vis measurements and small angle X-ray scattering to prove the homogeneous loading of the nonwoven with well-dispersed AuNPs. No agglomeration occurred after washing and drying of the hybrid nonwovens. The maximum loading capacity of a 1x1 cm^2 nonwoven was 41 µg of gold as revealed by inductively coupled plasma optical emission spectrometry (ICP-OES). The hybrid nonwoven was used as catalyst for the alcoholysis of dimethylphenylsilane with *n*-butanol at room temperature and showed a high catalytic activity. In comparison to literature, the reaction temperature and the time were decreased dramatically. Furthermore, the hybrid nonwoven used in this publication showed a stable performance in ten subsequent cycles of alcoholysis without loss of activity. ICP-OES proves the absence of leaching, which promises a high relevance in heterogeneous catalysis. As shown in Chapter 4, the amidated patches on the surface of the nonwoven provide an efficient stabilization for different types of NP's. This opens the way for other technical relevant catalytic reactions.
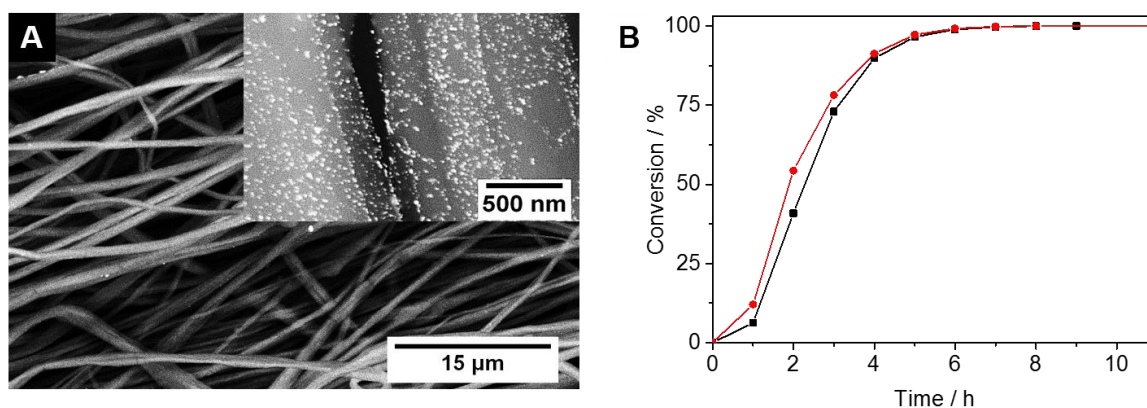
Figure 2.3-2. SEM micrograph of the hybrid nonwoven obtained by using a backscattered electron (BSE) detector (A) and conversion of dimethylphenylsilane with *n*-butanol in the first (black) and the tenth cycle (red) using the hybrid nonwoven as catalyst (B).

2.4 Clinical Wastewater Treatment: Photochemical Removal of an Anionic Antibiotic (Ciprofloxacin) by Mesostructured High Aspect Ratio ZnO Nanotubes

In addition to patchy wCCMs, which are the focus of the Chapters 3-5, also cylindrical polymer brushes (CPBs) formed by amorphous diblock copolymers (di-BCPs) are interesting template materials. Following the second concept of this thesis for synthesis of mesostructured catalysts, these CPBs provide different advantages. As the concept includes the pyrolytic removal of the polymeric template, a template, which shows a higher thermal stability than the wCCMs was needed. Furthermore, the CPBs provide a length scale of several µm, which enhances the stability of the formed inorganic catalyst. To use a catalyst like this for the photocatalytic degradation of antibiotics, we chose ZnONPs as inorganic component. These NPs provide a point of zero charge (PZC) of 9.3, which leads to a positive charge at a typical pH of 8 for clinical wastewater. Most antibiotics like ciprofloxacin bear a negative charge at this pH. Consequently, an electrostatically favored adsorption of the antibiotic on the ZnO surface is expected.

For CPB formation, di-BCPs of polybutadiene-*block*-poly(2-vinylpyridine) (PB-*b*-P2VP) were used. Quaternization of the P2VP corona with methyl iodide led to a stable solvent independent charge (Fig. 2.4-1 A). In this positively charged corona, phase pure, acetate-stabilized ZnONPs with a size of 3.2 nm were loaded to obtain hybrid cylinders (Fig. 2.4-1 B, C). Subsequent pyrolysis of these hybrid cylinders resulted in a mesostructured ZnO nonwoven (Fig. 2.4-1 D).
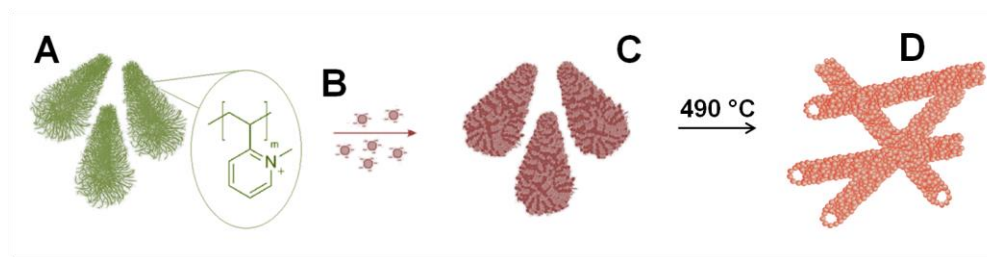
Figure 2.4-1. Scheme of the preparation of a mesostructured ZnO nonwoven. Cylindrical polymer brushes of a PB-*b*-P2VP diblock copolymer with quaternized corona (A) are loaded with ZnO NPs (B) and calcinated at 490 °C (C) to obtain the final mesostructured nonwoven (D).

SEM and TEM analysis of the ZnO hybrid material showed high loading densities of the polymeric corona due to electrostatic interactions between the positively charged corona and the negatively charged ZnONPs (Fig. 2.4-2 A, B). The core-shell structure of the hybrid cylinders is observable by a grey scale analysis (Fig. 2.4-2 inset in B). Pyrolysis of the polymeric template at 490 °C led to Ostwald ripening of the ZnONPs. However, the powder X-ray diffraction (PXRD) pattern confirmed that the nanoparticulate structure was preserved and ZnO crystals in the size range of 12 – 15 nm were obtained. The Ostwald ripening of the ZnONPs simultaneously led to sintering of the particles, which stabilizes the cylindrical structure. SEM and TEM revealed that the mesostructure was preserved after thermal treatment (Fig. 2.4-2. C, D) and the grey scale analysis of a single pyrolyzed cylinder showed the formation of nanotubes (Fig. 2.4-2 inset in D). The surface area was analyzed by Brunauer Emmett Teller measurements to yield a value of 31 m^2g^{-1}.
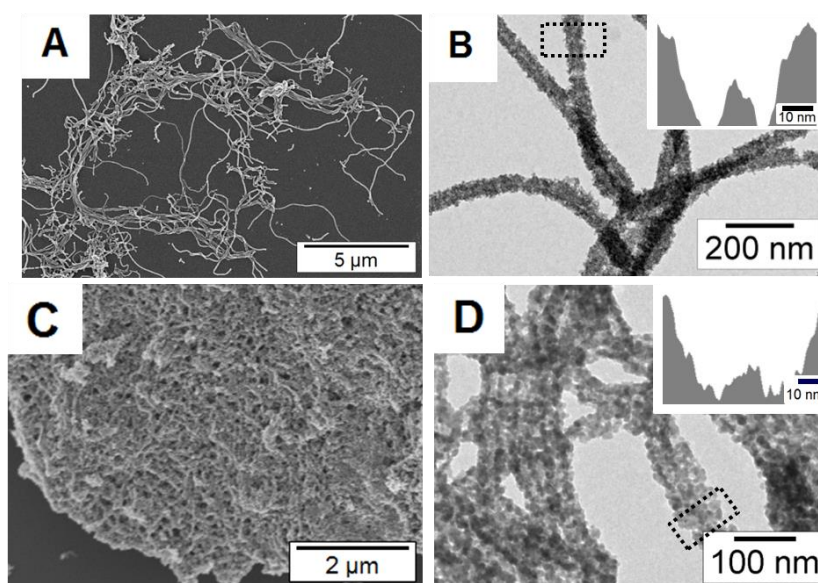
Figure 2.4-2. SEM and TEM micrographs of the ZnO hybrid material (A, B) and the pyrolyzed ZnO nanotubes (C, D). The insets show the grey scale analysis of both.

The pyrolyzed ZnO cylinders were tested in the photocatalytic degradation of ciprofloxacin, which is a common antibiotic in clinical wastewater. Here, the mesostructured ZnO catalyst showed a superior performance in comparison with Degussa P25, a common TiO$_2$ catalyst (2.9 times better degradation), and in the absence of any catalyst (33 times faster degradation). This is attributed to the above mentioned positive charge of the ZnO at a pH of 8 which favors electrostatic adsorption of the ciprofloxacin. In contrast, TiO$_2$ bears a negative charge at the same condition, as the PZC is 6.9.
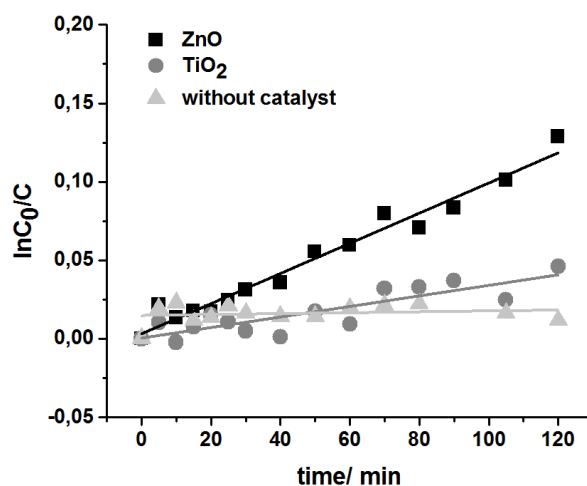
Figure 2.4-3. Kinetic plot of the photocatalytic degradation of ciprofloxacin with the pyrolyzed ZnO nanotube nonwoven, Degussa P25 (a common TiO$_2$ catalyst) and in the absence of any catalyst.

2.5 Mesostructured ZnO/Au Nanoparticle Composites with Enhanced Photocatalytic Activity

The optimization of catalyst performance is a major issue in heterogeneous catalysis. The ZnO catalyst material reported in Chapter 6 already showed an enhanced performance in the photocatalytic degradation of ciprofloxacin with respect to Degussa P25, a common used TiO$_2$ catalyst. However, the ZnO catalyst still offers a potential increase in activity by the use of synergistic effects with noble metals like AuNP. Here, the absorbance of visible light, which is used for the photocatalytic degradation of antibiotics, is enhanced by the LSPR of Au. The method reported in Chapter 6 for preparation of the catalyst material was slightly modified by addition of *in situ* synthesized AuNP to the ZnO hybrid cylinders. Pyrolysis of the ZnO/Au hybrid materials resulted in ZnO/Au nanowires (Fig. 2.5-1).
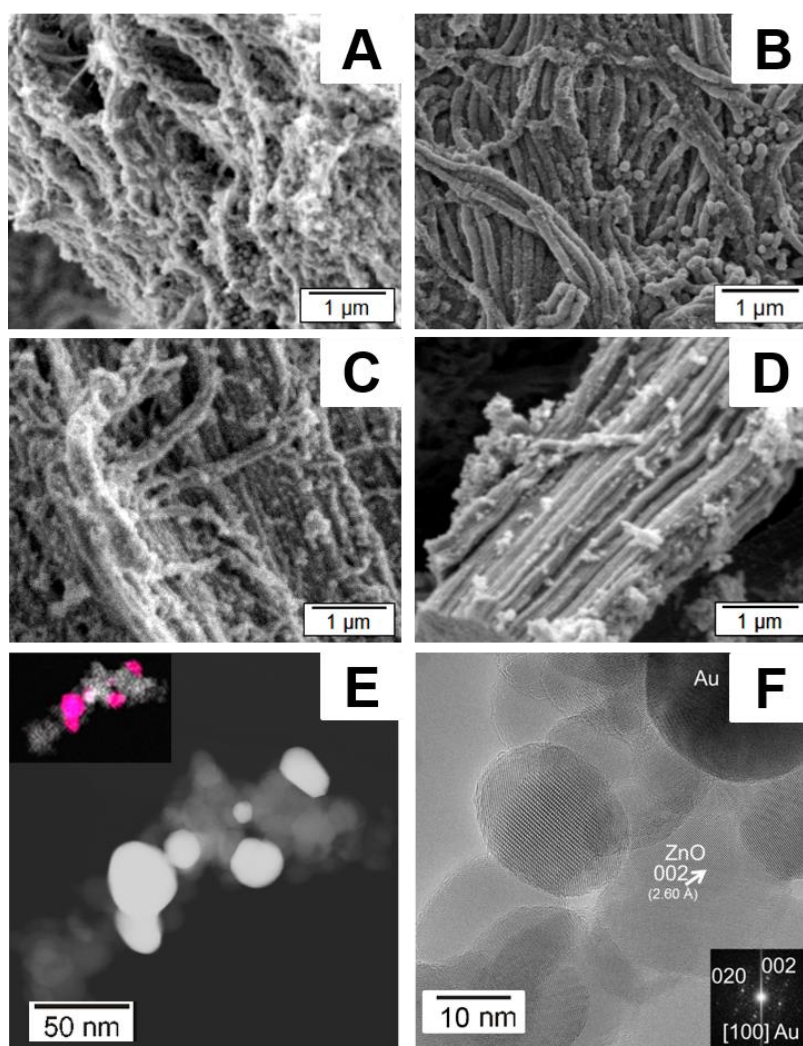
Figure 2.5-1. SEM micrographs of ZnO/Au nanoparticle composite nanowires with 8 % (A), 12 % (B), 15 % (C) and 26 % (D) Au. HAADF-STEM image (E), EDX mapping (inset in E) and HR-TEM micrograph (F) of the composite nanowires with 12 % Au. The inset in F shows the fast fourier transform (FFT) of the Au NP.

The ZnO/Au nanowires were prepared with an Au content of 8 %, 12 %, 15 % and 26 %. The SEM micrographs prove the preservation of the mesostructure after pyrolytic template removal. According to the PXRD pattern, the ZnO NP were grown from 3-4 nm before thermal treatment to 12-15 nm after thermal treatment. The AuNP tend to a more distinct growth from 4-5 nm to 18-24 nm. The HAADF-STEM image shows a clear difference in contrast of the ZnO and Au NP. The EDX mapping of the nanowire with 12 % Au content confirmes that the Au NPs are distributed statistically over the composite nanowires and the high resolution TEM micrograph clearly proves the presence of ZnO NP and Au NP within the composite nanowires.

For catalytic studies, the photocatalytic degradation of ciprofloxacin with the ZnO/Au composite nanowires was compared to the neat ZnO nanowires from Chapter 6. Only the ZnO/Au composite material with 12 % Au content showed an increased activity (1.4 times faster degradation) compared to the neat ZnO nonwovens. As the ZnO/Au composite material showed a smaller surface area (25 m^2g^{-1}) than the pure ZnO nanotubes (31 m^2g^{-1}), an effect of the surface area can be excluded and the enhancement in activity is attributed to synergistic effects. For a lower amount of Au, the synergistic effect is too weak to observe an enhancement of degradation. Higher amounts of Au result in electron-hole combinations, which lower the activity of the catalyst material. The catalytic photodegradation was also tested with another antibiotic, levofloxacin, which degrades in a similar process. Here, the same results were obtained, which is again attributed to the electrostatically favored adsorption of levofloxacin on ZnO and the synergistic effect of Au. This promises a broad applicability of the ZnO/Au composite catalyst also in other photocatalytic degradation processes, which will be the focus of future studies.
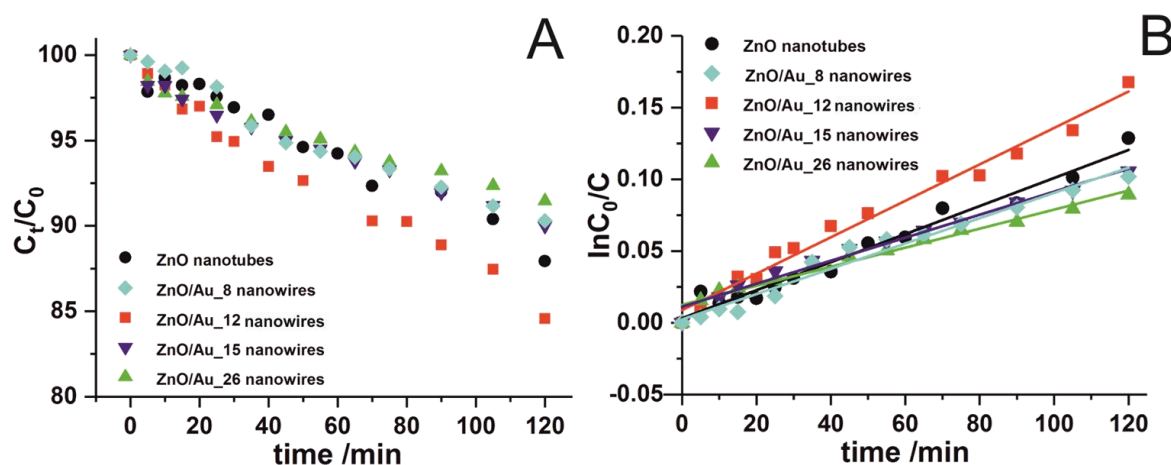
Figure 2.5-2. Kinetic plots of the photocatalytic degradation of ciprofloxacin with the ZnO/Au composite nanowires in comparison to pure ZnO nanowires.

2.6 Individual Contributions to Joint Publications

The publications included in this thesis are a collaborative work of several researchers. The individual contributions of all (co-)authors are specified in this section.

Chapter 3 is published in *Macromolecules*, **2016**, *49*, 2761 under the title

Patchy Worm-Like Micelles with Tailored Functionality by Crystallization-Driven Self-Assembly: A Versatile Platform for Mesostructured Hybrid Materials

by <u>Judith Schöbel</u>, Matthias Karg, Dominic Rosenbach, Gert Krauss, Andreas Greiner, and Holger Schmalz

I designed and conducted all experiments, did the main part of the analytics and wrote the manuscript except the part of dynamic light scattering. Matthias Karg conducted the dynamic light scattering experiments and wrote the corresponding section of the manuscript. Dominic Rosenbach and Gert Krauss were partly involved in the functionalization of PMMA and the synthesis of the gold nanoparticles and did these experiments under my supervision. Andreas Greiner co-supervised the project. Holger Schmalz supervised the project, co-designed the experiments and corrected the manuscript.

Chapter 4, to be submitted to *Nanoscale* under the title

Strategies for the Selective Loading of Patchy Worm-Like Micelles with Functional Nanoparticles

by <u>Judith Schöbel</u>, Anne Weckwerth, Mathias Schlenk, Carina Bojer, Josef Breu, Stephan Förster, Andreas Greiner, Matthias Karg, and Holger Schmalz

I designed and conducted the main part of the experiments, including the functionalization of the triblock terpolymers, the self-assembly and the synthesis of hybrid materials. I did the analytical part for all experiments. Furthermore, I was involved in the microfluidic experiments, the co-precipitation method and wrote the manuscript. Anne Weckwerth co-designed and conducted the main part of the experiments for the co-precipitation method. Mathias Schlenk co-designed and conducted the microfluidic experiments. Furthermore, he wrote a part of the manuscript. Carina Bojer synthesized the metal oxide nanoparticles. Josef Breu supervised the synthesis of metal oxide nanoparticles. Stephan Förster supervised the

microfluidic experiments. Andreas Greiner co-supervised the project. Matthias Karg supervised the co-precipitation experiments and corrected the manuscript. Holger Schmalz co-designed the experiments, supervised the project and corrected the manuscript.

Chapter 5 is published as a very important paper in *Angewandte Chemie – International Edition*, **2017**, *56*, 405 and in *Angewandte Chemie*, **2017**, *129*, 416. This paper was highlighted by Manners et al. in *Angewandte Chemie – International Edition*, **2017**, *56*, 2842 and in *Angewandte Chemie*, **2017**, *129*, 2886. The paper was published under the title

Bottom-Up Meets Top-Down: Patchy Hybrid Nonwovens as an Efficient Catalysis Platform

by Judith Schöbel, Matthias Burgard, Christian Hils, Roland Dersch, Martin Dulle, Kirsten Volk, Matthias Karg, Andreas Greiner, and Holger Schmalz

Matthias Burgard and I contributed equally to this publication. We both designed and conducted the experiments. Both of us were involved in the analytical part. I wrote the manuscript except the SAXS part. Matthias Burgard designed the figures for the manuscript and corrected the manuscript. We were both involved in the German translation of the manuscript. Christian Hils conducted a main part of the experiments under supervision of Matthias Burgard and me. Roland Dersch was involved in scientific discussions. Martin Dulle conducted the SAXS experiments and wrote the corresponding section of the manuscript. Kirsten Volk conducted the UV-Vis reflectance measurements. Matthias Karg supervised the UV-Vis reflectance measurements and was involved in the correction of the manuscript. Andreas Greiner co-supervised the project and was involved in scientific discussions. Holger Schmalz co-designed the experiments, supervised the project, corrected the manuscript and was involved in the German translation of the manuscript.

Chapter 6 is published in *Applied Catalysis B*, **2017**, *204*, 561 under the title

Clinical Wastewater Treatment: Photochemical Removal of an Anionic Antibiotic (Ciprofloxacin) by Mesostructured High Aspect Ratio ZnO Nanotubes

by Carina Bojer, Judith Schöbel, Thomas Martin, Michael Ertl, Holger Schmalz, and Josef Breu

This publication is a joint project of the departments Inorganic Chemistry I and Macromolecular Chemistry II of the University of Bayreuth in the frame of the Collaborative Research Center SFB840, project A2.

I co-authored this publication and synthesized the diblock copolymer. I was involved in the design of the experiments, scientific discussions and wrote a part of the manuscript. Carina Bojer designed and conducted all experiments and wrote the main part of the manuscript. Thomas Martin conducted the PXRD measurements and the Rietveld refinements. Michael Ertl designed and constructed the continuous flow reactor. Holger Schmalz was involved in scientific discussions and corrected a part of the manuscript. Josef Breu supervised the project and corrected the manuscript.

Chapter 7 is published in *Polymer*, **2017**, *128*, 65 under the title

Mesostructured ZnO/Au Nanoparticle Composites with Enhanced Photocatalytic Activity

by Carina Bojer, Judith Schöbel, Thomas Martin, Thomas Lunkenbein, Daniel R. Wagner, Andreas Greiner, Josef Breu, and Holger Schmalz

This publication is a joint project of the departments Inorganic Chemistry I and Macromolecular Chemistry II of the University of Bayreuth in the frame of the Collaborative Research Center SFB840, project A2.

Carina Bojer and I contributed equally to this publication. Both of us designed and conducted the experiments and wrote the manuscript. Thomas Martin conducted the PXRD measurements and the Rietveld refinements. Thomas Lunkenbein conducted the HR-TEM and HAADF measurements and wrote the corresponding section of the manuscript. Daniel R. Wagner was involved in the photocatalytic degradation experiments. Andreas Greiner co-

supervised the project. Josef Breu and Holger Schmalz supervised the project and corrected the manuscript.

3 Patchy Worm-Like Micelles with Tailored Functionality by Crystallization-Driven Self-Assembly: A Versatile Platform for Mesostructured Hybrid Materials

Judith Schöbel,[†] Matthias Karg,[‡] Dominic Rosenbach,[†] Gert Krauss,[†] Andreas Greiner,[†] Holger Schmalz[†,]*

[†] Makromolekulare Chemie II, Universität Bayreuth, 95440 Bayreuth, Germany

[‡] Physikalische Chemie I, Universität Bayreuth, 95440 Bayreuth, Germany
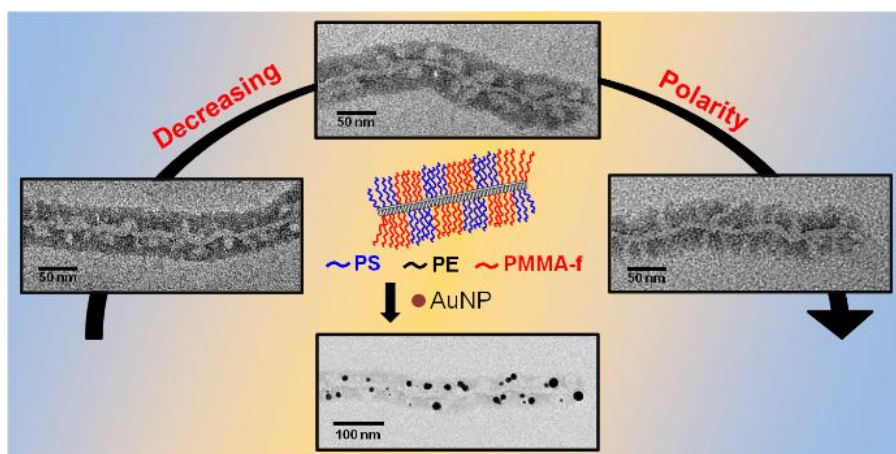
Abstract

One-dimensional patchy nanostructures are interesting materials due to their excellent interfacial activity and their potential use as carrier for functional nanoparticles. Up to now only worm-like crystalline-core micelles (wCCMs) with a non-functional patchy PS/PMMA corona were accessible using crystallization-driven self-assembly (CDSA) of polystyrene-*block*-polyethylene-*block*-poly(methyl methacrylate) (SEM) triblock terpolymers. Here, we present a facile approach toward functional, patchy wCCMs, bearing tertiary amino groups in one of the surface patches. The corona forming PMMA block of a SEM triblock terpolymer was functionalized by amidation with different *N,N*-dialkylethylenediamines in a polymer analogous fashion. The CDSA of the functionalized triblock terpolymers in THF was found to strongly depend on the polarity/solubility of the amidated PMMA block. The lower the polarity of the amidated PMMA block (increased solubility) the higher is the accessible degree of functionalization upon which defined, well-dispersed wCCMs are formed. Interestingly, also the structure of the patchy corona can be tuned by the composition/chemistry of the functional patch, giving rise to spherical patches for R = methyl, ethyl and rectangular patches for R = *iso*-propyl. Patchy wCCMs were successfully used as template for the selective incorporation of Au nanoparticles within the amidated corona patches, showing their potential as versatile platform for the construction of functional, mesostructured hybrid materials.

3.1 Introduction

The self-assembly of amorphous block copolymers (BCPs) is a well-established route for the production of tailor-made micellar nano- and microstructures. From simple micellar core-shell systems to more complex multicompartment micelles (MCMs) there is a wide range of accessible morphologies in solution, for example spherical,[1-4] cylindrical,[1,2,5-9] helical[8-12] and lamellar[13] structures. These morphologies are prepared by self-assembly in selective solvents[14-16] or by applying different external stimuli like temperature[17,18] and pH[19,20]. A broad variety of applications is accessible using especially MCMs, e.g., in drug delivery,[2,21-23] as template for the formation of hybrid materials with metal nanoparticles,[10,24,25] in optoelectronic devices[14,21,26] or in paints and cosmetics.[2,14]

In recent years, the crystallization-driven self-assembly (CDSA) of semi-crystalline BCPs has attracted increasing interest.[27-29] While cylindrical micelles, self-assembled by amorphous BCPs, are known to show a broad length distribution, CDSA facilitates the production of defined cylindrical micelles with a semi-crystalline core and a high aspect ratio.[30] This field was pioneered by the work of MANNERS and WINNIK et al. on the CDSA of diblock copolymers with a semi-crystalline polyferrocenyldimethylsilane (PFS) block.[31] The key advantage of CDSA over self-assembly of amorphous block copolymers is that CDSA can be conducted in a living manner, i.e. in analogy to the living polymerization of vinyl monomers, which allows to precisely control the length and length distribution of cylindrical micelles.[32-34] Moreover, this excellent control over self-assembly opens access to more complex micellar architectures, like block co-micelles[32,35,36] (the micellar analogues to block copolymers), non-centrosymmetric block co-micelles[37], patchy block co-micelles[38], branched micelles[39], 2D lenticular platelet micelles[40] and scarf-shaped micelles[35], hierarchical self-assemblies[41,42] and hybrid structures[43-45]. Living CDSA has also been reported for block copolymers with polyethylene[46,47], π-conjugated poly(3-hexylthiophene)[34], poly(ε-caprolactone)[48] and stereoregular polylactide[49] blocks.

Recently, we have shown that patchy worm-like micelles can be produced by the CDSA of polystyrene-*block*-polyethylene-*block*-poly(methyl methacrylate) (SEM) triblock terpolymers with a semi-crystalline polyethylene (PE) middle block.[50] Depending on the solvent quality for the PE block, spherical (sCCMs) or worm-like (wCCMs) crystalline-core micelles with a patch-like microphase-separated polystyrene/poly(methyl methacrylate) (PS/PMMA) corona were obtained.[51] Small-angle neutron scattering on a SEM triblock

terpolymer with a deuterated PS block clearly showed the presence of the patchy corona in solution, i.e., microphase-separation of the corona blocks occurs simultaneously with crystallization of the PE block upon cooling.[52] Taking advantage of the solvent dependence of self-assembly, sCCMs - which were prepared by self-assembly in dioxane - were used as seeds for the living CDSA of triblock co- and terpolymers with a semi-crystalline PE middle block and the formation of PE based block *co*-micelles.[47] Patchy wCCMs show excellent interfacial activities comparable to that of Janus cylinders, making them promising candidates for highly active surfactants and compatibilizers in polymer blends.[53] It is noted that spherical and cylindrical micelles as well as vesicles with a patch-like microphase-separated corona structure were also observed for amorphous block copolymers.[9,54-60]

So far, only wCCMs with a non-functional patchy PS/PMMA corona were accessible. The lack of suitable functional groups limits the applicability of these patchy micelles, e.g., as carriers for the incorporation of pre-formed nanoparticles or as nanoreactors for the selective *in-situ* synthesis of nanoparticles within one type of corona patch. There are some limitations arising from the triblock terpolymer synthesis, which complicate the preparation of such functional patchy micelles. The SEM triblock terpolymers are produced by catalytic hydrogenation of the corresponding poly(1,4-butadiene) containing triblock terpolymer, synthesized by sequential anionic polymerization.[50] Consequently, functional groups like amino groups cannot be introduced prior to hydrogenation, as this results in a poisoning of the hydrogenation catalyst and hydrogenation fails. Thus, we decided to introduce functional groups after the hydrogenation step *via* post-polymerization modification of the PMMA block in SEM triblock terpolymers. PMMA is reported to show low reactivity toward post-polymerization modifications. Frequently, a high excess of reactants is indispensable for hydrolysis,[61] transesterification[62] or amidation[63]. THEATO et al. showed that the use of organo-activating agents in the amidation of PMMA can dramatically increase conversions up to 70% within 48h reaction time.[64] However, an excess of amine and organo-activator is required, making additional purification steps necessary to remove residual organo-activator.

Here, we report on the preparation of wCCMs with a functional patchy corona, bearing tertiary amino groups in one of the surface patches, utilizing crystallization-driven self-assembly. To this end, the PMMA block of a SEM triblock terpolymer was functionalized by amidation with different *N,N*-dialkyethylenediamines. First, the post-polymerization modification was optimized on a PMMA homopolymer and then transferred to the SEM

triblock terpolymer. The influence of the degree of amidation and the polarity of the amidated PMMA block on CDSA of the functionalized triblock terpolymers is investigated by micro differential scanning calorimetry (μ-DSC), static (SLS) and dynamic (DLS) light scattering and transmission electron microscopy (TEM). It is shown that the solubility of the amidated PMMA block needs to be adjusted properly in order to get well-defined wCCMs with tailored patch functionality, which can be further used as templates for the selective incorporation of gold nanoparticles.

3.2 Experimental

Materials. *N,N*-Dimethylethylenediamine (DMEDA), *N,N*-diethylethylenediamine (DEEDA) and *N,N*-di*iso*propylethylenediamine (D*i*PEDA) were purchased from Acros Organics and were purified by distillation prior to use. Dimethyl sulfoxide (DMSO) and tetrahydrofuran (THF) were used as received (Sigma-Aldrich, p.a. grade). PMMA granulate with $M_n = 35000$ g mol^{-1} was purchased from Sigma-Aldrich. Hydrogen tetrachloroaurate(III) trihydrate (Alfa Aesar, 99.99%) and Superhydride® (LiEt$_3$BH, 1 M solution in THF, Sigma-Aldrich) were used as received.

Synthesis of the SEM triblock terpolymer. The polystyrene-*block*-polyethylene-*block*-poly(methyl methacrylate) (SEM) triblock terpolymer was synthesized by a combination of living anionic polymerization and catalytic hydrogenation, as reported elsewhere.[50] First, the corresponding polystyrene-*block*-poly(1,4-butadiene)-*block*-poly(methyl methacrylate) (SBM) precursor was synthesized by sequential anionic polymerization in toluene. The obtained SBM triblock terpolymer was extracted with cyclohexane, a selective solvent for polystyrene and polybutadiene, in order to remove small traces of remaining polystyrene homopolymer and polystyrene-*block*-poly(1,4-butadiene) diblock copolymer, originating from termination (Figure S3-1). The molecular weight and the composition of the SBM triblock terpolymer were determined by a combination of MALDI-TOF MS (Bruker Reflex III) and ^{1}H-NMR and resulted in S$_{40}$B$_{21}$M$_{39}$^{107} ($Đ_M$ = 1.03, THF-SEC calibrated with PS standards), where the subscripts correspond to the mass fraction of the blocks in wt % and the superscript denotes the overall molecular weight in kg mol^{-1}. Catalytic hydrogenation of the poly(1,4-butadiene) middle block using Wilkinson catalyst resulted in the corresponding polystyrene-*block*-polyethylene-*block*-poly(methyl methacrylate) (S$_{40}$E$_{21}$M$_{39}$^{108}) triblock terpolymer.

Amidation of PMMA and SEM. In a typical synthesis, 0.5 g PMMA (1 eq with respect to MMA units) was dissolved in 50 mL DMSO ($c = 10$ g L^{-1}) at room temperature. The solution and the amine were degassed with argon for 30 min in separate vessels. 30 eq of amine were added to the PMMA solution and heated to 130 °C under argon. Detailed information on the applied reaction times can be found in the *Results and Discussion* section. The amidated PMMA was purified by dialysis against water (Spectrapor 4 dialysis tubes from regenerated cellulose with MWCO of 12-14 kDa), followed by freeze-drying yielding a white powder.

For the $S_{40}E_{21}M_{39}^{108}$ triblock terpolymer, 0.5 g $S_{40}E_{21}M_{39}^{108}$ (1 eq with respect to MMA units) was dispersed in DMSO ($c = 10$ g L^{-1}) at 130 °C for 4 h. After cooling down to room temperature, the dispersion and the amine were degassed with argon for 30 min in separate vessels. 30 eq of amine were added to the polymer dispersion and heated to 130 °C under argon (details on applied reaction times in *Results and Discussion* section). The amidated triblock terpolymer was purified by dialysis against water and subsequent freeze-drying.

Sample Preparation. The amidated triblock terpolymers were dissolved at 65 °C in THF ($c = 10$ g L^{-1}) for 30 min and quenched to the crystallization temperature of the PE middle block, which was determined by µ-DSC measurements. Crystallization was conducted for 1 d in a thermo shaker (HLC MKR-13, Ditabis) at 200 rpm.

In situ **synthesis of gold nanoparticles.** A 10 g L^{-1} dispersion of $S_{38}E_{20}DEA_{42}^{114}$-31 in THF was heated to 65 °C for 30 min and subsequently quenched to 28 °C for 1 d for crystallization. The dispersion was diluted to 1 g L^{-1} and stirred for 1 h. Then, 15 µL of a 0.1 M solution of hydrogen tetrachloroaurate(III) trihydrate in THF (2.3 eq) was added to 2 ml of the $S_{38}E_{20}DEA_{42}^{114}$-31 dispersion (1 g L^{-1}, 1 eq with respect to tertiary amino groups in the amidated PMMA block) and stirred for 1 h. 7.5 µL of a 1 M solution of Superhydride® in THF (4.3 eq) was added to reduce the hydrogen tetrachloroaurate(III) trihydrate. The color changed immediately to violet. The solution was stirred for 1 h before preparation for TEM analysis.

Instruments. The amidated PMMA homopolymers were characterized by ^{1}H-NMR spectroscopy (Bruker Ultrashield 300 spectrometer) using deuterated DMSO with 1 vol % of trifluoroacetic acid as solvent. The signal assignment was supported by simulations with the NMR-software *MestReNova*.

FT-IR spectroscopy was conducted on a Digilab Excalibur Series FTS with a MIRacle ATR unit of Pike Technologies. The ester conversion was determined from the peak absorbances of the remaining ester vibration at 1717-1724 cm^{-1} and the amide I vibration at 1666 cm^{-1}.

The thermal properties of the amidated SEM triblock terpolymers in solution (10 g L^{-1} in THF) were studied by micro differential scanning calorimetry (SETARAM micro-DSC III). For the measurements closed batch cells and a scanning rate of 0.5 K/min were employed. Pure THF was used as reference.

The morphology of the patchy wCCMs was investigated by elastic bright-field transmission electron microscopy (TEM) using a ZEISS 922 Omega EFTEM (Zeiss NTS GmbH, Oberkochen, Germany) electron microscope operated at an acceleration voltage of 200 kV. Zero-loss filtered images were registered digitally on a bottom mounted CCD camera system (Ultrascan 1000, Gatan) and processed with a digital imaging processing system (Gatan Digital Micrograph 3.9 for GMS 1.4). The samples were diluted to 0.1 g L^{-1} and 10 µL were drop-coated onto a carbon-coated copper grid lying on a filter paper. After drying in a vacuum oven at room temperature and a pressure of 20 mbar, the samples were stained with RuO$_4$ vapor, which is known to selectively stain PS. For determination of the average length of the micelles, at least 100 wCCMs were measured. For the average size of the gold nanoparticles at least 150 particles were analyzed with the software *ImageJ*.

The hybrid material of S$_{38}$E$_{20}$DEA$_{42}$^{114}-31 wCCMs and gold nanoparticles in THF was analyzed by UV-Vis spectroscopy (V630-spectrophotometer from JASCO). The measurement was conducted in a fused silica cuvette (d = 0.1 cm) at room temperature.

Dynamic and static light scattering were measured on a 3D LS spectrometer (LS Instruments AG, Fribourg, Switzerland) in 2D operation. A continuous-wave HeNe laser emitting at λ = 632.8 nm (max. output power of 35 mW) was used as a light source. All measurements were performed in an angular range from θ = 30° - 150° yielding an accessible q-range of 0.007 – 0.027 nm^{-1}. The sample temperature was adjusted by a heat controlled decalin bath and controlled by a PT100 thermoelement that was placed in the vicinity of the sample. Prior to the measurements each sample was filtered using PTFE membranes (hydrophobic) with 5 µm pore size (Rotilabo). For static light scattering (SLS) the time-average scattered light intensity was measured in angular steps of 5° with 15 s acquisition time (3 runs each) and normalized by the laser intensity as monitored by a monitor diode. The scattered light was recorded by two APD detectors allowing for cross-correlation in dynamic light scattering

(DLS). DLS was performed in steps of 15° with 60 s acquisition time sufficiently long to reach convergence of the intercept and relaxation rate Γ as analyzed by second-order cumulant analysis. Hydrodynamic radii, R_h, were calculated using the Stokes-Einstein equation $R_h = \dfrac{k_B T}{6\pi\eta D_T}$, with k_B, the Boltzmann constant, T, the absolute temperature, η, the viscosity of the solvent and D_T, the translational diffusion coefficient.

3.3 Results and Discussion

We aimed on the preparation of worm-like crystalline-core micelles (wCCMs) with a functional patchy corona, bearing tertiary amino groups in one of the surface patches that can be utilized as templates for the selective incorporation of Au nanoparticles. To this end, a SEM triblock terpolymer was functionalized by amidation of the corona forming PMMA block with different *N,N*-dialkylethylenediamines (Scheme 3-1).
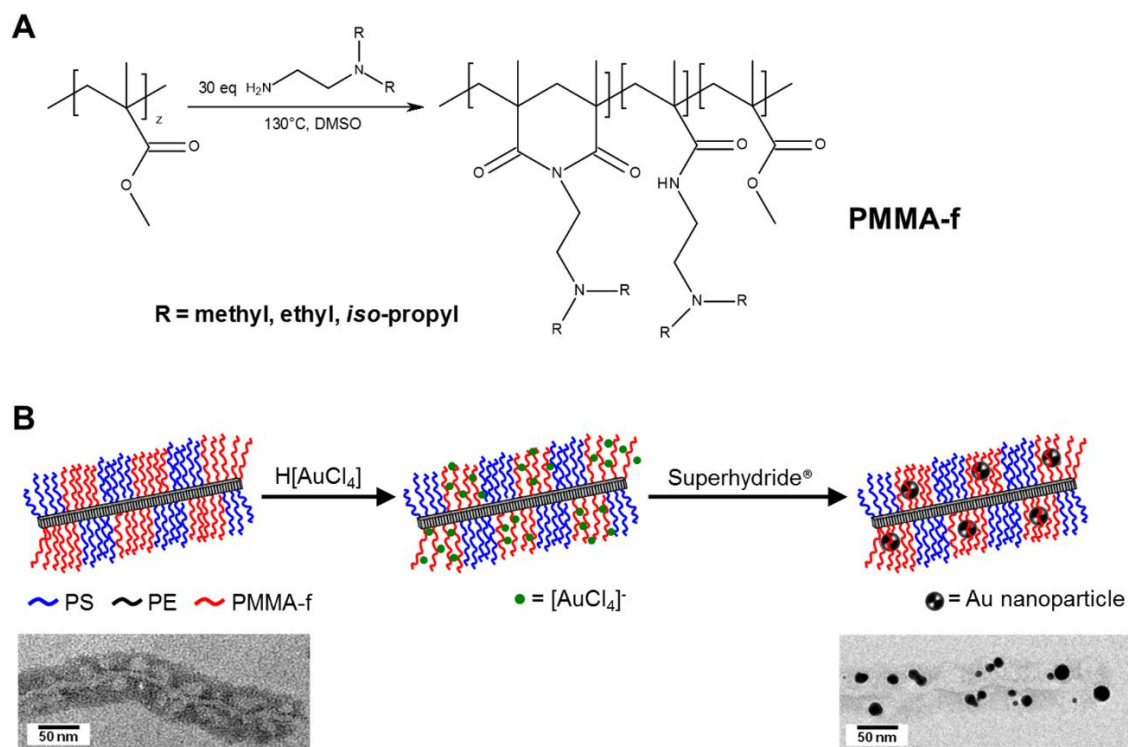
Scheme 3-1. A) Amidation of PMMA with *N,N*-dialkylethylenediamines. The reaction leads to a random copolymer with imide, amide and remaining ester units. B) Selective *in-situ* formation of Au nanoparticles within the amidated patches of functional wCCMs (TEM images correspond to $S_{36}E_{21}DEA_{43}{}^{114}$-31 wCCMs).

It is not possible to directly characterize the functionalized triblock terpolymers by ^{1}H-NMR. For NMR studies all blocks need to be soluble in the employed solvent. Due to the limited solubility of the PE middle block in organic solvents and the polarity of the amidated PMMA block only THF at elevated temperature, i.e. above the melting point of the PE block (ca. 50 °C), can be used. However, as THF shows a residual signal at 3.56 ppm, which overlaps with the remaining ester units of PMMA at 3.52 ppm (Figure S3-2), the conversion of ester units is not quantifiable by ^{1}H-NMR spectroscopy and can only be determined by means of FT-IR spectroscopy. Hence, we first studied the amidation of a PMMA homopolymer to provide a correlation between conversion from ^{1}H-NMR and FT-IR spectroscopy, which is transferrable to the SEM triblock terpolymers in order to get quantitative results from FT-IR spectroscopy.

Amidation of PMMA. PMMA ($M_n = 35,000$ g mol^{-1}) was amidated in the presence of excess amine (30 eq with respect to MMA units) at 130 °C in DMSO. The amines used in this study were *N,N*-dimethylethylenediamine (DMEDA), *N,N*-diethylethylenediamine (DEEDA) and *N,N*-di*iso*propylethylenediamine (D*i*PEDA) (Scheme 3-1). Successful amidation was proven by FT-IR and ^{1}H-NMR spectra, as shown for a representative DMEDA-functionalized PMMA in Figure S3. Besides characteristic amide I and amide II bands at 1666 cm^{-1} and 1526 cm^{-1}, respectively, a shift of the C=O stretching vibration of the pendant methyl ester units, which is typically found at 1728 cm^{-1} for PMMA, to 1716 cm^{-1} was observed. This indicates imide formation as a side reaction, which was also observed by THEATO et al.[64] ^{1}H-NMR spectroscopy confirms this assignment as there are typical proton signals for amide and imide units in the amidated PMMA (Figure S3-3B). Thus, the obtained amidated PMMA is a random copolymer composed of amide, imide, and residual MMA units (Scheme 3-1A). Size exclusion chromatography (SEC) shows that amidation proceeds without side reactions as the molecular weight distribution of the amidated PMMA is still monomodal and shifted to higher molecular weights compared to the neat PMMA homopolymer (Figure S3-4).

Figure 3-1A shows the conversion *vs*. time plot for the amidation with DMEDA as obtained from ^{1}H-NMR. A conversion of > 90% is already observed after 60 h and almost full conversion is reached after 100 h. This shows that even in the absence of an organo-activator a complete conversion of PMMA ester units can be achieved for the employed *N,N*-dimethylethylenediamine. From the integral of the specific imide and amide proton signals

(**5′** and **5** in Figure S3B, respectively), the fraction of imide units can be calculated to be $50 \pm 6\%$ and hardly depends on the conversion of PMMA ester units (Figure 3-1A).
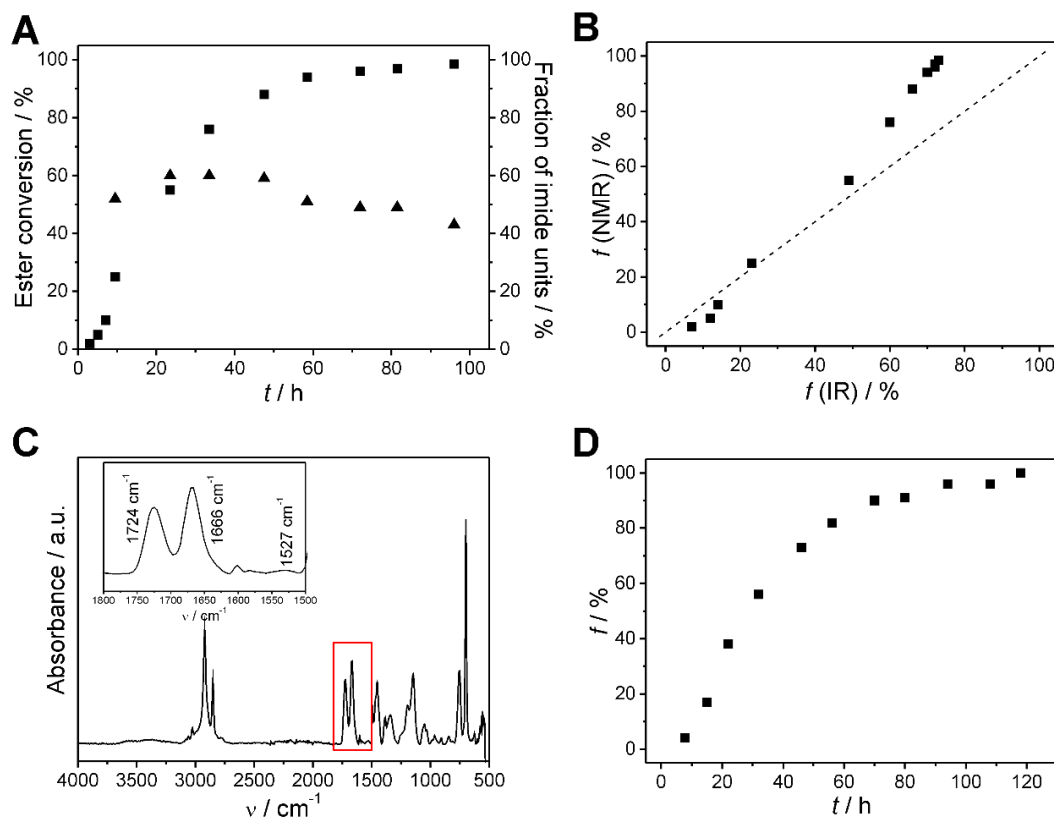

Figure 3-1. A) Kinetics of the amidation of PMMA with DMEDA (squares) and fraction of imide units in dependence on reaction time as determined from ^{1}H-NMR (triangles). B) Correlation of degree of functionalization, i.e. the fraction of consumed PMMA ester units, determined from ^{1}H-NMR and FT-IR (dashed line corresponds to ideal correlation with identical results from both methods). C) FT-IR spectrum of $S_{36}E_{19}DMA_{45}{}^{118}$-73, where the amide I band is observable at 1666 cm^{-1}. D) Kinetics of the amidation of SEM with DMEDA.

Figure 3-1B shows the correlation between the degree of functionalization (*f*), i.e. fraction of consumed ester units, determined quantitatively from ^{1}H-NMR with that extracted from the FT-IR spectra (qualitative results by comparing the intensity of ester (1716 cm^{-1}) and amide I bands (1666 cm^{-1})). This correlation shows comparable results from ^{1}H-NMR and FT-IR at low degrees of functionalization, but deviates at higher conversions with *f* determined from ^{1}H-NMR being systematically larger compared to that from FT-IR. This can be attributed to the presence of imide groups, whose absorption is overlaid with that of residual ester units and, thus, the degree of functionality is underestimated from FT-IR data especially at higher conversions (weaker absorption of remaining ester units).

Synthesis and self-assembly of DMEDA-amidated SEM triblock terpolymers (SEDMA). The selective amidation of the PMMA block within the SEM triblock terpolymer ($S_{40}E_{21}M_{39}^{108}$, subscripts denote weight fractions of the blocks and superscript gives M_n in kg mol^{-1}) with DMEDA was conducted in a similar way as for the PMMA homopolymer. In DMSO, the PS and the PMMA blocks are dissolved at 130 °C, but the molten PE block (T_m(bulk SEM) $\approx$ 88 °C[50]) is insoluble. Therefore, micelle formation was observed by a characteristic blue color of the dispersion (Tyndall effect) during the reaction. Nevertheless, FT-IR spectroscopy confirms successful functionalization of the SEM triblock terpolymer after amidation for 46 h (Figure 3-1C). The amide I and amide II bands are located at 1666 cm^{-1} and 1527 cm^{-1}, respectively, and the shift of the C=O vibration of the remaining PMMA ester units from 1728 cm^{-1} to 1724 cm^{-1} indicates the presence of imide units in the amidated SEM triblock terpolymer. This is consistent with the results obtained for the DMEDA-amidated PMMA homopolymer (Figure S3-3A). For the reaction kinetics (Figure 3-1D), the degree of functionalization (conversion of MMA ester units) was determined applying the ^{1}H-NMR/FT-IR correlation shown in Figure 3-1B. For almost full conversion of the PMMA ester units, a slightly longer reaction time of 120 h is required in comparison with the amidation of the PMMA homopolymer (100 h for full conversion). This can be attributed to the limited accessibility of the MMA units in the micellar corona slowing down the reaction.

Self-assembly studies on the neat SEM triblock terpolymers have shown that the presence of unimers prior to crystallization of the PE middle block is decisive for the formation of wCCMs in a good solvent for PE like THF.[51] Thus, the important question is whether we still get well-defined patchy wCCMs via CDSA after selective amidation of the PMMA block, which might influence the solubility of the triblock terpolymer. Figure 3-2A shows a TEM image of the structures obtained by CDSA (1 d at 25 °C, c = 10 g L^{-1} in THF) of the amidated SEM triblock with a degree of functionalization of f = 17% ($S_{39}E_{21}DMA_{40}^{110}$-17). Well-dispersed wCCMs with a bright appearing, continuous PE core and a patchy corona are formed. Due to the selective staining with RuO$_4$, the PS domains in the corona appear dark, whereas the bright patches correspond to the amidated PMMA (PDMA) block. In contrast to wCCMs formed by the neat SEM triblock terpolymer ($S_{40}E_{21}M_{39}^{108}$) in THF, which show an alternating arrangement of equally sized PS and PMMA domains, the $S_{39}E_{21}DMA_{40}^{110}$-17 wCCMs exhibit significantly smaller spherical PDMA domains. This is at a first glance unexpected, as both the PS and PDMA blocks have similar length and

accordingly should form patches of similar size. One possible explanation for the reduced PDMA patch size might be the limited solubility of the PDMA block in THF, as deduced from solubility studies on the corresponding amidated PMMA homopolymers (Table S3-1). A similar reduction in patch size was observed for the CDSA of SEM triblock terpolymers in toluene, which is a slightly better solvent for PS compared to PMMA. As a result, the PMMA patches were significantly smaller compared to the PS patches, despite the equal length of both corona blocks.[51]
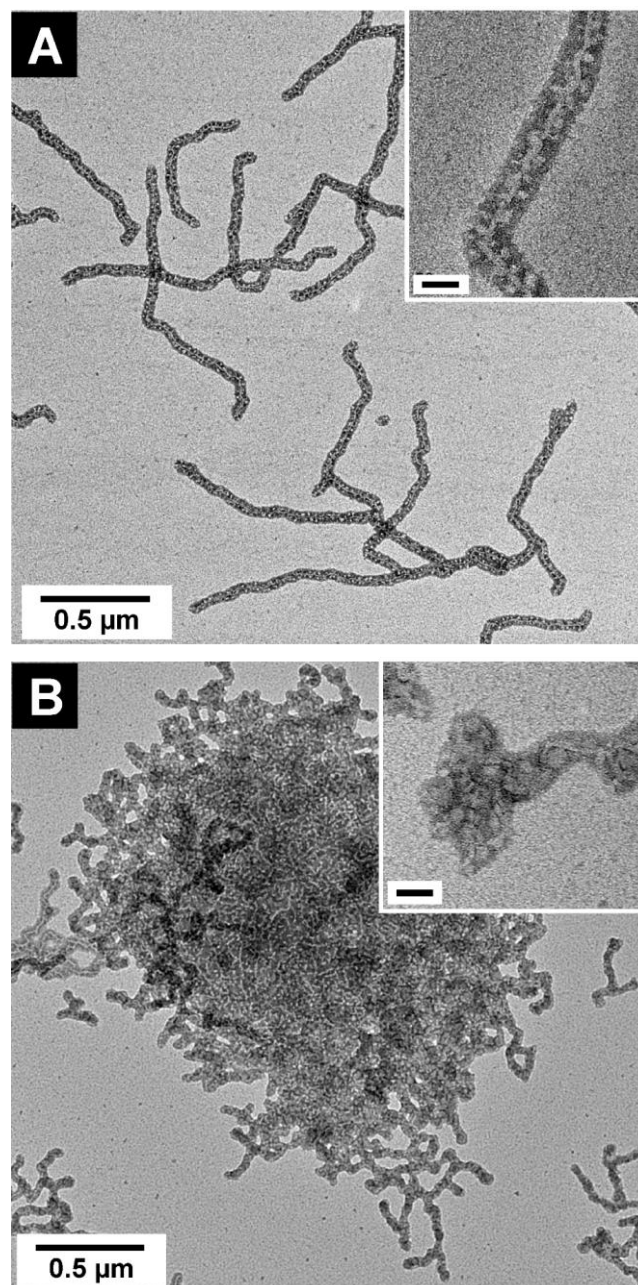
Figure 3-2. TEM micrographs of A) $S_{39}E_{21}DMA_{40}^{110}$-17 and B) $S_{36}E_{19}DMA_{45}^{118}$-73, the PS domains were selectively stained with RuO_4 and appear dark. Scale bars in the insets are 50 nm.

Increasing the degree of functionalization to 73% ($S_{36}E_{19}DMA_{45}{}^{118}$-73) results in a drastic change in micelle morphology (Figure 3-2B) and dispersion stability. The $S_{36}E_{19}DMA_{45}{}^{118}$-73 wCCMs form large agglomerates with a discontinuous, ill-defined PE core. The corona exhibits a rather undefined structure, with slightly larger PDMA patches compared to that in $S_{39}E_{21}DMA_{40}{}^{110}$-17 wCCMs. Moreover, the $S_{36}E_{19}DMA_{45}{}^{118}$-73 wCCMs are significantly shorter ($l = 360 \pm 190$ nm) with respect to $S_{39}E_{21}DMA_{40}{}^{110}$-17 ($l = 670 \pm 390$ nm) and SEM ($l = 520 \pm 140$ nm)[53] wCCMs, formed at identical polymer concentration ($c = 10$ g L^{-1} in THF).

The comparably strong aggregation of $S_{36}E_{19}DMA_{45}{}^{118}$-73 wCCMs is also evident from light scattering experiments. The time-averaged scattering intensity measured by static light scattering shows a clear difference between wCCMs formed by the SEM triblock terpolymer precursor and the amidated $S_{36}E_{19}DMA_{45}{}^{118}$-73 (Figure 3-3A). The scattering profile of the SEM wCCMs shows only a weak angular dependence with a slight, continuous decrease of the scattering intensity with increasing q. No clear features are visible which is related to the rather high length dispersity and relatively small dimensions of the well-dispersed SEM wCCMs. In contrast, the $S_{36}E_{19}DMA_{45}{}^{118}$-73 wCCMs show a much stronger angular dependence of the scattered light intensity with a strong increase at low q values. This is indicative of much larger structures, i.e. the formation of aggregates, as compared to the SEM triblock terpolymer. Dynamic light scattering supports this conclusion, as a strong shift of the autocorrelation function to longer decay times is observed for $S_{36}E_{19}DMA_{45}{}^{118}$-73, despite of the decreased average length of the $S_{36}E_{19}DMA_{45}{}^{118}$-73 wCCMs compared to that of SEM wCCMs (Figure S3-5). Moreover, the apparent hydrodynamic radius for $S_{36}E_{19}DMA_{45}{}^{118}$-73 ($R_{h, app} = 700$ nm), as determined from angular dependent DLS (Figure 3-3B), is significantly higher compared to that of SEM ($R_{h, app} = 120$ nm).

This undefined morphology and the observed strong aggregation of the highly functionalized triblock terpolymer is attributed to the insolubility of the PDMA block in THF at high degrees of functionalization (Table S3-1). The polarity of the PDMA block increases with the degree of functionalization, which leads to an insolubility in THF even at temperatures well above the melting point of the PE middle block ($T_m \approx 50$ °C) in the $S_{34}E_{21}DMA_{45}{}^{118}$-73 triblock terpolymer. Consequently, micelles with the insoluble PDMA block in the core are formed prior to PE crystallization. This is supported by DLS, revealing the presence of spherical micelles with a hydrodynamic radius of $R_h = 60$ nm at 65 °C (Figure 3-3B, S3-5B). Accordingly, a significant drop in scattering intensity by more than one order of magnitude

and a weak angular dependence is observed by SLS (Figure 3-3A). The presence of micelles prior to PE crystallization obviously hinders the formation of well-defined and dispersed wCCMs. In addition, the observed decrease in wCCM length can be attributed to the higher segment density of the still molten PE block in the micellar corona in comparison to unimolecularly dissolved triblock terpolymer chains. Thus, nucleation is enhanced, i.e. the number of active nuclei increases, leading to shorter wCCMs.

We have further studied the self-assembly of the DMEDA-functionalized triblock terpolymers (SEDMA-x, where x denotes the degree of functionalization) by μ-DSC in order to get a closer insight into the influence of patch solubility on CDSA. This method allows to study melting and crystallization of the PE middle block directly in solution and has proven to be a versatile method for studying crystallization-driven processes.[51] Figure 3-3C shows a comparison of the μ-DSC heating and cooling traces for the neat SEM and the DMEDA-functionalized $S_{38}E_{20}DMA_{42}{}^{113}$-38 triblock terpolymer, both in THF at a concentration of $c = 10$ g L^{-1}. Again, for $S_{38}E_{20}DMA_{42}{}^{113}$-38 strong aggregation was observed by TEM (Figure S3-6A). Whereas the melting point is not influenced by amidation, the crystallization temperature (T_c) shows a pronounced shift to higher temperatures for the amidated $S_{38}E_{20}DMA_{42}{}^{113}$-38 triblock terpolymer. This supports our assumption drawn from TEM (Figure 3-2) and light scattering that the solubility of the PDMA corona block in THF strongly influences the self-assembly behavior and in turn the crystallization of the PE middle block.
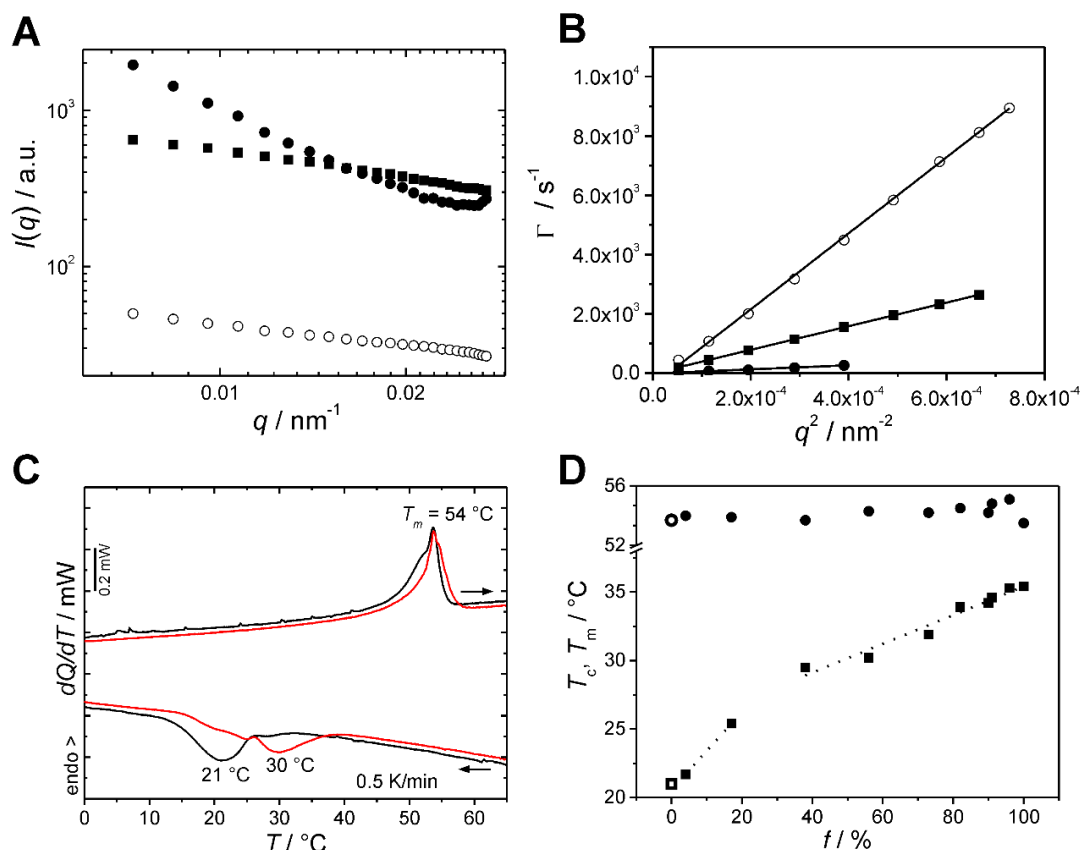
Figure 3-3. A) Scattering intensity from SLS for $S_{34}E_{21}DMA_{45}{}^{118}$-73 (filled circles) and SEM (filled squares) wCCMs measured at 25 °C and for $S_{34}E_{21}DMA_{45}{}^{118}$-73 at 65 °C (open circles). B) Results from second order cumulant analysis of the DLS data (sample code like in A)). The linear dependence of the relaxation rate Γ on the square of the momentum transfer q^2 indicates translational diffusion. The solid lines are linear fits according to: $D_T = \Gamma / q^2$, with D_T being the translational diffusion coefficient. C) μ-DSC heating and cooling traces of SEM (black) and $S_{35}E_{21}DMA_{44}{}^{116}$-38 (red); $c = 10$ g L^{-1} in THF. D) Peak melting (T_m, filled circles) and crystallization (T_c, filled squares) temperatures *vs.* degree of functionalization for DMEDA-amidated SEM. The open symbols correspond to the T_m and T_c values of the neat SEM triblock terpolymer ($S_{40}E_{21}M_{39}{}^{108}$).

The dependence of T_m and T_c on the degree of functionalization is shown in Figure 3-3D. The melting point of the PE middle block stays almost constant, even for the highly functionalized triblock terpolymers. In contrast, the crystallization temperature shows a distinct increase with increasing degree of functionalization. This can be explained by the decreasing solubility of the PDMA block with increasing functionalization (Table S3-1), leading to the formation of micelles with an insoluble PDMA block in the core prior to crystallization as discussed above. The increased segment density of the molten PE block in the micellar corona results in a more efficient nucleation and, thus, in the observed increase in T_c. Interestingly, the dependence of T_c on f seems to change for $f > 20\%$, as indicated by the slope change of the corresponding trend lines in Figure 3-3D (dashed lines). As strong

aggregation was observed starting with the triblock terpolymer with a degree of functionalization of $f = 38\%$ ($S_{38}E_{20}DMA_{42}^{113}$-38, $T_c = 30$ °C, Figure S3-6A), a T_c below 30 °C might be taken as an indicator for the formation of dispersed and well-defined wCCMs with a functional patchy corona. These results clearly show that the solubility of the corona forming blocks is an additional parameter, which strongly influences the CDSA of triblock terpolymers with a semi-crystalline middle block.

Influence of patch polarity on the self-assembly of amidated SEM triblock terpolymers.
The CDSA of SEDMA-x to well-defined and dispersed wCCMs was limited to low degrees of functionalization ($f < 20\%$) due to the poor solubility of the polar DMEDA-amidated PMMA block in THF. However, for an application of functional, patchy wCCMs as nanoreactor for the *in-situ* synthesis of nanoparticles, higher degrees of functionalization are desirable. Hence, the polarity of the system has to be adjusted. Since it is not possible to use more polar solvents for CDSA of the functionalized triblock terpolymers, as spherical crystalline-core micelles instead of wCCMs are formed,[51] the polarity of the functionalized PMMA block was decreased by employing *N,N*-dialkylethylenediamines with longer alkyl groups (R = ethyl (DEEDA), *iso*-propyl (D*i*PEDA)) at the tertiary amine moiety.

The amidation of the SEM triblock terpolymer with DEEDA and D*i*PEDA was conducted in a similar manner as for DMEDA. Again, the correlation between FT-IR and ^{1}H-NMR results, which was obtained from amidation of a PMMA homopolymer with DEEDA (Figure S3-7, S3-8) and D*i*PEDA (Figure S3-10, S3-11), was used to determine the degree of functionalization for the corresponding amidated triblock terpolymers from FT-IR measurements. Representative FT-IR spectra of SEDEA-68 and SED*i*PA-58 are displayed in Figure S3-9 and Figure S3-12, respectively. The amidation of the SEM triblock terpolymer with DEEDA and D*i*PEDA (Figure 3-4A) is slowed down with respect to the kinetics of amidation with DMEDA (Figure 3-1D). After amidation for 120 h, almost complete conversion was observed for DMEDA, whereas only about 80% of the PMMA ester units were consumed for DEEDA and 76% for D*i*PEDA. This is attributed to the increasing steric hindrance exerted by the *N,N*-dialkylethylenediamines upon increasing the length of the alkyl chain at the tertiary amino group.

The thermal properties of SEDEA-x and SED*i*PA-x in dependence on the degree of functionalization are shown in Figure 3-4B. For SEDEA-x, the trend of T_c *vs.* f is similar to

SEDMA-x (Figure 3-3D). Again, the dependence seems to change at a T_c of about 30 °C, as indicated by the slope change of the respective trend lines drawn to the data. However, this corresponds now to a slightly increased degree of functionalization of $f \approx 40\%$. This is attributed to the decreased polarity and in turn increased solubility of the PDEA block (Table S3-2) in comparison to that of the PDMA block in SEDMA-x. Consequently, a higher degree of functionalization is accessible for SEDEA-x, before the solubility of the PDEA block in THF becomes poor and, thus, influences the CDSA of the triblock terpolymer (indicated by $T_c > 30$ °C).
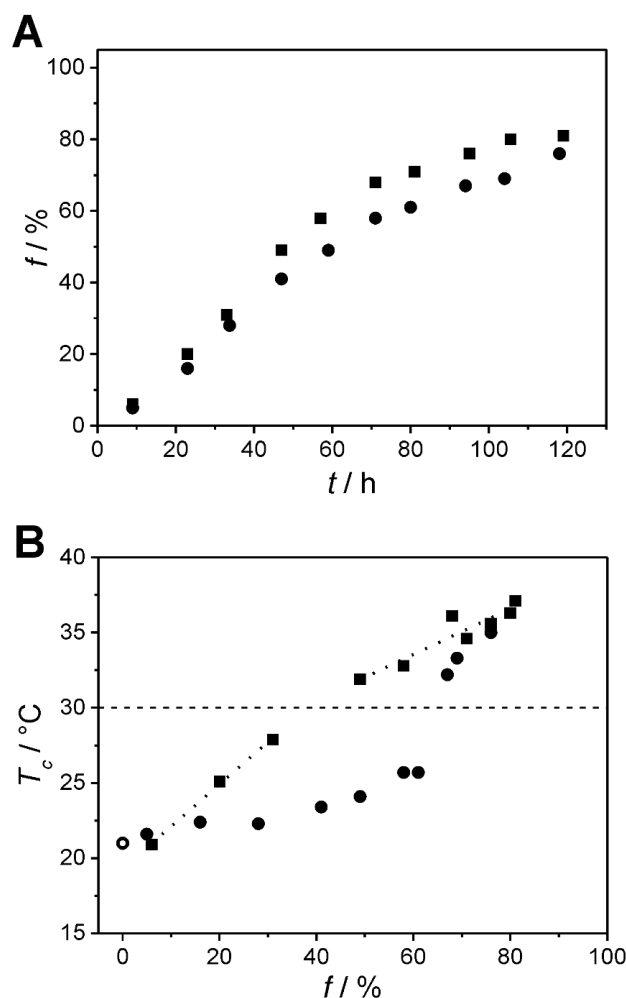
Figure 3-4. A) Kinetics of the amidation of SEM with DEEDA (SEDEA-x, squares) and DiPEDA (SEDiPA-x, circles). B) Crystallization temperature (T_c) of SEDEA-x (squares) and SEDiPA-x (circles) in dependence on the degree of functionalization (f), as determined by μ-DSC on 10 g L^{-1} THF solutions. The open symbol corresponds to the T_c value of the neat SEM triblock terpolymer (S$_{40}$E$_{21}$M$_{39}$[108]).

For SED*i*PA-x an even more distinct dependence of T_c on f is observed (Figure 3-4B), underlining our conclusion drawn from the results obtained for SEDMA and SEDEA. The T_c for SED*i*PA-x is significantly below 30 °C for degrees of functionalization up to $f \approx 60\%$, whereas upon further increasing f a steep increase in T_c is observed. This is again attributed to the amidated PMMA block becoming insoluble in THF (Table S3-3) at high degrees of functionalization ($f > 60\%$). For all three amidated triblock terpolymers, SEDMA-x (Figure 3-3D), SEDEA-x and SED*i*PA-x (Figure 3-4B), the T_c converges to about 35-37 °C when the amidated PMMA block becomes insoluble in THF. Thus, the μ-DSC results strongly indicate that upon decreasing the polarity of the amidated PMMA patch its solubility in THF increases and, in turn, functional patchy wCCMs with a higher degree of functionalization might be prepared.

The TEM image in Figure 3-5A shows wCCMs formed by $S_{38}E_{20}DEA_{42}{}^{114}$-31 (CDSA at $T_c = 28$ °C, $c = 10$ g L^{-1} in THF). Well-defined and dispersed wCCMs with an average length of $l = 690 \pm 310$ nm are formed, despite the higher degree of functionalization with respect to that for SEDMA-x (defined wCCMs only for $f < 20\%$). This fits nicely to the μ-DSC results, which showed that T_c is still below 30 °C for $S_{38}E_{20}DEA_{42}{}^{114}$-31, i.e. the PDEA block is soluble in THF even at $f = 31\%$ and the self-assembly to wCCMs is not disturbed. The morphology of the corona is similar to that observed for $S_{39}E_{21}DMA_{40}{}^{110}$-17 (Figure 3-2A). However, the spherical PDEA patches in the $S_{38}E_{20}DEA_{42}{}^{114}$-31 corona appear slightly larger than the PDMA patches in $S_{39}E_{21}DMA_{40}{}^{110}$-17. This reflects the increased solubility of the PDEA block in THF (more swollen PDEA patches) because of its decreased polarity in comparison to the dimethyl derivative (PDMA).
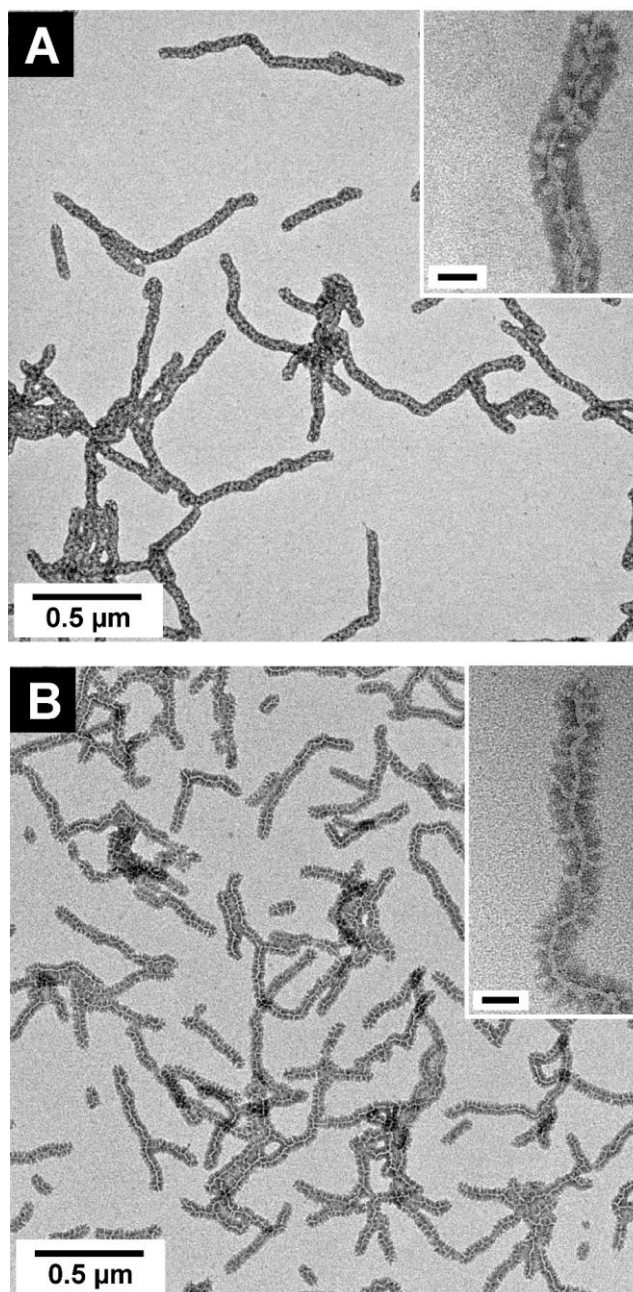
Figure 3-5. TEM micrographs of $S_{38}E_{20}DEA_{42}{}^{114}$-31 (A) and $S_{34}E_{18}DiPA_{48}{}^{128}$-58 (B) wCCMs stained with RuO_4. Scale bar in inset: 50 nm.

For SED*i*PA-x, well-defined and dispersed wCCMs are formed for even higher degrees of functionalization, as shown in Figure 3-5B for $S_{34}E_{18}DiPA_{48}{}^{128}$-58 (CDSA at $T_c = 26$ °C, $c = 10$ g L^{-1} in THF, $l = 460 \pm 290$ nm). This is again in line with the µ-DSC results, showing a T_c below 30 °C for $f < 60\%$ due to the increased solubility of the PD*i*PA block in THF (Figure 3-4B). Interestingly, the $S_{34}E_{18}DiPA_{48}{}^{128}$-58 wCCMs exhibit a significantly different corona structure, where the bright appearing PD*i*PA patches have a more rectangular shape and span from the PE core in the middle to the outer rim of the corona. We attribute this

change in patch shape to the increased degree of functionalization and connected with that the increased weight fraction of PDiPA in the wCCM corona and the increased incompatibility between PS and PDiPA. Similar to the phase diagram of diblock copolymers,[65] the morphology of the wCCM corona can be tuned by its composition and to a certain extend by the incompatibility of the corona blocks. It is noted that for both SEDEA-x and SEDiPA-x less-defined and aggregated wCCMs were observed for $f > 40\%$ (Figure S3-13A) and $f > 60\%$ (Figure S3-13B), respectively; i.e. under conditions where the amidated PMMA block is insoluble in THF.

Having access to well-defined wCCMs with a functional patchy corona, we explored their potential as template for the in-$situ$ synthesis of gold nanoparticles. Here, the aim was to utilize acid-base interactions between hydrogen tetrachloroaurate(III) and the tertiary amino groups in the amidated patches to selectively load the functional patches with tetrachloroaurate anions. Subsequent reduction with superhydride (LiEt$_3$BH) should then lead to the selective formation of Au nanoparticles within the functional patches of the wCCMs (Scheme 3-1B). As a proof of principle, the in-$situ$ synthesis of Au nanoparticles templated by S$_{38}$E$_{20}$DEA$_{42}$[114]-31 wCCMs was studied. The TEM image of the loaded wCCMs (Figure 3-6) confirms the successful formation of Au nanoparticles ($d = 8.2 \pm 3.1$ nm) and, importantly, the Au nanoparticles are selectively located within the bright-appearing amidated corona patches. In contrast, using SEM wCCMs as template, the formed Au nanoparticles are almost completely located outside of the wCCM corona, proving the necessity of the functional, amidated PMMA patches for the regio-selective incorporation of nanoparticles within the micellar corona (Figure S3-14).

The absorbance of the Au nanoparticle loaded S$_{38}$E$_{20}$DEA$_{42}$[114]-31 wCCMs recorded by UV-Vis spectroscopy confirms the formation of defined Au nanoparticles, showing the characteristic localized surface plasmon resonance (LSPR) at $\lambda = 533$ nm (inset in Figure 3-6). This resonance position is typical for small, spherical gold nanoparticles in organic solvent (higher refractive index as compared to water). In addition, the spectrum shows a clear signature of scattering from the wCCM templates as evident by the increase in absorbance toward lower wavelength. However, the patches are not homogeneously loaded, as there are highly loaded wCCMs next to ones bearing only a few or no Au nanoparticles. Thus, further studies will concentrate on improving the loading efficiency of the patches and to transfer this approach to other metal nanoparticles.
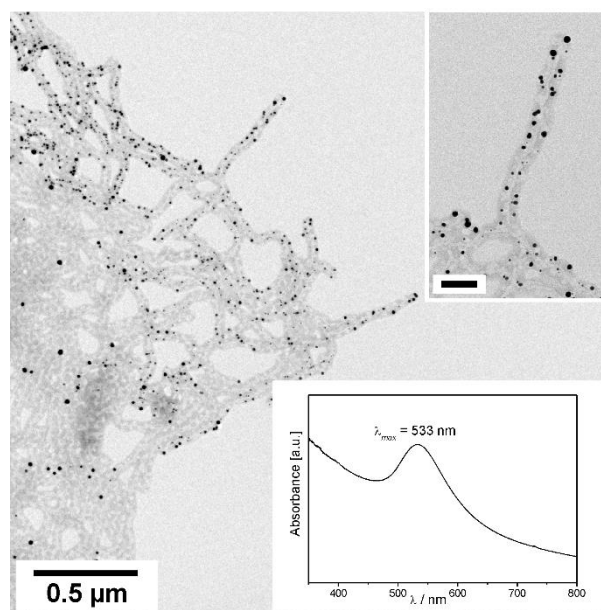
Figure3-6. TEM micrograph and UV-Vis spectrum of $S_{36}E_{21}DEA_{43}{}^{114}$-31 wCCMs selectively loaded with Au nanoparticles. Scale bar in the inset is 100 nm.

3.4 Conclusions

Within this work, we showed the successful preparation of worm-like crystalline-core micelles (wCCMs) with a functional, patchy corona. A polystyrene-*block*-polyethylene-*block*-poly(methyl methacrylate) (SEM) triblock terpolymer was functionalized by polymer analogous reaction of the PMMA block with different *N,N*-dialkylethylenediamines (alkyl = methyl, ethyl, *iso*-propyl), introducing tertiary amine units with varying polarity in the amidated PMMA block. Our results clearly show that the crystallization-driven self-assembly (CDSA) of amidated SEM triblock terpolymers strongly depends on the solubility of the amidated corona block in THF. Well-defined and dispersed wCCMs are formed only for sufficiently soluble corona blocks with matched polarity, i.e. the lower the polarity of the amidated corona block (higher solubility in THF) the higher is the degree of functionalization up to which well-defined wCCMs are accessible. It turned out that the observed crystallization temperature can be taken as an indicator, whether defined wCCMs are formed or aggregation occurs. A $T_c < 30\ °C$ lead to well-defined wCCMs and a $T_c > 30\ °C$ yielded in ill-defined and agglomerated wCCMs. Moreover, the structure of the microphase-separated corona can be tuned by the composition/compatibility of the corona patches, resulting either in spherical patches of the amidated block embedded within a matrix of PS, or a highly regular corona structure with rectangular functional patches.

Worm-like patchy micelles with a tailored functional corona are interesting templates for the selective binding or *in-situ* synthesis of nanoparticles within the surface compartments. The regular structure of the patchy corona with nano-sized dimensions offers the possibility for a precise assembly of nanoparticles without the frequently encountered problem of nanoparticle aggregation. An interesting application of these structures could be the study of confinement effects in nanoparticle catalysis, whereby the micellar template ensures long-term stability of the hybrid in solution.

Supporting Information

Characterization of SBM and SEM triblock terpolymers, further data on amidation of PMMA homopolymer and SEM triblock terpolymer with different *N,N*-dialkylethylenediamines, including ^{1}H-NMR, FT-IR, DLS and TEM results. This material is available free of charge via the Internet at http://pubs.acs.org.

Acknowledgements

3.5 References

(1)   Gohy, J.-F. Block Copolymer Micelles. *Adv. Polym. Sci.* **2005**, *190*, 65-136.

(2)   Rodríguez-Hernández, J.; Chécot, F.; Gnanou, Y.; Lecommandoux, S. 'Smart' Nano-Objects by Self-assembly of Block Copolymers in Solution. *Prog. Polym. Sci.* **2005**, *30*, 691-724.

(3)   Ishizone, T.; Sugiyama, K.; Sakano, Y.; Mori, H.; Hirao, A.; Nakahama, S. Anionic Polymerizations of Perfluoroalkyl Methacrylates and Synthesis of Well-Defined ABC Triblock Copolymers of Methacrylates Containing Hydrophilic, Hydrophobic, and Perfluoroalkyl Groups. *Polym. J.* **1999**, *31*, 983-988.

(4)   Gröschel, A. H.; Schacher, F. H.; Schmalz, H.; Borisov, O. V.; Zhulina, E. B.; Walther, A.; Müller, A. H. E. Precise Hierarchical Self-Assembly of Multicompartment Micelles. *Nat. Commun.* **2012**, *3*, 710-719.

(5)   Jain, S.; Bates, F. S. On the Origins of Morphological Complexity in Block Copolymer Surfactants. *Science* **2003**, *300*, 460-464.

(6)   Li, Z.; Kesselman, E.; Talmon, Y.; Hillmyer, M. A.; Lodge, T. P. Multicompartment Micelles from ABC Miktoarm Stars in Water. *Science* **2004**, *306*, 98-101.

(7)   Gröschel, A. H.; Walther, A.; Löbling, T. I.; Schacher, F. H.; Schmalz, H.; Müller, A. H. E. Guided Hierarchical Co-Assembly of Soft Patchy Nanoparticles. *Nature* **2013**, *503*, 247-251.

(8)   Dupont, J.; Liu, G.; Niihara, K.-I.; Kimoto, R.; Jinnai, H. Self-Assembled ABC Triblock Copolymer Double and Triple Helices. *Angew. Chem., Int. Ed.* 2009, *48*, 6144-6147.

(9)   Dou, H.; Liu, G.; Dupont, J.; Hong, L. Triblock Terpolymer Helices Self-Assembled under Special Solvation Conditions. *Soft Matter* **2010**, *6*, 4214-4222.

(10)   Schacher, F. H.; Rupar, P. A.; Manners, I. Functional Block Copolymers: Nanostructured Materials with Emerging Applications. *Angew. Chem. Int. Ed.* **2012**, *51*, 7898-7921.

(11)   Zhong, S.; Cui, H.; Chen, Z.; Wooley, K. L.; Pochan, D. J. Helix Self-Assembly Through the Coiling of Cylindrical Micelles. *Soft Matter* **2008**, *4*, 90-93.

(12)   Cornelissen, J. J. L. M.; Fischer, M.; Sommerdijk, N. A. J. M.; Nolte, R. J. M. Helical Superstructures from Charged Poly(styrene)-Poly(isocyanodipeptide) Block Copolymers. *Science* **1998**, *280*, 1427-1430.

(13)   Yang, P.; Ratcliffe, L. P. D.; Armes, S. P. Efficient Synthesis of Poly(methacrylic acid)-block-Poly(styrene-alt-N-phenylmaleimide) Diblock Copolymer Lamellae Using RAFT Dispersion Polymerization. *Macromolecules* **2013**, *46*, 8545-8556.

(14)   Cui, H.; Chen, Z.; Zhong, S.; Wooley, K. L.; Pochan, D. J. Block Copolymer Assembly via Kinetic Control. *Science* **2007**, *317*, 647-650.

(15)   Pitsikalis, M.; Siakali-Kioulafa, E.; Hadjichristidis, N. Block Copolymers of Styrene and Stearyl Methacrylate. Synthesis and Micellization Properties in Selective Solvents. *Macromolecules* **2000**, *33*, 5460-5469.

(16)   Jiang, T.; Wang, L.; Lin, S.; Lin, J.; Li, Y. Structural Evolution of Multicompartment Micelles Self-Assembled from Linear ABC Triblock Copolymer in Selective Solvents. *Langmuir* **2011**, *27*, 6440-6448.

(17)   Adelsberger, J.; Metwalli, E.; Diethert, A.; Grillo, I.; Bivigou-Koumba, A. M.; Laschewsky, A.; Müller-Buschbaum, P.; Papadakis, C. M. Kinetics of Collapse Transition and Cluster Formation in a Thermoresponsive Micellar Solution of P(S-*b*-NIPAM-*b*-S) Induced by a Temperature Jump *Macromol. Rapid Commun.* **2012**, *33*, 254-259.

(18) Pietsch, C.; Schubert, U. S.; Hoogenboom, R. Aqueous Polymeric Sensors Based on Temperature-Induced Polymer Phase Transitions and Solvatochromic Dyes. *Chem. Commun.* **2011**, *47*, 8750-8765.

(19) Schacher, F. H.; Betthausen, E.; Walther, A.; Schmalz, H.; Pergushov, D. V.; Müller, A. H. E. Interpolyelectrolyte Complexes of Dynamic Multicompartment Micelles. *ACS Nano* **2009**, *3*, 2095-2102.

(20) Schacher, F. H.; Walther, A.; Müller, A. H. E. Dynamic Multicompartment-Core Micelles in Aqueous Media. *Langmuir* **2009**, *25*, 10962-10969.

(21) Mai, Y.; Eisenberg, A. Self-Assembly of Block Copolymers. *Chem. Soc. Rev.* **2012**, *41*, 5969-5985.

(22) Zhang, Z.; Ma, R.; Shi, L. Cooperative Macromolecular Self-Assembly toward Polymeric Assemblies with Multiple and Bioactive Functions. *Acc. Chem. Res.* **2014**, *47*, 1426-1437.

(23) Moughton, A.; Hillmyer, M. A.; Lodge, T. P. Multicompartment Block Polymer Micelles. *Macromolecules* **2012**, *45*, 2-19.

(24) Mai, Y.; Eisenberg, A. Controlled Incorporation of Particles into the Central Portion of Vesicle Walls. *J. Am. Chem. Soc.* **2010**, *132*, 10078-10084.

(25) Gröschel, A. H.; Müller, A. H. E. Self-Assembly Concepts for Multicompartment Nanostructures. *Nanoscale* **2015**, *7*, 11841-11876.

(26) Wang, J.; Li, W.; Zhu, J. Encapsulation of Inorganic Nanoparticles into Block Copolymer Micellar Aggregates: Strategies and Precise Localization of Nanoparticles. *Polymer* **2014**, *55*, 1079-1096.

(27) Schmelz, J.; Schacher, F. H.; Schmalz, H. Cylindrical Crystalline-Core Micelles: Pushing the Limits of Solution Self-Assembly. *Soft Matter* **2013**, *9*, 2101-2107.

(28) Crassous, J. J.; Schurtenberger, P.; Ballauff, M.; Mihut, A. M. Design of Block Copolymer Micelles via Crystallization. *Polymer* **2015**, *62*, A1-A13.

(29) Lazzari, M.; Lopéz-Quintela, M. A. Micellization Phenomena in Semicrystalline Block Copolymers: Reflexive and Critical Views on the Formation of Cylindrical Micelles. *Macromol. Rapid Commun.* **2009**, *30*, 1785-1791.

(30) He, W.-N.; Xu, J.-T. Crystallization Assisted Self-Assembly of Semicrystalline Block Copolymers. *Prog. Polym. Sci.* **2012**, *37*, 1350-1400.

(31) Massey, J.; Power, K. N.; Manners, I.; Winnik, M. A. Self-Assembly of a Novel Organometallic-Inorganic Block Copolymer in Solution and the Solid State: Nonintrusive Observation of Novel Wormlike Poly(ferrocenyldimethylsilane)-*b*-Poly(dimethylsiloxane) Micelles. *J. Am. Chem. Soc.* **1998**, *120*, 9533-9540.

(32) Wang, X.; Guerin, G.; Wang, H.; Wang, Y.; Manners, I.; Winnik, M. A. Cylindrical Block Copolymer Micelles and Co-Micelles of Controlled Length and Architecture. *Science* **2007**, *317*, 644-647.

(33) Gilroy, J. B.; Gädt, T.; Whittell, G. R.; Chabanne, L.; Mitchels, J. M.; Richardson, R. M.; Winnik, M. A.; Manners, I. Monodisperse Cylindrical Micelles by Crystallization-Driven Living Self-Assembly. *Nat. Chem.* **2010**, *2*, 566-570.

(34) Qian, J.; Lu, Y.; Chia, A.; Zhang, M.; Rupar, P. A.; Gunari, N.; Walker, G. C.; Cambridge, G.; He, F.; Guerin, G.; Manners, I.; Winnik, M. A. Self-Seeding in One Dimension: A Route to Uniform Fiber-like Nanostructures from Block Copolymers with a Crystallizable Core-Forming Block. *ACS Nano* **2013**, *7*, 3754-3766.

(35) Gädt, T.; Ieong, N. S.; Cambridge, G.; Winnik, M. A.; Manners, I. Complex and Hierarchical Micelle Architectures from Diblock Copolymers Using Living, Crystallization-Driven Polymerizations. *Nat. Mater.* **2009**, *8*, 144-150.

(36) Hudson, Z. M.; Lunn, D. J.; Winnik, M. A.; Manners, I. Manners, I. Colour-Tunable Fluorescent Multiblock Micelles. *Nat. Commun.* **2013**, *5*, 3372-3379.

(37) Rupar P. A., Chabanne, L.; Winnik, M. A.; Manners I. Non-Centrosymmetric Cylindrical Micelles by Unidirectional Growth. *Science* **2012**, *337*, 559-562.

(38) Finnegan, J. R.; Lunn, D. J.; Gould, O. E. C.; Hudson, Z. M.; Whittell, G. R.; Winnik, M. A.; Manners, I. Gradient Crystallization-Driven Self-Assembly: Cylindrical Micelles with "Patchy" Segmented Coronas via the Coassembly of Linear and Brush Block Copolymers. *J. Am. Chem. Soc.* **2014**, *136*, 13835-13844.

(39) Qiu, H.; Gao, Y.; Du, V. A.; Harniman, R.; Winnik, M. A.; Manners, I. Branched Micelles by Living Crystallization-Driven Block Copolymer Self-Assembly under Kinetic Control. *J. Am. Chem. Soc.* **2015**, *137*, 2375-2385.

(40) Hudson, Z. M.; Boott C. E.; Robinson, M. E.; Rupar, P. A.; Winnik, M. A.; Manners, I. Tailored Hierarchical Micelle Architectures Using Living Crystallization-Driven Self-Assembly in Two Dimensions. *Nat. Chem.* **2014**, *6*, 893-898.

(41) Qiu, H.; Hudson, Z. M.; Winnik, M. A.; Manners, I. Multidimensional Hierarchical Self-Assembly of Amphiphilic Cylindrical Block Comicelles. *Science* **2015**, *347*, 1329-1332.

(42) Li, X.; Gao, Y.; Boott, C. E.; Winnik, M. A.; Manners, I. Non-Covalent Synthesis of Supermicelles with Complex Architectures Using Spatially Confined Hydrogen-Bonding Interactions. *Nat. Commun.* **2015**, *6*, 8127-8134.

(43) Wang, H.; Patil, A. J.; Liu, K.; Petrov, S.; Mann, S.; Winnik, M. A.; Manners, I. Fabrication of Continuous and Segmented Polymer/Metal Oxide Nanowires Using Cylindrical Micelles and Block Comicelles as Templates. *Adv. Mater.* **2009**, *21*, 1805-1808.

(44) Wang, H.; Lin, W.; Fritz, K. P.; Scholes, G. D.; Winnik, M. A.; Manners, I. Cylindrical Block Co-Micelles with Spatially Selective Functionalization by Nanoparticles. *J. Am. Chem. Soc.* **2007**, *129*, 12924-12925.

(45)   Jia, L.; Zhao, G.; Shi, W.; Coombs, N.; Gourevich, I.; Walker, G. C.; Guerin, G.; Manners, I.; Winnik, M. A. A Design Strategy for the Hierarchical Fabrication of Colloidal Hybrid Mesostructures. *Nat. Commun.* **2014**, *5*, 3882-3889.

(46)   Fan B.; Liu, L.; Li, J.-H.; Ke, X.-X.; Xu, J.-T.; Du, B.-Y.; Fan, Z.-Q. Crystallization-Driven One-Dimensional Self-Assembly of Polyethylene-*b*-Poly(*tert*-butylacrylate) Diblock Copolymers in DMF: Effects of Crystallization Temperature and the Corona-Forming Block. *Soft Matter* **2016**, *12*, 67-76.

(47)   Schmelz, J.; Schedl, A. E.; Steinlein, C.; Manners, I.; Schmalz, H. Length Control and Block-Type Architectures in Worm-like Micelles with Polyethylene Cores. *J. Am. Chem. Soc.* **2012**, *134*, 14217-14225.

(48)   He, W.-N.; Zhou, B.; Xu, J.-T.; Du, B.-Y.; Fan, Z.-Q. Two Growth Modes of Semicrystalline Cylindrical Poly(ε-caprolactone)-*b*-Poly(ethylene oxide) Micelles. *Macromolecules*, **2012**, *45*, 9768-9778.

(49)   Pitto-Barry, A.; Kirby, N.; Dove, A. P.; O'Reilly, R. K. Expanding the Scope of the Crystallization-Driven Self-Assembly of Polylactide-Containing Polymers. *Polym. Chem.* **2014**, *5*, 1427-1436.

(50)   Schmalz, H.; Schmelz, J.; Drechsler, M.; Yuan, J.; Walther, A.; Schweimer, K.; Mihut, A. Thermo-Reversible Formation of Wormlike Micelles with a Microphase-Separated Corona from a Semicrystalline Triblock Terpolymer. *Macromolecules* **2008**, *41*, 3235-3242.

(51)   Schmelz, J.; Karg, M.; Hellweg, T.; Schmalz, H. General Pathway toward Crystalline-Core Micelles with Tunable Morphology and Corona Segregation. *ACS Nano* **2011**, *5*, 9523-9534.

(52)   Rosenfeldt, S.; Lüdel, F.; Schulreich, C.; Hellweg, T.; Radulescu, A.; Schmelz, J.; Schmalz, H.; Harnau, L. Patchy Worm-Like Micelles: Solution Structure Studied by Small-Angle Neutron Scattering. *Phys. Chem. Chem. Phys.* **2012**, *14*, 12750-12756.

(53)   Schmelz, J.; Pirner, D.; Krekhova, M.; Ruhland, T. M.; Schmalz, H. Interfacial Activity of Patchy Worm-Like Micelles. *Soft Matter* **2013**, *9*, 11173-11177.

(54)   Hoppenbrouwers, E.; Li, Z.; Liu, G. Triblock Nanospheres with Amphilic Coronal Chains. *Macromolecules* **2003**, *36*, 876-881.

(55)   Njikang, G.; Han, D.; Wang, J.; Liu, G. ABC Triblock Copolymer Micelle-Like Aggregates in Selective Solvents for A and C. *Macromolecules* **2008**, *41*, 9727-9735.

(56)   Zheng, R.; Liu, G., Yan, X. Polymer Nano- and Microspheres with Bumpy and Chain-Segregated Surfaces. *J. Am. Chem. Soc.* **2005**, *127*, 15358-15359.

(57)   Kuo, S.-W.; Tung, P.-H.; Lai, C.-L.; Jeong, K.-U.; Chang, F.-C. Supramolecular Micellization of Diblock Copolymer Mixtures Mediated by Hydrogen Bonding for the Observation of Separated Coil and Chain Aggregation in Common Solvents. *Macromol. Rapid Commun.* **2008**, *29*, 229–233.

(58)   Du, J.; O'Reilly, R. K. Anisotropic Particles with Patchy, Multicompartment and Janus Architectures Preparation and Application. *Chem. Soc. Rev.* **2011**, *40*, 2402–2416.

(59)   LoPresti, C.; Massignani, M.; Fernyhough, C.; Blanazs, A.; Ryan, A. J.; Madsen, J.; Warren, N. J.; Armes, S. P.; Lewis, A. L.; Chirasatitsin, S. Controlling Polymersome Surface Topology at the Nanoscale by Membrane Confined Polymer/Polymer Phase Separation. *ACS Nano* **2011**, *5*, 1775–1784.

(60)   Christian, D. A.; Tian, A.; Ellenbroek, W. G.; Levental, I.; Rajagopal, K.; Janmey, P. A.; Liu, A. J.; Baumgart, T.; Discher, D. E. Spotted Vesicles, Striped Micelles and Janus Assemblies Induced by Ligand Binding. *Nat. Mater.*, **2009**, *8*, 843–849.

(61)   Erhardt, R.; Zhang, M.; Böker, A.; Zettl, H.; Abetz, C.; Frederik, P.; Krausch, G.; Abetz, V.; Müller, A. H. E. Amphiphilic Janus Micelles with Polystyrene and Poly(methacrylic acid) Hemispheres. *J. Am. Chem. Soc.* **2003**, *125*, 3260-3267.

(62)   Twaik, M. A.; Tahan, M.; Zilkha, A. Grafting of Poly(ethylene oxide) on Poly(methyl Methacrylate) by Transesterification. *J. Polym. Sci. A-1* **1969**, *7*, 2469-2480.

(63)   Fixe, F.; Dufva, M.; Telleman, P.; Christensen, C. B. V. Functionalization of Poly(methyl methacrylate) (PMMA) as a Substrate for DNA Microarrays. *Nucleic Acids Res.* **2004**, *32*, e9.

(64)   Kakuchi, R.; Wongsanoh, K.; Hoven, V. P.; Théato, P. Activation of Stable Polymeric Esters by Using Organo-Activated Acyl Transfer Reactions. *J. Polym. Sci. A* **2014**, *52*, 1353-1358.

(65)   Matsen, M. W.; Schick, M. Stable and Unstable Phases of a Diblock Copolymer Melt *Phys. Rev. Lett.* **1994**, *72*, 2660-2663.

3.6 Supporting Information

Characterization of SBM and SEM Triblock Terpolymers
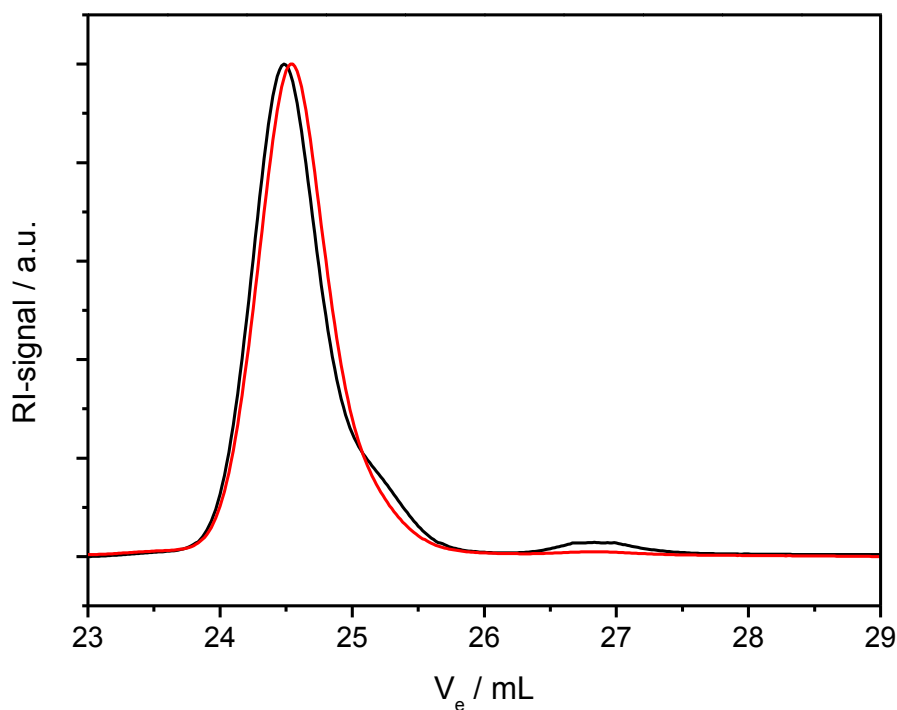
Figure S3-1. THF-SEC traces of $S_{40}B_{21}M_{39}^{107}$ before (black) and after (red) extraction with cyclohexane.
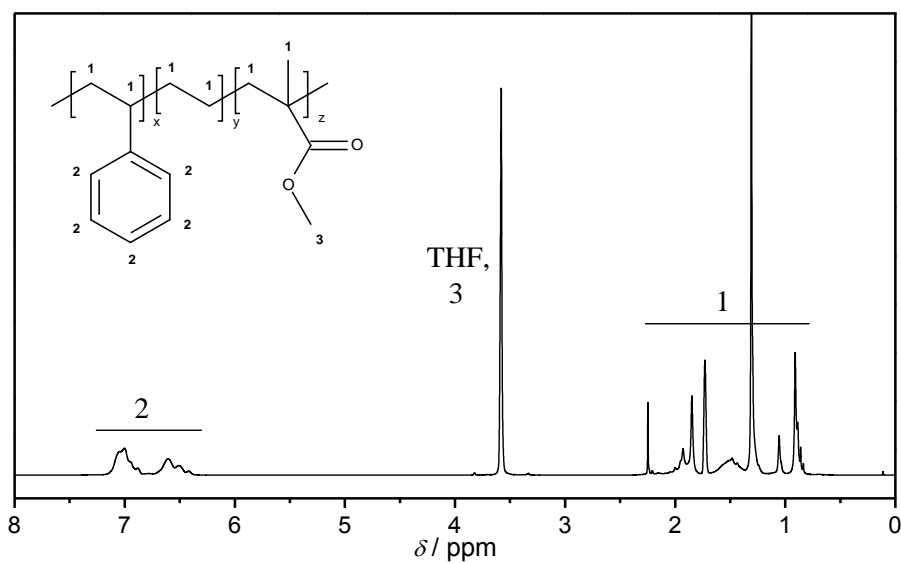

Figure S3-2. ^{1}H-NMR spectrum of $S_{40}E_{21}M_{39}^{108}$ measured in d_8-THF at 65 °C. The THF signal overlaps with the signal of the PMMA ester units (3) at 3.56 ppm.

DMEDA-Functionalized PMMA (PDMA) and SEM Triblock Terpolymers (SEDMA)

The FT-IR spectrum of a representative DMEDA-functionalized PMMA (Figure S3-3A) confirms the successful amidation by the presence of characteristic amide I and amide II bands at 1666 cm^{-1} and 1526 cm^{-1}, respectively. The intensity of these bands depends on the degree of functionalization. The C=O stretching vibration of the pendant methyl ester units, which is typically found at 1728 cm^{-1} for PMMA, is shifted to 1716 cm^{-1}. This indicates imide formation as a side reaction, which was already observed by THEATO et al.[1]

^{1}H-NMR spectroscopy confirms this assignment as there are typical proton signals for amide and imide units in the amidated PMMA (Figure S3-3B). The strong signal at 2.8 ppm is assigned to the dimethylamino groups (**7, 7′**) of the amide and imide units. At 3.1 ppm, the signal for the methylene protons of the -C*H*$_2$-N(CH$_3$)$_2$ groups (**6, 6′**) can be found. In contrast, the signals of the -CONH-C*H*$_2$- group are separated for amide (**5**, 3.3 ppm) and imide units (**5′**, 3.76 and 3.98 ppm, six-membered ring-structure of the imide). The signal for remaining methyl ester units is observed at 3.52 ppm (-O-C*H*$_3$, **3**) and is almost absent due to the high degree of functionalization of this sample. Thus, the obtained amidated PMMA is a random copolymer composed of amide, imide, and residual MMA units. The conversion of PMMA ester groups was calculated using the integral of these remaining ester units calibrated by the backbone protons (5 H), yielding a conversion of about 99%.

A

B
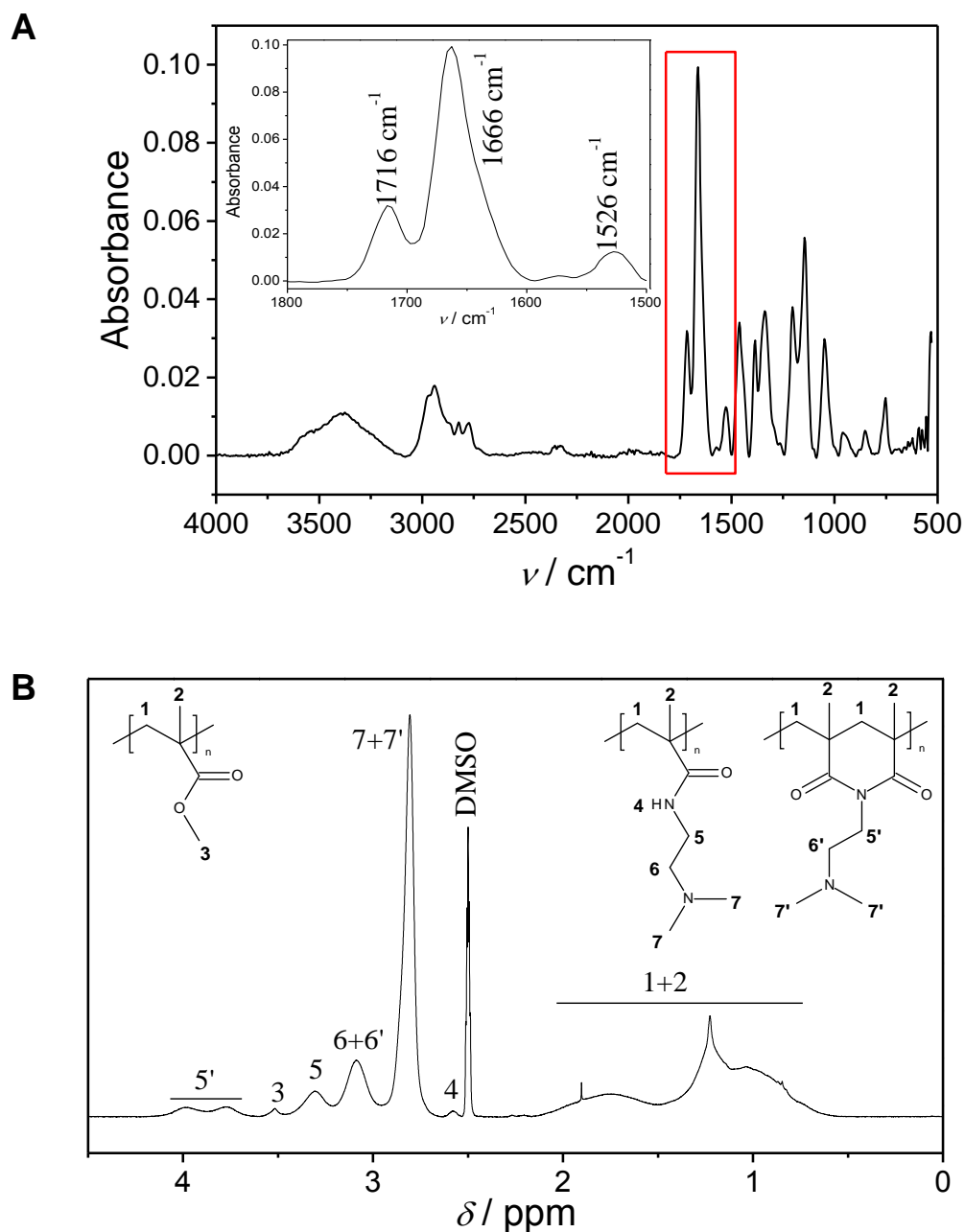
Figure S3-3. A) FT-IR and B) ^{1}H-NMR spectrum (d_6-DMSO with 1 vol % TFA) of PMMA amidated with DMEDA (degree of functionalization $f = 99\%$).
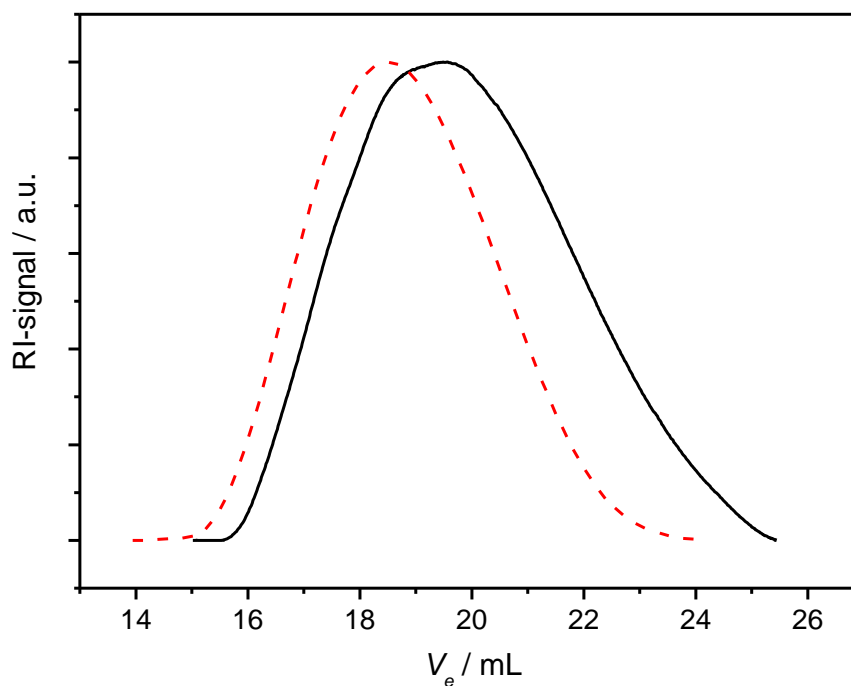
Figure S3-4. HFIP-SEC traces of PMMA (black) and a DMEDA-functionalized PMMA (99% conversion, red dotted line).

Solubility tests were done by mixing 2 - 5 mg of the DMEDA-functionalized PMMA homopolymer (PDMA-x) with 2 mL of the appropriate solvent. For DMSO, the dispersions were stirred for 1 d. For dichloromethane (CH_2Cl_2) and THF, the dispersions were heated directly to 65 °C for at least 1 h under stirring. The solubility of PDMA-x depends strongly on the degree of functionalization (Table S3-1). At room temperature, all samples were soluble in DMSO. The solubility in organic solvents like CH_2Cl_2 and THF is limited. In general, high temperatures (65 °C) are needed for dissolution. However, the maximum ester conversion possible for dissolution in THF is about 25%.

Table S3-1. Solubility of DMEDA-amidated PMMA (PDMA-x, where x denotes the degree of functionalization, i.e., fraction of consumed ester units) in different solvents

	CH$_2$Cl$_2$ (65 °C)	THF (65 °C)	DMSO (RT)
PDMA-2	✓	✓	✓
PDMA-5	✗	✓	✓
PDMA-10	✗	✓	✓
PDMA-25	✗	(✓)	✓
PDMA-55	✗	✗	✓
PDMA-76	✗	✗	✓
PDMA-88	✗	✗	✓
PDMA-94	✗	✗	✓
PDMA-96	✗	✗	✓
PDMA-97	✗	✗	✓
PDMA-99	✗	✗	✓

✓: soluble, ✗: not soluble

For all investigated samples and conditions the intensity-time autocorrelation functions determined by dynamic light scattering show monomodal decays (Figure S3-5). The fits from cumulant analysis describe the correlation functions well. The data for SEDMA-73 at 65 °C can be best described by the cumulant fit (PDI = 0.35), whereas some larger deviation between fit and experimental data is found for the SEM (PDI = 0.47) and SEDMA-73 (PDI = 0.53) wCCMs measured at 25 °C. This difference might be explained by the larger polydispersity, as expressed by the polydispersity indices calculated from the second cumulant.

A

B
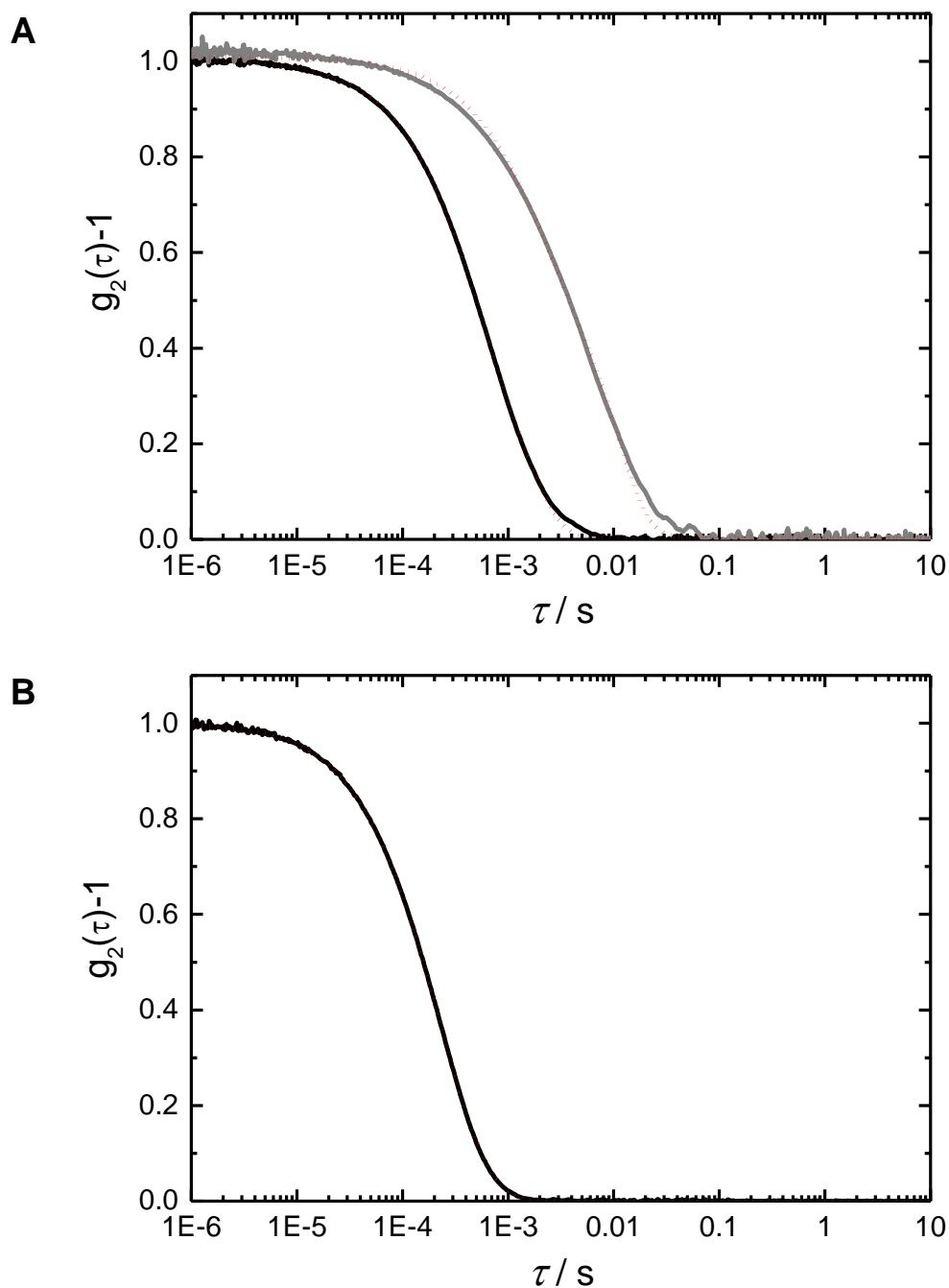
Figure S3-5. Intensity-time autocorrelation functions measured by DLS ($\theta = 60°$) at 25 °C for A) the SEM (black) and SEDMA-73 (grey) wCCMs, and B) SEDMA-73 at 65 °C. The red dotted lines are fits from cumulant analysis (2nd order).

The TEM micrographs of SEDMA-38 and SEDMA-56 (Figure S3-6) show the change in wCCM morphology with increasing degree of functionalization. SEDMA-56 tends to form larger agglomerates than SEDMA-38. The corona patches of SEDMA-38 increase in size in comparison with SEDMA-17 (Figure 3-2), but the PE core of SEDMA-38 shows a highly

irregular structure. For SEDMA-56, the discontinuous PE core is hardly observable and the amidated patches appear even larger than for SEDMA-36.
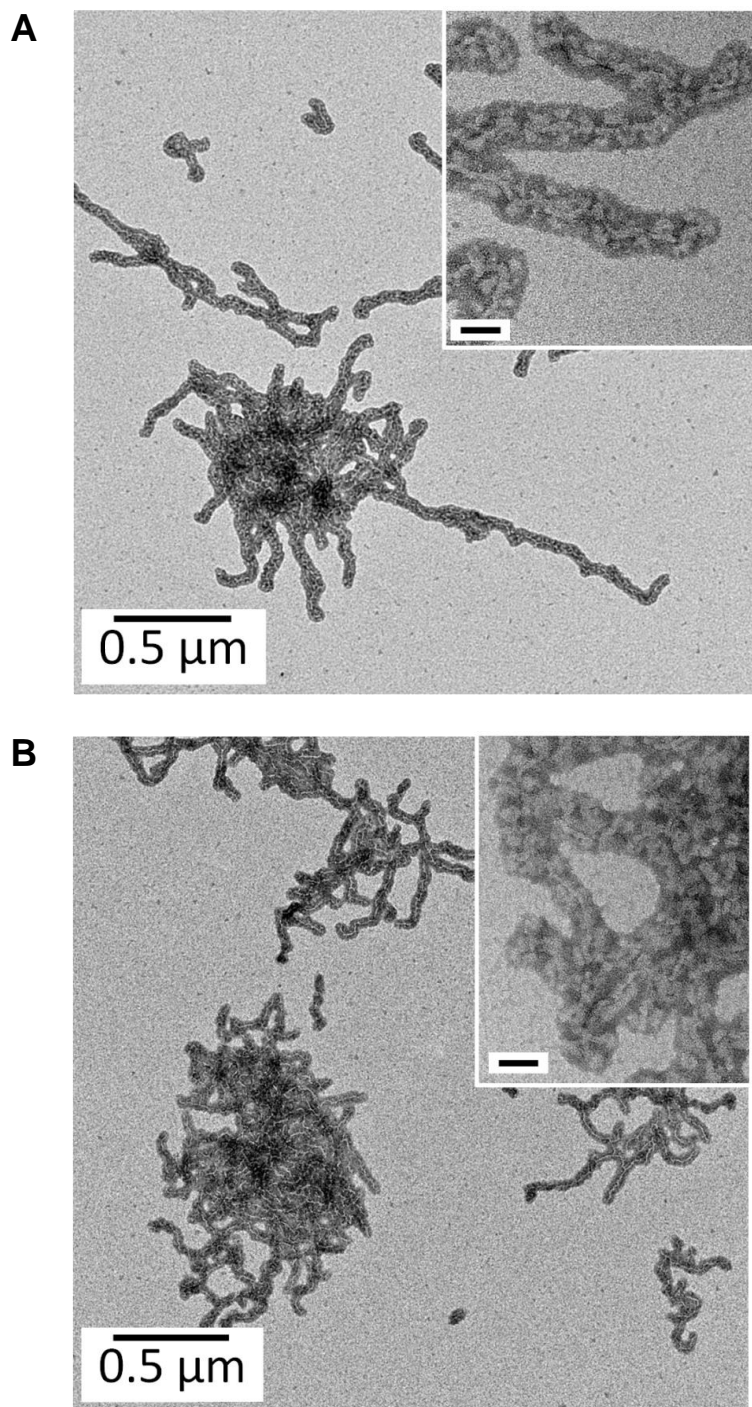
Figure S3-6. TEM micrographs of A) SEDMA-38 and B) SEDMA-56, the PS domains were selectively stained with RuO_4 and appear dark. Scale bars in the insets are 50 nm.

DEEDA-Functionalized PMMA (PDEA) and SEM Triblock Terpolymers (SEDEA)

For characterization of DEEDA-amidated PMMA homopolymer (PDEA-x, where x denotes the degree of functionalization) FT-IR and ^{1}H-NMR spectroscopy (Figure S3-7) were performed. The FT-IR spectrum (Figure S3-7A) shows characteristic signals for the amide I band (1666 cm^{-1}) and the amide II band (1526 cm^{-1}), as already observed for PDMA copolymers (Figure S3-3A). Remaining ester units of PMMA are indicated by the presence of the C=O stretching vibration at 1724 cm^{-1}, which shows a shift of 4 cm^{-1} compared to neat PMMA. This is again attributed to the imide formation.

The ^{1}H-NMR spectrum of PDEA-45 (Figure S3-7B) confirms successful ester conversion by a decrease of the signal intensity of the remaining PMMA ester units at 3.5 ppm (**3**). The proton signals for the amide units are assigned to the signals at 1.2 ppm (**8**), 3.0 ppm (**6**) and 3.2 ppm (**5**, **7**). Imide formation was observed by the presence of two proton signals at 3.8 and 4.0 ppm (**5'**). The fraction of consumed ester units (*f*) was calculated by the normalized integral of the remaining ester (A_{norm}(ester)), amide (A_{norm}(amide)) and imide units (A_{norm}(imide)) (eq. 1). Here, the imide units count double, since two ester units are converted to one imide unit.

$$f = \frac{A_{norm}(amide) + 2 \cdot A_{norm}(imide)}{A_{norm}(ester) + A_{norm}(amide) + 2 \cdot A_{norm}(imide)} \cdot 100 \qquad (eq.\,1)$$

with:

$$A_{norm}(ester) = \frac{A\,(\mathbf{3})}{3} \qquad (eq.\,2)$$
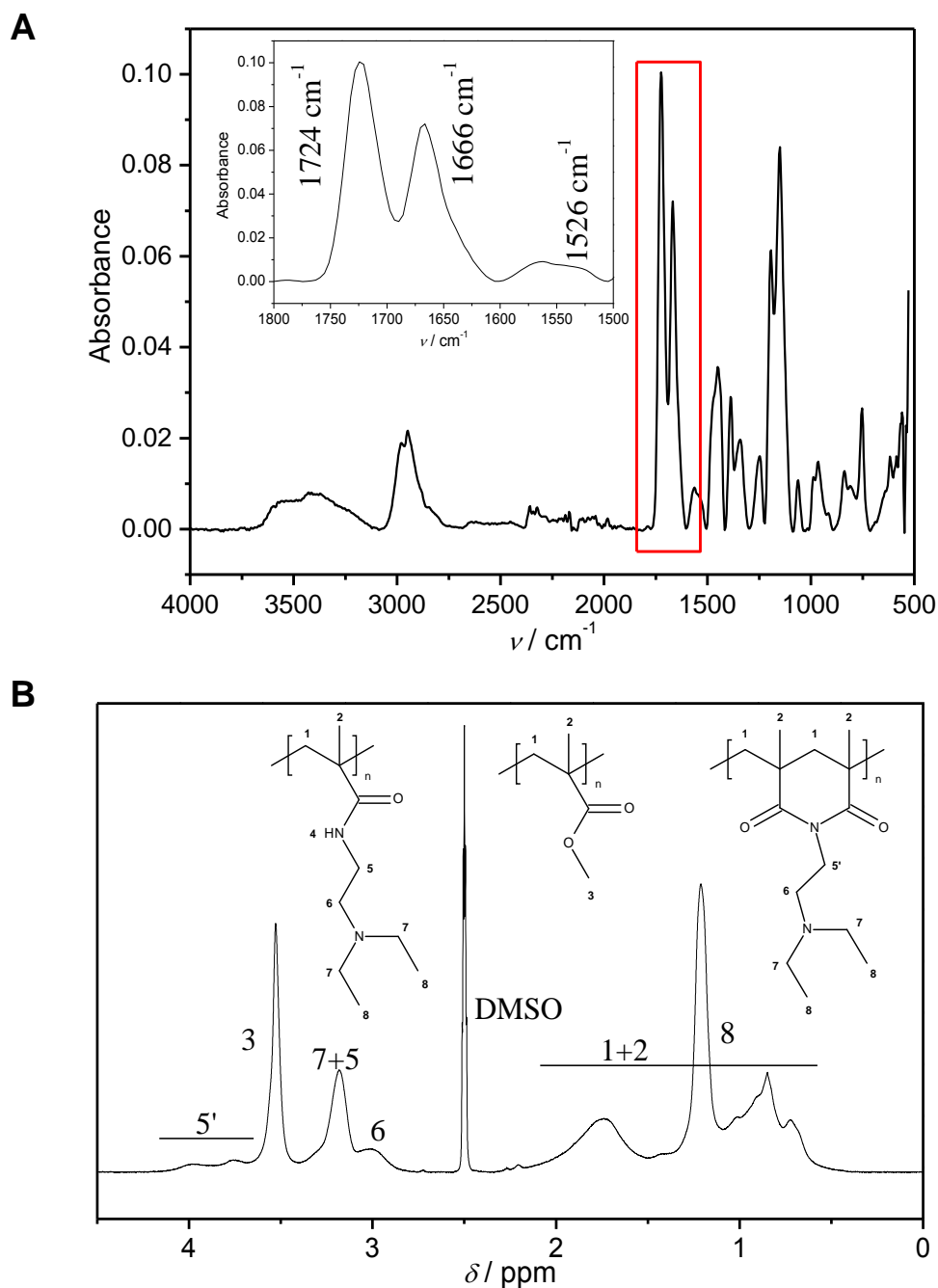
and

$$A_{norm}(imide) = \frac{A\,(\mathbf{5'})}{2} \qquad (eq.\,3).$$

The signal of the amide protons (**5**) overlaps with that of the imide protons (**6**, **7**). Thus, the contribution of the imide units has to be subtracted from the integral of units **5** - **7** (eq. 4) to get the normalized integral of amide units:
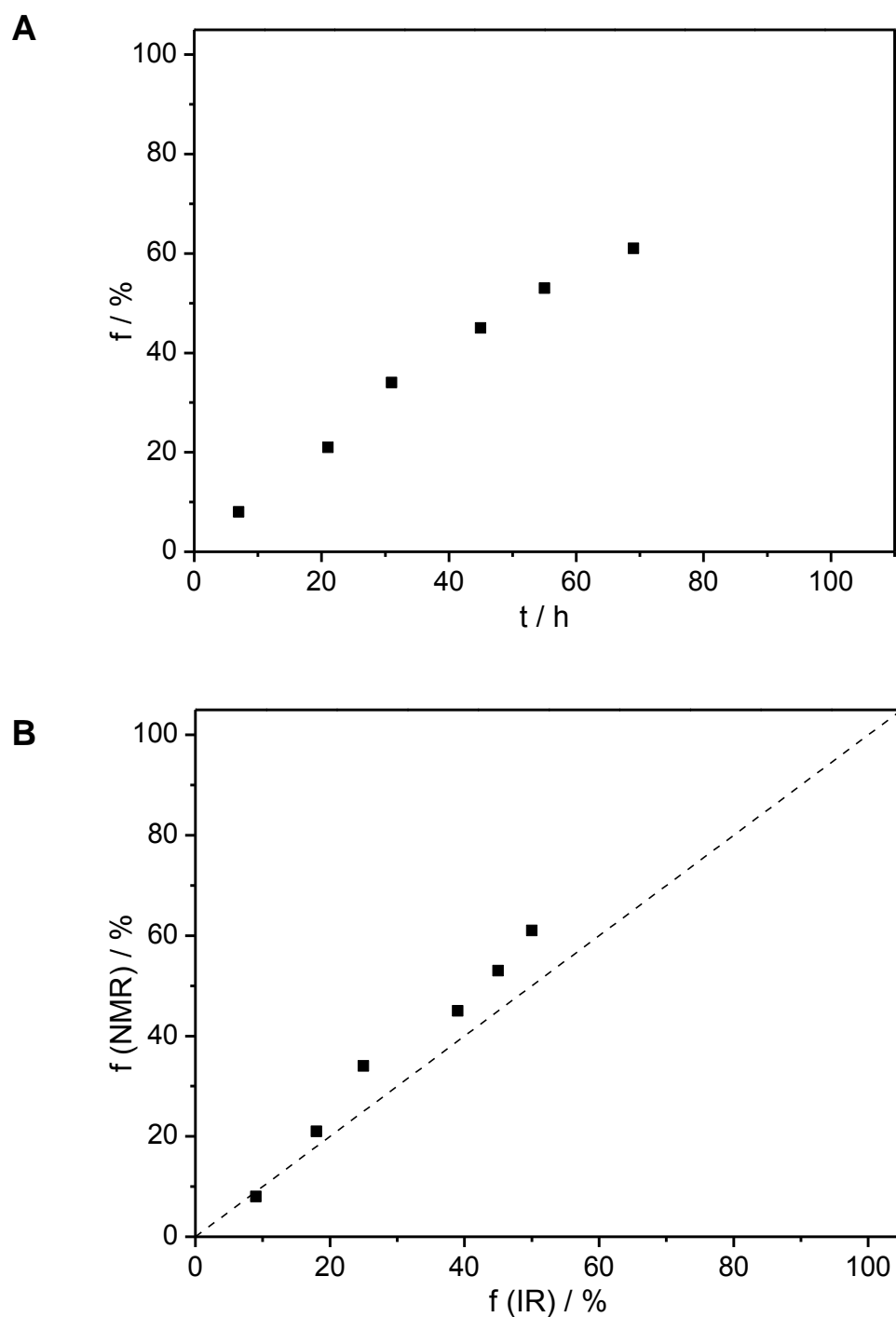
$$A_{norm}(amide) = \frac{A\,(\mathbf{5 - 7}) - 3 \cdot A(\mathbf{5'})}{8} \qquad (eq.\,4)$$

The fraction of imide units was determined to be 59 ± 5 % for all DEEDA-amidated PMMA samples.

A

B

Figure S3-7. A) FT-IR spectrum and B) ^{1}H-NMR spectrum (d$_6$-DMSO with 1 vol % TFA) of PDEA-45.

The conversion of ester units with reaction time for the amidation of PMMA with DEEDA (Figure S3-8) shows a similar trend as compared to the amidation with DMEDA (Figure 3-1A).

Figure S3-8. A) Kinetics of the amidation of PMMA with DEEDA. B) Correlation of the degree of functionalization, i.e., the fraction of reacted PMMA ester units, determined from ^{1}H-NMR and FT-IR for the amidation of PMMA with DEEDA.

However, the amidation with DEEDA proceeds slower than the amidation with DMEDA due to the steric hindrance exerted by the more bulky ethyl groups at the amine moiety. For amidation of PMMA with DMEDA a ester conversion of 90% was reached within 70 h, whereas for DEEDA only 60% ester conversion was obtained. The correlation of ^{1}H-NMR

and FT-IR results for the amidation with DEEDA is shown in Figure S3-8B and shows a deviation from the ideal linear correlation with increasing degree of functionalization, similar to that found for amidation with DMEDA (Figure 3-1B).

Solubility tests were done following the procedure described for PDMA (see Section 2.). The solubility of DEEDA-amidated PMMA (PDEA-x) in organic solvents is similar to that of PDMA-x, with a slightly increased solubility in CH_2Cl_2 at low degrees of functionalization (Table S3-2). The maximum degree of functionalization to be still soluble in THF and CH_2Cl_2 is about 20% at 65 °C. In SEDEA-x triblock terpolymers, the solubility in THF is slightly enhanced by the increase of hydrophobicity through the PS and PE block.

Table S3-2. Solubility of DEEDA-amidated PMMA (PDEA-x, where x denotes the degree of functionalization, i.e., fraction of consumed ester units) in different solvents.

	CH_2Cl_2 (65 °C)	THF (65 °C)	DMSO
PDEA-8	✓	✓	✓
PDEA-21	✓	✓	✓
PDEA-34	✗	✗	✓
PDEA-45	✗	✗	✓
PDEA-53	✗	✗	✓
PDEA-61	✗	✗	✓

✓: soluble, ✗: not soluble

FT-IR spectroscopy of SEDEA-x triblock terpolymers confirms successful amidation by the presence of the amide I band at 1666 cm^{-1} and the amide II band at 1539 cm^{-1} (Figure S3-9). The remaining C=O stretching vibration of PMMA ester units is observable at 1724 cm^{-1}. The shift of 4 cm^{-1} of this C=O stretching vibration (originally 1728 cm^{-1} for SEM) indicates imide formation.
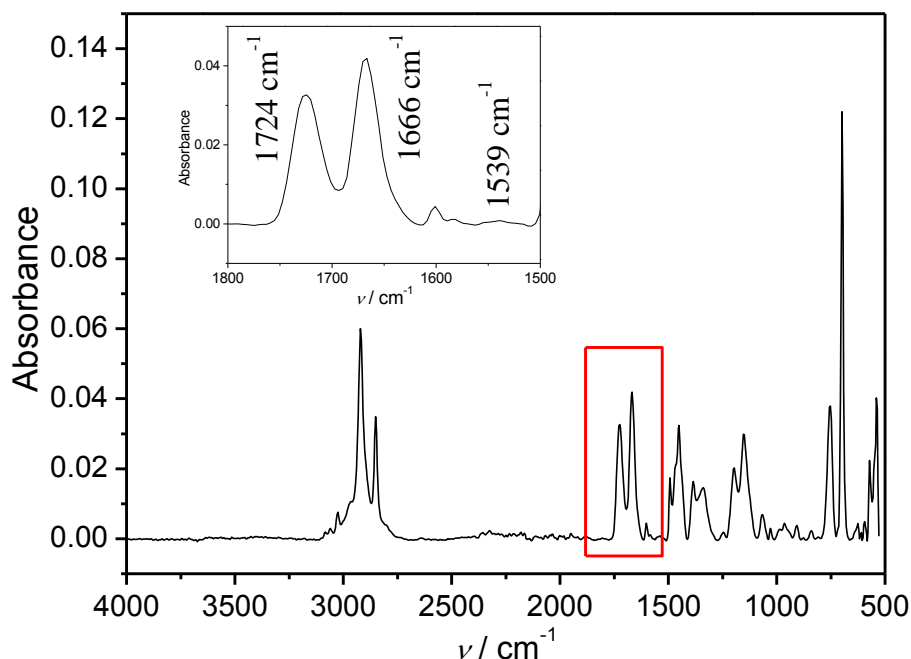
Figure S3-9. FT-IR spectrum of SEDEA-68.

D*i*PEDA-Functionalized PMMA (PD*i*PA) and SEM Triblock Terpolymers (SED*i*PA)

Similar to PDMA-x and PDEA-x, FT-IR spectroscopy confirms successful amidation by characteristic amide I (1666 cm^{-1}) and amide II (1519 cm^{-1}) bands (Figure S3-10A). At 1720 cm^{-1}, a shifted C=O stretching vibration of the remaining PMMA ester units is observable (original position in SEM: 1728 cm^{-1}). The 8 cm^{-1} shift indicates imide formation.

The corresponding ^{1}H-NMR spectrum Figure S3-10B) shows characteristic proton signals of the *iso*-propyl groups (-CH_3, **8**) at 1.3 ppm, the -N-CH_2 methylene group at 2.9 ppm (**6**), and the CONH-CH_2 and the N-CH(CH$_3$)$_2$ groups at 3.65 ppm (**5**, **7**). The fraction of consumed ester units was determined according to eq. 1 - 3, whereby the normalized integral of the amide units was calculated using eq. 5.

$$A_{norm}(amide) = \frac{A(\mathbf{6}) - A(\mathbf{5'})}{2} \qquad (eq.\,5)$$

The imide fraction determined from ^{1}H-NMR spectroscopy was determined to be 68 ± 9 %.

A

B
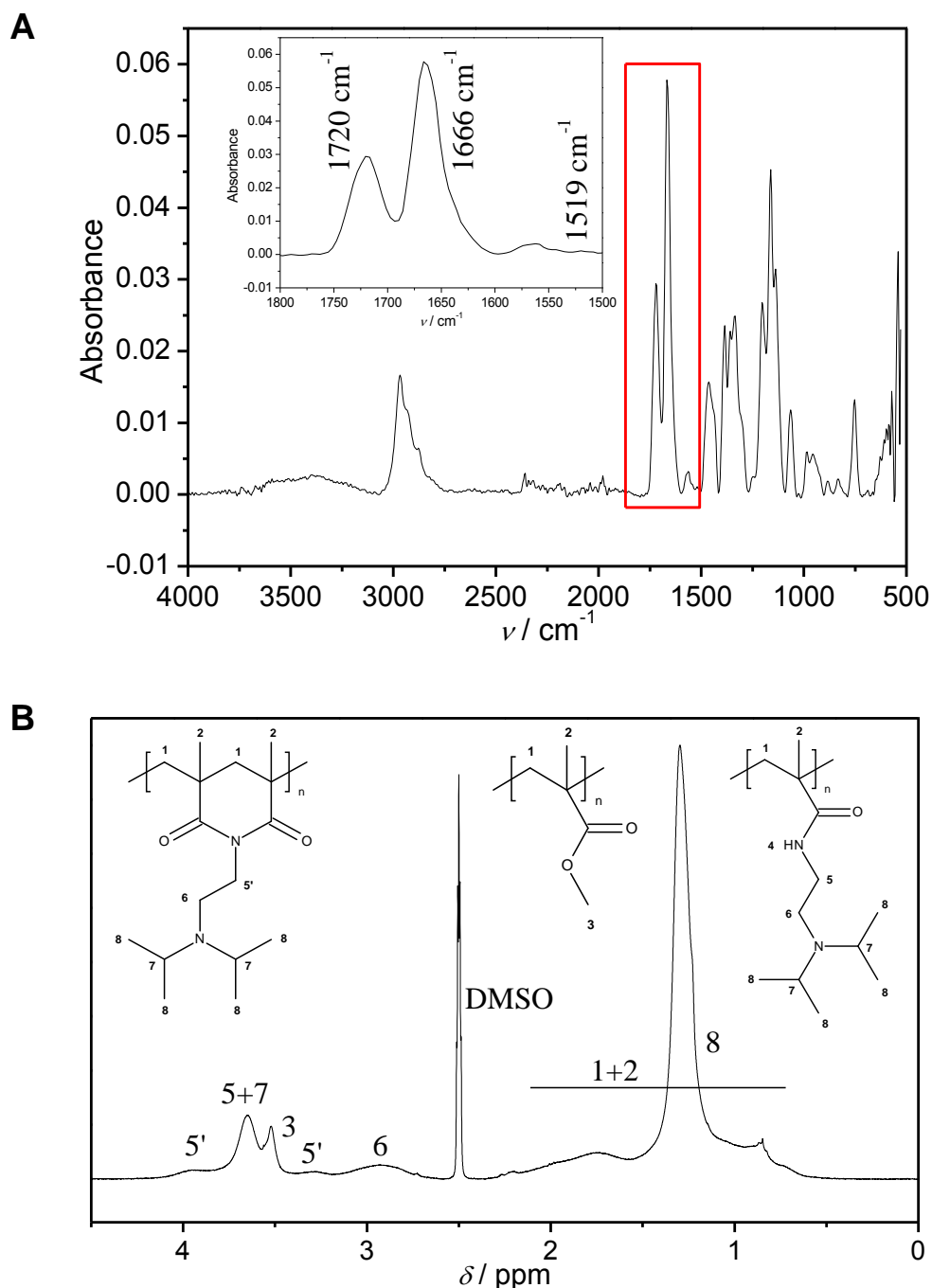
Figure S3-10. A) FT-IR spectrum and B) ^{1}H-NMR spectrum (d6-DMSO with 1 vol % TFA) of PDiPA-74.

The reaction kinetics of the amidation of PMMA with D*i*PEDA (Figure S3-11A) shows a similar trend as already observed for the amidation reactions with DMEDA and DEEDA. Analogous to the amidation with DEEDA, the reaction is slowed down by the sterical hindrance of the *iso*-propyl groups on the amine moiety. The correlation of the ester conversion determined by ^{1}H-NMR and FT-IR spectroscopy is displayed in Figure S3-11B.
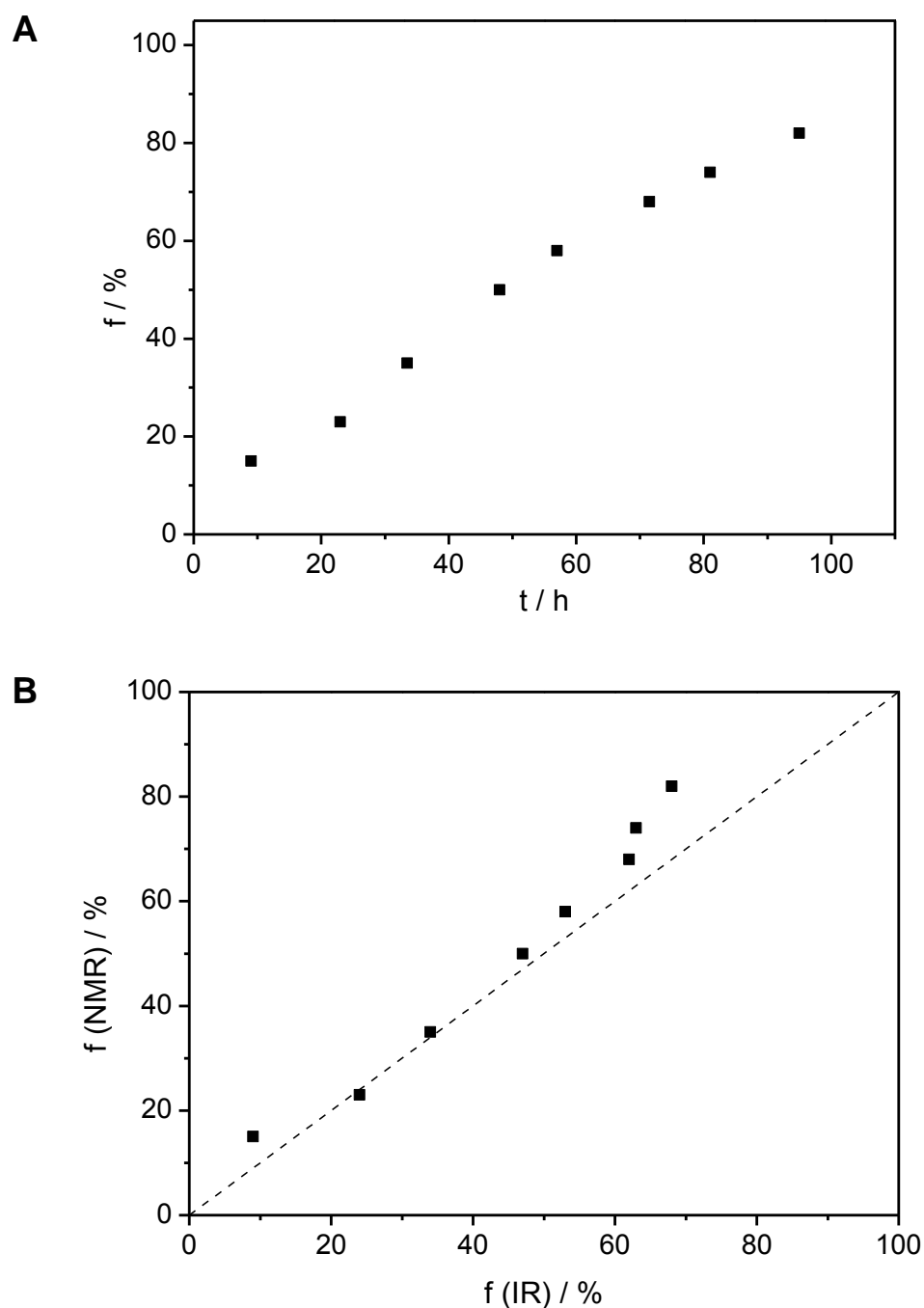
Figure S3-11. A) Kinetics of the amidation of PMMA with D*i*PEDA. B) Correlation of degree of functionalization, i.e. the fraction of reacted PMMA ester units, determined from ^{1}H-NMR and FT-IR for the amidation of PMMA with D*i*PEDA.

The solubility of PD*i*PA-x in organic solvents is enhanced compared to PDMA-x and PDEA-x (Table S3-3). At 65 °C, a PD*i*PA-58 is still soluble in THF and a PD*i*PA-35 in CH$_2$Cl$_2$. This is attributed to the increased hydrophobicity of the di(*iso*-propyl)amino groups in comparison to the dimethyl- and diethyl-amino groups of PDMA-x and PDEA-x.

Table S3-3. Solubility of D*i*PEDA-amidated PMMA (PD*i*PA-x, where x denotes the degree of functionalization, i.e., fraction of consumed ester units) in different solvents

	CH$_2$Cl$_2$ (65 °C)	THF (65 °C)	DMSO
PDiPA-15	✓	✓	✓
PDiPA-23	✓	✓	✓
PDiPA-35	✓	✓	✓
PDiPA-50	✗	✓	✓
PDiPA-58	✗	✓	✓
PDiPA-68	✗	✗	✓
PDiPA-74	✗	✗	✓
PDiPA-82	✗	✗	✓

✓: soluble, ✗: not soluble

The FT-IR spectrum of S$_{34}$E$_{18}$DiPA$_{48}$^{128}-58 shows the characteristic amide I (1666 cm^{-1}) band which confirms successful amidation (Figure S3-12). The stretching vibration of the remaining PMMA C=O is observable at 1728 cm^{-1}. This accords to the original SEM C=O stretching vibration at 1728 cm^{-1}. However, imides are formed in a side reaction as already observed for SEDMA-x and SEDEA-x, which was confirmed by ^{1}H-NMR and FT-IR spectroscopy of PDiPA-74 (Figure S3-10).
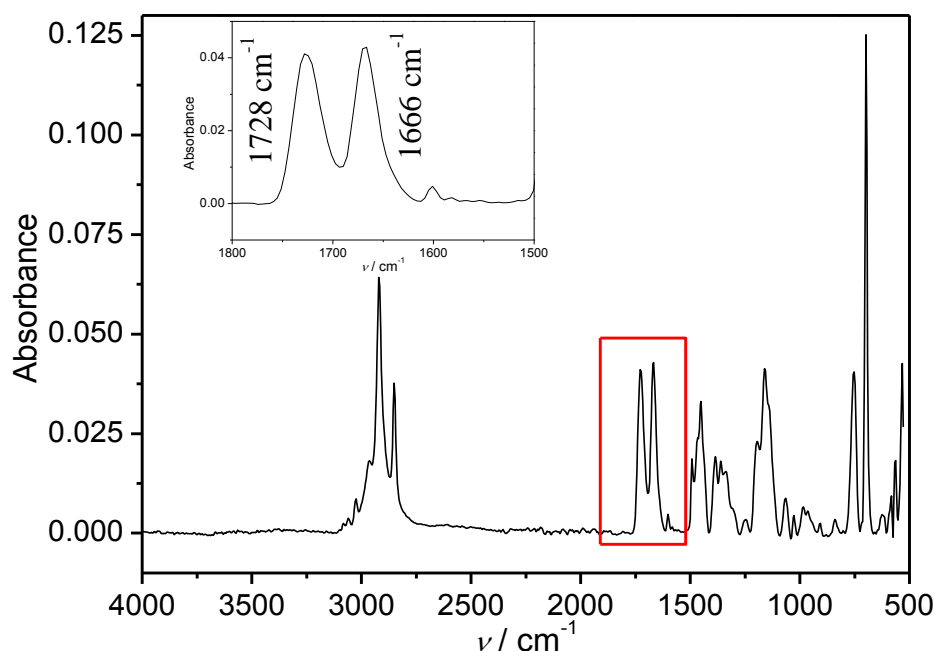

Figure S3-12. FT-IR spectrum of S$_{34}$E$_{18}$DiPA$_{48}$^{128}-58.

For high f (f > 30% for SEDEA-x and f > 60% for SEDiPA-x) and a $T_c \geq 30$ °C, agglomerated wCCMs with patchy corona were observed (Figure S3-13). The size of the PDEA and PDiPA corona patches is decreased, which is attributed to their decreased solubility in organic solvents in comparison to wCCMs with a lower degree of functionalization. For SEDEA-49, the patches retain the spherical shape. SEDiPA-64 wCCMs exhibit thin, but still rectangular PDiPA patches.
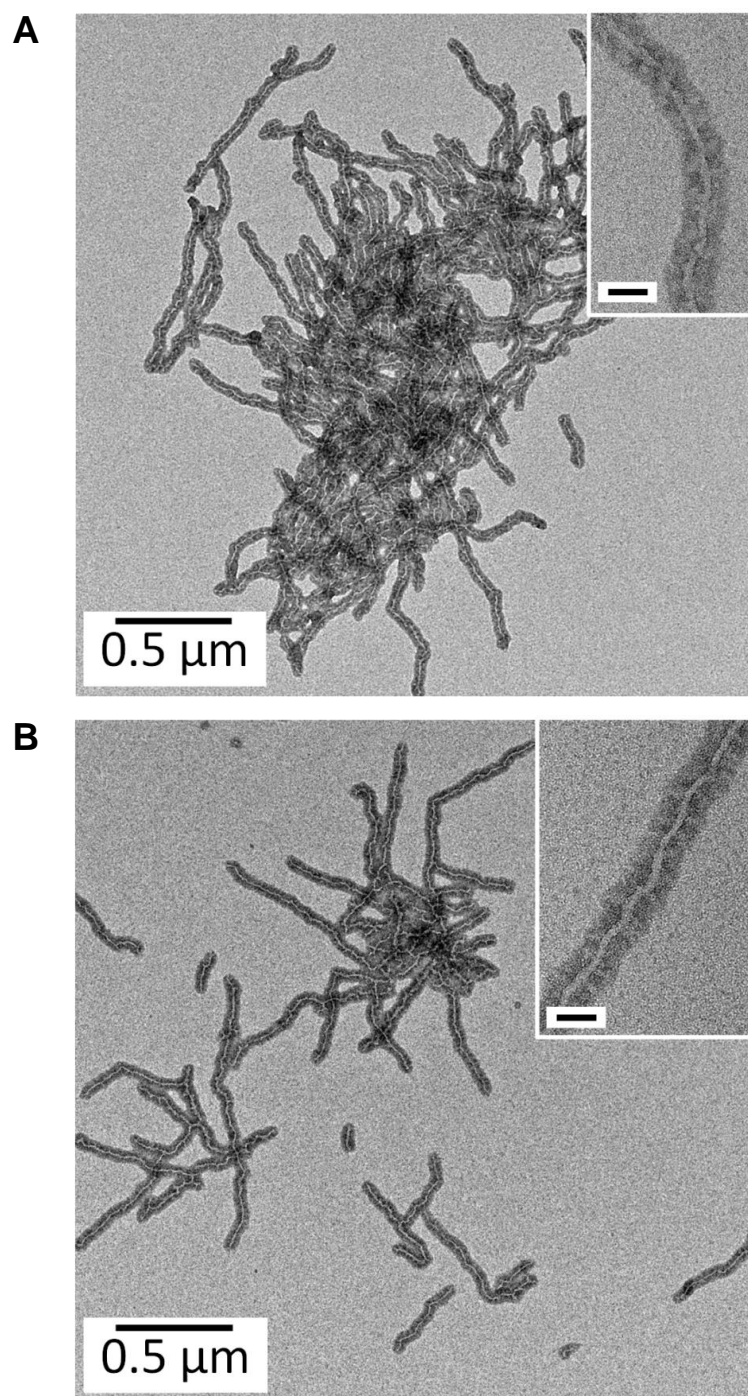
Figure S3-13. TEM micrographs of A) SEDEA-49 and B) SEDiPA-67, the PS domains were selectively stained with RuO$_4$ and appear dark. Scale bars in the insets are 50 nm.

Blank Test with SEM wCCMs as Template for the *in-situ* Synthesis of Au Nanoparticles
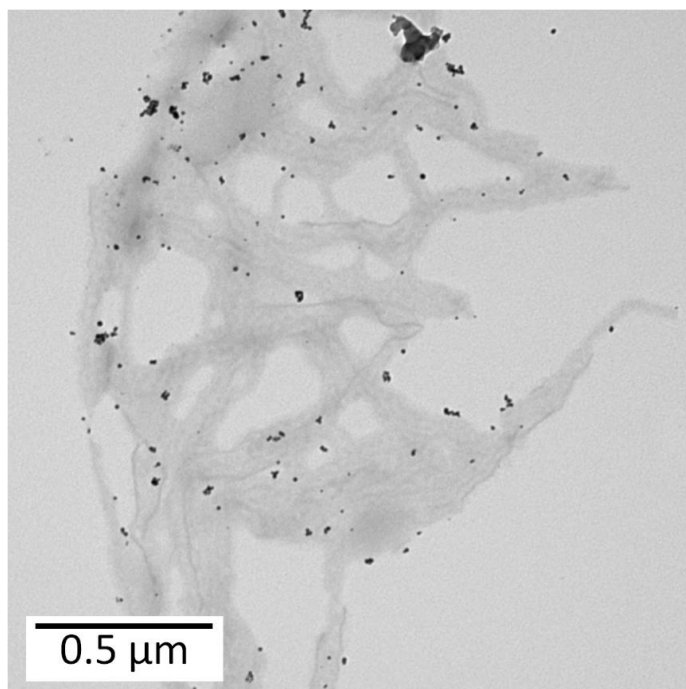
Figure S3-14: *In-situ* synthesis of Au nanoparticles using SEM wCCMs as template. The TEM image clearly reveals that in this case the Au nanoparticles are almost completely located outside the wCCM corona. Consequently, for an efficient templating and regio-selective incorporation of Au nanoparticles within one type of the surface patches functionalization of the PMMA patches by amidation is indispensable.

References

(1)   Kakuchi, R.; Wongsanoh, K.; Hoven, V. P.; Théato, P. Activation of Stable Polymeric Esters by Using Organo-Activated Acyl Transfer Reactions. *J. Polym. Sci. A* **2014**, *52*, 1353-1358.

4 Strategies for the Selective Loading of Patchy Worm-Like Micelles with Functional Nanoparticles

Judith Schöbel,[a] Anne Weckwerth,[b] Mathias Schlenk,[b] Carina Bojer,[c] Josef Breu,[c,d] Stephan Förster,[b,†] Andreas Greiner,[a,d] Matthias Karg,[b,‡] Holger Schmalz[a,d,]*

a) Makromolekulare Chemie II, Universität Bayreuth, 95440 Bayreuth, Germany

b) Physikalische Chemie I, Universität Bayreuth, 95440 Bayreuth, Germany

c) Anorganische Chemie I, Universität Bayreuth, 95440 Bayreuth, Germany

d) Bavarian Polymer Institute (BPI), Universität Bayreuth, 95440 Bayreuth, Germany

†) present address: JCNS-1/ICS-1, Forschungszentrum Jülich, 52425 Jülich, Germany

‡) present address: Physikalische Chemie I, Heinrich-Heine-Universität Düsseldorf, 40204 Düsseldorf, Germany
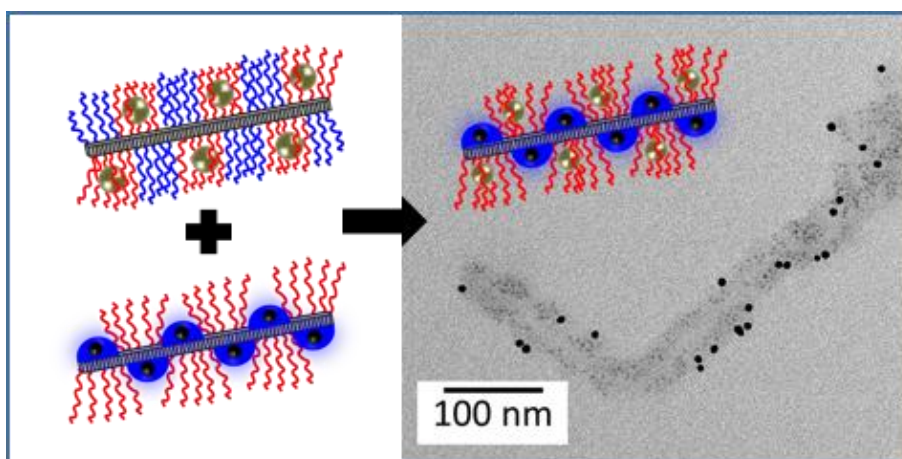
Abstract

Block copolymer self-assembly in solution paves the way to the construction of well-defined compartmentalised nanostructures. These are excellent templates for the incorporation and stabilisation of nanoparticles (NPs), giving rise to highly relevant applications in the field of catalysis or sensing. However, the regio-selective incorporation of NPs in specific compartments is still an issue, especially concerning the loading with different NP types. Using crystallisation-driven self-assembly (CDSA), functional worm-like crystalline-core micelles (wCCMs) with a tailor-made, nanometer-sized patchy corona were prepared as versatile templates for the incorporation and stabilisation of metal and metal oxide NPs. Different strategies, like ligand exchange or co-precipitation of polymer stabilised NPs with one surface patch, were developed that allow the incorporation of NPs in specific regions of the patchy wCCM corona. Employing a microfluidic setup even facilitates the selective loading of wCCMs with NPs in a continuous and well-controllable manner. Independent of the NP type and the incorporation method, the NPs showed no tendency for agglomeration and were fixed within the corona patches of the wCCMs. The binary loading of patchy micelles with metal and metal oxide NPs was realised by combining different loading strategies, yielding hybrids with homogeneously dispersed metal NPs dictated by the patchy structure of the template.

4.1 Introduction

A major challenge of today's materials science is the developing miniaturisation demanding for precisely tunable micro- and nanostructures. The self-assembly of amorphous block copolymers (BCPs) in solution proved to be an excellent tool to meet these demands, as a myriad of tailor-made micellar morphologies is accessible.[1] Spherical, cylindrical and helical micelles as well as vesicles are easily obtained by the use of selective solvents.[2–6] More complex preparation steps involving crosslinking or guided hierarchical self-assembly protocols enable the formation of Janus, patchy and multicompartment micelles (MCMs).[7-14] Among the MCMs, common examples include clover-, hamburger-, raspberry- and football-like micelles, as well as one-dimensional supracolloidal polymer chains.[15–18] Moreover, the MCMs serve as building blocks for the formation of hierarchical superstructures, opening the way to applications in optoelectronic devices, for drug delivery or as template for selective nanoparticle (NP) incorporation.[9,19–23] Although these state-of-the-art methods give access to manifold micelle morphologies, the preparation of well-defined cylindrical or worm-like micelles remains a challenge as, in general, the length of the micelles cannot be precisely controlled leading to broad length distributions.

To overcome these limitations in length control, crystallisation-driven self-assembly (CDSA) gained increasing attention since it is a powerful and very flexible method.[15,24] Similar to living polymerisation, CDSA can be conducted in a living manner, i.e., the ends of the cylindrical micelles remain active for the addition of unimers (molecularly dissolved BCPs bearing a crystallisable block). This was first reported by Manners and Winnik et al. who self-assembled poly(ferrocenyl dimethylsilane) (PFS) containing BCPs. [25,26] Using a seeded-growth protocol, the living CDSA enables a precise length control and opens the way for different micellar architectures like block comicelles (in analogy to BCPs), branched micelles, gradient block comicelles and hierarchical self-assemblies.[27–37] In addition to PFS-containing BCPs, a variety of other semi-crystalline polymers were reported to undergo CDSA, e.g. polyethylene (PE),[38,39] poly(L-lactide),[40,41] poly(3-hexylthiophene)[42,43] or poly(ε-caprolactone).[44,45] Recently, we showed that worm-like crystalline-core micelles (wCCMs) with a patch-like microphase-separated corona can be prepared by CDSA of polystyrene-*block*-polyethylene-*block*-poly(methyl methacrylate) (SEM) triblock terpolymers.[46,47] Here, the micellar corona is made of alternating nanometer-sized polystyrene (PS) and poly(methyl methacrylate) (PMMA) patches and the semi-crystalline polyethylene (PE) block forms the core. The concept of living CDSA was successfully

transferred to the self-assembly of SEM triblock terpolymers employing spherical crystalline-core micelles (sCCMs) as seeds, giving access to patchy micelles with controlled length and length distribution as well as more complex architectures like patchy block comicelles.[48]

Compartmentalised micelles are ideal templates for hybrid materials with inorganic NPs, as the structural complexity allows for a regio-selective incorporation of the NPs.[21,49] This opens the way to applications in the biomedical sector (drug delivery, imaging), in the optoelectronic sector (nanodevices, photovoltaics) or for sensing and catalysis.[50–59] Different hybrid materials derived from amorphous MCMs as well as crystalline-core micelles have been reported.[53,54,56,58,60–66] However, these publications are mainly focused on the incorporation of only one type of NPs, as the binary loading of compartmentalised micelles still remains a challenge and is hardly reported.[67,68] The unique patchy structure of the SEM wCCM corona provides an excellent platform for the construction of tailor-made binary loaded hybrid materials, but this demands for the efficient functionalisation of at least one of the corona forming blocks. Recently, we reported the post-polymerisation amidation of the PMMA block of SEM triblock terpolymers using a 30-fold excess of different N,N-dialkylethylenediamines (alkyl = methyl, ethyl, iso-propyl).[69] This method showed some disadvantages regarding the harsh reaction conditions ($\geq$ 60 h at 130 °C), formed side products and the required large excess of amine. In particular, the formation of a high fraction of imide units (ca. 50% with respect to the consumed PMMA units) resulted in low functionalisation degrees and limited solubility in organic solvents, especially for more polar N,N-dialkylethylenediamines (alkyl = methyl, ethyl). The limited solubility affected the CDSA and lead to ill-defined, short wCCMs for degrees of functionalisation above 20 % for the dimethyl derivative. Thus, only for nonpolar, sterically hindered alkyl substituents (iso-propyl groups) well-defined patchy wCCMs with a reasonable degree of functionalisation ($f = 55$ %) could be obtained. As a result, first loading experiments with NPs revealed only a partial and inhomogeneous loading, most probably due to the insufficient functionalisation of the amidated patches.

Here, we report the use of functionalised patchy wCCMs as versatile templates for the regio-selective incorporation of NPs. This is realised by amidation of the PMMA block of a SEM triblock terpolymer with activated N,N-dimethylethylenediamine, resulting in a nearly quantitative amidation. CDSA of the amidated SEM triblock terpolymer produces the desired patchy wCCMs, featuring highly functionalised corona patches for NP stabilisation.

Different strategies for the regio-selective loading of the amidated as well as non-functional PS patches with metal and metal oxide NPs are employed to yield in defined hybrid micelles. The use of an individually designed microfluidic double focus chip enables the controllable and continuous loading of the wCCMs *via in situ* synthesis of the NPs within the amidated patches and allows for a rapid screening of the reaction parameters. Finally, we present the successful binary loading of the patchy wCCMs with two types of NPs (gold and zinc oxide).

4.2 Experimental

Materials. All chemicals were purchased from Sigma-Aldrich unless otherwise noted. Tetrahydrofuran (THF) was dried over calcium hydride and potassium prior to use. *N,N*-dimethylethylenediamine (DMEDA, Acros Organics) was dried over calcium hydride prior to use. Ethanol (99.5 %), *n*-heptane, acetic acid (99.9 %), L-Selectride (1 M in THF), *n*-butyllithium (*n*-BuLi, 2.5 M in hexane), poly(methyl methacrylate) (PMMA, $M_w = 35$ kg mol^{-1}, Acros Organics), tetrachloroauric acid trihydrate (HAuCl$_4$· 3 H$_2$O, Alfa Aesar), silver trifluoroacetate (AgTFA), hexachloroplatinic acid hydrate (H$_2$PtCl$_6$·x H$_2$O, Alfa Aesar), zinc acetate dihydrate, copper acetate, sodium hydroxide and lithium hydroxide monohydrate were used as received.

SEM triblock terpolymer. The SEM triblock terpolymer was synthesised by a combination of living anionic polymerisation and catalytic hydrogenation, as published elsewhere.[69] The composition of the employed SEM triblock terpolymer is S$_{40}$E$_{21}$M$_{39}$[108], where the subscripts describe the mass fraction of the corresponding block in wt% and the superscript denotes the overall molecular weight in kg mol^{-1}.

Amidation of SEM. The PMMA block of the SEM triblock terpolymer was amidated under inert argon atmosphere. First, 0.86 mL DMEDA (7.8 mol, 2 equivalents with respect to MMA units of SEM) were dissolved in 20 mL dry THF and cooled to -78 °C by an acetone/dry ice bath. To this solution, 3.1 mL *n*-BuLi (7.8 mmol, 2 equivalents with respect to MMA units of SEM) were added dropwise under stirring followed by heating to room temperature. In another flask, 1 g SEM (3.9 mmol MMA units, 1 equivalent) was dissolved in 80 mL THF at 65 °C for 30 min. Subsequently, the solution was cooled to 40 °C and the

activated amine solution was added. The reaction was allowed to proceed for 24 h at 40 °C under stirring. Then, 1 mL of deionised water was added to deactivate excess amine and the obtained amidated SEM triblock terpolymer (SEDMA) was isolated by precipitation from pentane. For purification, the product was dissolved in THF at 65 °C ($c = 10$ g L^{-1}) and centrifuged at 40 °C with 5000 rpm for 15 min in order to remove residual lithium hydroxide. The supernatant was precipitated from pentane and dried in a vacuum oven (yield: 1 g (83 %)).

Formation of patchy wCCMs. The functional patchy wCCMs were prepared by crystallisation-driven self-assembly of the SEDMA triblock terpolymer in THF. To this end, SEDMA was dissolved in THF ($c = 10$ g L^{-1}) at 65 °C for 30 min and subsequently cooled to $T_c = 20$ °C in a thermostated shaker unit (HLC-MKR 13, Ditabis). The self-assembly process was allowed to proceed for 24 h at 20 °C at a shaking rate of 200 rpm.

Synthesis of ZnO and CuO NPs. The synthesis of ZnO and CuO NPs was conducted according to previously published protocols.[70,71] For preparation of the ZnO NPs, 0.04 mol of zinc acetate (1 equivalent) were added to 400 mL of boiling ethanol in order to dissolve the salt. After cooling the solution to room temperature, a lithium hydroxide monohydrate solution in ethanol (400 mL, $c = 140$ mM, 1.4 equivalents) was added and the reaction mixture was immediately cooled to 0 °C. The ZnO NPs were precipitated from n-heptane and redispersed in ethanol to yield a final concentration of 3.8 g L^{-1}. The average diameter obtained from TEM measurements was $D = 2.7 \pm 0.4$ nm.

The CuO NPs were synthesised by dissolving 5 mmol copper acetate (1 equivalent), 20 mmol sodium hydroxide (4 equivalents) and 10 mmol acetic acid (2 equivalents) in 500 mL ethanol. The reaction mixture was heated to 78 °C for 1 h to yield the CuO NPs. The CuO NP dispersion was precipitated from n-heptane and redispersed in ethanol to yield a final concentration of 1 g L^{-1}. The average diameter of the CuO NPs was determined to $D = 3.8 \pm 0.6$ nm by TEM. The full characterisation of the NPs can be found in the electronic supplementary information (Fig. S4-1).

Loading of patchy wCCMs via ligand exchange. To 2 mL of a SEDMA wCCM dispersion ($c = 1$ g L^{-1}, THF), 75 µL of the ZnO NP dispersion ($c = 3.8$ g L^{-1}, ethanol) was added and

the solution was stirred for 24 h. For incorporation of CuO NPs, the same procedure was used, employing 150 µL of the CuO NP dispersion (c = 1 g L^{-1}, ethanol).

$In~situ$ synthesis of gold (Au), silver (Ag) and platinum (Pt) NPs in patchy wCCMs. To 2 mL of a SEDMA wCCM dispersion (c = 1 g L^{-1}, THF), 40 µL of the corresponding metal salt dissolved in THF (c = 5 mM) was added. Immediately, 20 µL of L-Selectride (c = 1 M, THF) were added and the successful formation of the respective metal NPs was indicated by a characteristic colour change.

Continuous $in~situ$ loading of SEDMA wCCMs with Au NPs. The continuous, $in~situ$ loading of SEDMA wCCMs was accomplished by a PTFE based microfluidic chip with one main channel and four separate side channels for controlled fluid double focusing (Fig. 4-4). The microfluidic channels of the inner mixing part have a diameter of D = 500 µm. The outer chip holes are bigger with a diameter of D = 1000 µm in order to connect the five inlets via polyethylene (PE) tubes to the syringe pumps. The outlet is fixed to a glass capillary, which is used to run and investigate the laminar flow-controlled synthesis on a distance of 5 cm via optical microscopy. In a typical experiment, the main channel was fed with a SEDMA wCCM dispersion (c = 1 g L^{-1}, THF) at a flow rate of 2000 µL h^{-1}. The first two side channels were run with a HAuCl$_4$·3 H$_2$O solution (c = 2 mM, THF) at a flow rate of 2000 µL h^{-1} and the second two side channels with a L-Selectride solution (c = 20 mM, THF) at a flow rate of 1000 µL h^{-1}.

Synthesis of PS-stabilised Au NPs (PS@Au). PS@Au NPs were prepared via ligand exchange, starting from citrate-stabilised Au NPs synthesised via a seeded growth method reported by Piella et al.[72] A detailed characterisation of the citrate-stabilised Au NPs can be found in the electronic supplementary information (Fig. S4-2). A trithiocarbonate terminated PS (PS-TTC, M_n = 10400 g mol^{-1}, $Đ$ = 1.05, determined by THF GPC, Fig. S4-3A) was synthesised via reversible addition-fragmentation chain transfer (RAFT) polymerisation according to a previously published protocol.[73] UV-Vis spectroscopy confirmed the presence of the characteristic TTC absorption at λ = 315 nm (Fig. S4-3B). 120 mL of the as-synthesised aqueous citrate-stabilised Au NPs (D = 7.9 ± 0.7 nm) were overlaid with 40 mL of the PS-TTC solution in toluene (c = 10 mM). After 2 h of vigorous stirring, the phase-

transfer of the Au NPs was completed, i.e., the aqueous phase was clear and colourless, whereas the toluene phase showed a deep red colour, indicating a successful ligand exchange. The toluene phase was separated and centrifuged at 12 - 14000 rpm for 12 h to isolate the PS@Au NPs. The PS@Au NPs were purified from remaining free PS-TTC ligand by eight washing and centrifugation cycles with 2 mL toluene, respectively. The absence of free PS-TTC ligand was confirmed by gel permeation chromatography (GPC, Fig. S4-4A). The hydrodynamic radius of the PS@Au NPs was determined with DLS to R_h = 14.9 ± 0.7 nm (Fig. S4-4B). The concentration after final dispersion in toluene was determined by UV-Vis spectroscopy to $c = 5.3 \cdot 10^{17}$ NP L^{-1} (see electronic supplementary information for further details).

Loading of SEDMA wCCMs with PS@Au NPs by co-precipitation. 10 µL of SEDMA wCCMs ($c = 10$ g L^{-1}, THF), 37 µL PS@Au NPs ($c = 5.3 \cdot 10^{17}$ NP L^{-1}, toluene) and 53 µL THF were mixed in a vial. To this solution, 40 µL acetone were added in 4 steps under stirring with an equilibration time of 30 min, respectively. Subsequently, 860 µL of acetone were added to reach an overall acetone fraction of 90 vol%. The solution was stirred for at least 2 h before analysis.

Binary loading of SEDMA wCCMs with PS@Au and ZnO NPs. In a vial, 70 µL THF, 10 µL SEDMA wCCMs ($c = 10$ g L^{-1}, THF) and 7.5 µL ZnO NPs ($c = 3.8$ g L^{-1}, ethanol) were mixed and stirred for 1 h. Then, 27 µL of PS@Au NPs ($c = 5.3 \cdot 10^{17}$ NP L^{-1}, toluene) were added. To this solution, 40 µL acetone were added in 4 steps with an equilibration time of 30 min, respectively. Subsequently, 845 µL acetone were added to obtain an overall acetone fraction of 90 vol% and the solution was stirred for 2 h before analysis.

Instruments. For the microfluidic experiments, syringe pumps (Nemysis systems, Cetoni GmbH) were used and connected via polyethylene tubes (Scientific Commodities, Inc.) to a home-made PTFE chip (Fig. 4-4A). A glass capillary (Hilgenberg GmbH) with an inner diameter of $D = 980$ µm was connected to the end of the PTFE chip to elongate the reaction pathway. The Au NP formation was followed with an optical microscope IX71 (Olympus Co.) equipped with a D7000 digital camera (Nikon GmbH).

^{1}H-NMR spectroscopy was conducted on a Bruker Ultrashield 300 using deuterated chloroform as solvent at 300 MHz.

FT-IR spectroscopy was performed on a Digilab Excalibur Series FTS with a Miracle ATR unit of Pike Technologies. The spectra were measured with a resolution of 4 cm^{-1} and 16 scans were averaged per sample.

For GPC in THF SDV gel columns (300 x 8 mm, 5 µm particle size, PSS Mainz) with 10^5, 10^4, 10^3 and 10^2 Å pore sizes were used, together with a refractive index detector (RI 101, Techlab Shodex) and a UV detector operating at $\lambda = 254$ nm (Knauer). The applied flow rate was 1 mL min^{-1} at 40 °C. Narrowly distributed PS standards and toluene as internal reference were used for calibration.

GPC in hexafluoroisopropanol with potassium trifluoroacetate (8 g L^{-1}) was conducted on PFG gel columns (300 x 8 mm, 7 µm particle size, PSS Mainz) with 100 and 300 Å pore sizes using a flow rate of 0.5 mL min^{-1} at 23 °C. The signals were detected by a Gynkotec SE-61 refractive index detector. For calibration, narrowly distributed PMMA standards and toluene as internal reference were used.

For GPC in N,N-dimethylformamide with lithium bromide (5 g L^{-1}) GRAM columns (300 x 8 mm, 10 µm particle size, PSS Mainz) with 100 and 3000 Å pore sizes were used. The sample was measured at a flow rate of 0.5 mL min^{-1} at 23 °C using a DAD VL+ G1315C diode array UV detector (Agilent Technologies) operated at $\lambda = 270$ nm and 525 nm. For calibration, narrowly distributed PS standards and toluene as internal reference were used.

The thermal properties of the wCCMs were analysed by a SETARAM micro-DSC III. The sample ($c = 10$ g L^{-1} in THF) was measured in closed batch cells at a scanning rate of 0.5 K min^{-1} and THF was used as reference.

For UV-Vis measurements a JASCO V630 spectrophotometer and fused quartz cuvettes (Hellma) ($d = 0.2$ cm) were used. The samples were measured in THF ($c = 0.1$ g L^{-1}) and acetone at room temperature, using the corresponding pure solvent for background subtraction, respectively. For the binary loaded sample, pure acetone was used as reference.

Elastic bright-field transmission electron microscopy (TEM) was conducted on a Zeiss 922 Omega EFTEM (Zeiss NTS GmbH, Oberkochen, Germany) electron microscope operating at an acceleration voltage of 200 kV. A bottom mounted CCD camera system (Ultrascan 1000, Gatan) recorded the zero-loss filtered images, which were processed by the imaging

software Gatan Digital Micrograph 3.9 for GMS 1.4. The samples were diluted to 0.1 g L^{-1} and drop-coated onto carbon-coated copper grids. The solvent was blotted by filter paper and the samples were dried in a vacuum oven operating at 0.2 mbar at room temperature before staining with ruthenium tetroxide (RuO$_4$). The software ImageJ was used for analysis of particle sizes, wCCM length and patch sizes. To obtain representative average values, at least 100 measurements were done, respectively.

4.3 Results and Discussion

Functional wCCMs with amino group containing patches

The formation of hybrid materials of patchy wCCMs and NPs demands for an efficient functionalisation of one of the corona blocks of the employed S$_{40}$E$_{21}$M$_{39}$[108] (the subscripts describe the mass fraction of the corresponding block in wt% and the superscript denotes the overall molecular weight in kg mol^{-1}) triblock terpolymer. To this end, we chose an amidation of the PMMA block with *N,N*-dimethylethylenediamine (DMEDA), utilizing a prior activation of the amine with *n*-BuLi (Scheme 4-1A).[74] Due to the activation, the amount of DMEDA could be decreased to a 2-fold excess with respect to the amount of methyl ester units in the PMMA block (in comparison to the 30-fold excess used in our previous report[69]) and nearly quantitative conversion was obtained after 24 h under mild conditions (40 °C). The functionalisation proceeds without degradation of the polymer backbone, as shown by GPC of an amidated PMMA homopolymer, which was functionalised under identical conditions as the S$_{40}$E$_{21}$M$_{39}$[108] triblock terpolymer (Fig. S4-5).
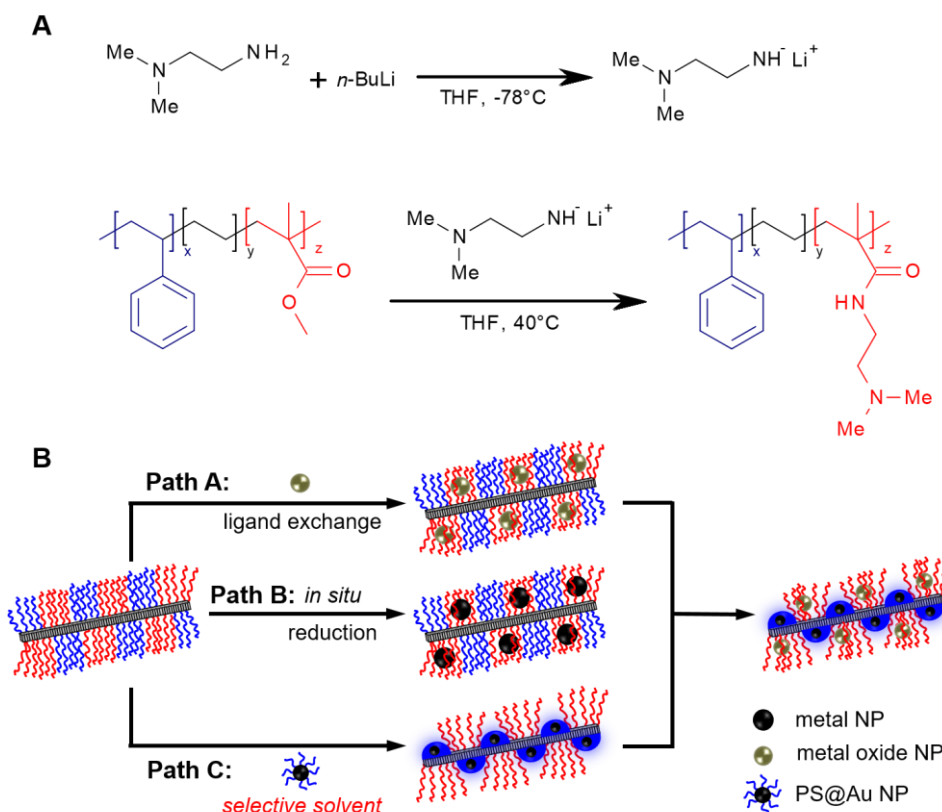
Scheme 4-1. Amidation of the $S_{40}E_{21}M_{39}^{108}$ triblock terpolymer with prior activation of the amine by *n*-BuLi (A). Strategies for the selective and binary loading of patchy wCCMs with metal and metal oxide NPs (B).

The amidated SEM triblock terpolymer was characterised by ^{1}H-NMR and FT-IR spectroscopy. The signals in the ^{1}H-NMR spectrum can be clearly assigned to the typical proton signals of the amide (Fig. 4-1A). There is only a weak signal of not consumed PMMA ester units at 3.6 ppm. From the integral of this signal, calibrated by the aromatic polystyrene protons (**5**, 5 H), a degree of amidation of 95 % results. Consequently, the composition and the overall molecular weight of the functional triblock terpolymer changes to $S_{33}E_{17}DMA_{50}^{131}$, which will be referred to as SEDMA in the following. A signal for imide formation, which would be expected at $3.7 - 4$ ppm,[69] is hardly observable. This indicates that the amidation proceeds without significant side reactions. The successful amidation is further confirmed by FT-IR spectroscopy (Fig. S4-6), showing the characteristic amide I and amide II vibrations at 1660 cm^{-1} and 1526 cm^{-1}, respectively, and only a very weak C=O vibration of the remaining PMMA units. The negligible fraction of imide units in the SEDMA triblock terpolymer is supported by its solubility in tetrahydrofuran (THF) and chloroform (CHCl$_3$), as in case of a high fraction of imide units the triblock terpolymer would be insoluble in both solvents.[69]
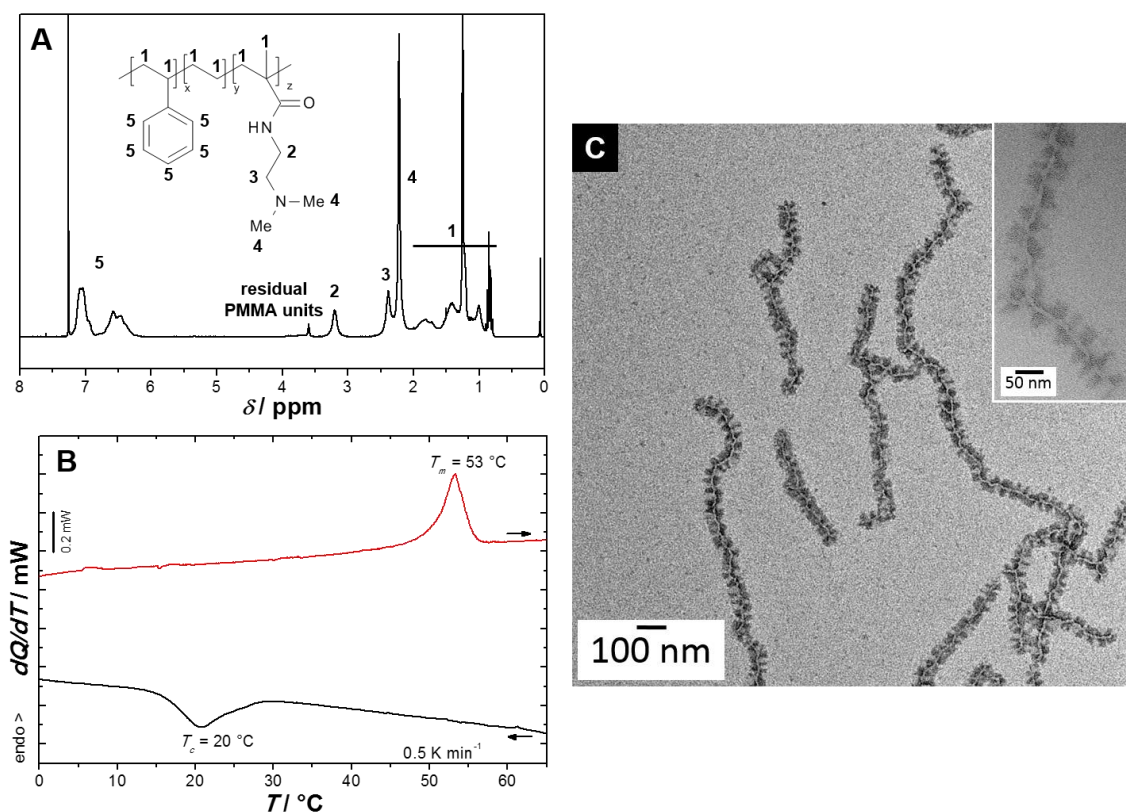
Fig. 4-1. Characterisation of SEDMA. ^{1}H-NMR spectrum measured in CDCl$_3$ (A), μ-DSC heating and cooling traces ($c = 10$ g L^{-1}, THF) (B) and TEM micrographs of SEDMA wCCMs, selectively stained with RuO$_4$ (C).

The solubility of the SEDMA triblock terpolymer in THF, which is used for CDSA, is crucial for the formation of well-defined patchy wCCMs. Previously, we have shown that the crystallisation temperature (T_c) of the PE middle block in solution is a very sensitive parameter to probe the solubility of the amidated triblock terpolymers.[69] With decreasing solubility an increase in the T_c of the PE block is observed with respect to that of the corresponding S$_{40}$E$_{21}$M$_{39}$^{108} precursor ($T_c = 21$ °C). For T_c values above 30 °C only ill-defined and strongly aggregated wCCMs are formed. This is attributed to aggregation caused by the limited solubility of the amidated PMMA block, which results in a higher PE segment density and, thus, a better nucleation of PE crystallisation. Micro differential scanning calorimetry (μDSC) for the synthesised SEDMA ($c = 10$ g L^{-1} in THF) shows a T_c at 20 °C (Fig. 4-1B), i.e., almost identical to the SEM precursor underlining its good solubility in THF. Consequently, CDSA of SEDMA in THF at 20 °C results in the formation of well-defined wCCMs with an average length of $l = 540 \pm 310$ nm, as revealed by TEM (Fig. 4-1C). The sample was stained with RuO$_4$, which is known for selective staining of the PS domains. Therefore, the PS patches in the corona appear black and the amidated PMMA

(PDMA) patches appear bright. Both patches exhibit a similar width of 18 ± 5 nm for PS and 17 ± 5 nm for PDMA, respectively, and are arranged in an alternating manner.

Selective loading of patchy wCCMs with NPs

The unique alternating structure of the functional patchy corona of the SEDMA wCCMs offers the possibility to incorporate two different types of NPs. The patchy morphology guarantees an efficient separation and at the same time a dense packing of single NPs. We developed three different strategies for the selective loading of the patches with metal and metal oxide NPs (Scheme 4-1B). Path A is based on selective interactions between the PDMA corona patch and the metal oxide NP, which are known to undergo ligand exchange if amino groups are offered.[75] Path B deals with the *in situ* synthesis of metal NPs within the PDMA patch of the SEDMA wCCMs, which provides tertiary amino groups as anchor groups for the efficient stabilisation of different metal NPs like gold (Au) or silver (Ag).[76] Path C is based on polymer-polymer and polymer-solvent interactions. The addition of a selective solvent for one of the corona patches leads to the collapse of the other corona patch. Thus, NPs that are stabilised with the same polymer as the collapsing corona patch are incorporated into the collapsing patch upon selective solvent addition. Combination of path A and C finally leads to binary loaded wCCMs.

Following path A, we investigated the ligand exchange for zinc oxide (ZnO) and copper oxide (CuO) NPs. Both types of NPs were synthesised in ethanol with acetate ligands for stabilisation and have average diameters of $D = 2.7 \pm 0.4$ nm for ZnO and $D = 3.8 \pm 0.6$ nm for CuO (determined from TEM). The obtained NPs are phase pure according to the powder X-ray diffraction pattern (PXRD, Fig. S4-1A) and exhibit a narrow particle size distribution (Fig. S4-1B). The concentration of the NP dispersions was adjusted to $1 - 4$ g L^{-1}, which ensures that the needed total amount of NP dispersion is less than 10 vol% with respect to the employed THF dispersion of SEDMA wCCMs. For higher volume fractions of ethanol, the wCCMs are insoluble and agglomerate before the ligand exchange is completed. The incorporation of the NPs was finished after 1 d and the SEDMA wCCMs were highly loaded with both types of NPs as revealed by TEM (Fig. 4-2A-C), pointing to a successful ligand exchange, i.e., acetate ligands vs. amino groups in the PDMA patch. In contrast to the neat SEDMA wCCMs, the hybrid samples were measured without prior staining with RuO$_4$ as the incorporated NPs provide an intrinsic staining of the patches. Both, the ZnO and CuO

NPs are homogeneously distributed within the PDMA patches of the SEDMA wCCMs without agglomeration.

The UV-Vis spectra of the neat wCCMs show a continuous increase in absorbance with decreasing wavelength, which is attributed to scattering from the worm-like micelles (Fig. 4-2D, E). This is supported by the blue colour of the neat SEDMA wCCM dispersion (Tyndall effect). The low wavelength part of the spectrum is dominated by a relatively weak absorption maximum at $\lambda_{max} = 250$ nm, deriving from the absorption of the PS units of the SEDMA wCCMs. The UV-Vis spectra of the pure ZnO and CuO NPs show absorption maxima at approximately 300 nm overlapping with the scattering contribution of the SEDMA wCCMs. Consequently, the UV-Vis spectrum of the CuO NP hybrid material is similar to the spectrum of the neat SEDMA wCCMs (Fig. 4-2E). In contrast, the ZnO NPs show a shoulder at $\lambda = 333$ nm, which is also observable in the UV-Vis spectrum of the ZnO NP loaded wCCMs (Fig. 4-2D), confirming the successful incorporation of the NPs in the patchy corona.
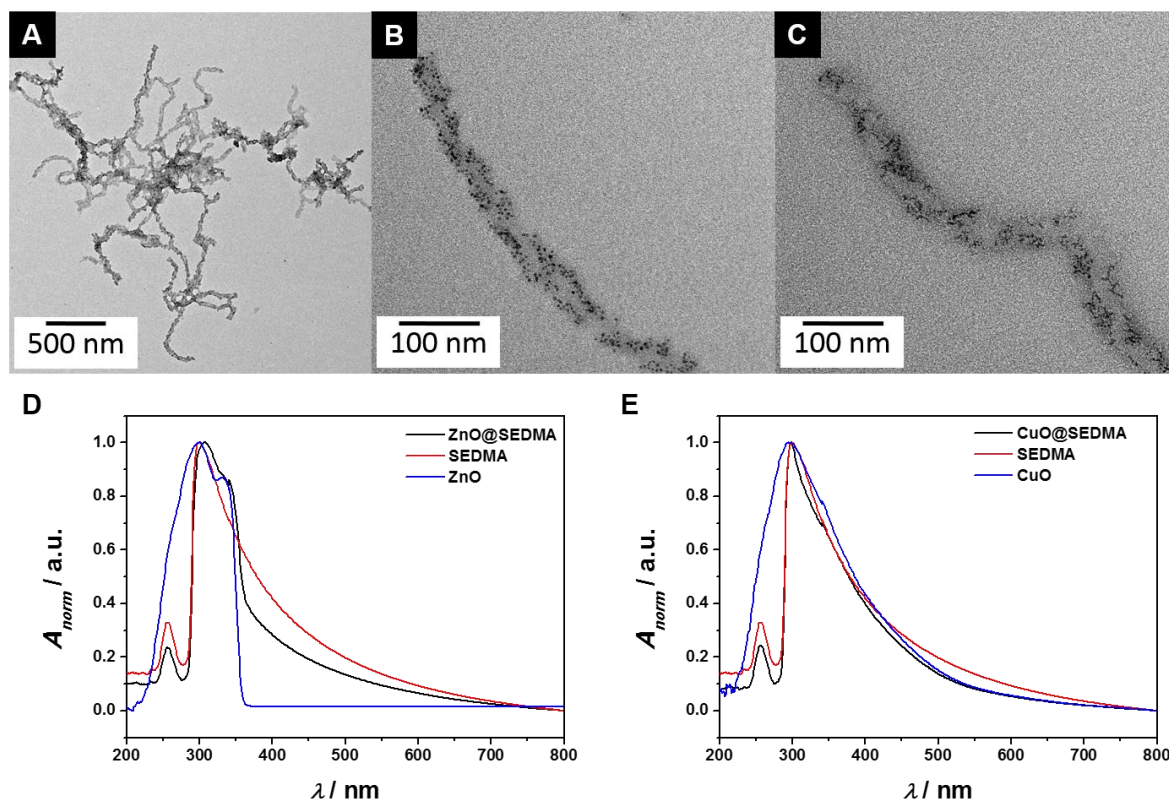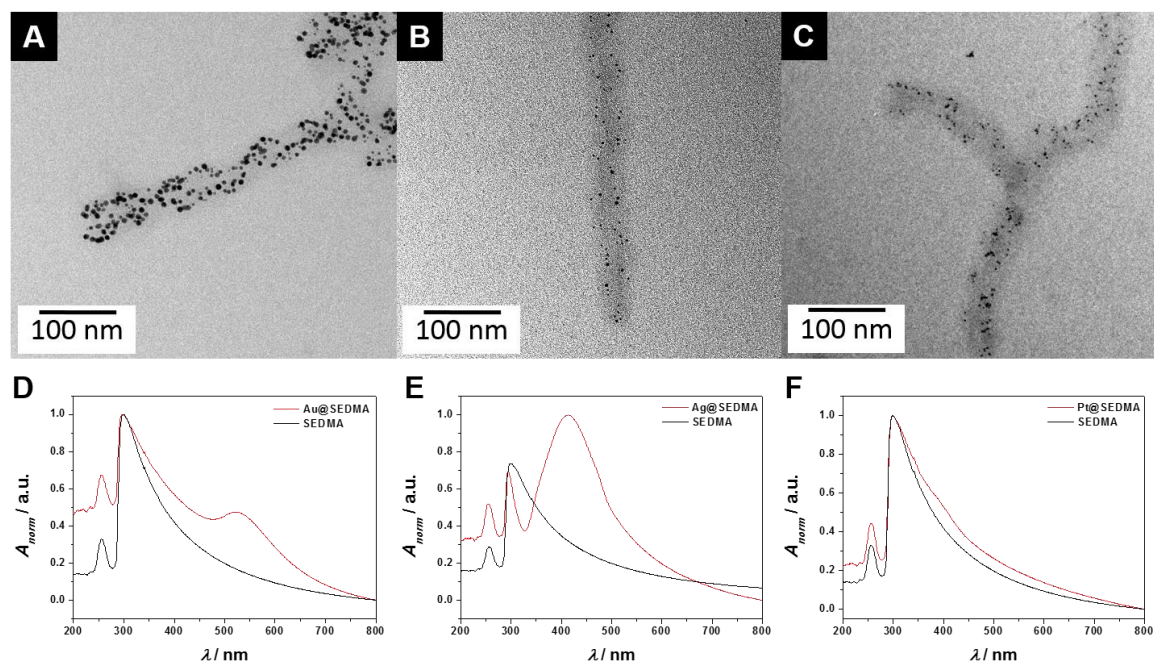

Fig. 4-2. TEM micrographs and corresponding UV-Vis spectra for the hybrid materials of SEDMA wCCMs with ZnO (A, B, D) and CuO NPs (C, E).

In path B we utilised the functionalised corona patches as nanoreactors for the simultaneous stabilisation and *in situ* syntheses of different metal NPs *via* reduction of the corresponding

metal salts, i.e., tetrachloroauric acid trihydrate (HAuCl$_4$·3 H$_2$O), silver trifluoroacetate (AgTFA) and hexachloroplatinic acid hydrate (H$_2$PtCl$_6$·x H$_2$O), with L-Selectride (lithium tri-*sec*-butylborohydride). We chose L-Selectride since it is a mild reduction agent that does not reduce ester or tertiary amide groups.[77] After addition of L-Selectride, the typical colour change of all solutions indicated a successful NP formation. The formation of NPs is further proven by the TEM micrographs shown in Fig. 4-3A-C. The Au, Ag and Pt NPs show a spherical shape and are selectively incorporated into the patchy corona of the SEDMA wCCMs. The diameters of the formed NPs are 4.7 ± 1.2 nm, 2.9 ± 0.8 nm and 1.7 ± 0.5 nm, respectively, as determined by TEM image analysis. The rather high size dispersity of the NPs might be attributed to the *in situ* reduction process, which does not allow a precise size control as nucleation and growth of the NPs happen almost simultaneously. For all hybrids, the patchy structure of the corona is still clearly recognizable, pointing to a selective formation of the NPs within the functional PDMA patches of the wCCMs. The Au NPs are homogeneously incorporated in the wCCMs and the PDMA patches are highly loaded with Au NPs without showing any significant agglomeration. This can be ascribed to the nearly quantitative amidation of the PMMA block, resulting in a high density of amino anchor groups in the PDMA patches. Fig. 4-3D compares the UV-Vis spectra of the wCCMs prior to and after the *in situ* synthesis of the Au NPs. Both absorbance spectra show the same spectral characteristics except for a peak at approximately $\lambda_{max} = 523$ nm that appears only for the Au NP loaded SEDMA wCCMs. This peak can be assigned to absorption due to the localised surface plasmon resonance (LSPR) of the Au NPs, which is characteristic for small, spherical Au NPs.[78] The low absorbance at wavelengths of 700 nm and higher manifests the good stabilisation and distribution of the Au NPs by the wCCMs and the absence of Au NP aggregates. Similar to the Au NPs, the Ag and Pt NPs are well distributed within the SEDMA wCCMs without agglomeration (Fig. 4-3B, C). The UV-Vis spectrum of the Ag NP loaded SEDMA wCCMs (Fig. 4-3E) shows a strong peak in absorbance at $\lambda_{max} = 415$ nm, superimposed to the wCCM absorbance. This peak is related to the LSPR of small, spherical Ag NPs.[79] Compared to the spectrum of the Au NP loaded wCCMs, the Ag NP containing system shows a much stronger LSPR contribution, which is attributed to the higher absorption cross-section of silver as compared to Au NPs of similar size. The narrow width of the LSPR resonance and the absence of significant absorbance at higher wavelengths underline the good stabilisation and distribution of the Ag NPs by the wCCMs. Comparing the UV-Vis spectra of the SEDMA wCCMs prior to and after loading with Pt NPs in Fig. 4-

3F reveals that the spectra are very similar, except for a slightly higher absorbance in the long wavelength scattering tail of the wCCMs. This can be attributed to the significantly smaller Pt NPs, which do not support LSPR resonances in the visible wavelength regime.[80]

Fig. 4-3. TEM micrographs and corresponding UV-Vis spectra for the hybrid materials of SEDMA wCCMs with Au (A, D), Ag (B, E) and Pt (C, F) NPs.

The selective loading of patchy micelles with metal NPs by *in situ* reduction of the corresponding metal salts is a one-pot reaction. In consequence, for each set of parameters (e.g. molar ratio of metal salt to amine units) a new experiment has to be conducted. This asks for the development of a stable and continuous process that allows an easy adjustment of reaction parameters, which can be realised employing an individually designed microfluidic device.[81] The laminar flow in microfluidic channels allows a very precise control over all reactants by varying the flow rate and channel geometry for adjustable fluid focusing.[82] To this end, a microfluidic device based on a home-made PTFE chip (Fig. 4-4A) with one main channel and a double-focusing cross made of four side channels was fabricated and connected with a glass capillary. As visible in the detailed CAD-design shown in Fig. 4-4B, the channels of the double-focusing section are produced with a small diameter of 500 µm in comparison to the bigger inlet and outlet holes, which are used for easy tube and capillary connection. The double-focusing design is used to add the reactants for the NP synthesis separately in order to avoid an uncontrolled reaction beforehand and to get the formed NPs in contact with the micelles as soon as they are formed by *in situ* reduction

(Fig. 4-4C).
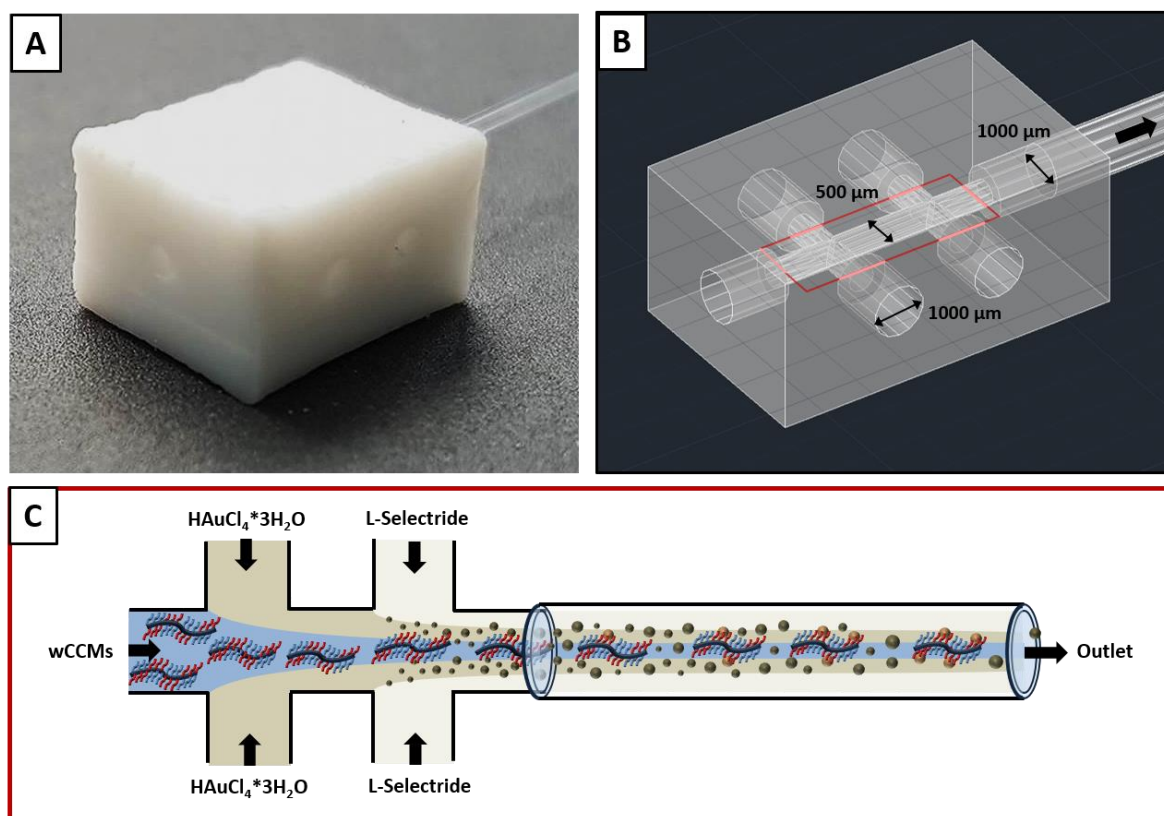
Fig. 4-4. Microfluidic PTFE double focus chip connected to a glass capillary with an inner diameter of $D = 980\,\mu m$ (A) as well as the detailed CAD design of the inner channel geometry (B). Illustration of the fluid focusing within the tailor-made microfluidic device (C).

In a continuous flow, the SEDMA wCCM dispersion was pumped through the main channel at a flow rate of 2000 µL h^{-1}. At the same time, HAuCl$_4$·3 H$_2$O was added through the first two side channels (2000 µL h^{-1}) and L-Selectride (1000 µL h^{-1}) was fed via the second two side channels. The resulting dispersion showed a purple colour, which is characteristic for the formation of Au NPs. The TEM micrograph reveals that the PDMA patches of the wCCMs are homogeneously and densely loaded with Au NPs, showing an average diameter of $D = 4.3 \pm 1.4$ nm (Fig. 4-5A). Thus, the NP loading strategy by *in situ* reduction could be successfully transferred to a continuous process. The diameter of the observed Au NPs is comparable to the diameter of the Au NPs synthesised by *in situ* batch reduction ($D = 4.7 \pm 1.2$ nm, Fig. 4-3A). The narrow LSPR resonance at approximately $\lambda_{max} = 532$ nm and the weak absorbance at wavelengths of 700 nm and higher again support the good stabilisation and distribution of Au NPs by the wCCMs (Fig. 4-5B). Compared to the Au NP hybrid wCCMs obtained by the *in situ* batch synthesis (Fig. 4-3D), the LSPR absorption of

the Au NPs is significantly stronger indicating a higher loading density. This becomes more pronounced by comparing the specific PS absorbances at $\lambda = 250$ nm and at the LSPR in both samples. As the PS content in the wCCMs is constant and the Au NP size is comparable in the samples, the LSPR/PS absorbance ratio can be taken as a measure for the incorporated amount of Au NPs.
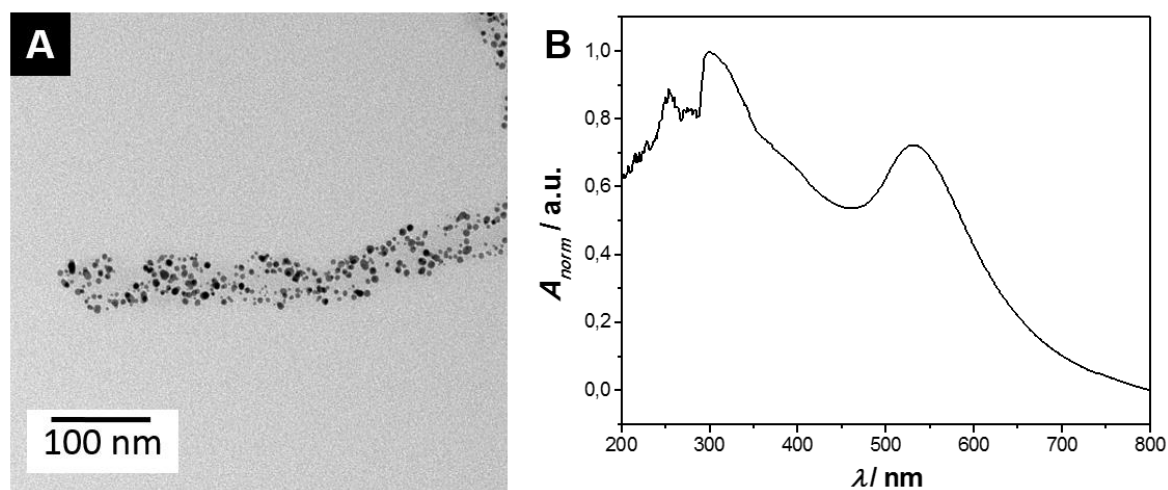
Fig. 4-5. TEM micrograph (A) and UV-Vis spectrum (B) of Au NP loaded SEDMA wCCMs, produced via a continuous microfluidic process.

Microfluidics additionally offers the advantage of a very simple parameter screening. Hence, we analyzed the potential of the continuous loading method with respect to the variation of different flow rates. By decreasing the flow rate for the addition of the $HAuCl_4 \cdot 3 \, H_2O$ solution (1000 $\mu L \, h^{-1}$), the loading density of the Au NP within the SEDMA wCCMs is reduced, which is confirmed by TEM and UV-vis spectroscopy (Fig. S4-7A, C). Here, the diminished volume concentration in comparison to the micelles solution seems to reduce the quantity of growing Au NPs within the total flow volume, which results in a lower loading density for the micelles. In addition to it, the decreased ratio of the $HAuCl_4 \cdot 3 \, H_2O$ to the reduction agent led to a smaller diameter of $D = 3.4 \pm 1.6$ nm for the Au NPs. These results verify the good control over the Au NP diameter by adjusting the flow rates. In a further step, we decreased the flow rates of all channels equally (SEDMA wCCMs: 1000 $\mu L \, h^{-1}$, $HAuCl_4 \cdot 3 \, H_2O$ and L-Selectride: 500 $\mu L \, h^{-1}$, respectively) whereby the relation of the flow rates between all channels remains constantly. These reduced flow rates yielded in a similar loading density of the wCCMs as confirmed by TEM and UV-vis spectroscopy (Fig. S4-7B, D). Normally, smaller flow rates lead to elongated reaction duration within the glass capillary and therefore, more Au NP could be incorporate within the amidated patches.

However, based on the used flow rates and the capillary diameter the flow velocity is quite low in comparison to the fast reduction process of the $HAuCl_4 \cdot 3\, H_2O$ with L-Selectride. Based on the capillary length of 5 cm, the time for the reaction pathway is calculated of about $t = 4$ s. Hence, there is enough time for the much faster incorporation process of the Au NP within the amidated patches to be finished far before. Consequently, an elongation of the reaction pathway is not needed here and shows no influence on the loading density.

Binary loading of patchy SEDMA wCCMs

For binary loading of the patchy SEDMA wCCMs with two different types of NPs also the non-functional PS patches need to be loaded. Therefore, we developed a co-precipitation method that offers the possibility to incorporate preformed, PS-stabilised NPs with precisely tailored dimensions within the PS patches of the wCCMs without the need for a preceding functionalisation of the patch (Scheme 4-1B, path C). This method is based on polymer-polymer and polymer-solvent interactions. We chose PS stabilised Au NPs (PS@Au NPs), being compatible with the PS patch of the SEDMA wCCMs. The PS@Au NPs were synthesised by a facile ligand exchange method starting from aqueous citrate-stabilised Au NPs with an average diameter of $D = 7.9 \pm 0.7$ nm (determined by TEM, Fig. S4-2) and trithiocarbonate-terminated PS (PS-TTC) in toluene, prepared by RAFT polymerisation (Fig. S4-3). After the biphasic ligand exchange, the PS@Au NPs were found well-dispersed in the organic phase. The TEM micrograph shown in Fig. 4-6A reveals that the PS@Au NPs are homogeneously distributed on the TEM grid without agglomeration and show a spherical shape. Due to the high electron density of the Au NPs, the PS shell is only visible as a pale-grey shell in the TEM micrograph. The PS@Au NPs show a characteristic LSPR at $\lambda_{max} = 527$ nm in toluene (Fig. 4-6B), which is red-shifted by 12 nm with respect to the LSPR of the citrate-stabilised Au NPs in water ($\lambda_{max} = 515$ nm). This red-shift is caused by the change in refractive index from the aqueous phase ($n = 1.33$) to the toluene phase ($n = 1.50$). DMF GPC using an UV-Vis diode array detector with two different wavelengths, characteristic for PS ($\lambda = 270$ nm) and the Au NPs ($\lambda = 525$ nm), shows that the PS-TTC is efficiently bound on the Au NP surface and there is only a small amount of residual free PS ligand (Fig. S4-4A). The hydrodynamic radius of the PS@Au NPs was determined by dynamic light scattering to $R_h = 14.7 \pm 0.1$ nm, confirming the PS shell around the Au NPs. Furthermore,

the small standard deviation supports the formation of narrowly dispersed PS@Au NPs without agglomerates.
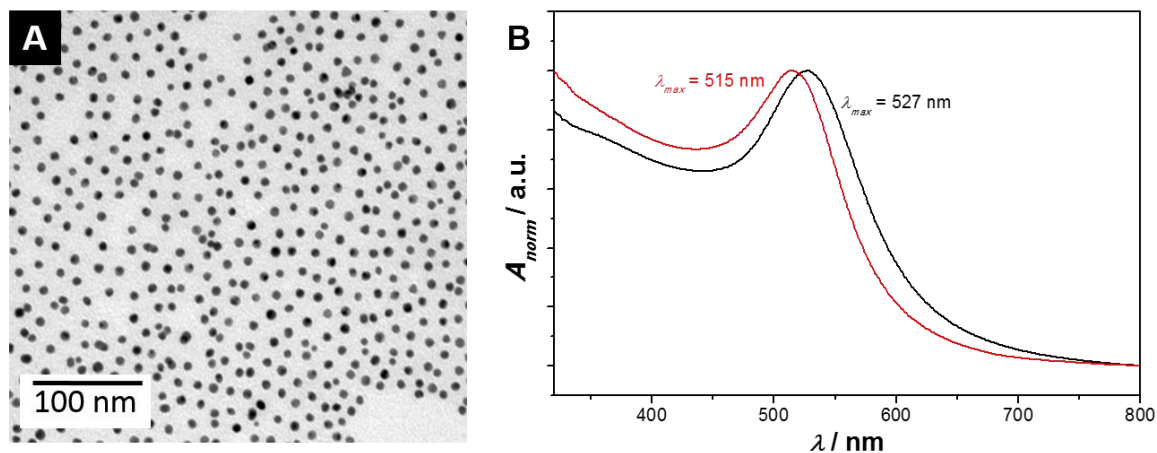
Fig. 4-6. TEM micrograph (A) and UV-Vis absorbance spectrum of the PS@Au NPs in toluene ($c = 8.8 \cdot 10^{15}$ NP L^{-1}, black trace in (B)). The red spectrum in (B) corresponds to the citrate-stabilised Au NPs in water ($c = 1.2 \cdot 10^{16}$ NP L^{-1}) measured prior to the ligand exchange with PS-TTC.

To identify suitable conditions for the incorporation of PS@Au NPs in the SEDMA wCCMs via co-precipitation, we first investigated the aggregation behaviour of pure PS@Au NPs in THF upon addition of acetone. Acetone will be used as selective solvent for the PDMA patch in the co-precipitation process and, thus, is expected to induce the collapse of the PS ligands. Due to the high sensitivity of the LSPR to particle stability, UV-Vis spectroscopy could be used to follow the solvent induced aggregation (Fig. S4-8). Analysis of the spectra reveals that a volume fraction of 33 vol% acetone is sufficient to induce the collapse of the PS shell around the Au NPs, indicated by a broadening of the LSPR, and upon further addition of acetone no significant changes in the UV-Vis absorption maximum were observed.

For co-precipitation, the PS@Au NP dispersion in toluene was mixed with the SEDMA wCCMs in THF, a good solvent for both the PS and PDMA patches. Details on the used amounts can be found in the experimental section. The addition of acetone was done in two steps. First, 40 µL acetone (28 vol% with respect to the overall volume) were added in 10 µL portions, employing an equilibration time of 30 min after each addition. Until this point, the PS@Au NPs do not aggregate. However, the solvent quality for PS is slowly decreasing and the PS@Au NPs start to interact with the PS patches of the SEDMA wCCMs. In the second addition step, the volume fraction of acetone was increased to 90 vol% to ensure a complete co-precipitation of the PS@Au NPs within the PS corona patches. The TEM micrograph of

the loaded wCCMs reveals the successful incorporation of the Au NPs, which are statistically distributed over the whole SEDMA wCCMs (Fig. 4-7A). The PS shell around the Au NPs prevents agglomeration of the NPs even if they are in close proximity to each other. The UV-Vis spectrum clearly shows the LSPR of the Au NPs with a maximum absorbance at $\lambda_{max} = 530$ nm (Fig. 4-7C), which is close to the position of the LSPR of the neat Au@PS NPs ($\lambda_{max} = 527$ nm, Fig. 4-6B). Furthermore, the resonance width did not significantly change and the absorbance quickly drops to values close to zero, which supports the absence of aggregates.

Combining path A and C, binary loading of the patchy SEDMA wCCMs with ZnO and PS@Au NPs is possible (Scheme 4-1B, Fig. 4-7B). First, the ligand exchange route was employed to incorporate acetate-stabilised ZnO NPs in the PDMA patches of the SEDMA wCCMs. Subsequently, the PS@Au NPs were loaded into the PS patches by co-precipitation. The overall amount of acetone was adjusted to 90 vol%, as this leads to complete incorporation of the PS@Au NPs. The binary loaded hybrid micelles show no agglomeration of both NP types, but a homogeneous distribution over the whole SEDMA wCCMs contouring the bright-appearing semi-crystalline polyethylene core. The UV-Vis spectrum (Fig. 4-7D) shows the typical LSPR of Au NPs at $\lambda_{max} = 538$ nm as well as a signal for the ZnO NP at $\lambda_{max} = 333$ nm, as already observed for the single loaded hybrid materials, respectively. This shows that patchy wCCMs are efficient templates for the preparation of binary loaded hybrid materials, as the patchy structure of the corona directs the controlled incorporation of different NP types in discrete patches. This leads to a homogeneous distribution of both NP types over the whole wCCMs and, thus, ensures a large interface between the different NPs.
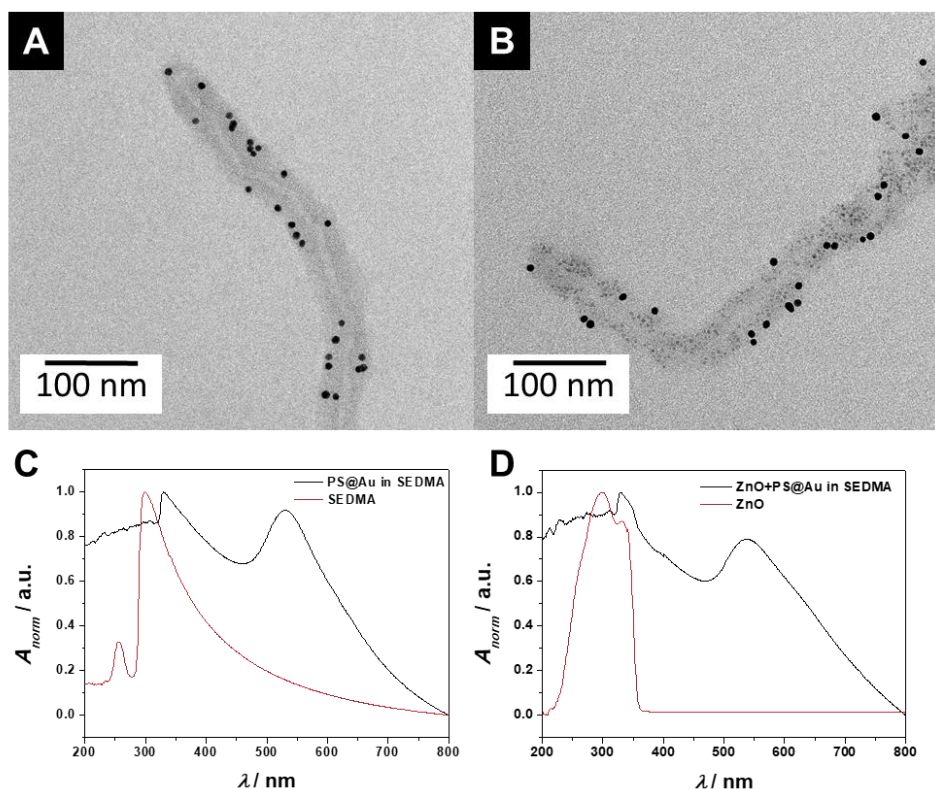
Fig. 4-7. Hybrid materials of SEDMA wCCMs with PS@Au NPs prepared by co-precipitation (A) and binary loaded SEDMA wCCMs with PS@Au and ZnO NPs (B). (C) and (D) show the corresponding UV-Vis spectra.

4.4 Conclusion

In this work, we demonstrated that worm-like micelles with a patch-like microphase-separated corona are highly versatile templates for the regio-selective incorporation of inorganic NPs. Introducing specific anchor groups in one of the corona patches allows to direct the incorporation of metal and metal oxide NPs exclusively in the functionalised patches, either by *in situ* synthesis of the NPs within the patches or by ligand exchange with preformed NPs. In addition, NPs that are stabilised by the same polymer as one of the corona patches can be selectively incorporated by co-precipitation employing selective solvents. Using a home-built microfluidic device, it was possible to perform a continuous *in situ*-loading of the patchy micelles with metal NPs, enabling a rapid screening of reaction parameters to optimise the loading process. The patchy corona of the worm-like micelles provides an excellent stabilisation of the incorporated NPs. This in turn results in a high and easily accessible catalytically active NP surface area, which is highly favourable for heterogeneous catalysis.[59] The combination of different loading strategies enabled the formation of binary loaded hybrid materials with two types of NPs placed in different

compartments of the patchy wCCM corona. These binary loaded hybrids might be promising materials for the development of heterogeneous catalysts, since the homogeneous distribution of the different NPs in the micellar corona ensures a high interface between the NPs. This could enhance synergistic effects on catalysis, as for example reported for the combination of ZnO and Au NPs.[83,84]

4.5 References

1   J.-F. Lutz, J.-M. Lehn, E. W. Meijer and K. Matyjaszewski, *Nat. Rev. Mater.*, 2016, **1**, 16024–16037.

2   J. Rodríguez-Hernández, F. Chécot, Y. Gnanou and S. Lecommandoux, *Prog. Polym. Sci.*, 2005, **30**, 691–724.

3   J.-F. Gohy, *Adv. Polym. Sci.*, 2005, **190**, 65–136.

4   Y. Mai and A. Eisenberg, *Chem. Soc. Rev.*, 2012, **41**, 5969–5985.

5   J. Dupont, G. Liu, K. I. Niihara, R. Kimoto and H. Jinnai, *Angew. Chem. Int. Ed.*, 2009, **48**, 6144–6147.

6   S. Zhong, H. Cui, Z. Chen, K. L. Wooley and D. J. Pochan, *Soft Matter*, 2008, **4**, 90–93.

7   I. S. Jo, S. Lee, J. Zhu, T. S. Shim and G. R. Yi, *Curr. Opin. Colloid Interface Sci.*, 2017, **30**, 97–105.

8   A. O. Moughton, M. A. Hillmyer and T. P. Lodge, *Macromolecules*, 2012, **45**, 2–19.

9   J. Du and R. K. O'Reilly, *Chem. Soc. Rev.*, 2011, **40**, 2402–2416.

10   A. Walther and A. H. E. Müller, *Chem. Rev.*, 2013, **113**, 5194–5261.

11   D. J. Pochan, J. Zhu, K. Zhang, K. L. Wooley, C. Miesch and T. Emrick, *Soft Matter*, 2011, **7**, 2500–2506.

12   D. J. Pochan, *Science*, 2004, **306**, 94–97.

13   H. Cui, Z. Chen, S. Zhong, K. L. Wooley and D. J. Pochan, *Science*, 2007, **317**, 647–650.

14   A. H. Gröschel and A. H. E. Müller, *Nanoscale*, 2015, **7**, 11841–11876.

15   U. Tritschler, S. Pearce, J. Gwyther, G. R. Whittell and I. Manners, *Macromolecules*, 2017, **50**, 3439–3463.

16   Z. Li, M. A. Hillmyer and T. P. Lodge, *Langmuir*, 2006, **22**, 9409–9417.

17   A. H. Gröschel, A. Walther, T. I. Löbling, F. H. Schacher, H. Schmalz and A. H. E. Müller, *Nature*, 2013, **503**, 247–251.

18   T. I. Löbling, O. Borisov, J. S. Haataja, O. Ikkala, A. H. Gröschel and A. H. E. Müller, *Nat. Commun.*, 2016, **7**, 12097–12106.

19   A. H. Gröschel and A. H. E. Müller, *Nanoscale*, 2015, **7**, 11841–11876.

20   J. Hu, G. Liu and G. Nijkang, *J. Am. Chem. Soc.*, 2008, **130**, 3236–3237.

21   F. H. Schacher, P. A. Rupar and I. Manners, *Angew. Chem. Int. Ed.*, 2012, **51**, 7898–7921.

22   R. K. O'Reilly, C. J. Hawker and K. L. Wooley, *Chem. Soc. Rev.*, 2006, **35**, 1068–1083.

23   T. H. Epps, III and R. K. O'Reilly, *Chem. Sci.*, 2016, **7**, 1674–1689.

24   J. Schmelz, F. H. Schacher and H. Schmalz, *Soft Matter*, 2013, **9**, 2101–2107.

25   X. Wang, G. Guerin, H. Wang, Y. Wang, I. Manners and M. A. Winnik, *Science*, 2007, **317**, 644–647.

26   J. B. Gilroy, T. Gädt, G. R. Whittell, L. Chabanne, J. M. Mitchels, R. M. Richardson, M. A. Winnik and I. Manners, *Nat Chem*, 2010, **2**, 566–570.

27   T. Gädt, N. S. Ieong, G. Cambridge, M. A. Winnik and I. Manners, *Nat. Mater.*, 2009, **8**, 144–150.

28   F. He, T. Gädt, I. Manners and M. A. Winnik, *J. Am. Chem. Soc.*, 2011, **133**, 9095–9103.

29   P. A. Rupar, L. Chabanne, M. A. Winnik and I. Manners, *Science*, 2012, **337**, 559–562.

30   J. Qian, Y. Lu, A. Chia, M. Zhang, P. A. Rupar, N. Gunari, G. C. Walker, G. Cambridge, F. He, G. Guerin, I. Manners and M. A. Winnik, *ACS Nano*, 2013, **7**, 3754–3766.

31   J. R. Finnegan, D. J. Lunn, O. E. C. Gould, Z. M. Hudson, G. R. Whittell, M. A. Winnik and I. Manners, *J. Am. Chem. Soc.*, 2014, **136**, 13835–13844.

32   Z. M. Hudson, D. J. Lunn, M. A. Winnik and I. Manners, *Nat. Commun.*, 2014, **5**, 3372–3379.

33   Z. M. Hudson, C. E. Boott, M. E. Robinson, P. A. Rupar, M. A. Winnik and I. Manners, *Nat. Chem.*, 2014, **6**, 893–898.

34   H. Qiu, Y. Gao, V. A. Du, R. Harniman, M. A. Winnik and I. Manners, *J. Am. Chem. Soc.*, 2015, **137**, 2375–2385.

35   H. Qiu, Z. M. Hudson, M. A. Winnik and I. Manners, *Science*, 2015, **347**, 1329–1332.

36   X. Li, Y. Gao, C. E. Boott, M. A. Winnik and I. Manners, *Nat. Commun.*, 2015, **6**, 8127–8134.

37   X. Li, Y. Gao, C. E. Boott, D. W. Hayward, R. Harniman, G. R. Whittell, R. M. Richardson, M. A. Winnik and I. Manners, *J. Am. Chem. Soc.*, 2016, **138**, 4087–4095.

38   H. Schmalz, J. Schmelz, M. Drechsler, J. Yuan, A. Walther, K. Schweimer and A. M. Mihut, *Macromolecules*, 2008, **41**, 3235–3242.

39   B. Fan, L. Liu, J.-H. Li, X.-X. Ke, J.-T. Xu, B.-Y. Du and Z.-Q. Fan, *Soft Matter*, 2016, **12**, 67–76.

40   L. Sun, A. Pitto-Barry, A. W. Thomas, M. Inam, K. Doncom, A. P. Dove and R. K. O'Reilly, *Polym. Chem.*, 2016, **7**, 2337–2341.

41   L. Sun, A. Pitto-Barry, N. Kirby, T. L. Schiller, A. M. Sanchez, M. A. Dyson, J. Sloan, N. R. Wilson, R. K. O'Reilly and A. P. Dove, *Nat. Commun.*, 2014, **5**, 5746–5754.

42   J. Qian, X. Li, D. J. Lunn, J. Gwyther, Z. M. Hudson, E. Kynaston, P. A. Rupar, M. A. Winnik and I. Manners, *J. Am. Chem. Soc.*, 2014, **136**, 4121–4124.

43   J. Li, X. Li, D. Ni, J. Wang, G. Tu and J. Zhu, *J. Appl. Polym. Sci.*, 2014, **131**, 41186–41196.

44   G. Rizis, T. G. M. van de Ven and A. Eisenberg, *Soft Matter*, 2014, **10**, 2825–2835.

45   J. Wang, W. Zhu, B. Peng and Y. Chen, *Polymer*, 2013, **54**, 6760–6767.

46   J. Schmelz, M. Karg, T. Hellweg and H. Schmalz, *ACS Nano*, 2011, **5**, 9523–9534.

47   S. Rosenfeldt, F. Lüdel, C. Schulreich, T. Hellweg, A. Radulescu, J. Schmelz, H. Schmalz and L. Harnau, *Phys. Chem. Chem. Phys.*, 2012, **14**, 12750–12756.

48   J. Schmelz, A. E. Schedl, C. Steinlein, I. Manners and H. Schmalz, *J. Am. Chem. Soc.*, 2012, **134**, 14217–14225.

49   Y. Mai and A. Eisenberg, *Acc. Chem. Res.*, 2012, **45**, 1657–1666.

50   S. Suárez-Suárez, G. A. Carriedo and A. P. Soto, *Chem. Eur. J.*, 2015, **21**, 14129–14139.

51   B. Nandan and A. Horechyy, *ACS Appl. Mater. Interfaces*, 2015, **7**, 12539–12558.

52   M. Changez, N.-G. Kang, D. W. Kim and J.-S. Lee, *Nanoscale*, 2013, **5**, 11554–11560.

53   K. H. Ku, J. M. Shin, M. P. Kim, C. H. Lee, M. K. Seo, G. R. Yi, S. G. Jang and B. J. Kim, *J. Am. Chem. Soc.*, 2014, **136**, 9982–9989.

54   F. Schacher, E. Betthausen, A. Walther, H. Schmalz, D. V. Pergushov and A. H. E. Müller, *ACS Nano*, 2009, **3**, 2095–2102.

55   R. J. Hickey, Q. Luo and S. J. Park, *ACS Macro Lett.*, 2013, **2**, 805–808.

56   M. P. Kim, K. H. Ku, H. J. Kim, S. G. Jang, G. R. Yi and B. J. Kim, *Chem. Mater.*, 2013, **25**, 4416–4422.

57   A. Walther, J. Yuan, V. Abetz and A. H. E. Müller, *Nano Lett.*, 2009, **9**, 2026–2030.

58   Y. Guo, S. Harirchian-Saei, C. M. S. Izumi and M. G. Moffitt, *ACS Nano*, 2011, **5**, 3309–3318.

59   J. Schöbel, M. Burgard, C. Hils, R. Dersch, M. Dulle, K. Volk, M. Karg, A. Greiner and H. Schmalz, *Angew. Chem. Int. Ed.*, 2017, **56**, 405–408.

60   H. Wang, W. Lin, K. P. Fritz, G. D. Scholes, M. A. Winnik and I. Manners, *J. Am. Chem. Soc.*, 2007, **129**, 12924–12925.

61   H. Cui, Z. Chen, S. Zhong, K. L. Wooley and D. J. Pochan, *Science*, 2007, **317**, 647–650.

62   H. Wang, X. Wang, M. A. Winnik and I. Manners, *J. Am. Chem. Soc.*, 2008, **130**, 12921–12930.

63   H. Wang, A. J. Patil, K. Liu, S. Petrov, S. Mann, M. A. Winnik and I. Manners, *Adv. Mater.*, 2009, **21**, 1805–1808.

64   F. H. Schacher, T. Rudolph, M. Drechsler and A. H. E. Müller, *Nanoscale*, 2011, **3**, 288–297.

65   S. G. Jang, D. J. Audus, D. Klinger, D. V. Krogstad, B. J. Kim, A. Cameron, S. W. Kim, K. T. Delaney, S. M. Hur, K. L. Killops, G. H. Fredrickson, E. J. Kramer and C. J. Hawker, *J. Am. Chem. Soc.*, 2013, **135**, 6649–6657.

66   L. Jia, G. Zhao, W. Shi, N. Coombs, I. Gourevich, G. C. Walker, G. Guerin, I. Manners and M. A. Winnik, *Nat. Commun.*, 2014, **5**, 3882–3889.

67   S. H. Jo, H. W. Kim, M. Song, N. J. Je, S. H. Oh, B. Y. Chang, J. Yoon, J. H. Kim, B. Chung and S. Il Yoo, *ACS Appl. Mater. Interfaces*, 2015, **7**, 18778–18785.

68   S. Mei, J. Cao and Y. Lu, *J. Mater. Chem. A*, 2015, **3**, 3382–3389.

69   J. Schöbel, M. Karg, D. Rosenbach, G. Krauss, A. Greiner and H. Schmalz, *Macromolecules*, 2016, **49**, 2761–2771.

70   C. Bojer, J. Schöbel, T. Martin, M. Ertl, H. Schmalz and J. Breu, *Appl. Catal. B Environ.*, 2017, **204**, 561–565.

71   T. Kida, T. Oka, M. Nagano, Y. Ishiwata and X. G. Zheng, *J. Am. Ceram. Soc.*, 2007, **90**, 107–110.

72   J. Piella, N. G. Bastús and V. Puntes, *Chem. Mater.*, 2016, **28**, 1066–1075.

73   G. Moad, J. Chiefari, Y. K. Chong, J. Krstina, R. T. A. Mayadunne, A. Postma, E. Rizzardo and S. H. Thang, *Polym. Int.*, 2000, **49**, 993–1001.

74   A. C. Henry, T. J. Tutt, M. Galloway, Y. Y. Davidson, C. S. McWhorter, S. A. Soper and R. L. McCarley, *Anal. Chem.*, 2000, **72**, 5331–5337.

75   S. Ehlert, S. M. Taheri, D. Pirner, M. Drechsler, H. W. Schmidt and S. Förster, *ACS Nano*, 2014, **8**, 6114–6122.

76   M. R. Jones, K. D. Osberg, R. J. MacFarlane, M. R. Langille and C. A. Mirkin, *Chem. Rev.*, 2011, **111**, 3736–3827.

77   S. W. B. Schonecker, *Makromol. Chem.*, 1996, **338**, 759–762.

78   N. R. Jana, L. Gearheart and C. J. Murphy, *Langmuir*, 2001, **17**, 6782–6786.

79   H. Pletsch, L. Peng, F. Mitschang, A. Schaper, M. Hellwig, D. Nette, A. Seubert, A. Greiner and S. Agarwal, *Small*, 2014, **10**, 201–208.

80   A. Henglein, B. G. Ershov and M. Malow, *J. Phys. Chem.*, 1995, **99**, 14129–14136.

81   G. M. Whitesides, *Nature*, 2006, **442**, 368–373.

82   R. Karnik, F. Gu, P. Basto, C. Cannizaro, L. Dean, W. Kyei-Manu, R. Langer and O. C. Farokhzad, *Nano Lett.*, 2008, **8**, 2906–2912.

83   C. Bojer, J. Schöbel, T. Martin, T. Lunkenbein, D. R. Wagner, A. Greiner, J. Breu and H. Schmalz, *Polymer*, 2017, **128**, 65–70.

84   L. Sun, D. Zhao, Z. Song, C. Shan, Z. Zhang, B. Li and D. Shen, *J. Colloid Interface Sci.*, 2011, **363**, 175–181.

4.6 Supporting Information

Characterisation of ZnO NP and CuO NP

The ZnO and CuO NPs were analysed by powder X-Ray diffraction to confirm the phase purity (Fig. S4-1A). For both types of NPs, the measured peaks can be clearly assigned to ZnO (PDF: 00-036-1451) and CuO (PDF: 45-0937), respectively. For CuO NPs, only the two most intense peaks can be found as reported by Kida et. al.[1] The peaks of both NP types show a high full width at half maximum (FWHM), confirming the formation of NPs. Dynamic light scattering (DLS) yields in narrow particle size distributions (Fig. S4-1B) with average hydrodynamic diameters of 3.2 ±0.1 nm for ZnO and 5.8 ±1.4 nm for CuO NPs, respectively. From TEM image analysis (Fig. S4-1C, D) average diameters of 2.7 ± 0.4 nm for ZnO NPs and 3.8 ± 0.6 nm for CuO NPs were obtained. As expected, the sizes from DLS are slightly higher compared to that determined by TEM, as DLS probes the hydrodynamic diameters.
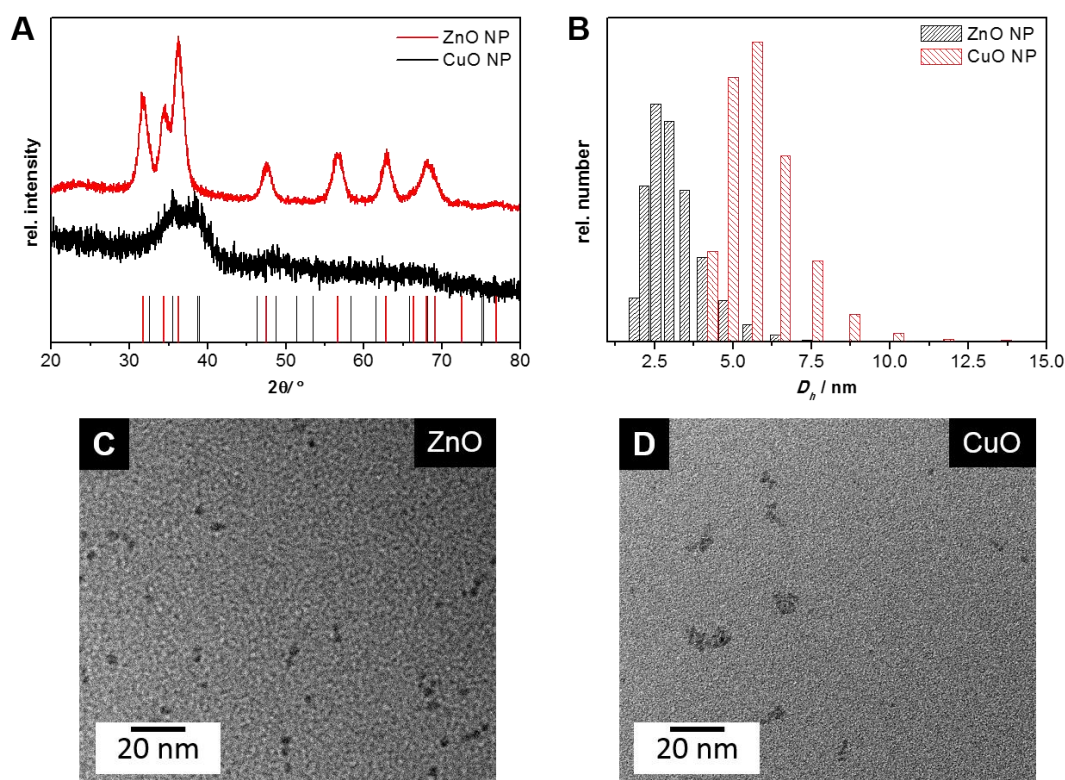
Fig. S4-1. PXRD pattern (A), particle size distribution obtained from DLS measurements (B) and TEM micrographs of the ZnO and CuO NPs (C, D).

Characterisation of citrate-stabilised Au NPs

Au NPs were synthesised according to a seeded-growth protocol by Piella et al.[2] In a first batch, citrate-stabilised seed particles ($D = 4 \pm 0.6$ nm) were produced. In two consecutive steps, these seed particles were grown to $D = 7.9 \pm 0.7$ nm, as revealed by TEM (Fig. S4-2A, B). These spherical Au NPs showed a characteristic LSPR at $\lambda_{max} = 515$ nm (Fig. S4-2C).
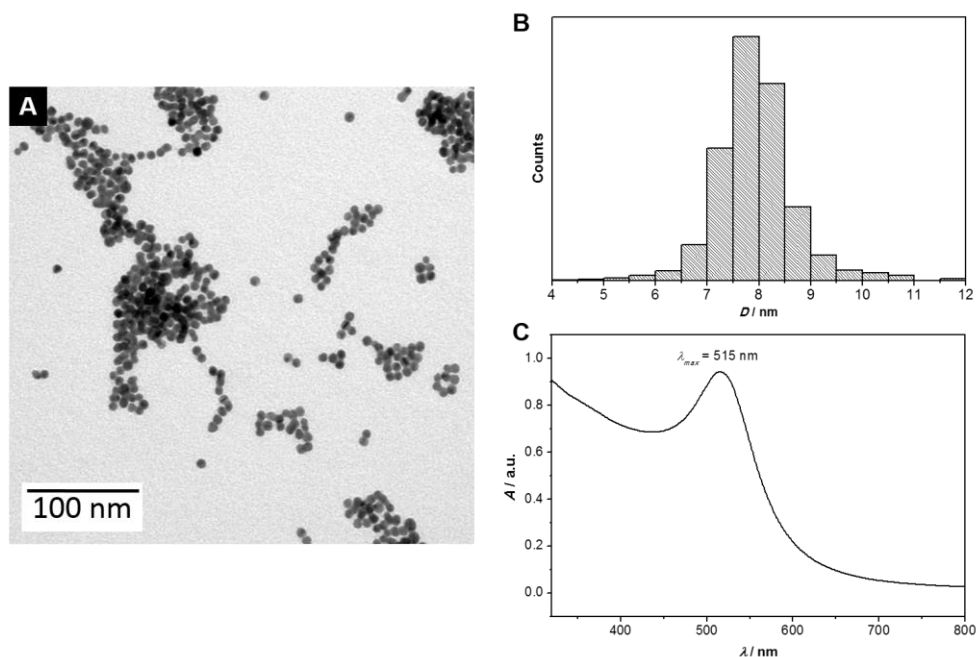

Fig. S4-2. TEM micrograph (A), size distribution (B) and UV-Vis spectrum in water (C) of citrate-stabilised AuNPs.

Characterisation of trithiocarbonate-terminated PS

Trithiocarbonate-terminated PS (PS-TTC) was synthesised by reversible addition-fragmentation chain transfer (RAFT) polymerisation according to a protocol of Moad et al.[3] To this end, styrene and 2-cyano-2-propyl dodecyl trithiocarbonate (8.55 mM L^{-1}) were mixed in a ratio of 169:1. The reaction mixture was degassed for 20 min with nitrogen and subsequently heated to 110 °C for 46 h in an oil bath. The polymerisation was terminated by quenching to 0 °C with an ice bath. The product was dissolved in THF and precipitated from cold methanol.

The molecular weight of the trithiocarbonate-terminated PS was determined by THF GPC to $M_n = 10.4$ kg mol^{-1} with a dispersity of $Đ = 1.05$ (Fig. S4-3A). The monomodal distribution and the low dispersity prove the controlled polymerisation of styrene. The UV-

Vis spectrum shows the typical absorbance of the PS-TTC. The PS shows an absorbance maximum at about $\lambda = 250$ nm, whereas the TTC end group shows a maximum at $\lambda = 315$ nm (Fig. S4-3B).
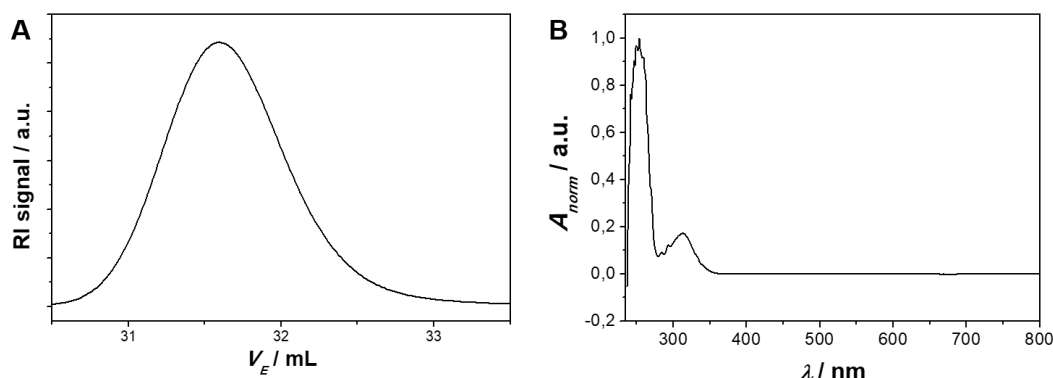
Fig. S4-3. THF GPC trace (A) and UV-Vis spectrum of PS-TTC ($c = 0.1$ mg mL^{-1} in chloroform, (B)).

Characterisation of PS-stabilised Au NP

DMF GPC using a UV-Vis diode-array-detector was performed to show whether the PS ligands are completely bound to the Au NP surface or if free PS ligands are still present (Fig. S4-4A). Two different wavelengths were selected for detection, being characteristic for the PS ligand ($\lambda = 270$ nm) as well as the Au NPs ($\lambda = 525$ nm). The peak elution volume of the Au NPs is at $V_E = 19$ min (detection at $\lambda = 525$ nm). The corresponding GPC trace for $\lambda = 270$ nm, i.e. specific to PS, shows a bimodal distribution. The main peak at $V_E = 19$ min corresponds to the PS ligands bound to the Au NPs´ surface and the minor peak at $V_E = 23$ min to some residual free PS ligands. Dynamic light scattering (DLS) results in an average hydrodynamic radius of $R_h = 14.7 \pm 0.1$ nm, proving the PS shell around the Au NPs (Fig. S4-4B). The small standard deviation indicates the absence of agglomerates in solution.
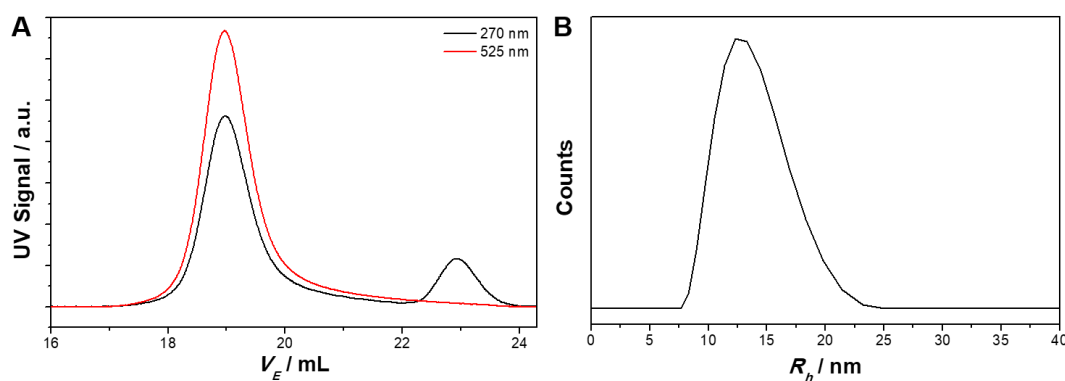
Fig. S4-4. DMF GPC traces (A) and particle size distribution obtained by DLS (B) of PS@Au NPs.

Determination of Au NP concentration

The concentration of the PS@Au NPs in the final toluene dispersion was determined using a method reported by Hendel et al.[4] To this end, the absorbance of the PS@Au NP dispersion at 400 nm before normalisation of the spectrum and the corresponding dilution factor f were used to calculate the concentration of elemental Au (equation 1).

$$[Au] = \frac{A_{400} \cdot f \cdot 1.25 \cdot 10^{-4} \; mol \; L^{-1}}{0.3} \tag{1}$$

The absorbance measured for the PS@Au NP in toluene was $A_{400} = 0.5584$ with a dilution factor of $f = 60$. To calculate the concentration of Au NPs in the dispersion, the radius of the Au NPs from TEM measurements ($R_{TEM} = 4$ nm), the molar mass of Au ($M_{Au} = 196.97$ g mol^{-1}) and the density of Au ($\rho_{Au} = 19.3 \cdot 10^6$ g m^{-3}) is needed. Equation 2 is used to calculate the final Au NP concentration.

$$[Au \; NP] = \frac{[Au] \cdot M_{Au}}{\frac{4}{3} \cdot R_{TEM}^3 \cdot \pi \cdot \rho_{Au}} \tag{2}$$

This yields in an Au NP concentration of $[Au \; NP] = 5.3 \cdot 10^{17}$ NP L^{-1}.

Characterisation of the amidated PMMA homopolymer
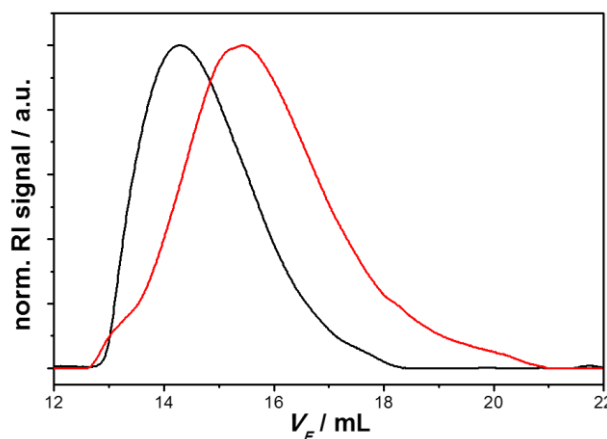
Fig. S4-5. HFIP GPC traces of PMMA (red) and amidated PMMA (black).

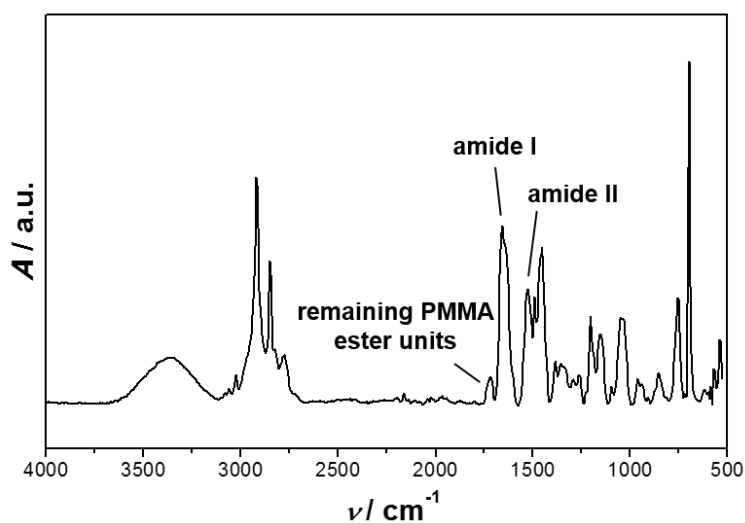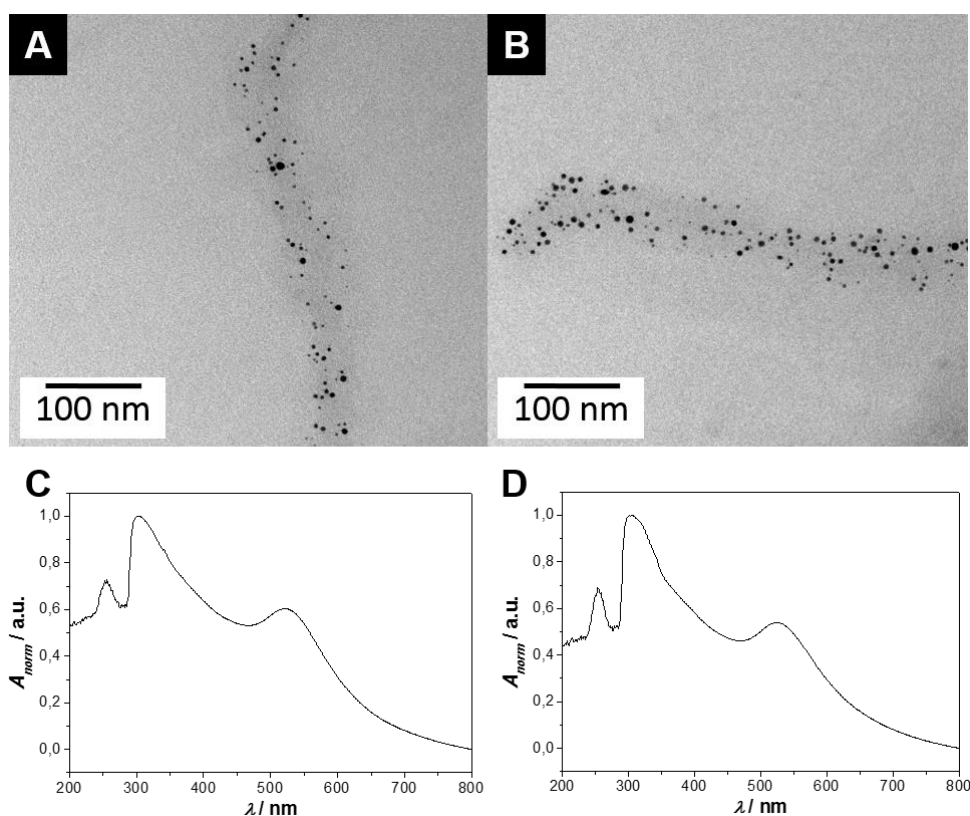**Characterisation of the SEDMA triblock terpolymer**

Fig. S4-6. FT-IR spectrum of SEDMA.

9. Continuous loading of SEDMA wCCMs

Fig. S4-7. TEM micrographs and UV-Vis spectra of SEDMA wCCMs loaded in a continuous microfluidic process at different flow rates: (A) wCCMs: 2000 µL h^{-1}, HAuCl$_4$·3H$_2$O: 1000 µL h^{-1}, L-Selectride: 1000 µL h^{-1}; (B) wCCMs: 1000 µL h^{-1}, HAuCl$_4$·3H$_2$O: 500 µL h^{-1}, L-Selectride: 500 µL h^{-1}.

Aggregation behaviour of PS@Au NP
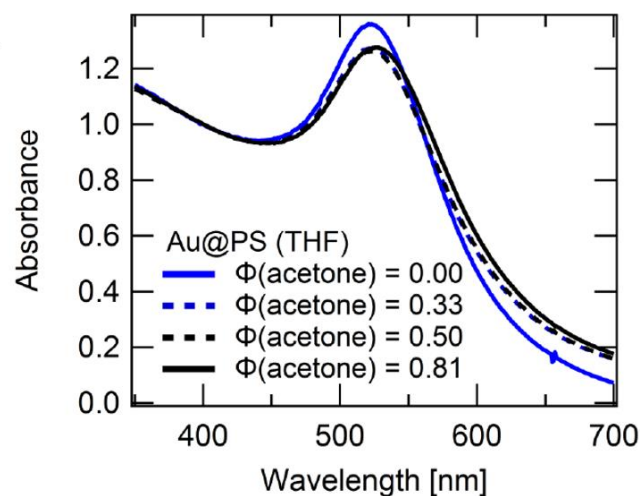
Fig. S4-8. UV-Vis spectra of PS@Au NPs in different solvent mixtures of THF and acetone.

References

1   T. Kida, T. Oka, M. Nagano, Y. Ishiwata and X. G. Zheng, *J. Am. Ceram. Soc.*, 2007, **90**, 107–110.

2   J. Piella, N. G. Bastús and V. Puntes, *Chem. Mater.*, 2016, **28**, 1066–1075.

3   G. Moad, J. Chiefari, Y. K. Chong, J. Krstina, R. T. A. Mayadunne, A. Postma, E. Rizzardo and S. H. Thang, *Polym. Int.*, 2000, **49**, 993–1001.

4   T. Hendel, M. Wuithschick, F. Kettemann, A. Birnbaum, K. Rademann and J. Polte, *Anal. Chem.*, 2014, **86**, 11115–11124.

# 5 Bottom-up Meets Top-down: Patchy Hybrid Nonwovens as Efficient Catalysis Platform

*Judith Schöbel,[a], † Matthias Burgard,[a], † Christian Hils,[a] Roland Dersch,[a] Martin Dulle,[b] Kirsten Volk,[b] Matthias Karg,[b], ‡ Andreas Greiner,[a], * Holger Schmalz[a], ***

[a] Makromolekulare Chemie II, Universität Bayreuth, 95440 Bayreuth, Germany

[b] Physikalische Chemie I, Universität Bayreuth, 95440 Bayreuth, Germany

[†] The authors contributed equally to this work.

[‡] present address: Physikalische Chemie I, Heinrich-Heine-Universität Düsseldorf, 40204 Düsseldorf, Germany
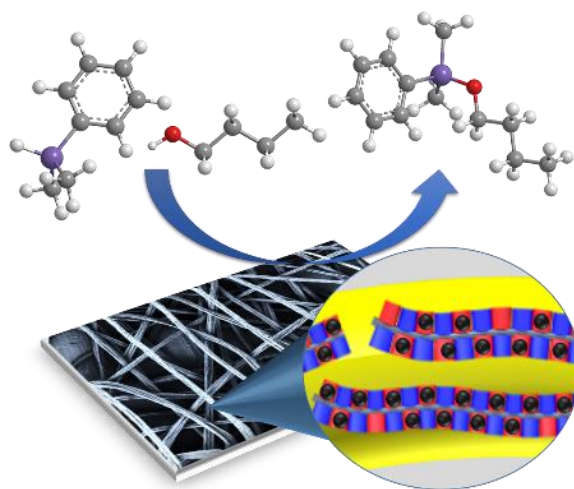
Abstract

Heterogeneous catalysis with supported nanoparticles (NPs) is a highly active field of research. However, the efficient stabilization of NPs without deteriorating their catalytic activity is challenging. By combining top-down (coaxial electrospinning) and bottom-up (crystallization-driven self-assembly) approaches, we prepared patchy nonwovens with functional, nanometer-sized patches on the surface. These patches can selectively bind and efficiently stabilize gold nanoparticles (AuNPs). The use of these AuNP-loaded patchy nonwovens in the alcoholysis of dimethylphenylsilane led to full conversion under comparably mild conditions and in short reaction times. The absence of gold leaching or a slowing down of the reaction even after ten subsequent cycles manifests the excellent reusability of this catalyst system. The flexibility of the presented approach allows for easy transfer to other nonwoven supports and catalytically active NPs, which promises broad applicability.

The unique properties of metal nanoparticles (NPs) pave the way for various multidisciplinary applications, for example, in catalysis, drug delivery, or optoelectronic devices.[1] For decades, gold was considered as a poor catalyst because of its use in the bulk state. In the 1970s, first studies showed that AuNPs are able to catalyze hydrogenation reactions owing to their high surface-to-volume ratios.[2,3] Since then, research on AuNPs has gained increasing attention in the field of catalysis, for example, for CO oxidation, alkyne hydrogenation, or nitrophenol reduction.[2,4] To preserve the excellent catalytic activity, NP aggregation, and hence a loss of surface area, needs to be efficiently prevented.[5] At the same time, however, the AuNPs can only be reused if they can be efficiently separated from the reaction mixture after the catalysis. Supported heterogeneous catalysts provide an ideal platform to fulfill these requirements, as has been shown for AuNPs supported on transition-metal oxides, carbon, or polymers, for example.[6] NPs immobilized in spherical polyelectrolyte brushes (SPBs) show excellent catalytic activity and reusability but can only be used in aqueous media because of the solubility of the SPBs.[7] Other studies dealt with metal-organic frameworks (MOFs) as host materials, which can be used in organic solvents; however, with these systems, catalyst recovery and reusability are limited.[8] The immobilization of NPs on the surface of nanofibers enables their use in different reaction media as the polymer template can be removed by heat treatment.[9,10] A facile separation and reusability of the catalytically active nonwoven is realizable but these hybrid nonwovens lack in a precise confinement of the NPs as the template removal leads to sintering of the NPs, which reduces the surface-to-volume ratio.

Herein, we present a versatile approach towards patchy hybrid nonwovens as efficient catalysis platform, utilizing coaxial electrospinning as a precise top-down coating technique (Scheme 5-1 A).[10,11] The fiber core consists of polystyrene (PS) and acts as carrier for functional, patchy worm-like crystalline-core micelles (wCCMs) forming the shell. The patchy wCCMs were produced by crystallization-driven self-assembly (CDSA, "bottom-up"), which is a versatile method for the formation of well-defined cylindrical micelles.[12] Owing to the living nature of CDSA, this method provides access to cylindrical micelles of defined length and length dispersity,[13] as well as to a variety of complex micellar architectures and superstructures.[14] In this work, patchy wCCMs with a semicrystalline polyethylene (PE) core and a corona consisting of alternating nanometer-sized PS and functional, diisopropylamino-group containing patches were employed. To this end, the poly(methyl methacrylate) block of a polystyrene-*block*-polyethylene-*block*-poly(methyl

methacrylate) (SEM) triblock terpolymer was functionalized by post-polymerization modification to introduce the diisopropylamino groups. The functional, patchy wCCMs were then prepared by dissolving the triblock terpolymer in THF above the melting point of the semicrystalline PE block followed by cooling to induce CDSA (for a more detailed description of the wCCM preparation, see the Supporting Information).[15,16] The PS patches guarantee a good adhesion of the wCCMs to the PS core fiber, and the functional corona patches with the diisopropylamino groups were tailored for efficient AuNP binding. In the next step, the patchy nonwovens were loaded with preformed citrate-stabilized AuNPs by a facile dipping method (Scheme 5-1 B). The patchy structure of the surface of the nonwovens leads to spatial separation of the embedded AuNPs ("nanoconfinement"), which efficiently prevents aggregation and thus ensures a large catalytically active surface area.
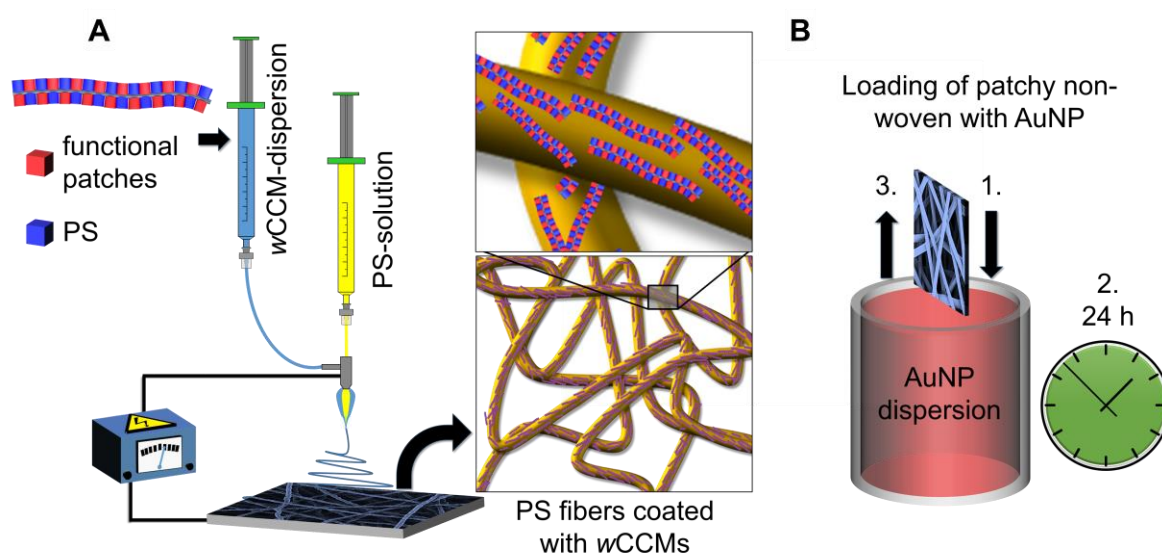
Scheme 5-1. Preparation of catalytically active hybrid nonwovens: functional, patchy nonwovens are produced by coaxial electrospinning of PS (core, yellow) and wCCMs (shell, blue) (A), followed by loading with AuNPs by a simple dipping process (B).

The use of a carrier material is indispensable for the preparation of patchy nonwovens by coaxial electrospinning as neat wCCM dispersions tend to form particles ("electrospraying") in conventional electrospinning processes. To this end, high-molecular-weight PS (M_n=1.4×10^6 g mol^{-1}) was used as it forms well-defined, bead-free, and comparably thin fibers under the conditions (low applied voltage) employed for coaxial electrospinning (for details see the Supporting Information). The neat electrospun PS nanofibers have an average diameter of D=1.2±0.2 μm and exhibit a rather rough surface structure as revealed by scanning electron microscopy (SEM; Figure 5-1 A).
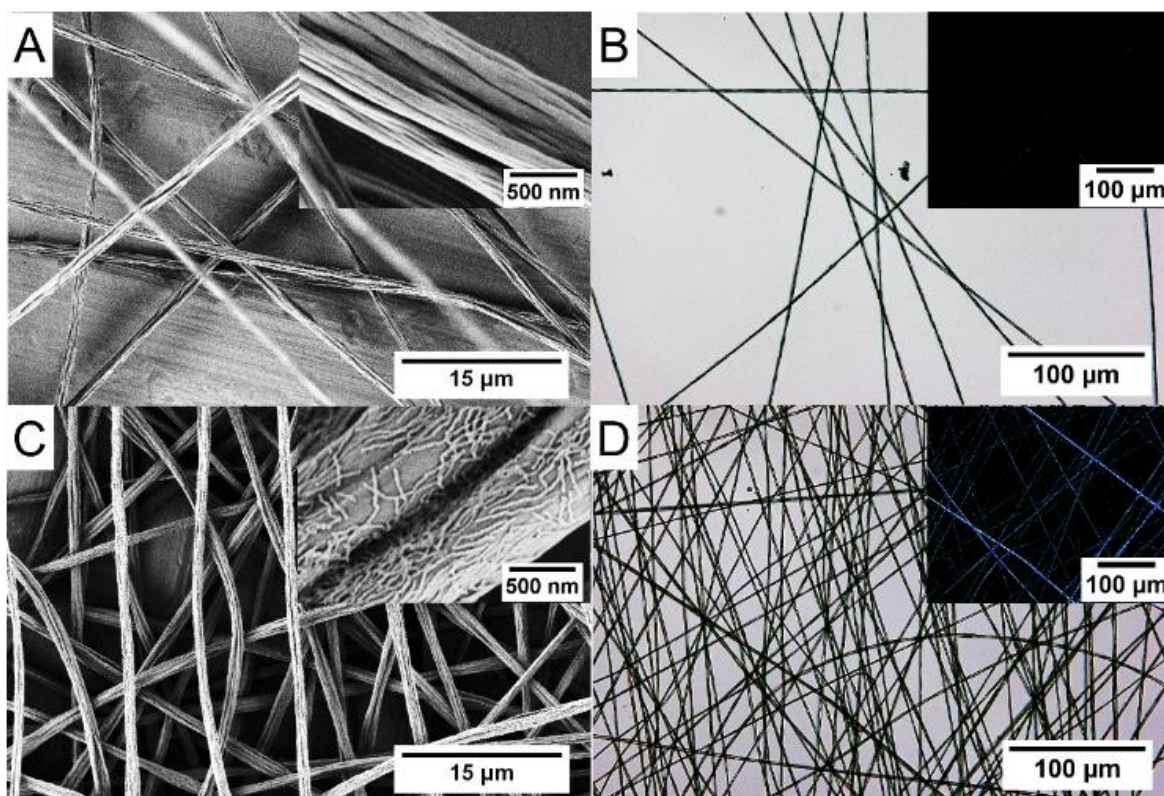
Figure 5-1. SEM and optical micrographs of a neat PS (A, B) and a patchy nonwoven (C, D). The insets in B) and D) show polarized optical microscopy images.

Upon coaxial electrospinning, the morphology of the fibers changes significantly as they appear smoother in comparison to the neat PS fibers, and the wCCMs are clearly observable on the surface of the fibers (Figure 5-1 C). The length of the wCCMs determined from SEM ($L=470\pm210$ nm) is in good agreement with the wCCM length in the initial dispersion used for electrospinning ($L=500\pm155$ nm), as determined by transmission electron microscopy (see the Supporting Information, Figure S5-1). This result confirms the stability of the wCCMs during the electrospinning process. The preferential orientation of the wCCMs along the long axis of the PS fibers is a result of shear forces during electrospinning. Polarized optical microscopy confirmed the successful coating of the PS fibers with wCCMs (Figure 5-1 B, D). In contrast to the neat amorphous PS fibers, the wCCM-coated fibers show distinct birefringence, which was attributed to the semicrystalline PE core of the wCCMs on the fiber surface. This was further supported by the presence of characteristic bands for the wCCMs in the corresponding FTIR spectrum of the patchy nonwoven (Figure S5-2).

Next, the patchy nonwoven was loaded with AuNPs (Scheme 5-1 B and Figure 5-2 A) by dipping into an aqueous dispersion of preformed citrate-stabilized AuNPs (Figure S5-3,

D=11±3 nm), prepared by a method reported by Schaal and co-workers.[17] The discoloration of the aqueous AuNP dispersion and the corresponding red-purple color of the patchy nonwoven indicate successful loading with the AuNPs. The tertiary amino group containing patches of the wCCMs stabilize the AuNPs as amines are well known as efficient anchor groups in AuNP synthesis.[16] We assume that the strong binding of the AuNPs to the patchy nonwovens is mainly due to replacement of the citrate ligands by the multidentate, amino-group containing patches, as under the employed conditions (AuNP dispersion shows a pH of 8), electrostatic interactions might be neglected as the amino groups in the functional patches are uncharged.
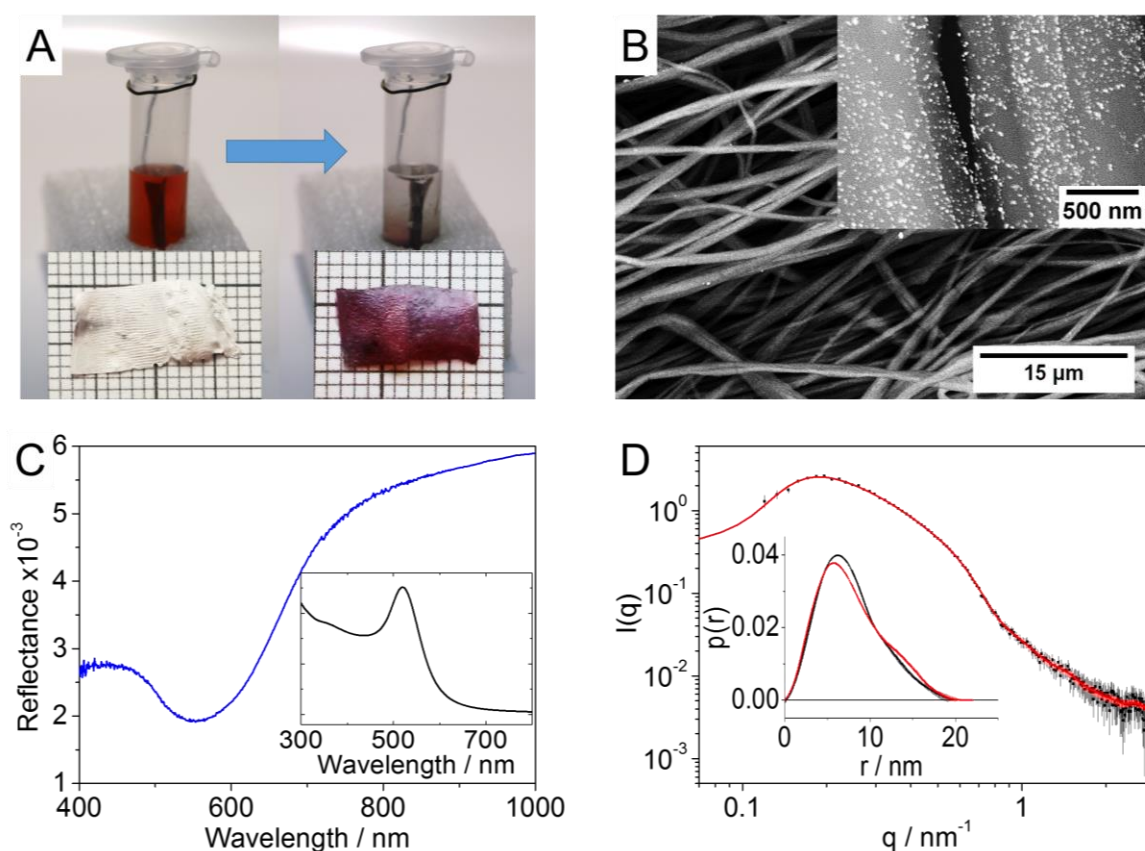
Figure 5-2. A) Loading of a patchy nonwoven with AuNPs by dipping into an aqueous AuNP dispersion. B) SEM micrographs of a AuNP loaded patchy nonwoven analyzed with a backscattered electron detector; the AuNPs appear as bright dots. C) UV-Vis reflectance spectrum of the AuNP loaded patchy nonwoven. Inset: UV-Vis absorbance spectrum of the employed aqueous, citrate-stabilized AuNP dispersion. D) SAXS profiles (black) of the AuNPs immobilized in the patchy nonwoven and the corresponding GIFT fitting function (red). Inset: PDDF of AuNPs in the patchy nonwoven (red) and in the corresponding aqueous dispersion (black).

The AuNPs immobilized on the surface of the patchy nonwoven are well separated, as revealed by SEM using a backscattered electron detector (Figure 5-2 B). Here, the AuNPs appear bright as they feature a higher scattering intensity than the polymeric fibers. In contrast, loading a patchy nonwoven with poly(methyl methacrylate) patches instead of functional patches (the nonwoven is decorated with SEM wCCMs) leads to the formation of AuNP aggregates on the surface of the nonwoven (Figure S5-4). The UV/Vis reflectance spectrum of the patchy hybrid nonwoven shows a well-defined localized surface plasmon resonance (LSPR) at $\lambda=550$ nm, further supporting the presence of homogeneously distributed AuNPs (Figure 5-2 C). The relatively large red shift of 30 nm compared to the LSPR in solution ($\lambda=520$ nm) can be explained by changes in the surrounding refractive index and weak plasmon resonance coupling with AuNPs in close proximity. The presence of plasmon resonance coupling is also supported by the slightly broadened resonance peak as compared to the LSPR of the AuNPs in dispersion. This is reasonable as the inter-particle distance of the AuNPs on the surface of the patchy nonwoven is predefined by the patch size of the wCCMs (14 ± 3 nm), which is in the range of the size of the AuNPs ($D=11\pm3$ nm, Figure S5-3). Hence, we expect that at least a fraction of the adsorbed AuNPs will have inter-particle distances in the order of a few nanometers. At such short distances, plasmon resonance coupling will occur and contribute to the spectrum.

The AuNP-loaded nonwoven was further characterized by small-angle X-ray scattering (SAXS). The SAXS data of the aqueous AuNP dispersion as well as the patchy nonwoven before and after loading can be found in Figure S5-5 and S5-6, respectively. The scattering data of the NP dispersion showed no indication of the presence of NP aggregates. The data can be well described by a form factor fit using a simple model for polydisperse spherical particles, providing a particle diameter of $D_{SAXS}=11\pm2.2$ nm (Figure S5-5). This value agrees very well with that obtained from the TEM analysis ($D=11\pm3$ nm, Figure S5-3).[18] The scattering intensity of the AuNPs immobilized in the patchy nonwoven (Figure 5-2 D) was extracted by subtracting the scattering intensity of the AuNP-loaded nonwoven from that of the neat patchy nonwoven (see the Supporting Information for details). The scattering of the embedded AuNPs showed no sign of aggregation, which would be apparent by a steep increase in scattering intensity towards lower q values. On the contrary, it even showed a small decline. This decline could stem from the close proximity of the NPs on the surface of the patchy nonwoven and can be interpreted as a structure factor contribution to the scattering curve. With the use of the GIFT routine,[19] we determined the pair distance

distribution function (PDDF) of the embedded NPs as well as an apparent structure factor. To compare the AuNPs before and after incorporation, we also calculated the PDDF of the dispersion. The PDDFs of the AuNPs before and after incorporation are virtually identical, which shows that the AuNPs are still well dispersed and separated after immobilization on the functional patchy surface of the nonwoven. The mean center-to-center distance, obtained from the structure factor peak, is 15.1 nm and fits well with the domain size of the patchy micelles (14±3 nm). This finding strengthens our claim that the NPs sit on individual patches on the surface of the fibers and are accessible for catalysis.

We studied the catalytic activity of the AuNP-loaded nonwoven in the alcoholysis of dimethylphenylsilane with *n*-butanol as the model reaction (Figure 5-3 A). Using AuNPs supported on aluminum oxide (*D*=3-4 nm, 0.05 mol % Au with respect to the silane), a conversion of 99 % was previously reported under rather harsh conditions (3 h at 100 °C).[20] A significant improvement could be achieved with a teabag-like catalyst system consisting of AuNPs immobilized in poly(*para*-xylylene) tubes, showing quantitative conversion after 26 h at room temperature (6.6 mol % Au with respect to the silane).[21]
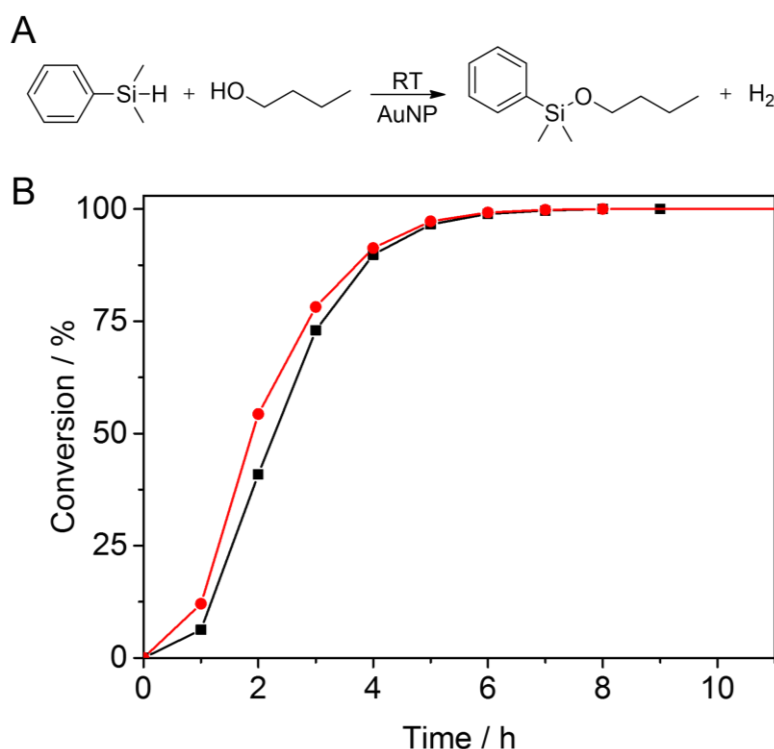
Figure 5-3. A) Catalytic alcoholysis of dimethylphenylsilane with *n*-butanol. B) Corresponding reaction kinetics using an AuNP loaded patchy nonwoven as catalyst (cycle 1: black; cycle 10: red).

Using a AuNP-loaded patchy nonwoven (10×10 mm, 720 µg; 41 µg Au, 0.1 mol % Au with respect to the silane) quantitative conversion of dimethylphenylsilane at room temperature was already observed after 7 h (Figure 5-3 B; see the Supporting Information for experimental details). This is significantly faster compared to the reaction times reported in the literature[21] even though the amount of Au used is about 70 times lower. This is attributed to the high accessibility of the well separated AuNPs on the patchy nonwoven surface, which prevents diffusion limitations and provides a high catalytically active surface area. It should be noted that the patchy nonwoven was preswollen in *n*-butanol prior to catalysis as this turned out to significantly increase the reaction rate (Figure S5-7). Even after ten cycles, the catalytic activity remained almost constant. The leaching of gold from the nonwoven during catalysis is effectively prevented as confirmed by inductively coupled plasma optical emission spectrometry (ICP-OES) studies.

Herein, we have presented AuNP-loaded patchy nonwovens that were prepared by combining top-down (coaxial electrospinning) and bottom-up (crystallization-driven self-assembly) approaches as a highly efficient and reusable catalysis platform. This system showed superior stability and performance in the catalytic alcoholysis of dimethylphenylsilane, which was attributed to the immobilization of the AuNPs within the functional patches of the nonwoven ("nanoconfinement"), which efficiently stabilizes the NPs while not reducing their catalytic activity. The modular design of this catalysis platform allows for facile modification of the supporting nonwoven, which can be rendered hydrophilic, thermally stable, or elastic, for example. Furthermore, the functionality of the patchy wCCMs coated on the fiber surface can be tailored to meet the demands with respect to stabilization of the incorporated NPs. This should enable the selective incorporation of NPs of various types, shapes, and sizes for application in heterogeneous catalysis, which will be the focus of further studies.

References

[1]   a) P. Herves, M. Perez-Lorenzo, L. M. Liz-Marzan, J. Dzubiella, Y. Lu, M. Ballauff, *Chem. Soc. Rev.* **2012**, *41*, 5577–5587; b) S. Kango, S. Kalia, A. Celli, J. Njuguna, Y. Habibi, R. Kumar, *Prog. Polym. Sci.* **2013**, *38*, 1232–1261.

[2]   M. Haruta, *Chem. Rec.* **2003**, *3*, 75–87.

[3]   C. Burda, X. Chen, R. Narayanan, M. A. El-Sayed, *Chem. Rev.* **2005**, *105*, 1025–1102.

[4]   M. Daté, M. Okumura, S. Tsubota, M. Haruta, *Angew. Chem., Int. Ed.* **2004**, *43*, 2129–2132; *Angew. Chem.* **2004**, *116*, 2181-2184.

[5]   A. Cao, R. Lu, G. Veser, *Phys. Chem. Chem. Phys.* **2010**, *12*, 13499–13510.

[6]   a) D. Astruc, F. Lu, J. R. Aranzaes, *Angew. Chem., Int. Ed.* **2005**, *44*, 7852–7872; *Angew. Chem.* **2005**, *117*, 8062–8083; b) M. Stratakis, H. Garcia, *Chem. Rev.* **2012**, *112*, 4469–4506.

[7]   Y. Lu, M. Ballauff, *Prog. Polym. Sci.* **2016**, *59*, 86–104.

[8]   A. Dhakshinamoorthy, H. Garcia, *Chem. Soc. Rev.* **2012**, *41*, 5262–5284.

[9]   C.-L. Zhang, S.-H. Yu, *Chem. Soc. Rev.* **2014**, *43*, 4423–4448.

[10]   S. Agarwal, A. Greiner, J. H. Wendorff, *Prog. Polym. Sci.* **2013**, *38*, 963–991.

[11]   A. Greiner, J. H. Wendorff, *Angew. Chem., Int. Ed.* **2007**, *46*, 5670–5703; *Angew. Chem.* **2007**, *119*, 5770–5805.

[12]   J. Schmelz, F. H. Schacher, H. Schmalz, *Soft Matter* **2013**, *9*, 2101–2107.

[13]   X. Wang, G. Guerin, H. Wang, Y. Wang, I. Manners, M. A. Winnik, *Science* **2007**, *317*, 644–647.

[14]   a) Z. M. Hudson, C. E. Boott, M. E. Robinson, P. A. Rupar, M. A. Winnik, I. Manners, *Nat. Chem.* **2014**, *6*, 893–898; b) P. A. Rupar, L. Chabanne, M. A. Winnik, I. Manners, *Science* **2012**, *337*, 559–562.

[15]   J. Schmelz, M. Karg, T. Hellweg, H. Schmalz, *ACS Nano* **2011**, *5*, 9523–9534.

[16] J. Schöbel, M. Karg, D. Rosenbach, G. Krauss, A. Greiner, H. Schmalz, *Macromolecules* **2016**, *49*, 2761–2771.

[17] P. A. Schaal, U. Simon, *Beilstein J. Nanotechnol.* **2013**, *4*, 336–344.

[18] A. Guinier, G. Fournet, *Small-Angle Scattering of X-Rays*, John Wiley and Sons, Chapman and Hall, New York, London, **1955**.

[19] A. Bergmann, G. Fritz, O. Glatter, *J. Appl. Crystallogr.* **2000**, *33*, 1212–1216.

[20] P. Raffa, C. Evangelisti, G. Vitulli, P. Salvadori, *Tetrahedron Lett.* **2008**, *49*, 3221–3224.

[21] F. Mitschang, H. Schmalz, S. Agarwal, A. Greiner, *Angew. Chem., Int. Ed.* **2014**, *53*, 4972–4975; *Angew. Chem.* **2014**, *126*, 5073-5076.

Supporting Information

Materials

All chemicals were used as received unless otherwise noted. DMF, DMSO and THF: Sigma Aldrich, p.a. grade. PS: synthesized by anionic polymerization, $M_n = 1.4 \times 10^6$ g mol^{-1}, $Đ = 1.08$. $S_{40}E_{21}M_{39}$[108]: prepared by a combination of sequential anionic polymerization and subsequent hydrogenation as published elsewhere.[1] *N,N*-diisopropylethylenediamine: Acros Organics, 97 %, purified by distillation prior to use; tetrachloroauric acid trihydrate: Alfa Aesar, 99.99 %, $\geq$ 49 % Au basis; sodium borohydride: Fluka, $\geq$ 96 %; sodium citrate: Sigma-Aldrich, $\geq$ 98 %, anhydrous; dimethylphenylsilane: Sigma-Aldrich, $\geq$ 98 %; *n*-butanol: Sigma-Aldrich, 99.8 %, anhydrous.

Methods

Scanning Electron Microscopy (SEM). SEM micrographs were obtained by using a LEO 1530 (Gemini) scanning electron microscope at an acceleration voltage of 1-10 kV. For detection, a SE2- and a backscattered electron detector were used. The samples were sputter-coated with 2.0 nm of platinum with a Cressington sputter coater (208HR, 40 mA) before measurement. The average diameter of the fibers was determined by measuring at least 100 fibers using the software *ImageJ*.

Transmission Electron Microscopy (TEM). For determination of wCCM length and morphology, elastic bright-field transmission electron microscopy (TEM) on a Zeiss 922 Omega EFTEM (Zeiss NTS GmbH, Oberkochen, Germany) was done. Zero-loss filtered images were recorded digitally on a bottom mounted CCD camera system (Ultrascan 1000, Gatan) at an acceleration voltage of 200 kV. The micrographs were processed with the digital imaging processing system of Gatan (Digital Micrograph 3.9 for GMS 1.4). Before measurement, the samples were diluted to 0.1 g L^{-1} and one droplet was placed onto a carbon coated copper grid. The residual solvent was immediately blotted by filter paper. The samples were dried in a vacuum oven (20 mbar, room temperature) and stained with RuO$_4$ vapor, which selectively stains PS. The average length and patch size of the micelles and the

average size of AuNPs were determined by measuring at least 100 micelles/NPs using the software *ImageJ*.

Optical Microscopy and Polarized Optical Microscopy. The optical micrographs were recorded using a Keyence VHX-100 with a VH-Z500 unit. Polarized optical microscopy was performed on a Leica DMRX equipped with a Leica DC 200 camera.

UV-Vis Spectroscopy. Reflection spectra were recorded with a Cary 5000 (2.23) from Agilent Technologies equipped with a universal measurement accessory (UMA) unit. The samples were fixed onto glass slides (Thermo Scientific, 76 x 26 mm) with scotch tape and measured at an angle of incidence of -10° and detection of +10°. Spectra were recorded in the wavelength range of 300 to 1000 nm. The spectra were background corrected.

Gas Chromatography Coupled with Mass-Spectrometry (GC-MS). For GC-MS, a GC 7890 B with a 30 m capillary column (Agilent HP-5ms; 30 m x 0.25 mm x 0.25 µm) and a mass spectrometer 5977 A from Agilent Technologies were used. The heating profile was set as following: the starting temperature of 50 °C was kept for 2 min; subsequently, the temperature of the oven was raised to 150 °C applying a heating rate of 10 K min^{-1}, followed by heating to 300 °C at 35 K min^{-1}. The applied carrier gas was helium (5.6; purified with a Agilent CP17973 gas clean filter). For the determination of conversion, undecane was added as a reference. For calculation, the ratio of integrals of dimethylphenylsilane ($R_t = 6.41$ min, $m\,z^{-1} = 136$ [M], 121 [M-(CH$_3$)]$^+$, 105 [C$_6$H$_5$Si]$^+$) and butoxydimethylphenylsilane ($R_t = 12.40$ min, $m\,z^{-1} = 193$ [M-(CH$_3$)]$^+$, 137 [C$_6$H$_5$Si(CH$_3$) (OH)]$^+$, 91 [C$_6$H$_5$CH$_3$]$^+$) to the reference were used.

Inductively Coupled Plasma-Optical Emission Spectrometry (ICP-OES). ICP-OES was measured on a VARIAN Vista-Pro (40 MHz, Argon Plasma) equipped with a ASX-510 autosampler, an Echelle polychromator and an Argon humidifier. Before measurement, 0.3 g of the samples were dried at 60 °C. The residue was dissolved in 0.5 mL aqua regia and diluted with 9.5 mL of ultrapure water. A CCD semiconductor detector was used for the detection.

Small-Angle X-Ray Scattering (SAXS). All SAXS data were measured using the small-angle X-ray system "Double Ganesha AIR" (SAXSLAB, Denmark). The X-ray source of this laboratory-based system is a rotating anode (copper, MicoMax 007HF, Rigaku Corporation, Japan) providing a micro-focused beam at $\lambda = 0.154$ nm. The data were

recorded by a position sensitive detector (PILATUS 300K, Dectris). The circularly averaged data were normalized to incident beam, sample thickness and measurement time.

Synthesis and Supplementary Analytical Data

Synthesis of SEDiPA-55. For synthesis of SED*i*PA-55, 1 g of a polystyrene-*block*-polyethylene-*block*-poly(methyl methacrylate) ($S_{40}E_{21}M_{39}{}^{108}$, where subscripts denote the weight fraction and superscript gives the overall molecular weight) triblock terpolymer (1 eq with respect to MMA units) was dispersed in DMSO ($c = 10$ g L^{-1}) at 130 °C for 4 h. Afterwards, the dispersion was cooled to room temperature and degassed for 30 min with argon. 20 mL of freshly distilled and degassed *N,N*-di*iso*propylethylenediamine (30 eq.) were added to the dispersion. The dispersion was heated to 130 °C for 65 h. The product was purified by dialysis against deionized water and subsequent freeze-drying. This post polymerization modification of the PMMA block leads to a random copolymer consisting of remaining MMA, amide and imide units (Scheme S5-1).[2] The amidation resulted in $S_{35}E_{19}DiPA_{46}{}^{123}$ with a degree of functionalization of $f = 55\%$.
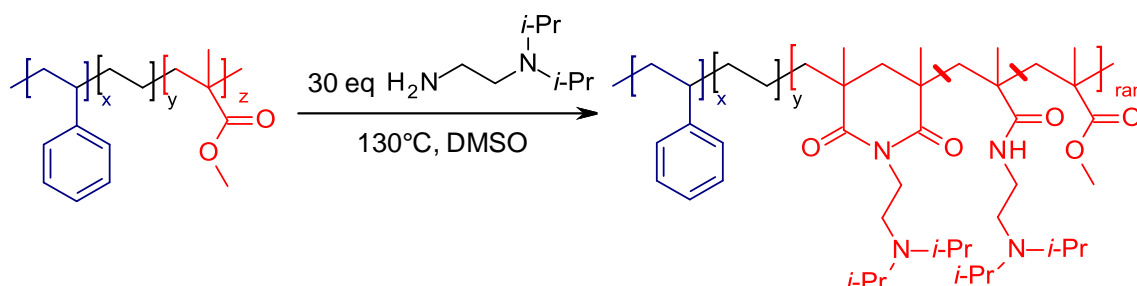

Scheme S5-1. Amidation of a SEM triblock terpolymer to SED*i*PA-*f*.

CDSA of SEDiPA-55. A 20 g L^{-1} dispersion of SED*i*PA-55 in THF was heated to 65 °C for 30 min in order to dissolve the polymer. Subsequent quenching of the solution to 27 °C for 24 h leads to crystallization driven self-assembly into wCCMs with a patchy corona (Figure S5-1).
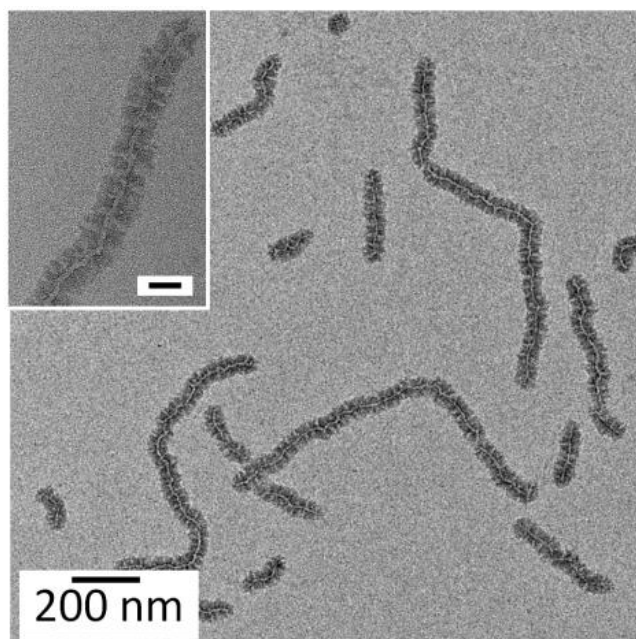
Figure S5-1. SED*i*PA-55 wCCMs obtained by crystallization driven self-assembly in THF (20 g L^{-1}, T_c = 27 °C). The sample was stained with RuO$_4$, which selectively stains the PS patches in the wCCM corona. Scale bar in inset: 50nm.

Coaxial Electrospinning of SEDiPA-55@PS Nonwovens. For coaxial electrospinning of SED*i*PA-55@PS nonwovens two different solutions were prepared. For the core a 7 wt% PS (M_n = 1.4 x 10^6 g mol^{-1}) solution in *N,N*-dimethylformamide and for the shell a 20 g L^{-1} dispersion of SED*i*PA-55 wCCMs in THF were used. The fibers were spun on a fast rotating collector (800 rpm) in a distance of 5 cm at a temperature of 20.6 °C and a relative humidity of ca. 53%, using a homemade coaxial nozzle. For electrospinning a high voltage of 9.3 kV at the nozzle and -1.0 kV at the collector was used. The feed rate of the PS core solution was 1.0 mL h^{-1} and that of the SED*i*PA-55 wCCMs shell dispersion 0.9 mL h^{-1}, respectively. The parameter settings for the coaxial electrospinning were found to be crucial for the successful preparation of the patchy nonwovens. The voltage at the nozzle was set to values below 10 kV in order to ensure coating of the wCCMs on the PS support fibers. For these comparably low voltages, a high molecular weight PS was needed to guarantee a stable electrospinning process producing bead-free fibers.
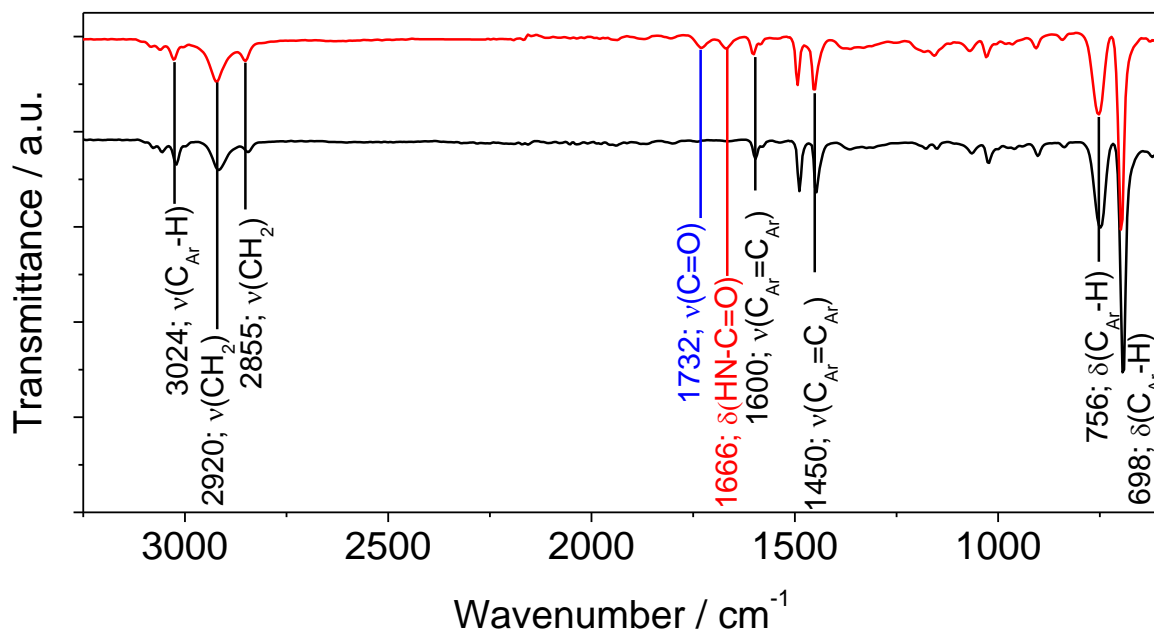
Figure S5-2. ATR FT-IR spectra of pure PS fibers (black) and PS fibers coated with SED*i*PA-55 wCCMs (red). The latter shows the characteristic vibrations of ester (1732 cm^{-1}) and amide (1666 cm^{-1}) units corresponding to the SED*i*PA-55 wCCMs. The spectra were shifted vertically for better visualization.

Synthesis of AuNP. The citrate-stabilized AuNPs were prepared according to the procedure reported by Schaal et al.[3] The average size of the nanoparticles was determined by TEM to $D = 11 \pm 3$ nm (Figure S5-3).
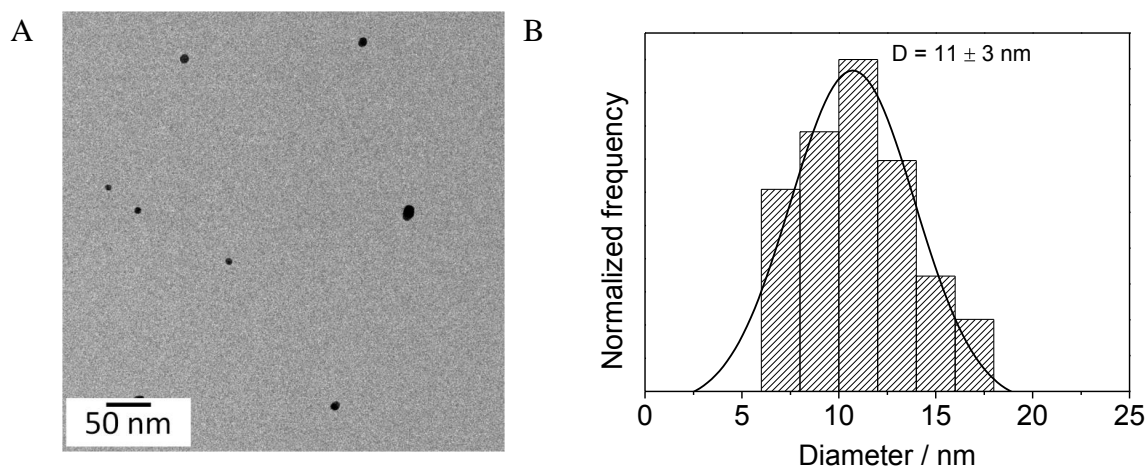

Figure S5-3. TEM micrograph (A) and size distribution (B) of the synthesized AuNPs. For calculating the average diameter, 100 NPs were measured.

Incorporation of AuNPs in SEDiPA-55@PS Nonwovens. The loading of the nonwovens was done by dipping a piece of nonwoven (10 x 10 mm, 720 µg) fixed in a cage made of stainless steel mesh into the aqueous dispersion of the preformed citrate-stabilized AuNPs

for 24 h. After incorporation of the AuNPs, the nonwovens were subsequently washed with a 5 mM sodium citrate solution and ultrapure water in order to remove excess, non-bound AuNPs. The nonwovens were dried in a vacuum oven (< 5 mbar, 40 °C) for 15 h.

The amount of Au in the patchy nonwovens was determined by inductively coupled plasma-optical emission spectrometry (ICP-OES). The aqueous AuNP dispersions before and after loading of the patchy nonwovens were evaporated to dryness and each of the obtained residues were dissolved in 0.5 mL auqa regia. The solutions were diluted by addition of 9.5 mL ultrapure water before ICP-OES measurements. Consequently, the difference in Au content of the dispersion before and after loading corresponds to the amount of Au immobilized in the patchy nonwoven.
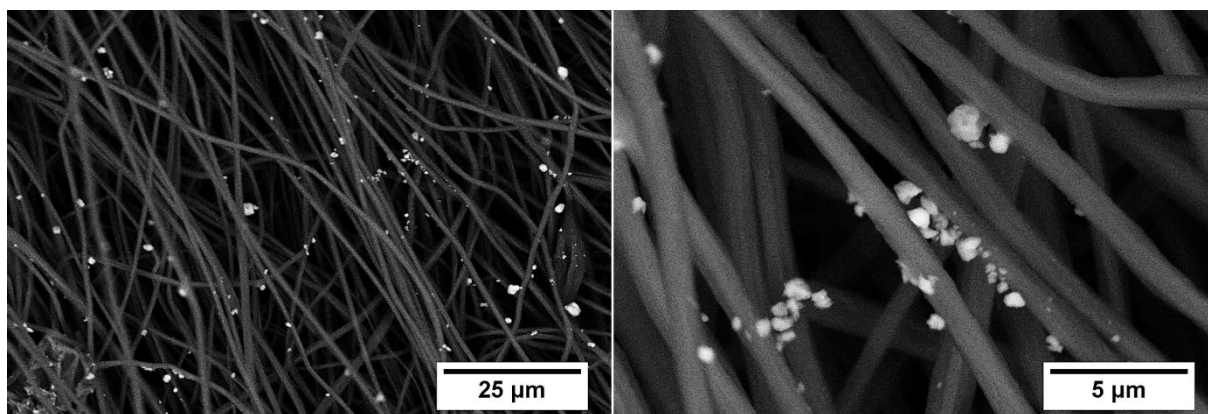
**Figure S5-4.** Scanning electron micrographs (backscattered electron detector) of a patchy nonwoven without functional patches after loading with AuNPs. The nonwoven was prepared by coaxial electrospinning employing wCCMs with non-functional PS and PMMA patches as shell (prepared by CDSA of a $S_{40}E_{21}M_{39}$[108] triblock terpolymer). The AuNPs aggregate due to insufficient stabilization (Au appears bright).

SAXS Analysis of AuNP Dispersion and SEDiPA-55@PS Nonwovens.
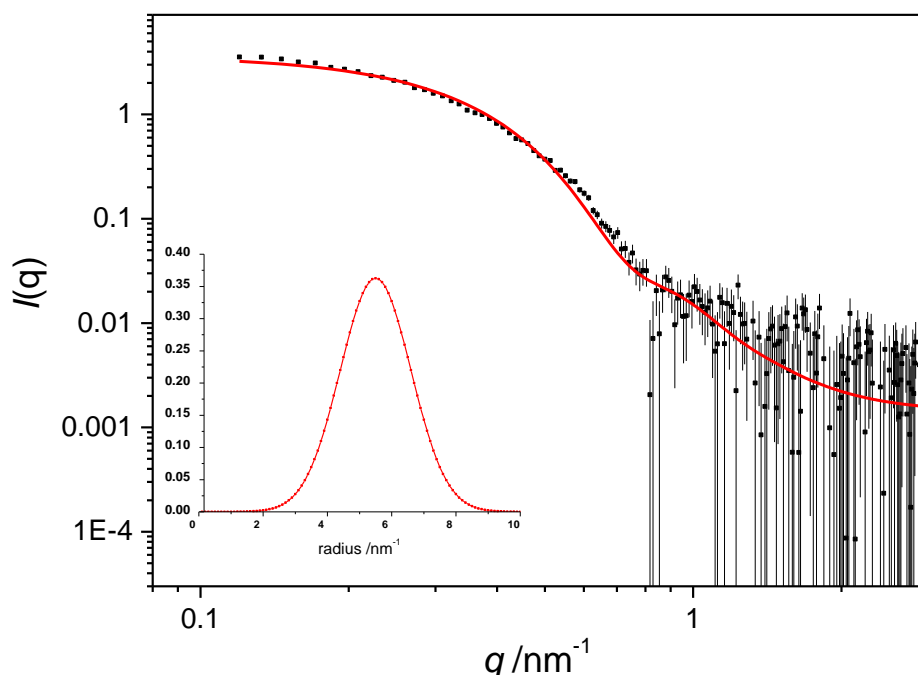
Figure S5-5. Scattering intensity for the aqueous, citrate-stabilized AuNP dispersion determined by SAXS. The inset shows the NP size distribution obtained from a form factor fit using a simple spherical model with polydispersity of the radius.

The neat patchy nonwoven, i.e., before loading with AuNPs, shows no distinct scattering features except a decay for I(q) to q^{-4}, which is typical for large structures where only the surface scattering can be obtained (Figure S5-6). This scattering curve was used as background for the AuNP loaded patchy nonwoven. Here, the scattering cross-terms of NPs and the nonwoven is neglected. This is reasonable as the scattering contrast of the AuNPs is much higher compared to that of the nonwoven and, thus, these cross-terms are very weak. Consequently, by subtracting the scattering intensity of the AuNP loaded nonwoven with that of the patchy nonwoven before loading results in the scattering intensity of the embedded AuNPs in the patchy nonwoven (Figure 5-2, main text).
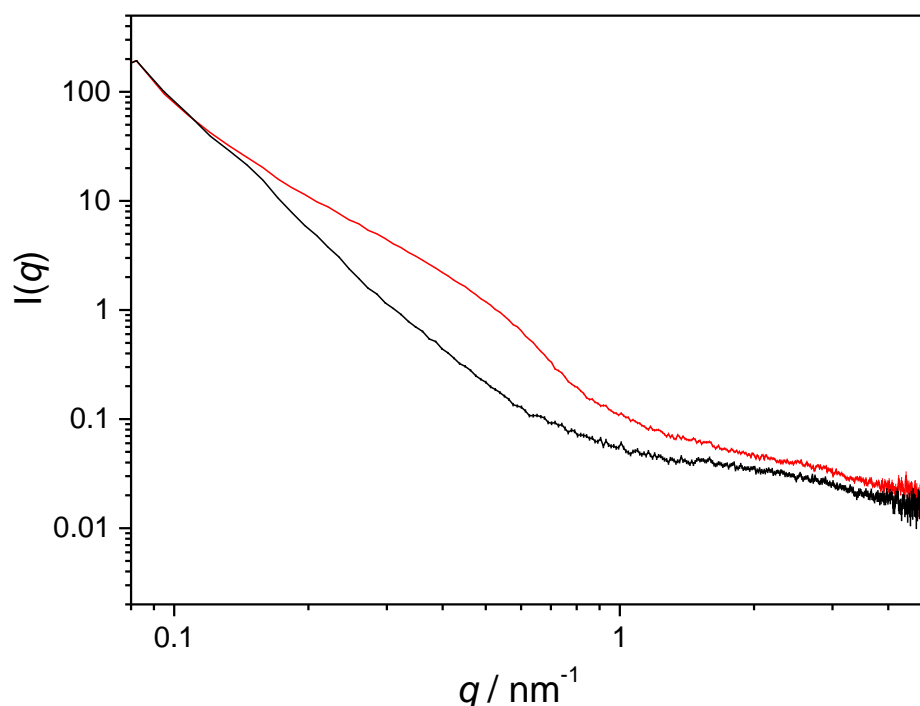
Figure S5-6. Scattering intensity of the patchy nonwoven before (black) and after (red) loading with AuNPs determined by SAXS.

Catalytic Alcoholysis of Dimethylphenylsilane. In a typical synthesis, 32 mg of dimethylphenylsilane and 36.7 mg of undecane (reference for GC-MS) were dissolved in 4 g of dry *n*-butanol. The solution was overlaid by argon. An AuNP loaded nonwoven (720 µg, amount of Au in fibermat: 41 µg, 0.1 mol% with respect to silane), which was pre-swollen for 24 h in pure *n*-butanol, was placed in the reaction solution. The reaction was shaken at 400 rpm (Heidolph Multi Reax Shaker) for 24 h, taking aliquots of 4 µL of the reaction solution after different periods of time. The aliquots were diluted by 1 mL of acetone for GC-MS measurement. This procedure was repeated 9 times using the same AuNP loaded nonwoven and a freshly prepared reaction mixture. Before reuse, the AuNP nonwoven was washed with *n*-butanol. After each catalysis cycle, ICP-OES measurements of the reaction mixtures proved the absence of AuNP leaching. Furthermore, a neat patchy nonwoven, i.e., without AuNP, was tested for catalytic activity. Here, no significant conversion was observed even after 24 h.
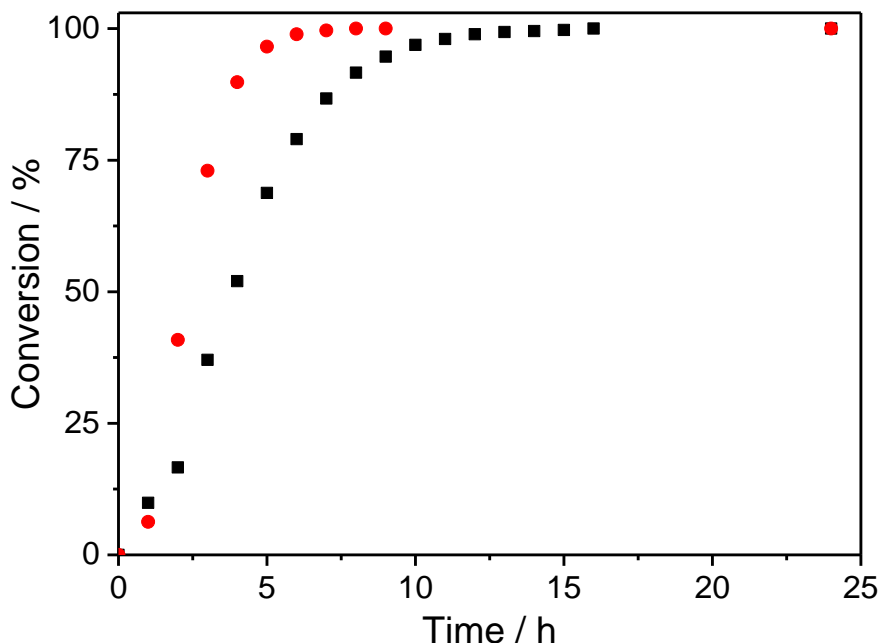
Figure S5-7. Conversion of dimethylphenylsilane for a pre-swollen (24 h in *n*-butanol, red circles) and a non-pre-swollen AuNP loaded nonwoven (black cubes) as catalyst.

The pre-swelling of the hybrid nonwovens in *n*-butanol was determined to be crucial for a fast conversion of dimethylphenylsilane, which is attributed to the hydrophobicity of the nonwovens. The tertiary amino groups containing patches, which bear the AuNPs, have to swell in *n*-butanol to give access of the reaction mixture to the surface of the AuNPs. Thus, swelling prior to catalysis ensures the accessibility of the embedded AuNPs across the whole nonwoven. Consequently, the reaction rate is significantly enhanced.

References

[1]   H. Schmalz, J. Schmelz, M. Drechsler, J. Yuan, A. Walther, K. Schweimer, A. M. Mihut, *Macromolecules* **2008**, *41*, 3235–3242.

[2]   J. Schöbel, M. Karg, D. Rosenbach, G. Krauss, A. Greiner, H. Schmalz, *Macromolecules* **2016**, *49*, 2761–2771.

[3]   P. A. Schaal, U. Simon, *Beilstein J. Nanotechnol.* **2013**, *4*, 336–344.

6 Clinical Wastewater Treatment: Photochemical Removal of an Anionic Antibiotic (Ciprofloxacin) by Mesostructured High Aspect Ratio ZnO Nanotubes

Carina Bojer[1], Judith Schöbel[2], Thomas Martin[1], Michael Ertl[1], Holger Schmalz[2] and Josef Breu[1]*

[1] Anorganische Chemie I, Universität Bayreuth, 95440 Bayreuth, Germany

[2] Makromolekulare Chemie II, Universität Bayreuth, 95440 Bayreuth, Germany
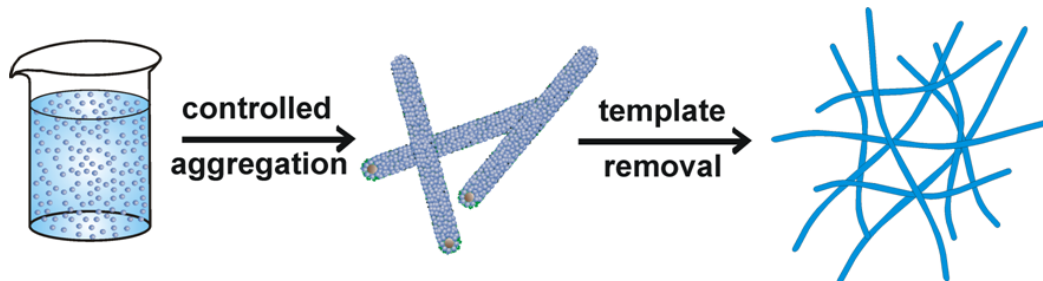
Abstract

Zinc oxide (ZnO) nanoparticles were mesostructured by polybutadiene-*block*-poly(2-vinylpyridine) cylindrical polymer brushes as a template. Loading the positively charged vinylpyridine block with ZnO nanoparticles produced hybrid rods with high aspect ratio. Mesostructured ZnO nanotubes obtained by pyrolytic template removal show high activity in the photocatalytic degradation of ciprofloxacin using a continuous flow reactor and irradiation with terrestrial solar spectrum. In comparison with Degussa P25, a titanium dioxide photocatalyst, the degradation is 2.9 times faster. Due to its non-woven microstructure, the photocatalyst, moreover, can be easily separated from fluid reaction media by filtration.

6.1. Introduction

Active pharmaceutical ingredients like beta blockers, antiphlogistics or antibiotics have been detected in considerable quantities in wastewater and even in drinking water [1]. In Europe, the most commonly prescribed quinolone antibiotic is ciprofloxacin. It is applied to skin infections and sexually transmitted diseases [2]. Ciprofloxacin belongs to the family of fluoroquinolones and is a broad-spectrum antibacterial compound used in private households, veterinary medicine and hospitals. Focusing on hospitals a daily water consumption of 260 to 940 L per bed is usual. This wastewater has an antibiotics pollution e.g. with ciprofloxacin up to 101 μgL^{-1} [3,4].

Clinical wastewater consequently needs pretreatment before it can be handled by community wastewater facilities triggering intensive research into methods and active catalysts for the degradation of these medical pollutants [5]. One promising approach are advanced oxidation processes (AOPs). In AOPs a reactive radical species is *in situ* generated by energy like solar energy, which is one of the most abundant clean energy sources available [6–8]. Promising photocatalysts in environmental waste management systems are amongst others titanium dioxide (TiO_2), zinc oxide (ZnO), iron(III) oxide (Fe_2O_3) or vanadium(V) oxide (V_2O_5) [9–11].

ZnO is an important direct wide bandgap II-VI semiconductor with a bandgap of 3.37 eV [12]. Its large exciton binding energy of 60 meV, the good biocompatibility, low costs, strong oxidation ability and mechanical strength are reasons for the potential applications in photocatalysis [13–17].

6.2. Photocatalysis of ciprofloxacin in clinical wastewater treatment

Most active pharmaceutical ingredients are formulated as ions to assure solubility in body fluids. Therefore, very commonly carboxylate groups are introduced into the molecular structure and at pH values above $\approx$ 6 such molecules carry a negative charge [18]. Ciprofloxacin has its isoelectric point (zwitterion) at pH 7.4 resulting from the pK_a values of 6.09 for the carboxylic group and 8.74 for the nitrogen of the piperazinyl ring [19]. At the same time the surface of oxidic semiconductors also carries a negative charge above an pH value higher than the point of zero charge (PZC). For hospital wastewater typically an average pH of around 8 was determined [3,20]. It happens that this pH is between the PZC

of rather acidic TiO_2 and more basic ZnO. Consequently, the surface of Degussa P25 (P25) with a PZC of 6.9 is negatively charged [21] while the ZnO surface with a PZC of 9.3 will be positively charged at the pH of typical hospital sewage [22]. Since, as mentioned above, ciprofloxacin is anionic in alkaline conditions, it is expected that adsorption of ciprofloxacin on the ZnO surface should be electrostatically favored contrary to the disfavored adsorption at the like-charged P25 surface. In this line, it has been reported that the photodegradation of the anionic pollutant RED-3BA on TiO_2 was more efficient at pH 4 compared with tests at pH 7 and pH 11, values above the PZC of TiO_2 where the surface of the photocatalyst become negatively charged [23].

While in a first approximation, efficiency increases with the surface area of the catalyst, photodegradation in a fluid medium like clinical wastewater treatment requires the separation from the wastewater e.g. by filtration or in continuous flow reactors. Consequently, mesostructuring of nanoparticles as applied in this work represents a good compromise between maximizing the catalyst surface and the possibility to separate or recycle the catalyst. Hence, it is necessary to build macroscopic structures of nanoparticles like nanotubular aggregates.

In this work, ZnO nanotubes were prepared by self-assembly of ZnO nanoparticles using electrostatic interactions between ZnO nanoparticles and the block copolymer template (Scheme 6-1). This mesostructured ZnO obtained after pyrolysis is compared to P25 in respect to the photodegradation efficiency of ciprofloxacin.
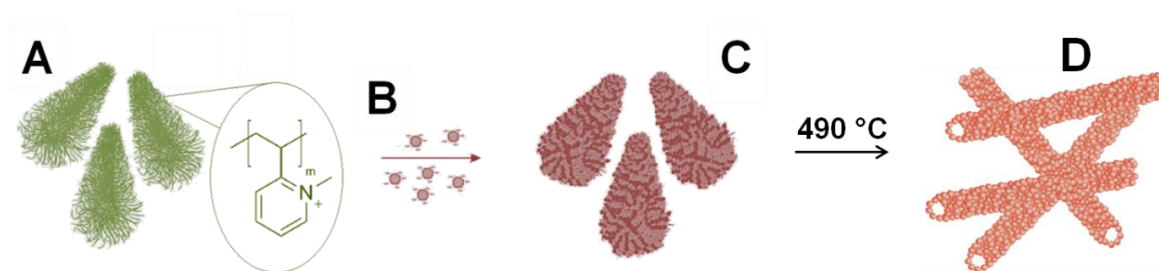
Scheme 6-1. (A) Methylated cationic cylindrical polymer brushes were loaded with (B) ZnO nanoparticles resulting in a (C) ZnO hybridmaterial that was (D) pyrolysed to mesostructured ZnO with a non-woven microstructure.

6.3 Materials and methods

Chemicals

If not mentioned otherwise, all chemicals were purchased from Sigma Aldrich, Germany and used as obtained.

Preparation of the block copolymer template

The polybutadiene-*block*-poly(2-vinylpyridine) (BV) diblock copolymer precursor used for the preparation of cylindrical polymer brushes (CPBs) was synthesized via living anionic polymerization in THF. Details on the diblock copolymer synthesis can be found in the Supplementary Information. To obtain the positive charged CPBs first 1 g of diblock copolymer was dissolved in 20 mL chloroform with 0.1 g of the photoinitiator Lucirin TPO (BASF). The solvent was allowed to evaporate slowly and resulted in hexagonally packed cylinders of polybutadiene (PB) segments in a poly(2-vinylpyridine) (P2VP) matrix. The PB core of the CPBs in the cast film was crosslinked using a UV-lamp (each side 2 h). The crosslinked polymer film (1 g) was dissolved in 200 mL chloroform and a tenfold excess of iodomethane solution (99 %, 3 mL) was dropwise added. After one day the precipitated product was washed and freeze dried.

Preparation of ZnO nanoparticles

ZnO nanoparticles were synthesized following a slightly modified published protocol [24]. Zinc acetate dihydrate (8.76 g, 0.04 mol) was dissolved in boiling ethanol (400 mL, 10 min). Lithium hydroxide monohydrate (2.348 g, 0.056 mol) was dissolved in ethanol (400 mL, 15 min) using ultrasonification. The lithium hydroxide solution was added to the zinc acetate solution at room temperature and directly cooled to 0 °C. The resulting ZnO nanoparticles were purified by precipitation in n-heptane (4 L) and subsequently redispersed in ethanol (500 mL).

Preparation of ZnO nanotubes

In a typical ZnO/BV hybrid material synthesis (1 g) with a weight ratio of 4:1, the ZnO nanoparticle dispersion (800 mg ZnO) was dropwise added to the the BV solution (200 mg,

1 gL^{-1} in DMSO). After 2 h the hybrid material was dialyzed against DMSO and washed with DMSO and water.

Template removal was done in a tube furnace with a heating and cooling rate of 180 °Ch^{-1} and a maximum temperature of 490 °C, which was hold for 5 min.

Photocatalytical degradation tests

For photocatalytical degradation of ciprofloxacin, 14 mg of the catalyst were added on a glass microfiber filter (Whatman, 37 mm diameter). The filter was adjusted in a self-constructed continuous flow reactor (Scheme S6-1). A ciprofloxacin solution (0.4 L, 2x10^{-5} molL^{-1}) circulated through the reactor with an irradiated volume of 0.1 L and a flow rate of 12 Lh^{-1}. The remaining volume is necessary to maintain a continuous circulation of the ciprofloxacin solution. After every 5-15 min of irradiation with solar spectrum from a 300 W Xenon lamp using an AM1.5 filter (1000 Wm^{-2}), the ciprofloxacin concentration was determined photometrically by UV-Vis.

Instruments and measurements

Powder X-ray diffraction (PXRD) measurements were performed applying a STOE Stadi P diffractometer with CuK$_\alpha$ radiation, equipped with a Mythen 1K silicon strip-detector. Rietveld analysis was performed with TOPAS Academic applying a fundamental parameters approach for profile fitting. Implemented macros were used to obtain crystallite sizes. Assuming spherical particles resulted in a volume weighted average crystallite size

Dynamic light scattering (DLS) measurements were performed with a Malvern Zetasizer NS measuring three times 20 s at room temperature.

Transmission electron microscopy (TEM) images were taken on a Zeiss CEM 922 at accelerating voltages of 200 kV. All samples with the exception of the polymer film were prepared on a copper grid (200 mesh) with a carbon film by drop coating from ethanolic solution. The polymer film was cut ultrathin (30-80 nm) with a Reichert-Jung Ultracut E equipped with a diamond knife.

Scanning electron microscopy (SEM) micrographs were measured with a scanning electron microscope, LEO 1530 FESEM, equipped with a field emission cathode. All samples were

drop-coated on a silicon wafer and sputtered with platinum. Energy dispersive X-ray scattering was performed with 20 kV.

Determination of surface area with N_2 was conducted at 77 K on a Quantachrome Autosorb 1 after degassing the sample at 363 K for 12 h.

Photocatalytic measurements were done in a continuous flow reactor with a flow rate of 10 Lh^{-1}. Irradiation was done using a LOT Quantum Design 300 W Xe Arc Lamp (LSN254) with an AM1.5 filter.

UV-Vis absorption spectra were measured by a Varian Cary 300 spectrometer using Hellma precisions cells made of Quartz SUPRASIL (type 100-QS, light path 10 mm).

PZC of ZnO nanotubes was determined using a ParticleMetrix Stabisizer PMX 200C. 50 mg ZnO nanotubes in 10 mL water with a pH of 10.5 (adjusted with 0.01 M NaOH) were titrated with 0.05 M HCl until the streaming potential was 0.

6.4 Results and discussion

Characterization of the diblock copolymer template

The BV contained 19 wt % PB and had molar mass dispersity $Đ_M$ of 1.02 and molecular weight of 60000 $gmol^{-1}$ as determined by SEC (Fig. S6-1), MALDI-TOF and NMR (Fig. S6-2) experiments. This composition was chosen to obtain hexagonal PB cylinders in a P2VP matrix in the bulk state. A permanent positive charge of CPBs was obtained by redispersing the core-crosslinked polymer film followed by methylation of the P2VP block. All steps were controlled by TEM micrographs (Fig. S6-3).
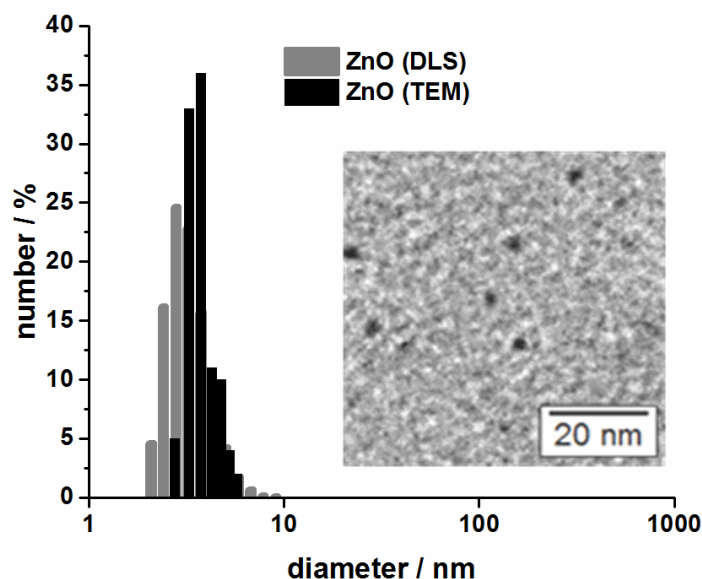
Characterization of ZnO nanoparticles

Phase purity of ZnO nanoparticles was confirmed by PXRD measurement (Fig. 6-1a). All peaks can be related to ZnO (marked by vertical ticks in Fig. 6-1; PDF: 00-036-1451) and the high full width at half maximum (FWHM) of the peaks indicates that nanoparticles were synthesized.
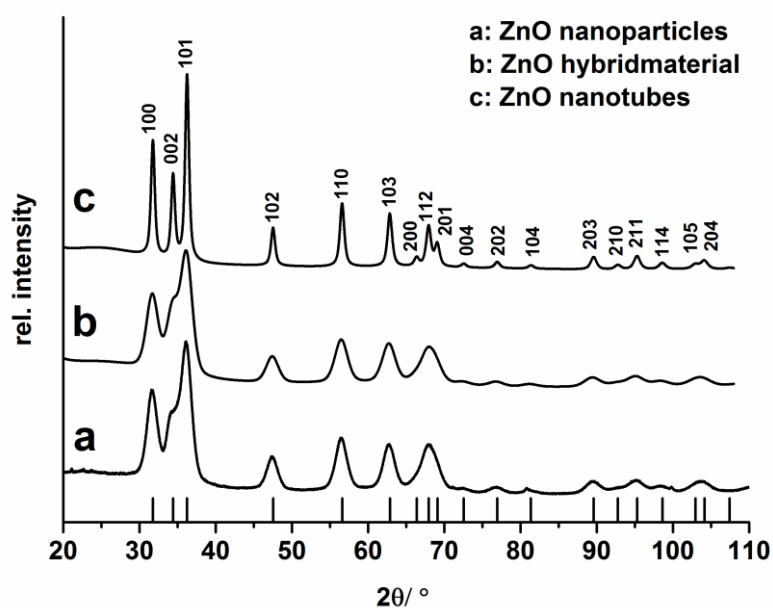
Figure 6-1. PXRD pattern of a) ZnO nanoparticles, b) hybrid material and c) after template removal with a reference of ZnO (vertical ticks PDF: 00-036-1451) and the Miller's indices.

Particle size distributions of ZnO nanoparticles were determined independently by DLS (Fig. 6-2 dark grey) and TEM (Fig. 6-2 black). Average crystallite (coherently diffraction domain size) size was obtained by Rietveld analysis of PXRD measurement (Fig S6-4, Tab. S6-1) [25]. DLS gives a number weighted apparent hydrodynamic diameter of 3.2 nm. As expected, TEM (Fig 6-2 inset) and PXRD measurements give slightly different values. Examination of 100 nanoparticles using TEM micrographs yielded a median particle size of 2 nm. Rietveld analysis indicated coherent scattering domains of around 5 nm. TEM images and DLS measurements confirm that there was no aggregation or agglomeration of the nanoparticles.

Figure 6-2. Particle size distribution of ZnO nanoparticles determined by DLS measurements (dark grey) and TEM images (black). The inset shows a TEM image of ZnO nanoparticles.

Formation of ZnO nanotubes

ZnO nanoparticles are surface modified with acetate and therefore carry a negative charge that allows for a robust hybrid formation driven by electrostatic interactions with the positively charged CPBs [26]. As judged by the diffraction pattern, hybrid formation does not affect the crystallite size nor the phase purity (Fig. 6-1b). All peaks can be assigned to wurtzite. The CPBs are amorphous and contribute no peaks. Upon template removal by calcinations, the FWHM of the peaks decreases. As expected the nanocrystals grow during calcination but less than expected for a heat treatment at 490 °C. Rietveld refinements (Fig. S6-4-6, Tab. S6-1-3) yield in an average coherent scattering domain of 4.49(4)-5.05(4) nm for the nanoparticles, 4.21(5)-4.56(5) nm for the hybrid material and 12.0(1)–15.1(1) nm for calcinated material, respectively. Apparently the confinement to one dimension limits the crystallite growth.
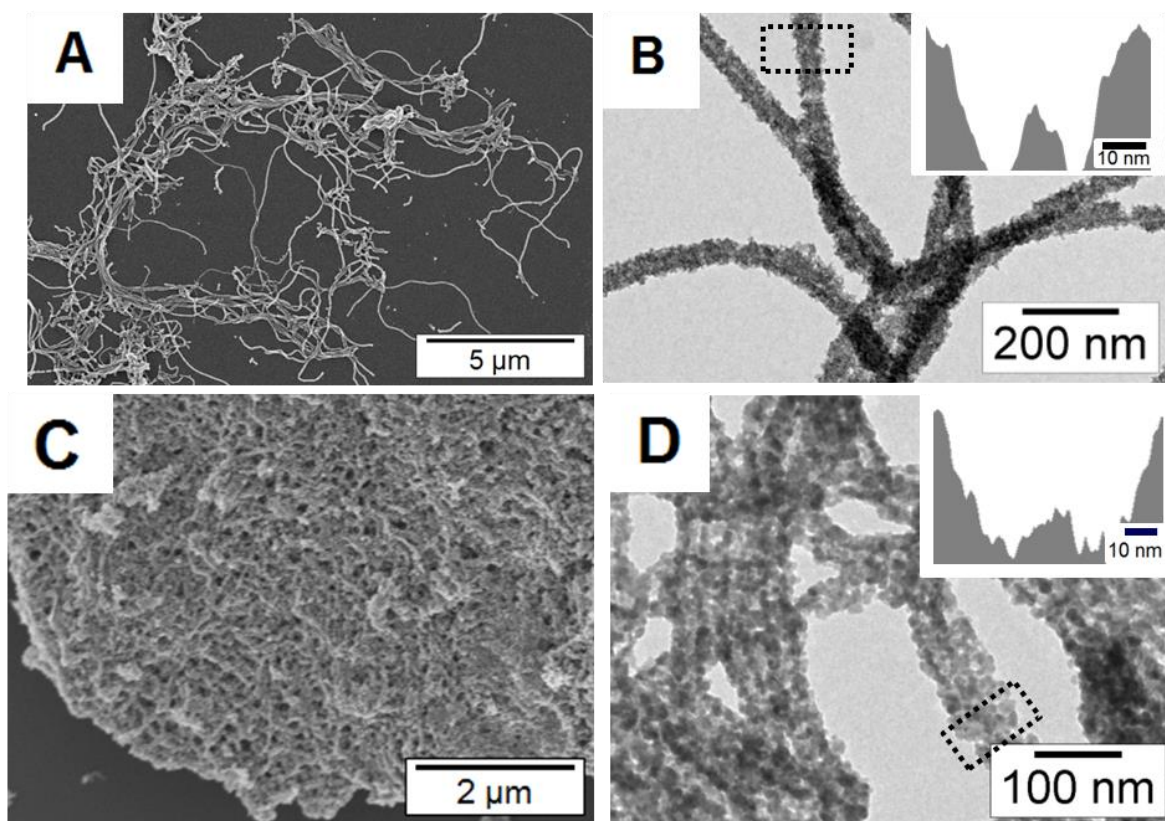
Figure 6-3. A) SEM and B) TEM micrographs of the ZnO hybrid material; and C) SEM and D) TEM micrographs after template removal. Inset in B and D are grey value analyses performed with the package "image J".

The pristine unloaded CPBs have diameters of approximately 100 ± 11 nm and the PB core 30 ± 9 nm [27]. The diameter of the hybrid material is around 55 nm (Fig. 6-3). The contraction of the P2VP corona is in good agreement with similar work on TiO_2 hybrid formation [28]. The rods of hybrid material have high aspect ratio and the core shell structure was preserved (grey value analysis Fig. 6-3B inset). After drying of the hybrid material the worm-like character can still be observed and a non-woven microstructure is formed by self-assembly (Fig. 6-3A). The surface area of dried hybrid material determined by Brunauer-Emmett-Teller measurements with nitrogen physisorption was 44 m^2g^{-1} (Fig. 6-4A).

Finally the loaded CPBs were calcinated in air at 490 °C. The polymer template was removed during temperature treatment. The nanorods are converted into nanotubes as evidenced by a grey scale analysis (Fig. 6-3C, D and inset). Elemental analysis proved that carbon was completely removed (less than 0.1 %) during temperature treatment. Due to the crystal growth, the surface area decreased from 44 m^2g^{-1} to 31 m^2g^{-1} (Fig. 6-4). The amount

of ZnO was determined by EDX measurements to be 96 wt% for ZnO nanotubes (Fig. S6-8).
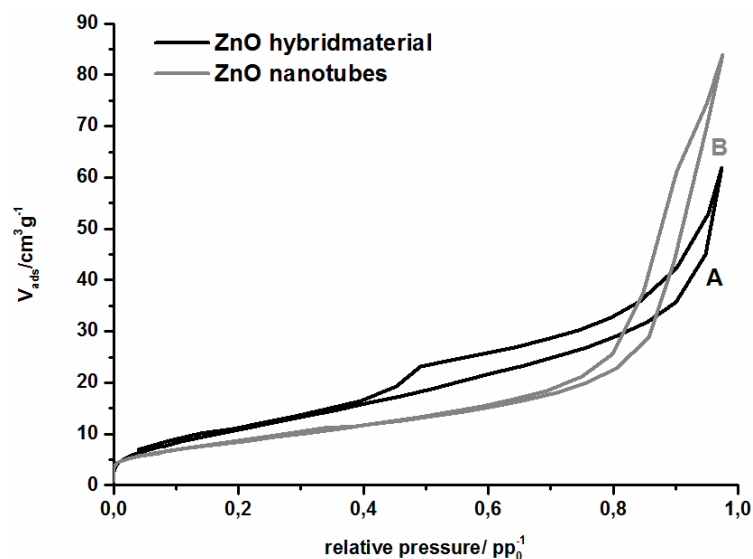
Figure 6-4. N_2-sorption isotherm of A) ZnO hybrid material (black) and B) ZnO nanotubes (dark grey).

Photocatalytical degradation of Ciprofloxacin

Preliminary test for photochemical wastewater treatment with the calcinated material demonstrated activity using a terrestrial solar spectrum. The bad gap of ZnO nanotubes was determined using UV-vis reflectance spectra of the powdered samples. The absorption data were calculated applying the Kubelka-Munk relation for diffuse reflectance data and yielded a band gap of 3.55 eV (Fig. S6-9) [29]. The PZC of 8.9 of synthesized ZnO nanotubes was determined by pH dependant streaming potential measurements and is in good agreement with the literature [21]. After an irradiation time of 120 min a comparative measurement without catalyst showed that $\approx$ 1 % of ciprofloxacin was degraded (Fig. 6-5 light grey triangles). After an irradiation time of 120 min, ZnO nanotubes have degraded 12 % of initial ciprofloxacin concentration (Fig. 6-5 black squares) while P25 degraded only 5 % (Fig. 6-5 dark grey circles). In comparison with P25, the ZnO nanotube catalyst is significantly more efficient at a pH=8. The higher efficiency is observed despite a lower surface area of mesostructured ZnO as compared to P25 (56 m^2g^{-1}) [30].
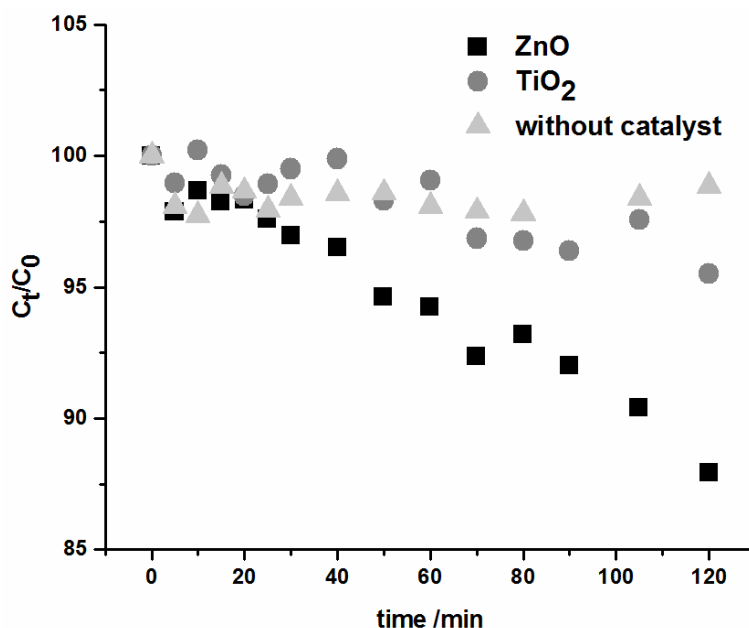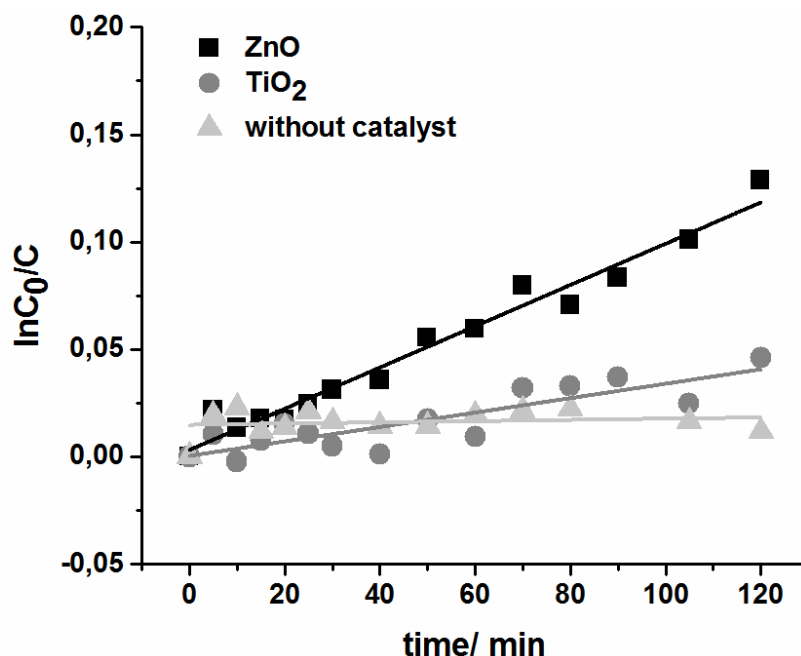
Figure 6-5. Time dependent decrease of ciprofloxacin during irradiation with ZnO nanotubes (black squares), P25 (dark grey circles) and without catalyst (light grey triangles).

The apparent rate constant k' can be calculated by the gradient of $\ln C_0/C_t = f(t)$ because the degradation follows a pseudo-first order kinetics. The k' value without catalyst equals 2.86×10^{-5} min^{-1}. ZnO nanotubes have a k' value of 9.61×10^{-4} min^{-1} as compared to P25 with k'=3.36×10^{-4} min^{-1} (Fig. 6-6). Degradation with as little as 3.5 ppm of ZnO nanotubes is more than 33 times faster as without a catalyst. Compared to P25, ZnO nanotubes are 2.9 times more efficient. A possible explanation is the electrostatically favoured adsorption of ciprofloxacin on the positively charged ZnO surface as mentioned earlier. Obviously the photocatalytic degradation is also highly influenced by the separation of electron hole pairs [31]. Cavaleri et al. determined a decay time of 50 ps for ZnO nanocrystals of comparable size [32]. It has recently been shown for ZnO single crystals of varying habitus that the recombination probability is influenced by the aspect ratio and surface defects [33]. Mesostructuring of nanocrystalline ZnO into tubular structures as done here might influence both surface defects and aspect ratio and thus may have some influence on photocatalysis. This influence will be superimposed on the effect of surface charge discussed here to be advantageous for the degradation of ciprofloxacin by ZnO.

After the degradation tests, the filter with the ZnO nanotubes and the P25 catalyst was removed and dried. Both catalysts could be quantitatively recovered (14 mg and 13.6 mg of ZnO nanotubes and P25, respectively) catalyst left. No weight loss was observed in the

technically benign continuous flow reactor. Contrary to ZnO nanoparticles the mesostructured ZnO nanotubes are big enough to remain completely on the glass microfiber filter. There is no need to use techniques like ultracentrifugation to separate and recycle the ZnO catalyst.

Figure 6-6. First order kinetics plots for ZnO nanotubes (black squares), P25 (dark grey circles) and without catalyst (light grey triangles).

6.5 Conclusion

In conclusion, we were able to transfer our previous work on TiO_2 hybrid formation with negative charged CPBs on ZnO with positively charged CPBs [27, 28, 34–37]. At slightly basic pH, as typically found for hospital wastewater, basic ZnO was shown to be clearly superior to more acidic P25 in the photodegradation of ciprofloxacin, a model compound for wide-spread anionic pollutants due to its positive surface charge.

This colloidal route seems to be a general route for mesostructuring transition metal oxide nanoparticles. Even mixtures of different nanoparticles may be structured in the future. So this should allow for much better efficiency in the photocatalytical degradation by e.g. using ZnO and gold or silver nanoparticles.

The mesostructured ZnO with a non-woven microstructure was used in a continuous flow of wastewater applying a terrestrial solar spectrum. The mesostructured ZnO nanotubes

showed good activity in degradation of ciprofloxacin and there was no loss of catalyst observed. Using P25 showed 2.9 times lower activity.

6.6 References

[1]   N.M. Vieno, H. Härkki, T. Tuhkanen, L. Kronberg, Environ. Sci. Technol. 41 (2007) 5077–5084.

[2]   X. Van Doorslaer, K. Demeestere, P.M. Heynderickx, H. Van Langenhove, J. Dewulf, Appl. Catal. B Environ. 101 (2011) 540–547.

[3]   S. Gartiser, L. Brinker, T. Erbe, K. Kümmerer, R. Willmund, Acta Hydrochim. Hydrobiol. 24 (1996) 90–97.

[4]   R. Lindberg, P.-Å. Jarnheimer, B. Olsen, M. Johansson, M. Tysklind, Chemosphere. 57 (2004) 1479–1488.

[5]   A. Cincinelli, T. Martellini, E. Coppini, D. Fibbi, A. Katsoyiannis, J. Nanosci. Nanotechnol. 15 (2015) 3333–3347.

[6]   U.I. Gaya, A.H. Abdullah, J. Photochem. Photobiol. C Photochem. Rev. 9 (2008) 1–12.

[7]   N.S. Lewis, Science 315 (2007) 798–801.

[8]   G. Rytwo, T. Klein, S. Margalit, O. Mor, A. Naftali, G. Daskal, Desalin. Water Treat. 57 (2016) 16424–16434.

[9]   A. Kudo, Y. Miseki, Chem. Soc. Rev. 38 (2009) 253–278.

[10]   K.M. Lee, C.W. Lai, K.S. Ngai, J.C. Juan, Water Res. 88 (2016) 428–448.

[11]   I. Kazeminezhad, A. Sadollahkhani, Mater. Lett. 120 (2014) 267-270.

[12]   Z.L. Wang, ACS Nano. 2 (2008) 1987–1992.

[13]   U. Özgür, Y.I. Alivov, C. Liu, A. Teke, M.A. Reshchikov, S. Doğan, V. Avrutin, S.-J. Cho, H. Morkoç, J. Appl. Phys. 98 (2005) 41301-41404.

[14]   A. Janotti, C.G. Van de Walle, Reports Prog. Phys. 72 (2009) 126501-126531.

[15]   A. Mclaren, T. Valdes-Solis, G. Li, S.C. Tsang, J. Am. Chem. Soc. 131 (2009) 12540–12541.

[16]   M.A. Mohd Adnan, N.M. Julkapli, S.B. Abd Hamid, Rev. Inorg. Chem. 36 (2016) 77–104.

[17]   J. Yu, X. Yu, Environ. Sci. Technol. 42 (2008) 4902–4907.

[18]   L.J.M. Githinji, M.K. Musey, R.O. Ankumah, Water, Air, Soil Pollut. 219 (2011) 191–201.

[19]   K. Torniainen, S. Tammilehto, V. Ulvi, Int. J. Pharm. 132 (1996) 53–61.

[20]   C. Boillot, C. Bazin, F. Tissot-Guerraz, J. Droguet, M. Perraud, J.C. Cetre, D. Trepo, Y. Perrodin, Sci. Total Environ. 403 (2008) 113–129.

[21]   M. Kosmulski, J. Colloid Interface Sci. 298 (2006) 730–741.

[22]   M. Kosmulski, J. Colloid Interface Sci. 275 (2004) 214–224.

[23]   N.T. Dung, N. Van Khoa, J.-M. Herrmann, Int. J. Photoenergy. 7 (2005) 11–15.

[24]   R. Marczak, F. Werner, J.-F. Gnichwitz, A. Hirsch, D.M. Guldi, W. Peukert, J. Phys. Chem. C. 113 (2009) 4669–4678.

[25]   G. Nabiyouni, M. Seraj, I. Kazeminezhad, B. Ghanbari, J. Mater. Sci. Mater. Electron. 26 (2015) 8047–8053.

[26]   .D. Yang, S. Tripathy, Y. Li, H.-J. Sue, Chem. Phys. Lett. 411 (2005) 150–154.

[27]   M. Schieder, T. Lunkenbein, T. Martin, W. Milius, G. Auffermann, J. Breu, J. Mater. Chem. A. 1 (2013) 381–387.

[28]   M. Müllner, T. Lunkenbein, N. Miyajima, J. Breu, A.H.E. Müller, Small. 8 (2012) 2636–2640.

[29]   M.K. Debanath, S. Karmakar, Mater. Lett. 111 (2013) 116–119.

[30]   K. Joseph, A. Raj, B. Viswanathan, Indian J. Chem. 48 (2009) 1378–1382.

[31]   S. Ikeda, N. Sugiyama, B. Pal, G. Marcí, L. Palmisano, H. Noguchi, K. Uosaki, B. Ohtani, Phys. Chem. Chem. Phys. 3 (2001) 267–273.

[32]   J.J. Cavaleri, D.E. Skinner, D.P. Colombo, R.M. Bowman, J. Chem. Phys. 103 (1995) 5378.

[33]   X. Zhang, J. Qin, Y. Xue, P. Yu, B. Zhang, L. Wang, R. Liu, Sci. Rep. 4 (2014) 845–910.

[34]   M. Müllner, T. Lunkenbein, M. Schieder, A.H. Gröschel, N. Miyajima, M. Förtsch, J. Breu, F. Caruso, A.H.E. Müller, Macromolecules. 45 (2012) 6981–6988.

[35]   M. Müllner, T. Lunkenbein, J. Breu, F. Caruso, A.H.E. Müller, Chem. Mater. 24 (2012) 1802–1810.

[36]   M. Schieder, T. Lunkenbein, C. Bojer, M. Dulle, J. Vom Stein, G. Auffermann, T. Löbling, J. Schöbel, H. Schmalz, J. Breu, Z. anorg. allg. Chem. 641 (2015) 1829-1834.

[37]   R.S. Yelamanchili, Y. Lu, T. Lunkenbein, N. Miyajima, L.T. Yan, M. Ballauff, J. Breu, Small 5 (2009) 1326–1333.

6.7 Supporting Information

Synthesis of Polybutadiene-block-poly(2-vinylpyridine)

The polybutadiene-*block*-poly(2-vinylpyridine) (BV) diblock copolymer was synthesized by sequential living anionic polymerization in a thermostated laboratory autoclave (Büchi AG) using dry THF as solvent. For initiation of the polymerization, 0.54 mL *sec*-BuLi (0.78 mmol, 1 eq) were added to the THF at -70 °C. To this, 13.5 mL butadiene (0.165 mol, 210 eq), which was precooled to -20 °C, were added and the reaction mixture was stirred at -10 °C for 6 h. For analysis an aliquot of the reaction mixture was precipitated from degassed methanol. Then, the reaction mixture was cooled to -70 °C and 0.28 mL 1,1-diphenylethylene (DPE, 1.56 mmol, 2 eq) were added. After stirring for 30 min, 41.4 mL 2-vinylpyridine (2VP, 0.385 mol, 492 eq) were added and stirred for 45 min. The reaction was terminated by addition of 1 mL degassed methanol. The polymer was obtained by precipitation from deionzied water. After filtration, the PB-*b*-P2VP diblock copolymer was dried in a vacuum oven at 40 °C for 24 h.

Characterization of the BV diblock copolymer

For size exclusion chromatography (SEC) in THF PSS SDV gel columns (300 x 8 mm, 5 µm particle size) with 10^5, 10^4, 10^3 and 10^2 Å pore sizes were used. The signals were recorded by a RI 101 detector from Techlab Shodex and a UV detector ($\lambda = 254$ nm) from Knauer. For measurement, a flow rate of 1 mL min^{-1} at 40 °C was used. The calibration was performed by narrowly distributed PS standards and toluene as internal reference. The dispersity of the PB-precursor was determined to $Đ = 1.03$ and of the $B_{19}V_{81}^{60}$ diblock copolymer to $Đ_m = 1.04$.
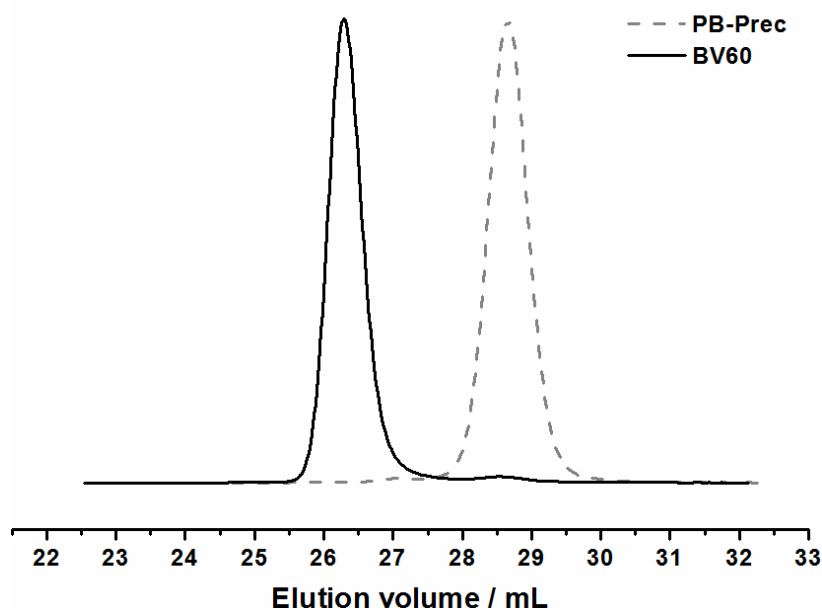
Figure S6-1. SEC traces of $B_{19}V_{81}^{60}$ (solid line) and the corresponding PB-Precursor (dashed line) in THF.

For determination of the molecular weight of the $B_{19}V_{81}^{60}$ diblock copolymer a combination of MALDI-TOF and ^{1}H-NMR spectroscopy was used. To this end, the molecular weight of the PB precursor was determined by MALDI-TOF using a Bruker Reflex III in linear mode (Figure 6-2) equipped with a nitrogen laser (Laser Inc., $\lambda = 337$ nm). For sample preparation, the *dried droplet* method was used. Therefore, the matrix *trans*-2-[3-(4-*tert*-butylphenyl)-2-methyl-2-propenylidene]malononitrile (DCTB, Sigma Aldrich, 99 %, $c = 20$ g L^{-1} in THF) was mixed in a ratio of 20:5:1 with the PB-precursor ($c = 10$ g L^{-1} in THF) and silver trifluoroacetate (Sigma Aldrich, 99.99 %, $c = 10$ g L^{-1} in THF), respectively, before applying 0.5 µL per spot of the mixture to the sample target. The solvent was evaporated before measurement yielding a thin film of matrix, polymer and salt. The molecular weight of the PB-precursor was determined to $M_n = 11700$ g mol^{-1}.

Using the molecular weight of the PB precursor determined by MALDI-TOF, the signals a, b and c, assigned to the PB protons, of the ^{1}H-NMR spectrum of the $B_{19}V_{81}^{60}$ diblock copolymer, measured in THF-d$_8$ (Deutero, 99.5 %) on a Bruker Ultrashield AC300 at 300 MHz, were calibrated in order to determine the molecular weight of the P2VP-block and the overall molecular weight. Comparison of the integrals of the characteristic PB- and P2VP protons yields in the composition of the diblock copolymer (19 wt % PB and 81 wt % P2VP)

and the molecular weight of the P2VP block ($M_n = 48500$ g mol^{-1}). The overall molecular weight was calculated to $M_n = 60200$ g mol^{-1}.
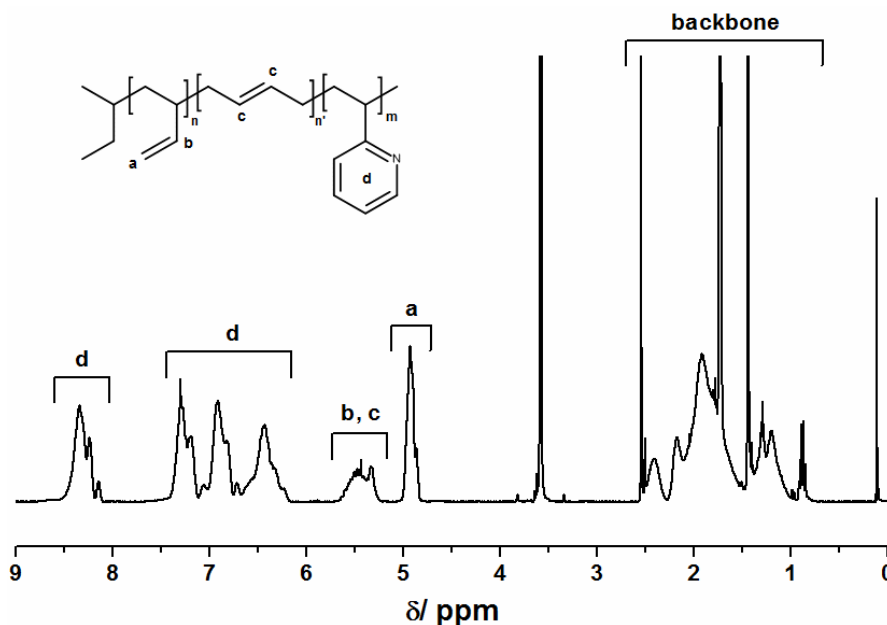
Figure S6-2. ^{1}H-NMR spectrum of the B$_{19}$V$_{81}$^{60} diblock copolymer measured in THF-d$_8$.

The polymerfilm containing hexagonal PB cylinders in a P2VP matrix (Fig. S6-3A) was crosslinked. After dispersing this polymerfilm in HCl a worm-like structure was developed (Fig. S6-3B). So, the cylindrical morphologie was still intact. This worm-like structure was preserved after methylation of the P2VP groups.
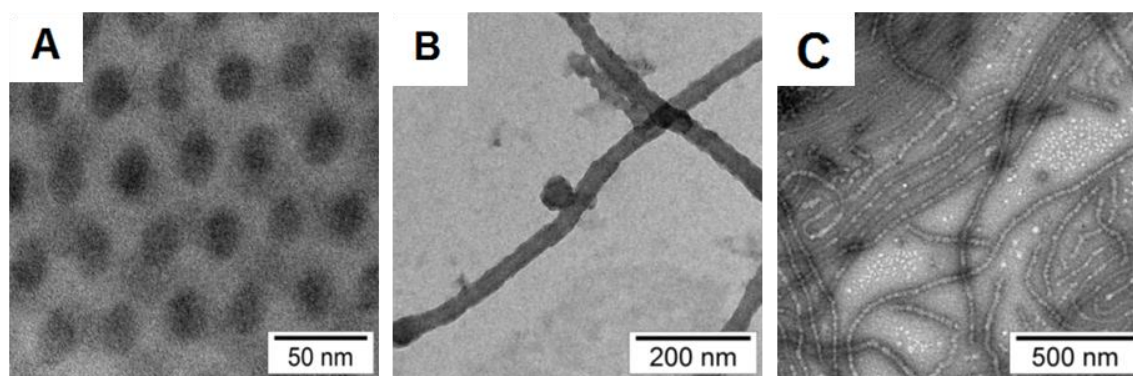
Figure S6-3. TEM micrographs of A) hexagonally ordered B$_{19}$V$_{81}$^{60} diblock copolymer film after crosslinking, B) CPBs after redispersion of the film in HCl and C) methylated, cationic CBPs dispersed in DMSO (B, C selectively stained with OsO$_4$).

Design of the photocatalytic reator
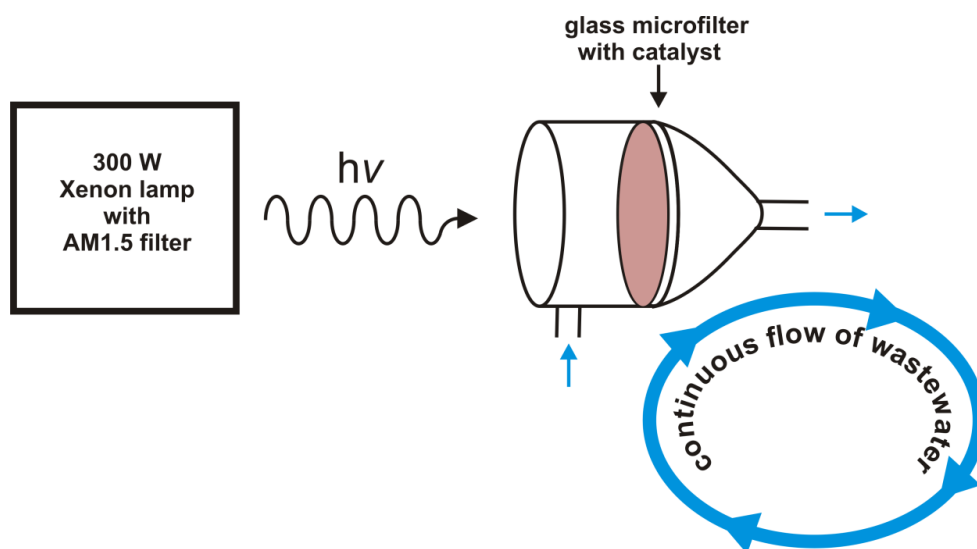
Scheme S6-1. Schematic alignment of the photocatalytic reactor.

Rietveld data of ZnO nanoparticles, hybridmaterial and ZnO nanotubes
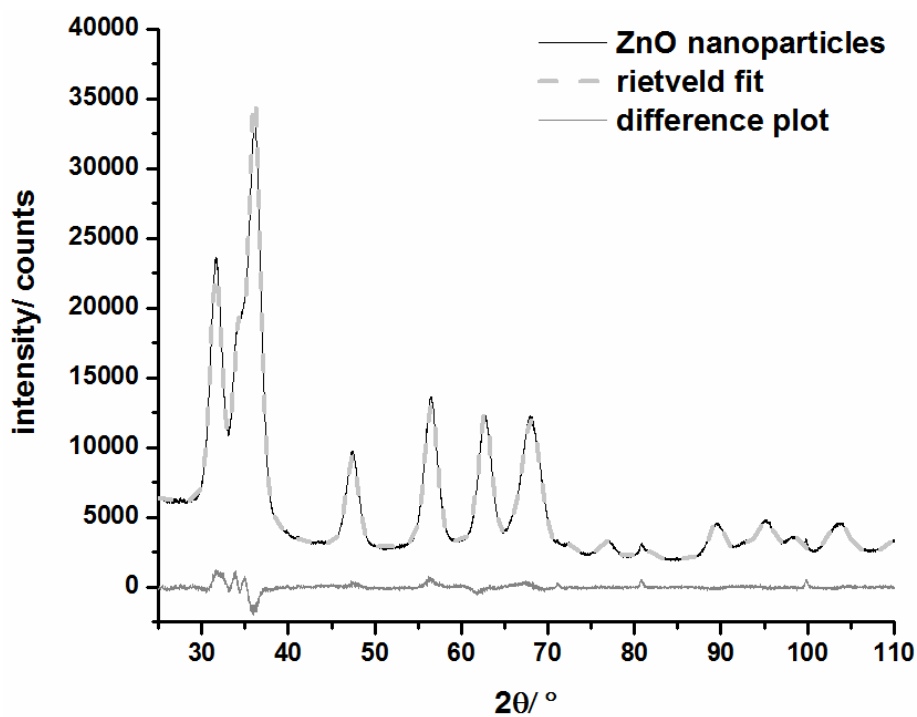
Figure S6-5. XRD data of ZnO nanoparticles (black), calculated Rietveld refinement (light grey) and difference plot (dark grey).

Table S6-1. Refinement parameters for ZnO nanoparticles.

Space group	P6$_3$mc
R(wp)	2.87
R(p)	2.26
R(bragg)	1.71
Cell constants [Å]:	
a	3.245(2)
b	3.245(2)
c	5.210(2)
Zero point correction	-0.097(2)
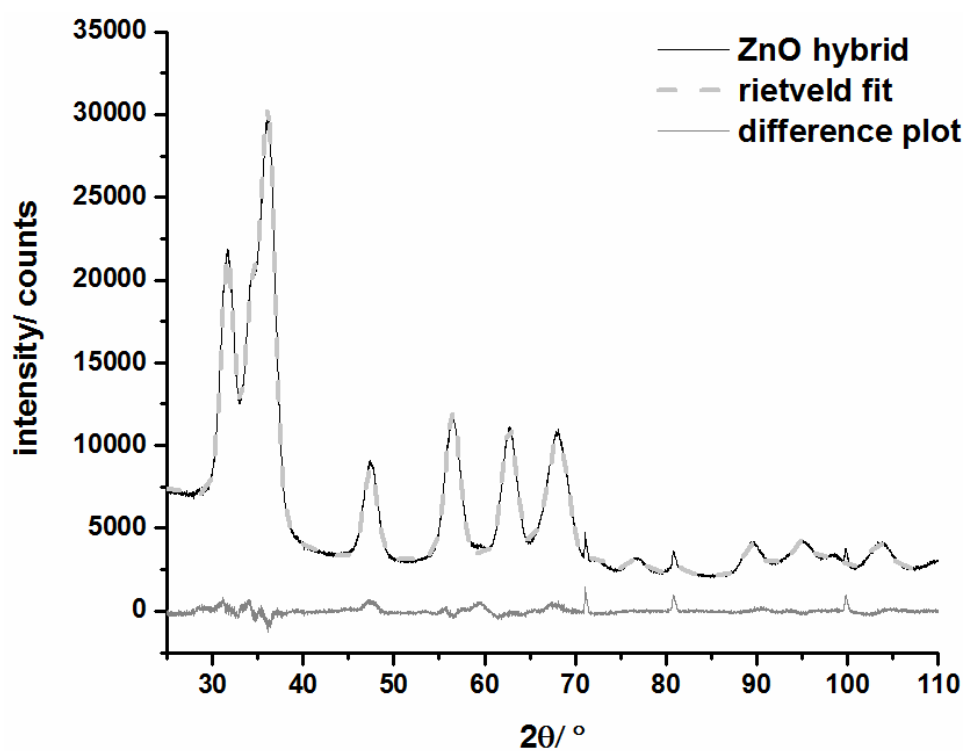
Figure S6-6. XRD data of ZnO hybridmaterial (black), calculated Rietveld refinement (light grey) and difference plot (dark grey).

Table S6-2. Refinement parameters for ZnO hybridmaterial.

Space group	P6₃mc
R(wp)	3.37
R(p)	2.27
R(bragg)	1.62
Cell constants [Å]:	
a	3.255(1)
b	3.255(1)
c	5.215(3)
Zero point correction	-0.018(2)
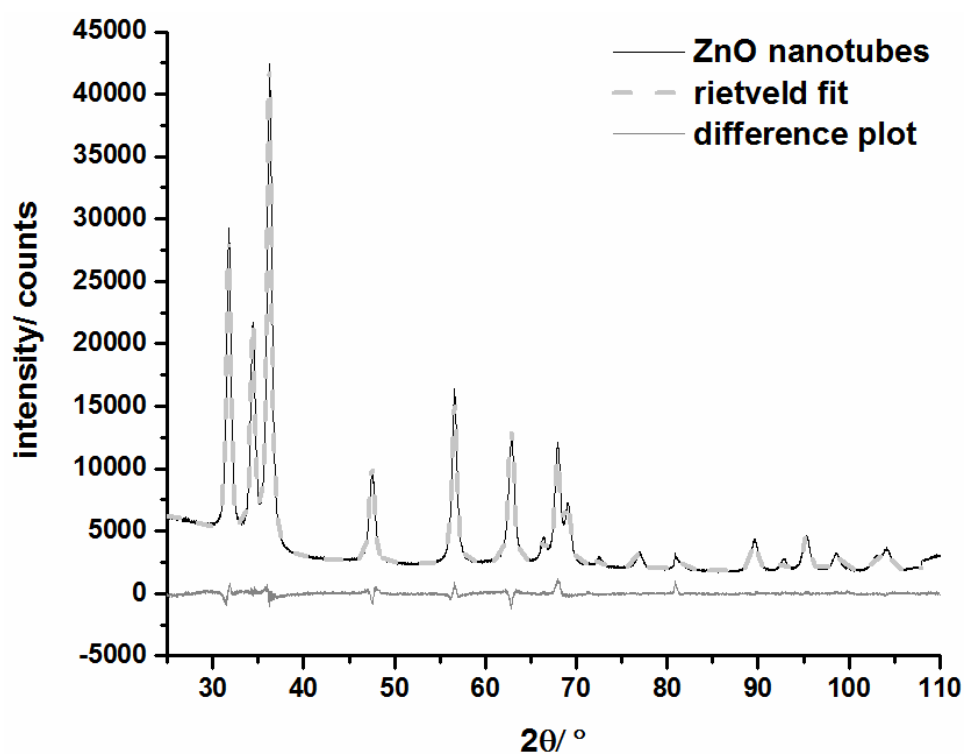
Figure S6-7. XRD data of ZnO nanotubes (black), calculated Rietveld refinement (light grey) and difference plot (dark grey).

Table S6-3. Refinement parameters for ZnO nanotubes.

Space group	$P6_3mc$
R(wp)	3.10
R(p)	2.26
R(bragg)	0.79
Cell constants [Å]:	
a	3.251(2)
b	3.251(2)
c	5.208(4)
Zero point correction	0.015(8)
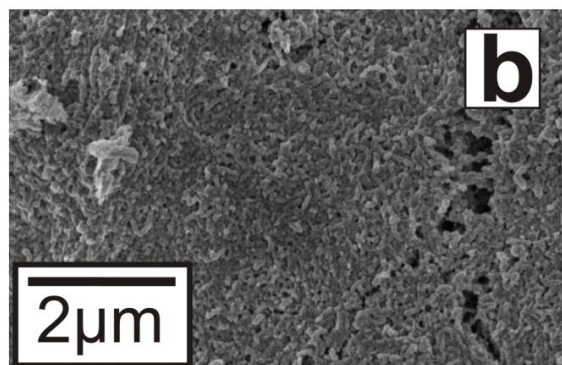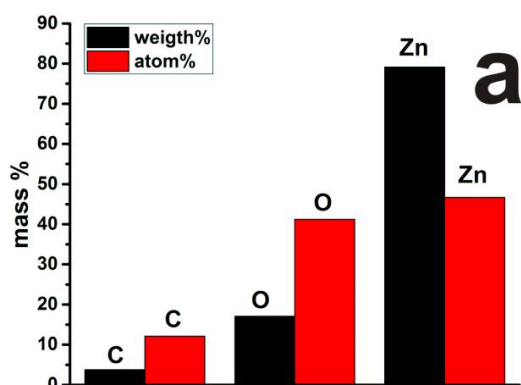
Figure S6-8. a) Weight- (black) and atom percent (red) of the ZnO nanotubes taken from EDX measurements in the range of b) SEM image.
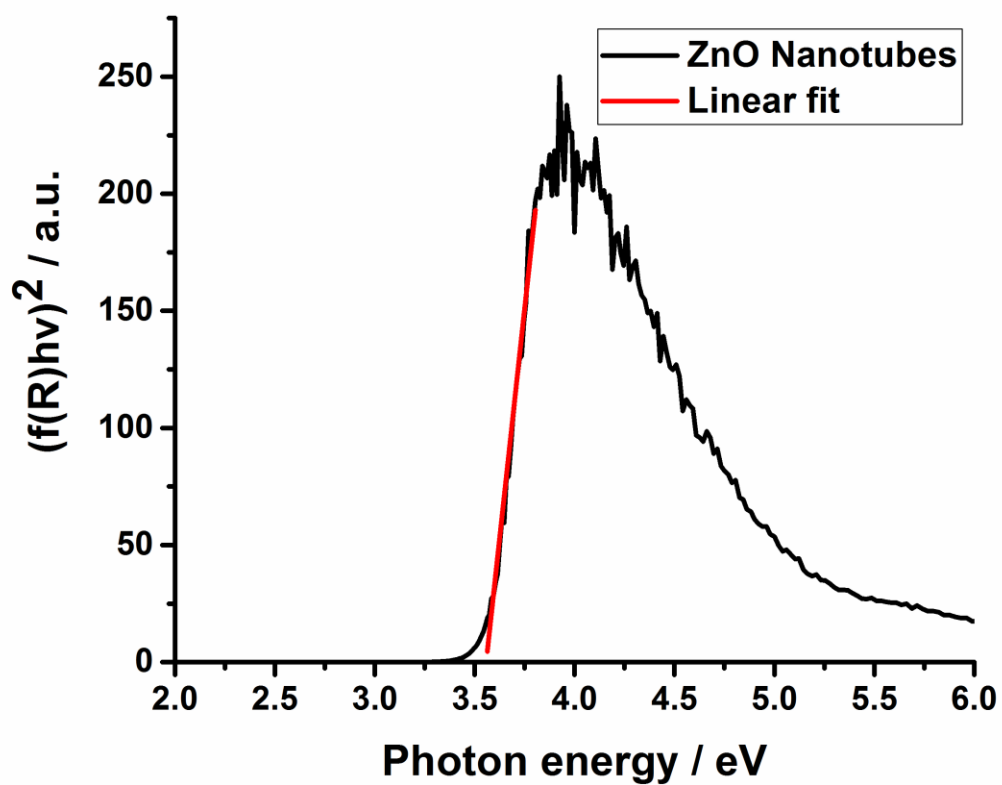
Figure S6-9. Optical band gap of ZnO nanotubes.

7 Mesostructured ZnO/Au Nanoparticle Composites with Enhanced Photocatalytic Activity

Carina Bojer,[1+] Judith Schöbel,[2+] Thomas Martin,[1] Thomas Lunkenbein,[3] Daniel R. Wagner,[1] Andreas Greiner,[2,4] Josef Breu[1,4] and Holger Schmalz[2,4*]*

[1] Anorganische Chemie I, Universität Bayreuth, 95440 Bayreuth, Germany

[2] Makromolekulare Chemie II, Universität Bayreuth, 95440 Bayreuth, Germany

[3] Abteilung für Anorganische Chemie, Fritz-Haber Institut der Max-Planck Gesellschaft, 14195 Berlin, Germany

[4] Bavarian Polymer Institute (BPI), Universität Bayreuth, 95440 Bayreuth, Germany

[+] C.B. and J.S. contributed equally to this work.
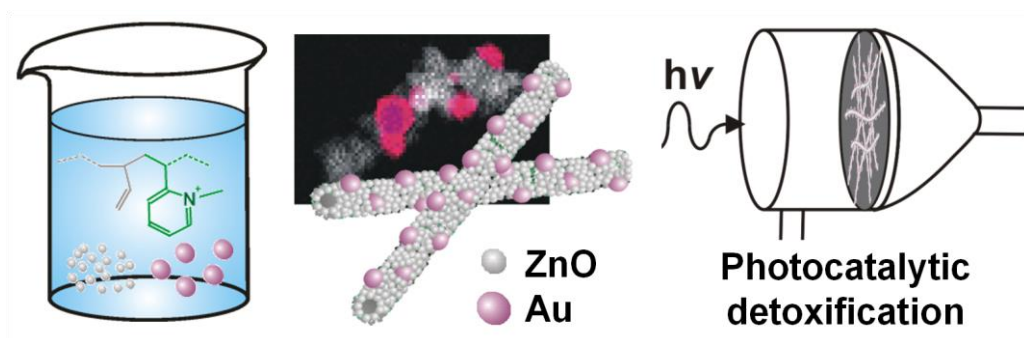
Abstract

Ease of catalyst separation from reaction mixtures represents a significant advantage in heterogeneous photocatalytic wastewater treatment. However, the activity of the catalyst strongly depends on its surface-to-volume ratio. Here, we present an approach based on cylindrical polybutadiene-*block*-poly(2-vinylpyridine) polymer brushes as template, which can be simultaneously loaded with zinc oxide (ZnO) and gold (Au) nanoparticles. Pyrolytic template removal of the polymer yields in mesostructured ZnO/Au composites, showing higher efficiencies in the photocatalytic degradation of ciprofloxacin and levofloxacin (generic antibiotics present in clinical wastewater) as compared to neat mesostructured ZnO. Upscaling of the presented catalyst is straightforward promising high technical relevance.

7.1 Introduction

The removal of pharmaceuticals from clinical wastewater is a burning issue in environmental science. Efficient removal of active drugs like, antibiotics, cytostatics, beta-blockers or antiphlogistics, is required before treatment by standard biological purification techniques in sewage plants.[1–5] For instance, ciprofloxacin, a widely employed antibiotic from the fluoroquinolone group, is problematic due to its gentoxicity.[6,7] Consequently, high stability, low biodegradability and toxicity of these active agents limit the use of mild biological degradation processes and there is a demand for chemical oxidation.[8] Advanced oxidation processes (AOP), which are based on the formation of highly reactive hydroxyl radicals, provide promising results in the catalytic degradation of organic pollutants. In particular, photocatalytic AOPs are of special interest, as in addition to UV light only a transition metal oxide catalyst, e.g. titanium dioxide (TiO_2) or zinc oxide (ZnO), is needed.[9–11] If solar energy, consisting of UV and visible light, is applied to the catalyst, an enhancement of the activity by doping the transition metal oxide with noble metal nanoparticles (NPs), e.g., gold, platinum or silver, has been observed. This effect is attributed to the localized surface plasmon resonance of the noble metal NPs, which causes an increased absorption of visible light and a charge-transfer to the transition metal oxide.[12–15]

With respect to clinical wastewater (typical pH = 8), the catalyst has to fulfil different requirements.[16,17] Most pharmaceuticals are rendered soluble in body fluids by deprotonated carboxylic acid groups. For ciprofloxacin the isoelectric point of the zwitterion is at a pH value of 7.4.[18] Thus, a catalyst bearing a positive surface charge at a pH of 8 is advantageous, as this will enhance the electrostatic interactions between antibiotic and catalyst. Previous studies showed that in contrast to Degussa P25, a TiO_2 catalyst with its point of zero charge (PZC) at a pH of 6.9, ZnO fulfils this requirement as its PZC is 9.2.[19,20] Another important criterion for increasing catalytic activity is the accessible surface area of the catalyst. Using nanomaterials, like nanoparticles, -tubes, or -wires, the active surface can be maximized due to their high surface-to-volume ratio, resulting in an increased performance for example in environmental remediation.[4] However, the reusability of NP catalysts is limited due to the inherently difficult separation of NPs from a fluid reaction media. Applying polymer templates for the controlled assembly of NPs into mesostructured hybrid materials represents a good compromise between preserving a high accessible surface area while allowing for filtration of the catalyst (Scheme 7-1). In

particular, cylindrical polymer brushes (CPBs) proved to be promising template materials, as their composition and functionality can be tailored to meet the demands for an efficient mesostructuring of NPs.[21–24] As shown with different transition metal oxides, like TiO_2 or WO_3, these supports are able to prevent segregation and, therefore, a loss of surface area.[25–27] Pyrolytic removal of the polymeric template leads to mesostructured one-dimensional aggregates where adjacent NPs become connected *via* necks during sintering. [28,29] The resulting nonwoven structures provide sufficient mechanical stability to be used in continuous flow cells, while at the same time offering a high accessible surface area.[30]

Herein, we report the synthesis of mesostructured ZnO/Au NP composites for the efficient detoxification of hospital wastewater, exemplified on the photocatalytic degradation of ciprofloxacin and levofloxacin. To this end, cationic CPBs, consisting of a cross-linked polybutadiene (PB) core and a quaternized poly(2-vinylpyridine) (P2VP) corona, were used as template for the simultaneous mesostructuring of ZnO and Au NPs. Pyrolytic removal of the polymeric template leads to hierarchically structured nonwovens composed of catalytically active ZnO/Au nanowires (Scheme 7-1).
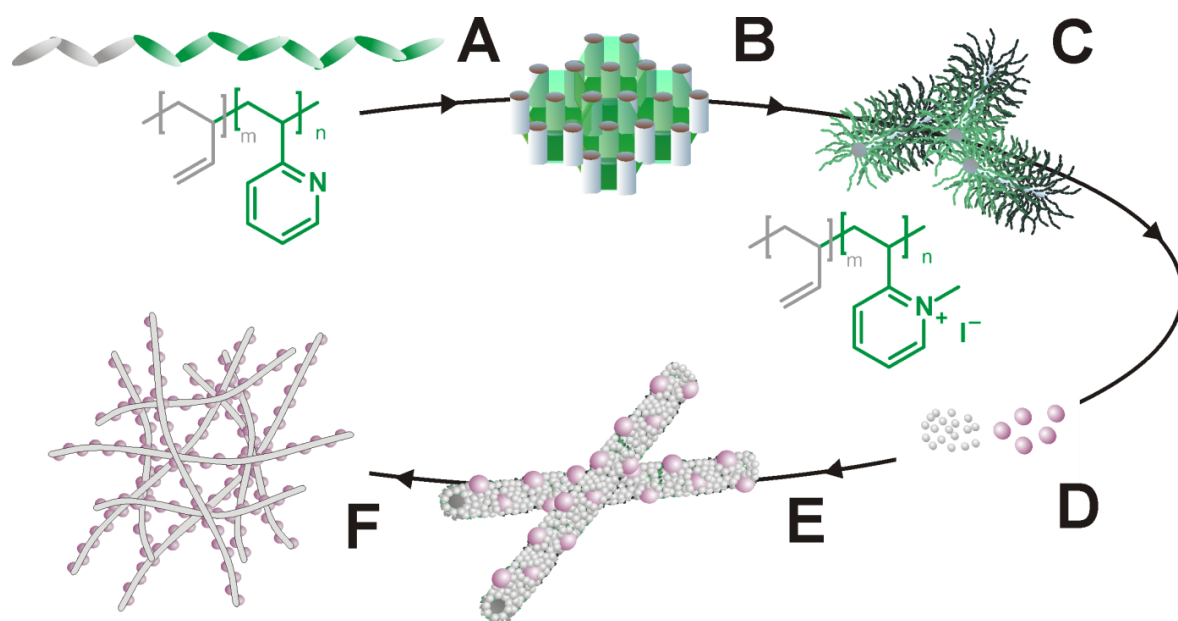
Scheme 7-1. Self-assembly of a BV diblock copolymer (A) results in a cylindrical bulk morphology with hexagonally packed PB cylinders in a P2VP matrix (B). Crosslinking the PB cylinders and quaternization of the P2VP corona blocks produces cationic CPBs (C). These CPBs are used as templates for the simultaneous loading with ZnO and Au NPs (D). The resulting hybrid (E) is transformed into a mesostructured nonwoven (F) consisting of ZnO/Au nanowires by calcination.

7.2 Experimental Part

Chemicals

All chemicals were purchased from Sigma-Aldrich (Germany) and used as received if not otherwise noted.

Synthesis of the BV diblock copolymer

The polybutadiene-*block*-poly(2-vinylpyridine) (BV) diblock copolymer was synthesized by sequential living anionic polymerization in THF with *sec*-butyllithium as initiator, as published elsewhere.[28] The molecular weight and the composition of the BV diblock copolymer were determined by a combination of ^{1}H-NMR spectroscopy (Bruker Ultrashield AC300) and MALDI-TOF MS (Bruker Reflex III) and resulted in $B_{19}V_{81}^{60}$ (subscripts denote the mass fraction of the corresponding block in wt-% and the superscript gives the overall molecular weight in kg mol^{-1}). The molar mass dispersity of the BV diblock copolymer was determined by THF-SEC to $Đ_M = 1.02$.

Formation of the cationic CPB template

Typically, 1 g of a $B_{19}V_{81}^{60}$ film with 0.1 g of the photoinitiator Lucirin TPO (BASF) was prepared by solvent-casting from chloroform. The resulting hexagonally ordered film was crosslinked using a UV hand lamp (Hoenle, 2 h per side). The crosslinked $B_{19}V_{81}^{60}$ film was dissolved in 200 mL chloroform and 3 mL of an iodomethane solution (99 %) was added dropwise for quaternization of the poly(2-vinylpyridine) (P2VP) block. The solvent and the iodomethane solution were allowed to evaporate. The quaternized product (BV_q) was washed with pentane, dissolved in water and freeze-dried.

Synthesis of the hybrid material and calcination

As an example, for the synthesis of the ZnO/Au_12 hybrid material 200 mg of BV_q was dissolved in 200 mL DMSO. To this solution, 6 mL of tetrachloroauric acid trihydrate (Alfa Aesar, 0.1 M in THF) was added. Subsequently, 3 mL of a sodium borohydride solution (1 M in deionized water) was added and the colour changed to deep purple. Immediately, 125 mL of an acetate-stabilized ZnO NP dispersion (6.9 g L^{-1} in ethanol, synthesis reported

in Ref. 30) was added. The reaction mixture was stirred for 10 min. The purple precipitate was isolated by centrifugation (3 min, 7000 rpm) and washed 5 times with ethanol and one time with deionized water and then freeze-dried. The details of all synthesized materials are summarized in Table S7-1. Heat treatment at 490 °C for 5 min in a tube furnace (heating/cooling rate 180 K h^{-1}) under air lead to the removal of the organic CPB template and sintering into an all-inorganic nonwoven composite structure.

Photocatalytic degradation

Photocatalytic degradation of anionic antibiotics (ciprofloxacin and levofloxacin) was realized in a self-constructed continuous flow reactor (Scheme S7-1). The synthesized ZnO/Au nanowire photocatalyst (15 mg) was drop coated on a glass microfiber filter (Whatman, 37 mm diameter) and 400 mL of the ciprofloxacin or levofloxacin solution ($c = 2 \cdot 10^{-5}$ mol L^{-1}, pH = 8 (borate/HCl buffer, Titrisol)) was circulated at a flow rate of 12 L h^{-1}. The degradation with solar spectrum (300 W Xenon lamp, AM1.5 filter, 1000 W m^{-2}) was monitored using UV-Vis spectroscopy (samples taken every 5-15 min). The experiments were done without catalyst as a reference, with Degussa P25, ZnO nanotubes and ZnO/Au nanowire composites with different ZnO/Au ratios. All catalysts were tested at least three times to guarantee reproducible results.

Instruments

Powder X-ray diffraction (PXRD) measurements were done using a STOE Stadi P diffractometer. CuK$_{\alpha 1}$ radiation and a Mythen 1K silicon strip-detector were used. Rietveld analysis was done with TOPAS Academic (fundamental parameters approach for profile fitting). The crystallite sizes were determined using implemented macros (elliptical particles) and the composition was estimated using quantitative Rietveld-refinement.

Transmission electron microscopy (TEM) micrographs were acquired using a Zeiss 922 Omega EFTEM (Zeiss NTS GmbH, Oberkochen, Germany), operating at an accelerating voltage of 200 kV. Zero-loss filtered images were taken with a bottom-mounted CCD camera system (Ultrascan 1000, Gatan). The micrographs were processed by the digital imaging processing software Gatan Digital Micrograph 3.9 for GMS 1.4. The samples were

prepared by drop-coating of dilute dispersions of the hybrid materials/composites in ethanol ($c = 0.1$ g L^{-1}) onto carbon-coated copper grids, followed by blotting with a filter paper.

High resolution TEM and local energy dispersive X-ray (EDX) maps were recorded on a double corrected JEOL ARM-200CF equipped with a high angle Silicon Drift EDX detector with a solid angle of up to 0.98 sterradians.

Scanning electron microscopy (SEM) images and energy dispersive X-ray analysis (EDX) data were obtained with a LEO 1530 FESEM scanning electron microscope equipped with a field emission cathode.

A Quantachrome Autosorb 1 was used to determine the surface area with N_2 at 77 K after degassing the sample at 363 K for 12 h.

UV-Vis absorption spectra were measured with a Varian Cary 300 spectrometer using Hellma precision cells made of Quartz SUPRASIL (type 100-QS, light path 10 mm).

Thermal gravimetric analysis (TGA) was performed on a Netzsch TG 209F1 Libra under synthetic air. The samples were heated from 25-800 °C at a heating rate of 10 K min^{-1}.

The PZC was determined using a ParticleMetrix StabiSizer PMX 200C. 50 mg catalyst in 10 mL water with a pH of 10.5 (adjusted with 0.01 M NaOH) were titrated with 0.05 M HCl until the streaming potential was zero.

7.3 Results and Discussion

Formation of cylindrical ZnO/Au hybrids

ZnO/Au hybrids were prepared by employing cationic CPBs as template for the simultaneous loading with Au and ZnO NPs (Scheme 7-1). The cationic CPBs were obtained from a polybutadiene-*block*-poly(2-vinylpyridine) (BV) diblock copolymer (B$_{19}$V$_{81}$^{60}: subscripts denote the mass fraction of the corresponding block in wt-% and the superscript gives the molecular weight in kg mol^{-1}), which forms a bulk morphology with hexagonally arranged PB cylinders embedded in a P2VP matrix (Scheme 7-1A, B). Subsequent photo-crosslinking of the PB cylinders followed by dissolution and quaternization of the P2VP block resulted in the desired CPBs with a positively charged corona (Scheme 7-1C). The Au NPs were generated *in situ* by reduction of tetrachloroauric acid trihydrate and as a ZnO source phase pure, acetate-stabilized ZnO NPs with a number-weighted hydrodynamic

diameter of $D_h = 3.2$ nm were used (Scheme 7-1D, E; Table S7-1). Details on the synthesis and characterization of the used monodisperse ZnO NPs can be found elsewhere.[30] To investigate the effect of the Au content on the photocatalytic degradation of antibiotics (ciprofloxacin and levofloxacin), four different ZnO/Au hybrid materials (8 , 12 , 15 and 26 wt-% Au with respect to the overall amount of inorganic material in the hybrid) were synthesized. The notation ZnO/Au_x, with x denoting the Au content in wt-%, will be used in the following. The total amount of ZnO and Au immobilized by the cationic CPB template was determined by TGA measurements to 74-79 wt-% (Fig. S7-1). This is in good agreement with the employed amounts of the CPB template, ZnO NP and Au precursor in the synthesis of the hybrid materials (80 wt-% CPB template).

The TEM micrographs of the obtained hybrids reveal the controlled co-assembly of ZnO and Au NPs under preservation of the cylindrical structure of the cationic CPB template (Fig. 7-1). The cylindrical PB core of the CPB template can be clearly identified in the corresponding greyscale analysis for the ZnO/Au_12 hybrid, shown in the inset of Fig. 7-1B.
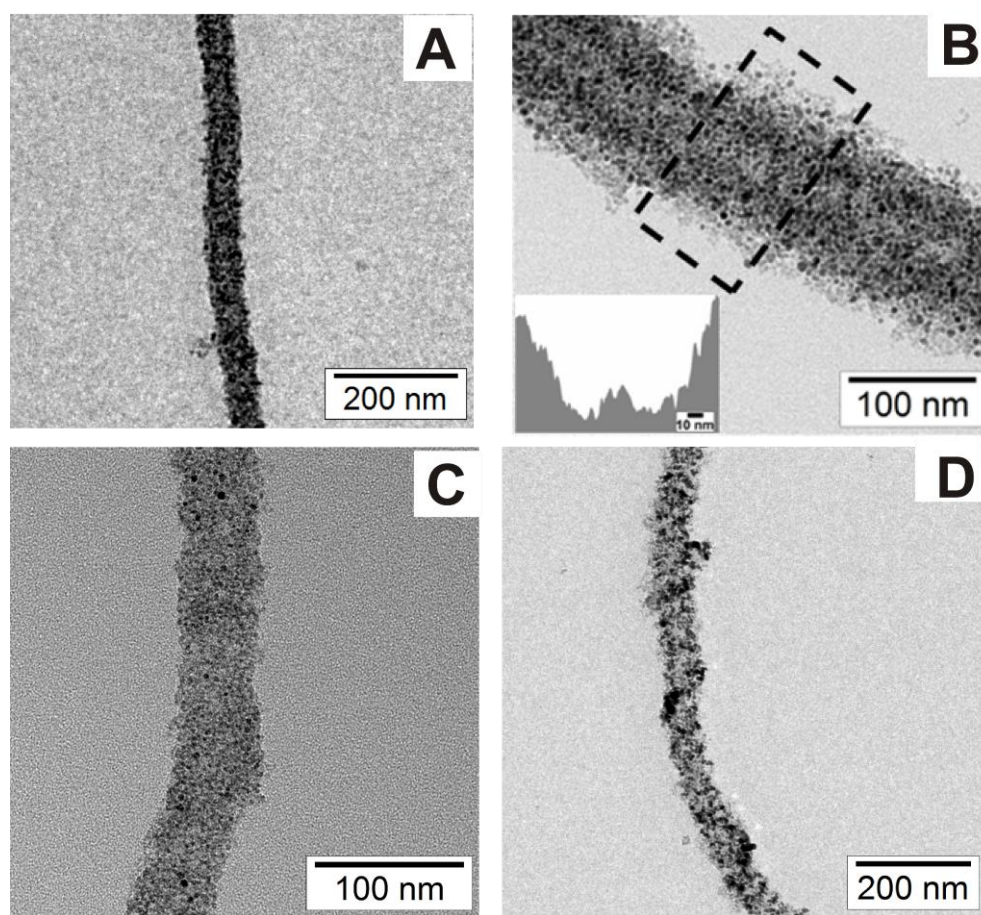
Fig. 7-1. TEM images of the ZnO/Au_8 (A), ZnO/Au_12 (B; inset in B: grey scale analysis), ZnO/Au_15 (C) and the ZnO/Au_26 hybrid materials (D).

Formation of ZnO/Au composite nanowires

ZnO/Au composite nanowires were obtained by pyrolysis of the ZnO/Au hybrid cylinders in air at 490 °C. After template removal, the one-dimensional structure of the CPB template was retained, resulting in the formation of mesostructured ZnO/Au composite nonwovens (Fig. 7-2A-D). Only for the ZnO/Au_26 nonwoven a partial agglomeration of the hybrid cylinders upon calcination can be observed. The composition of the obtained ZnO/Au nanowires was determined by EDX measurements (Table S7-2) and is in good agreement with the used amount of educts. Elemental analysis (Table S7-3) and TGA measurements (Fig. 7-S1) confirm the absence of organic material after pyrolysis (less than 0.2 %), indicating the complete removal of the organic CPB template. The mesostructured nonwovens show high specific surface areas of 25 - 48 m^2g^{-1}, as determined by nitrogen physisorption (Fig. S7-2, Table S7-4). The high-angle annular dark-field scanning transmission electron microscopy (HAADF-STEM) image of ZnO/Au_12 nanowires (Fig. 7-2E) confirms the retention of the wire-like mesostructure. In HAADF-STEM the contrast is due to Rutherford scattering, which is almost proportional to Z^2. Thus, Au (bright) and ZnO (grey) moieties are directly distinguishable and can further be identified by an energy dispersive X-ray (EDX) map of the same particles (Fig. 7-2E, inset). The HAADF-STEM image reveals a partial wetting of the Au NPs on top of the ZnO nanocrystals, thus, increasing the Au/ZnO perimeter. In addition, the HR-TEM image in Fig. 7-3F highlights a representative mesostructure of the nanowires, which is composed of randomly oriented, individual ZnO nanocrystals that form intraparticular mesopores. Those intraparticular mesopores may ensure a higher mass transport in the photocatalytic liquid phase detoxification reaction. Moreover, the ZnO nanowires are partially decorated by isolated Au nanoparticles.
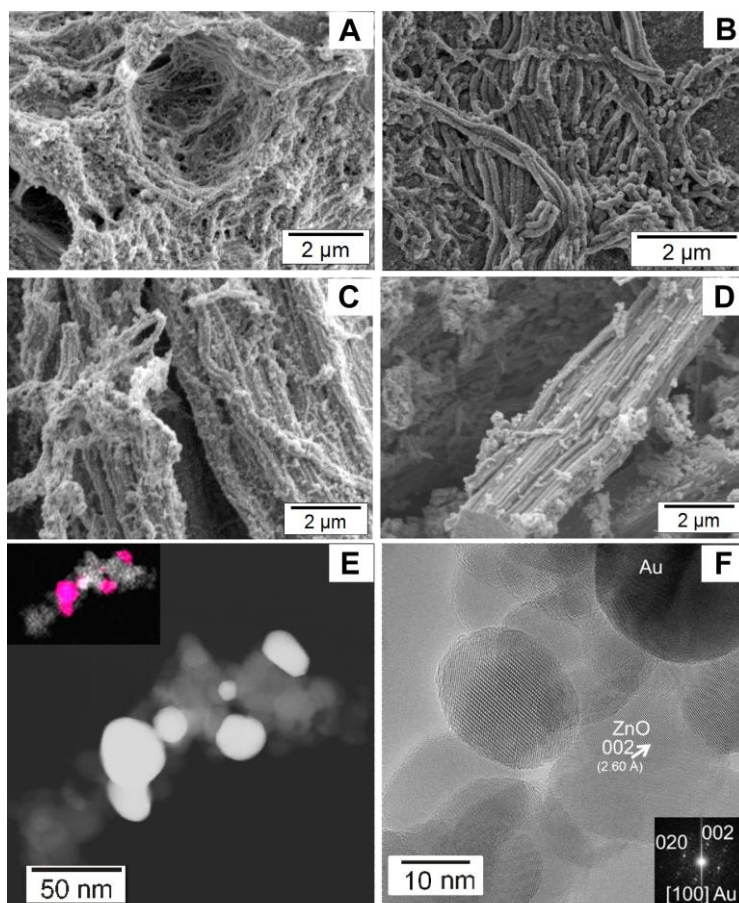
Fig. 7-2. SEM images of ZnO/Au_8 (A), ZnO/Au_12 (B), ZnO/Au_15 (C) and ZnO/Au_26 nanowires (D). HAADF-STEM image of ZnO/Au_12 nanowires (E, inset: EDX map of the same particle; white – ZnO; red – Au). HR-TEM image of ZnO/Au_12 nanowires (F); the inset denotes the Fast Fourier Transform (FFT) of the region that is labelled with Au.

In order to get a closer insight into the calcination process and its impact on the Au and ZnO NP sizes, the morphological changes for the ZnO/Au_12 and ZnO/Au_26 hybrid cylinders upon calcination were studied by PXRD (Fig. 7-3A, B). The PXRD data show a halo in the range of $2\theta = 20\text{-}30°$, which is characteristic for the amorphous CPB template. The crystalline reflections of the hybrid materials can be assigned to ZnO and Au, respectively. For ZnO/Au_12 Rietveld refinement yields average coherent scattering domains of 3.4(2) x 3.7(2) nm for ZnO and 3.5(2) x 4.9(2) nm for Au, respectively (Fig. S7-3, Table S7-5). For ZnO/Au_26 domain sizes of 3.5(2) x 4.4(3) nm for ZnO and 3.7(6) x 5.3(4) nm for Au (Fig. S7-4 and Table S7-6) were obtained.
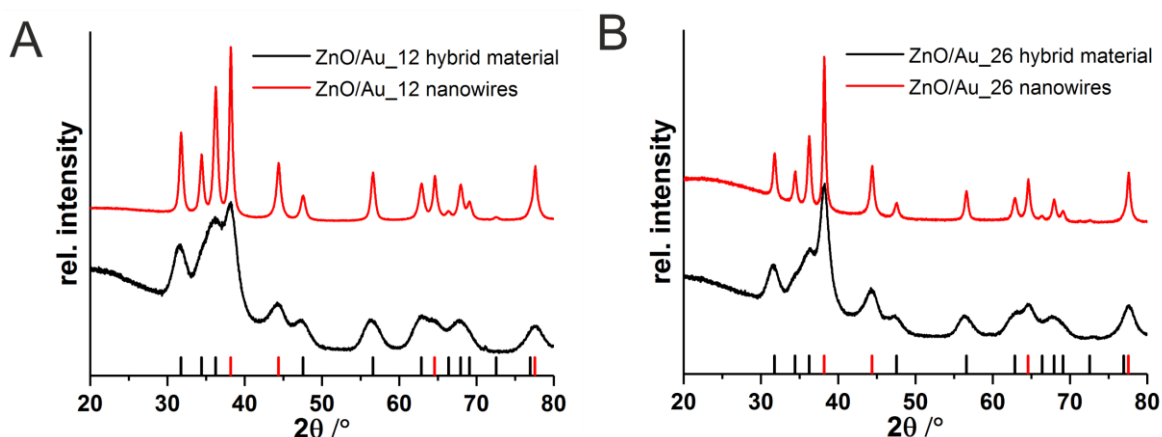
Fig. 7-3. PXRD patterns of ZnO/Au_12 (A) and ZnO/Au_26 (B) hybrid cylinders and nanowires with the reference cards of ZnO (black ticks PDF-Nr.: 00-036-145) and Au (red ticks PDF-Nr.: 00-004-0784).

The decrease of the full width at half maxima of PXRD peaks (ZnO/Au_12, Fig. 7-3A; ZnO/Au_26, Fig. 7-3B) indicates Ostwald ripening upon pyrolysis. For ZnO/Au_12 Rietveld analysis confirms the growth to a crystallite size of 12.5(4) x 15.5(4) nm for ZnO and 17.5(4) x 24.4(5) nm for Au, respectively (Fig. S7-5 and Table S7-7). A similar trend is observed for ZnO/Au_26, showing increased crystallite sizes of 14.5(8) x 16.9(8) for ZnO and 16.9(3) x 23.7(5) for Au (Fig. S7-6 and Table S7-8). The composition of the calcinated ZnO/Au_12 and ZnO/Au_26 composites is confirmed by Rietveld analysis and is in good agreement with the educt stoichiometry (12 wt-% Au and 26 wt-% Au, respectively) and EDX measurements (Table S7-2).

Photocatalytic degradation of negatively charged antibiotics

The photocatalytic degradation of ciprofloxacin and levofloxacin (isoelectric points (zwitter-ion): 7.4 and 6.8, respectively)[18], applying the ZnO/Au composite nanowires as catalysts, was studied using a continuous flow reactor. For comparative studies, neat ZnO nanotubes and Degussa P25 (TiO$_2$ based photocatalyst) were used. In the continuous flow reactor, 3.5 ppm of the catalyst material (with respect to ciprofloxacin or levofloxacin) was placed onto a filter paper to guarantee a homogeneous flow and the photocatalytic degradation of the two antibiotics was monitored at pH = 8 for 120 min applying terrestrial solar spectrum. No significant degradation was observed in the absence of a catalyst (Fig. S7-7A). The ZnO/Au_12 composite nanowires revealed the highest efficiency in the photocatalytic degradation of ciprofloxacin with a degradation of 16% in 120 min (Fig. 7-4A). For

composite nanowires with a lower (8 wt-%) as well as higher (15 and 26 wt-%) Au content a significantly lower conversion was observed. Similar results were obtained for the degradation of levofloxacin (Fig. S7-8A), i.e., the ZnO/Au_12 composite nanowires showed the highest efficiency in photocatalytic degradation within the tested catalysts. The inferior behaviour for higher Au-loading can be attributed to electron-hole recombination centres, which limit the synergistic effect of the ZnO/Au composite.[31] The reduced performance of ZnO/Au_15 and ZnO/Au_26 also indicates that thermal effects due to the strong localized surface plasmon resonance absorption of Au NPs can be neglected, as in this case a higher activity would be expected for composites with higher Au contents. In comparison to previous studies on the degradation of ciprofloxacin with neat ZnO nanotubes,[30] the ZnO/Au_12 composite material shows a ca. 40% improved performance, as with the ZnO nanotubes a conversion of only 12% could be achieved under identical reaction conditions (Fig. S7-7A). A similar effect was observed for the photocatalytic degradation of levofloxacin (Fig. S7-8A).

The photocatalytic activity of the ZnO/Au_12 nanowires in the degradation of ciprofloxacin is moreover significantly improved with respect to Degussa P25, a commercial TiO_2 based photocatalyst (Fig. S7-7A). The advantage of ZnO/Au nanowire composites (PZC: 8.8) over Degussa P25 (PZC: 6.9)[19, 20] can be attributed to the opposite surface charge of ZnO based catalysts and ciprofloxacin (isoelectric point (zwitterion): 7.4)[18] at pH = 8 that favours drug adsorption on the catalyst surface. Any influence attributed to differences in the specific surface area of the catalysts can be ruled out, as the ZnO/Au_12 catalyst, showing the highest activity, exhibits the lowest specific surface area (25 m^2 g^{-1}, Table S7-4).
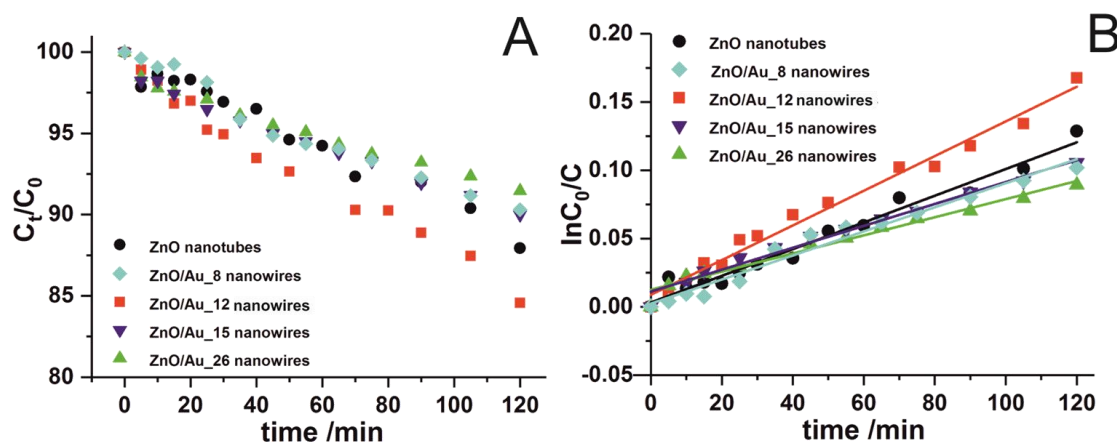
Fig. 7-4. Time-dependent decrease of ciprofloxacin concentration during irradiation with terrestrial solar spectrum (A) and corresponding first-order kinetics plots (B) for ZnO nanotubes and ZnO/Au composite nanowires.

As the photocatalytic degradation of ciprofloxacin using a ZnO or TiO$_2$ based catalyst already showed, this reaction follows a pseudo first-order kinetics and the apparent rate constants k' can be calculated from the slope of the corresponding first-order kinetics plot (Fig. 7-4B). The k' value for ZnO/Au_12 nanowires is $1.3 \cdot 10^{-3}$ min^{-1}. Compared with the k' value of neat ZnO nanotubes ($k' = 9.6 \cdot 10^{-4}$ min^{-1}) the ZnO/Au_12 catalyst is 1.4 times faster. With reference to previous results, the ciprofloxacin degradation with ZnO/Au_12 nanowires is 3.7 times faster as compared to the standard Degussa P25 (Fig. S7-7B, Table S7-9). In case of levofloxacin, a 1.6 times faster degradation was observed for ZnO/Au_12 nanowires (Fig. S7-8B, Table S7-10). Conseqeuently, combining the electrostatically favoured adsorption of the antibiotics on the positively charged ZnO surface with the enhancement of Au NPs in mesostructured ZnO/Au_12 nonwovens has a distinct synergistic effect on the photocatalytic degradation. This results in an increase in degradation rate of about 40% for ciprofloxacin and 60% for levofloxacin, respectively, compared to neat ZnO nanotubes.

7.4 Conclusion

In this study, we used cationic CPBs as template for mesostructuring two different types of NPs with the aim of taking advantage of synergistic effects for the photocatalytic degradation of antibiotics in wastewater. ZnO and Au NPs were assembled simultaneously in a random fashion on cationic CPBs, resulting in mesostructured, nonwoven-like networks of ZnO/Au nanowires after pyrolytic template removal. The ZnO/Au nanowires with 12 wt-% Au show a significantly enhanced efficiency in the photocatalytic degradation of ciprofloxacin and levofloxacin with terrestrial solar spectrum, both with respect to neat ZnO nanotubes and Degussa P25 NPs, respectively. This can be ascribed to the improved adsorption of the antibiotics, which are negatively charged at the slightly basic pH of hospital wastewater, on the positively charged ZnO surface combined with the enhancement due to the localized surface plasmon resonance of the Au NPs. The assembly of different types of NPs allows not only the synthesis of tailor-made catalyst systems for photocatalytical processes, but can also be transferred to other NP combinations with interesting catalytic properties. The non-woven structure of the catalyst ensures an easy recovery from the fluid reaction medium and, thus, excellent reusability, making this system highly interesting for technical applications.

7.5 References

[1]   N.M. Vieno, H. Härkki, T. Tuhkanen, L. Kronberg, Occurrence of Pharmaceuticals in River Water and Their Elimination in a Pilot-Scale Drinking Water Treatment Plant, Environ. Sci. Technol. 41 (2007) 5077–5084.

[2]   E. Carraro, S. Bonetta, C. Bertino, E. Lorenzi, S. Bonetta, G. Gilli, Hospital Effluents Management: Chemical, Physical, Microbiological Risks and Legislation in Different Countries, J. Environ. Manage. 168 (2016) 185–199.

[3]   J. Rivera-Utrilla, M. Sánchez-Polo, M.Á. Ferro-García, G. Prados-Joya, R. Ocampo-Pérez, Pharmaceuticals as Emerging Contaminants and their Removal from Water. A Review, Chemosphere 93 (2013) 1268–1287.

[4]   M.M. Khin, A.S. Nair, V.J. Babu, R. Murugan, S. Ramakrishna, F. Yinjun, L. Junkang, C.W. Zhou, J. Choi, J. Paek, K. Lee, Y.S. Lee, D.H. Jeong, M.H. Cho, A Review on Nanomaterials for Environmental Remediation, Energy Environ. Sci. 5 (2012) 8075-819.

[5]   A. Alsbaiee, B.J. Smith, L. Xiao, Y. Ling, D.E. Helbling, W.R. Dichtel, Rapid Removal of Organic Micropollutants from Water by a Porous β-Cyclodextrin Polymer, Nature 529 (2016) 190-194.

[6]   D.G.J. Larsson, C. de Pedro, N. Paxeus, Effluent from Drug Manufactures Contains Extremely High Levels of Pharmaceuticals, J. Hazard. Mater. 148 (2007) 751–755.

[7]   J.W. Beaber, B. Hochhut, M.K. Waldor, SOS Response Promotes Horizontal Dissemination of Antibiotic Resistance Genes, Nature 427 (2004) 72–74.

[8]   A. Cincinelli, T. Martellini, E. Coppini, D. Fibbi, A. Katsoyiannis, Nanotechnologies for Removal of Pharmaceuticals and Personal Care Products from Water and Wastewater. A Review, J. Nanosci. Nanotechnol. 15 (2015) 3333–3347.

[9]   U.I. Gaya, A.H. Abdullah, Heterogeneous Photocatalytic Degradation of Organic Contaminants over Titanium Dioxide: A Review of Fundamentals, Progress and Problems, J. Photochem. Photobiol. C 9 (2008) 1–12.

[10]   N.S. Lewis, Toward Cost-Effective Solar Energy Use, Science 315 (2007) 798–801.

[11]   K.M. Lee, C.W. Lai, K.S. Ngai, J.C. Juan, Recent Developments of Zinc Oxide Based Photocatalyst in Water Treatment Technology: A Review, Water Res. 88 (2016) 428–448.

[12]   R. Georgekutty, M.K. Seery, S.C. Pillai, A Highly Efficient Ag-ZnO Photocatalyst: Synthesis, Properties, and Mechanism, J. Phys. Chem. C 112 (2008) 13563–13570.

[13]   A. Primo, A. Corma, H. García, Titania Supported Gold Nanoparticles as Photocatalyst, Phys. Chem. Chem. Phys. 13 (2011) 886–910.

[14]   D. Tsukamoto, Y. Shiraishi, Y. Sugano, S. Ichikawa, S. Tanaka, T. Hirai, Gold Nanoparticles Located at the Interface of Anatase/Rutile TiO_2 Particles as Active Plasmonic Photocatalysts for Aerobic Oxidation, J. Am. Chem. Soc. 134 (2012) 6309–6315.

[15]   R.M. Mohamed, D. McKinney, M.W. Kadi, I.A. Mkhalid, W. Sigmund, Platinum/Zinc Oxide Nanoparticles: Enhanced Photocatalysts Degrade Malachite Green Dye Under Visible Light Conditions, Ceram. Int. 42 (2016) 9375–9381.

[16]   S. Gartiser, L. Brinker, T. Erbe, K. Kümmerer, R. Willmund, Belastung von Krankenhausabwasser mit gefährlichen Stoffen im Sinne § 7a WHG, Acta Hydroch. Hydrob. 24 (1996) 90–97.

[17]   C. Boillot, C. Bazin, F. Tissot-Guerraz, J. Droguet, M. Perraud, J.C. Cetre, D. Trepo, Y. Perrodin, Daily Physicochemical, Microbiological and Ecotoxicological Fluctuations of a Hospital Effluent According to Technical and Care Activities, Sci. Total Environ. 403 (2008) 113–129.

[18]   A. Dalhoff, S. Schubert, A. Vente, Pharmacodynamics of Finafloxacin, Ciprofloxacin, and Levofloxacin in Serum and Urine against TEM- and SHV-Type Extended-Spectrum-β-Lactamase-Producing Enterobacteriaceae Isolates from Patients with Urinary Tract Infections, Antimicrob. Agents Chemother. 61 (2017) e02446-16.

[19]   M. Kosmulski, pH-Dependent Surface Charging and Points of Zero Charge II. Update, J. Colloid Interface Sci. 275 (2004) 214–224.

[20] M. Kosmulski, pH-Dependent Surface Charging and Points of Zero Charge, J. Colloid Interface Sci. 298 (2006) 730–741.

[21] M. Müllner, A.H.E. Müller, Cylindrical Polymer Brushes - Anisotropic Building Blocks, Unimolecular Templates and Particulate Nanocarriers, Polymer 98 (2016) 389–401.

[22] J. Yuan, Y. Xu, A. Walther, S. Bolisetty, M. Schumacher, H. Schmalz, M. Ballauff, A.H.E. Müller, Water-Soluble Organo-Silica Hybrid Nanowires, Nat. Mater. 7 (2008) 718–722.

[23] Y. Xu, J. Yuan, B. Fang, M. Drechsler, M. Müllner, S. Bolisetty, M. Ballauff, A.H.E. Müller, Hybrids of Magnetic Nanoparticles with Double-Hydrophilic Core/Shell Cylindrical Polymer Brushes and Their Alignment in a Magnetic Field, Adv. Funct. Mater. 20 (2010) 4182–4189.

[24] S.S. Sheiko, B.S. Sumerlin, K. Matyjaszewski, Cylindrical Molecular Brushes: Synthesis, Characterization and Properties, Prog. Polym. Sci. 33 (2008) 759–785.

[25] M. Müllner, T. Lunkenbein, N. Miyajima, J. Breu, A.H.E. Müller, A Facile Polymer Templating Route Toward High-Aspect-Ratio Crystalline Titania Nanostructures, Small 8 (2012) 2636–2640.

[26] M. Müllner, T. Lunkenbein, M. Schieder, A.H. Gröschel, N. Miyajima, M. Förtsch, J. Breu, F. Caruso, A.H.E. Müller, Template-Directed Mild Synthesis of Anatase Hybrid Nanotubes within Cylindrical Core-Shell-Corona Polymer Brushes, Macromolecules 45 (2012) 6981–6988.

[27] M. Schieder, T. Lunkenbein, T. Martin, W. Milius, G. Auffermann, J. Breu, Hierarchically Porous Tungsten Oxide Nanotubes with Crystalline Walls Made of the Metastable Orthorhombic Polymorph, J. Mater. Chem. A 1 (2013) 381–387.

[28] T. Lunkenbein, D. Rosenthal, T. Otremba, F. Girgsdies, Z. Li, H. Sai, C. Bojer, G. Auffermann, U. Wiesner, J. Breu, Access to Ordered Porous Molybdenum Oxycarbide/Carbon Nanocomposites, Angew. Chem. Int. Ed. 51 (2012) 12892–12896.

[29] M. Schieder, C. Bojer, J. vom Stein, S. Koch, T. Martin, H. Schmalz, J. Breu, T. Lunkenbein, Template Removal via Boudouard Equilibrium Allows for Synthesis of Mesostructured Molybdenum Compounds, Angew. Chem. Int. Ed. (2017), DOI: 10.1002/anie.201610786.

[30] C. Bojer, J. Schöbel, T. Martin, M. Ertl, H. Schmalz, J. Breu, Clinical Wastewater Treatment: Photochemical Removal of an Anionic Antibiotic (Ciprofloxacin) by Mesostructured High Aspect Ratio ZnO Nanotubes, Appl. Catal. B Environ. 204 (2017) 561–565.

[31] L. Sun, D. Zhao, Z. Song, C. Shan, Z. Zhang, B. Li, D. Shen, Gold Nanoparticles Modified ZnO Nanorods with Improved Photocatalytic Activity, J. Colloid Interface Sci. 363 (2011) 175–181.

7.6 Supporting Information
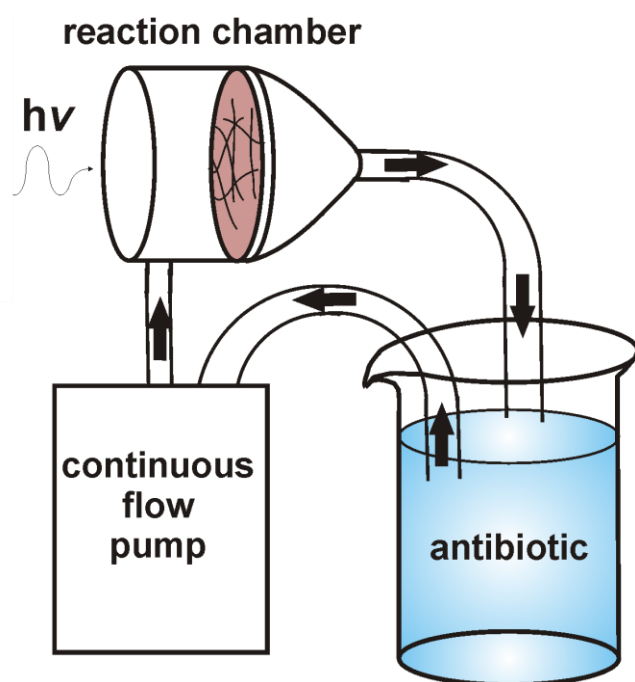
Scheme S7-1. Schematical setup of the employed self-constructed continuous flow reactor.

Table S7-1.
Used amounts of chemicals for the synthesis of the ZnO/Au hybrid materials.

	ZnO/Au_8	ZnO/Au_12	ZnO/Au_15	ZnO/Au_26
$HAuCl_4$ (0.1 M in THF) / mL	5.4	6	6.2	6
$NaBH_4$ (1 M in H_2O) / mL	2.7	3	3.1	3
ZnO NP (ethanol) / mL	122 (6.5 g L^{-1})	125 (6.9 g L^{-1})	126 (5.5 g L^{-1})	91 (3.8 g L^{-1})
ZnO/Au (w/w)	92/8	88/12	85/15	74/26
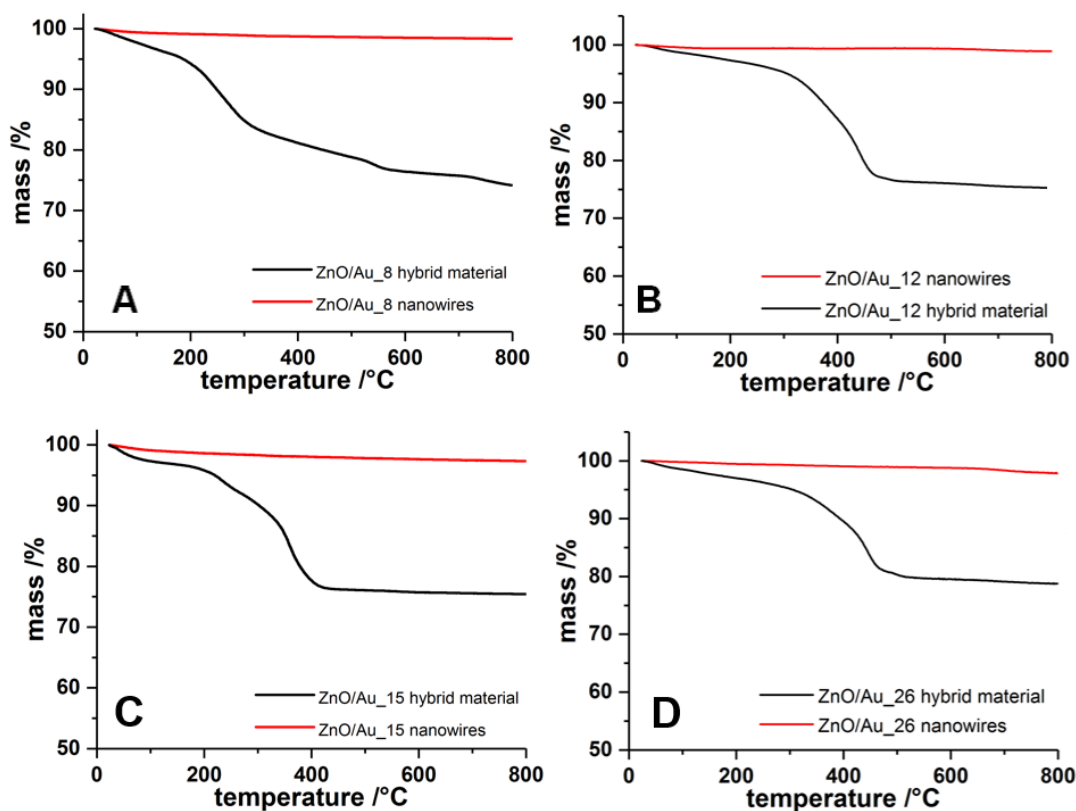
Fig. S7-1. TGA measurements (synthetic air, heating rate 10 Kmin^{-1}) of the ZnO/Au hybrid materials and nanowires.

Table S7-2.
Composition of ZnO/Au composites determined by EDX and Rietveld measurements in comparison to the theoretical compositions.

	ZnO/Au_8 nanowires	*ZnO/Au_12 nanowires*	*ZnO/Au_15 nanowires*	*ZnO/Au_26 nanowires*
ZnO/Au (w/w) (EDX)	92:8	89:11	86:14	79:21
ZnO/Au (w/w) (Rietveld)	-	87:13	-	73:27
ZnO/Au (w/w) (used amount)	92:8	88:12	85:15	74:26

Table S7-3.
Elemental analysis for the ZnO/Au_12 and ZnO/Au_26 hybrid materials and ZnO/Au_12 and ZnO/Au_26 nanowires, respectively.

	C content /wt%	H content /wt%	N content /wt%
ZnO/Au_12 hybrid material	16.8	2.6	2.1
ZnO/Au_12 nanowires	0.1	0.3	0.3
ZnO/Au_26 hybrid material	11.6	1.9	1.7
ZnO/Au_26 nanowires	0.2	0.2	0.2
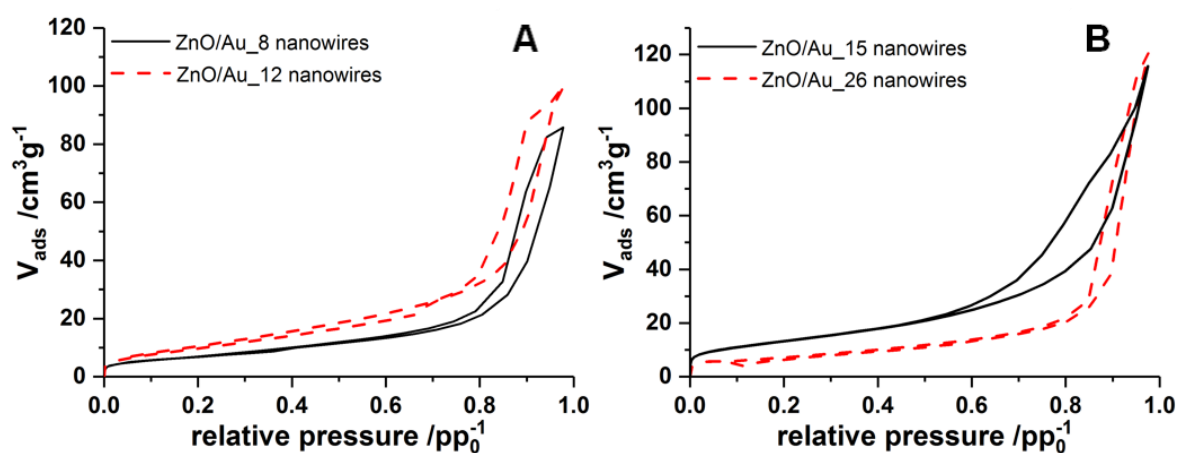
Fig. S7-2. Nitrogen physisorption isotherms of ZnO/Au_8, ZnO/Au_12 (A) and ZnO/Au_15 ZnO/Au_26 nanowires (B).

Table S7-4.
BET surface areas of the catalysts employed in photocatalytic degradation.

	Degussa P25	ZnO nanotubes	ZnO/Au_8 nanowires	ZnO/Au_12 nanowires	ZnO/Au_15 nanowires	ZnO/Au_26 nanowires
Specific surface area / m^2g^{-1}	56	44	39	25	48	30

Fig. S7-3. XRD data of the ZnO/Au_12 hybrid material, calculated Rietveld refinement and difference plot.

Table S7-5.
Refinement parameters for the ZnO/Au_12 hybrid material.

Space group ZnO	P6$_3$mc	Space group Au	Fm3m
R(wp)	3.65	R(wp)	3.65
R(p)	2.47	R(p)	2.47
R(Bragg) ZnO	1.42	R(Bragg) Au	0.442
Cell constants [Å] ZnO:		Cell constants [Å] Au:	
a	3.254(3)	a	4.070(3)
b	3.254(3)	b	4.070(3)
c	5.218(4)	c	4.070(3)
Crystallite size (nm) ZnO	3.4(2) x 3.7(2)	Crystallite size (nm) Au	3.5(2) x 4.9(2)
Amount (%) ZnO	78.9(4)	Amount (%) Au	21.1(4)

Fig. S7-4. XRD data of the ZnO/Au_26 hybrid material, calculated Rietveld refinement and difference plot.

Table S7-6.
Refinement parameters for the ZnO/Au_26 hybrid material.

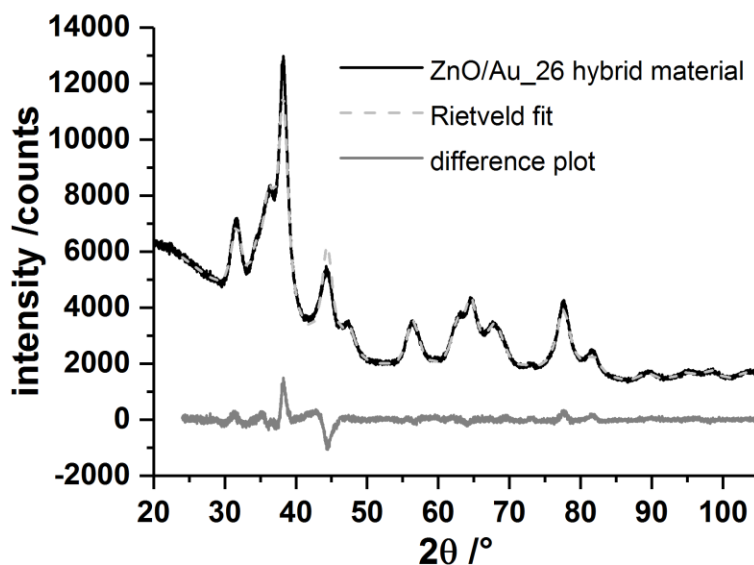| Space group ZnO	$P6_3mc$	Space group Au	$Fm3m$
R(wp)	3.846	R(wp)	3.846
R(p)	2.610	R(p)	2.610
R(Bragg) ZnO	0.157	R(Bragg) Au	0.157
Cell constants [Å] ZnO:		Cell constants [Å] Au:	
a	3.258(2)	a	4.076(3)
b	3.258(2)	b	4.076(3)
c	5.210(0)	c	4.076(3)
Crystallite size (nm) ZnO	3.5(2) x 4.4(3)	Crystallite size (nm) Au	3.7(6) x 5.3(4)
Amount (%) ZnO	71.4(4)	Amount (%) Au	28.6(4)

Fig. S7-5. XRD data of the ZnO/Au_12 nanowires, calculated Rietveld refinement and difference plot.

Table S7-7.
Refinement parameters for ZnO/Au_12 nanowires.

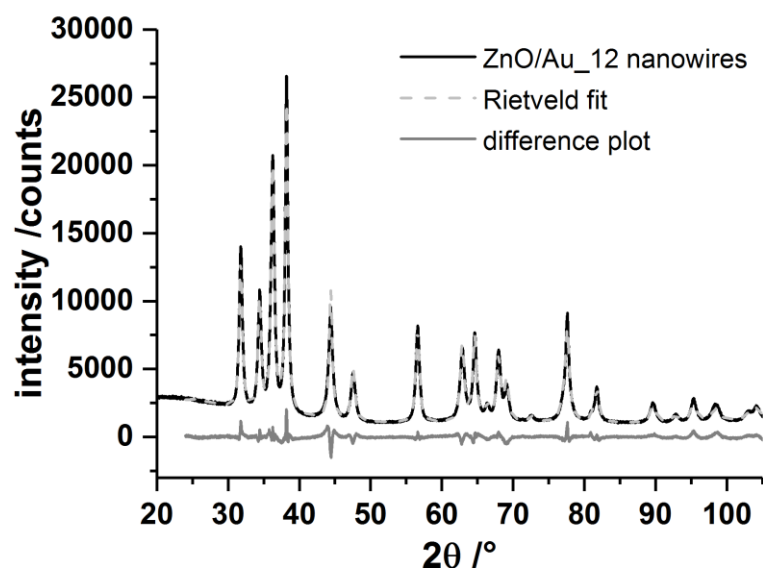| Space group ZnO	P6$_3$mc	Space group Au	Fm3m
R(wp)	5.10	R(wp)	5.10
R(p)	3.80	R(p)	3.80
R(Bragg) ZnO	1.28	R(Bragg) Au	0.564
Cell constants [Å] ZnO:		Cell constants [Å] Au:	
a	3.247(5)	a	4.074(5)
b	3.247(5)	b	4.074(5)
c	5.203(2)	c	4.074(5)
Crystallite size (nm) ZnO	12.5(4) x 15.5(4)	Crystallite size (nm) Au	17.5(4) x 24.4(5)
Amount (%) ZnO	87.2(1)	Amount (%) Au	12.8(1)
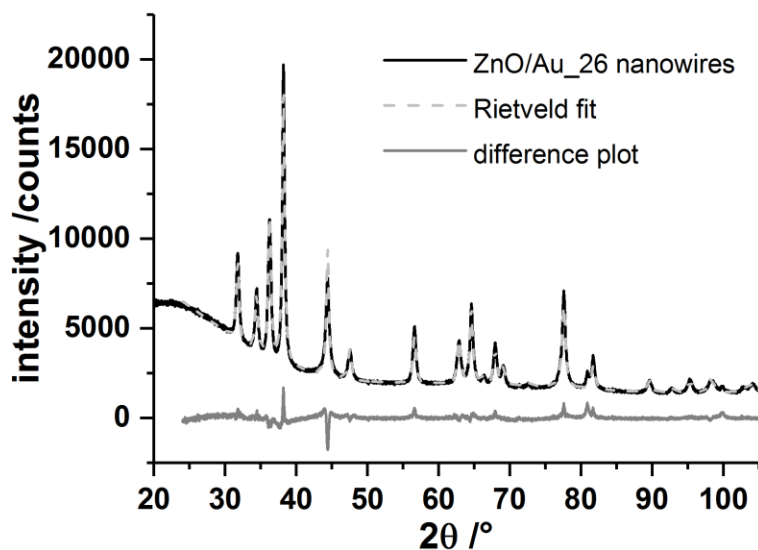
Fig. S7-6. XRD data of the ZnO/Au_26 nanowires, calculated Rietveld refinement and difference plot.

Table S7-8.
Refinement parameters for the ZnO/Au_26 nanowires.

Space group ZnO	P6$_3$mc	Space group Au	Fm3m
R(wp)	4.689	R(wp)	4.689
R(p)	3.276	R(p)	3.276
R(Bragg) ZnO	2.358	R(Bragg) Au	2.563
Cell constants [Å] ZnO:		Cell constants [Å] Au:	
a	3.250(4)	a	4.078(6)
b	3.250(4)	b	4.078(6)
c	5.207(4)	c	4.078(6)
Crystallite size (nm) ZnO	14.5(8) x 16.9(8)	Crystallite size (nm) Au	16.9(3) x 23.7(5)
Amount (%) ZnO	72.9(3)	Amount (%) Au	27.1(3)
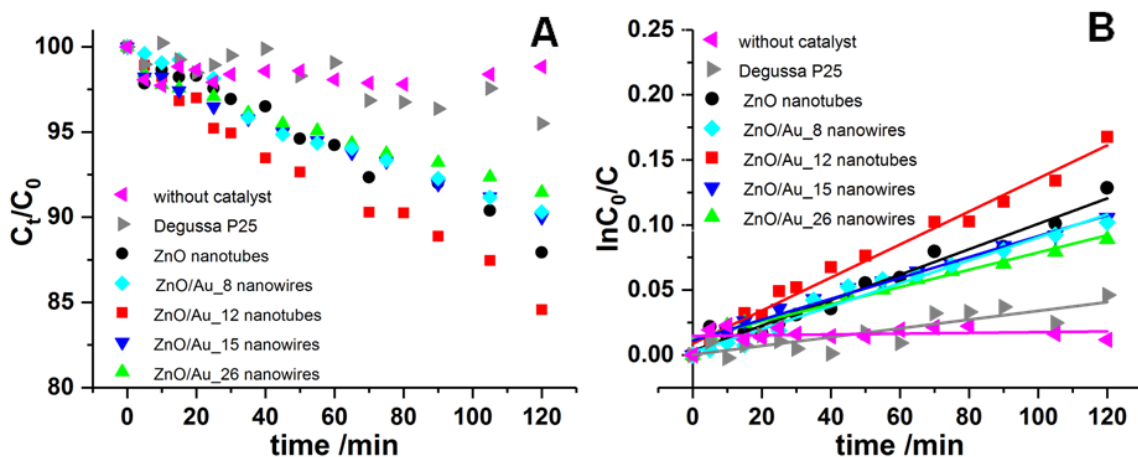
Fig. S7-7. Time-dependent decrease of ciprofloxacin during irradiation with terrestrial solar spectrum (A) and corresponding first-order kinetics plots (B) in the absence of a catalyst and employing Degussa P25, ZnO nanotubes, and ZnO/Au nanowires as catalysts.[1]

Table S7-9.
k' values for the different catalysts employed in the photocatalytic degradation of ciprofloxacin.

	without catalyst	*Degussa P25*	*ZnO nanotubes*	*ZnO/Au_8 nanowires*	*ZnO/Au_12 nanowires*	*ZnO/Au_15 nanowires*	*ZnO/Au_26 nanowires*
k'/ min^{-1}	$2.9*10^{-5}$	$3.5*10^{-4}$	$9.6*10^{-4}$	$8.8*10^{-4}$	$1.3*10^{-3}$	$8.0*10^{-4}$	$6.6*10^{-4}$
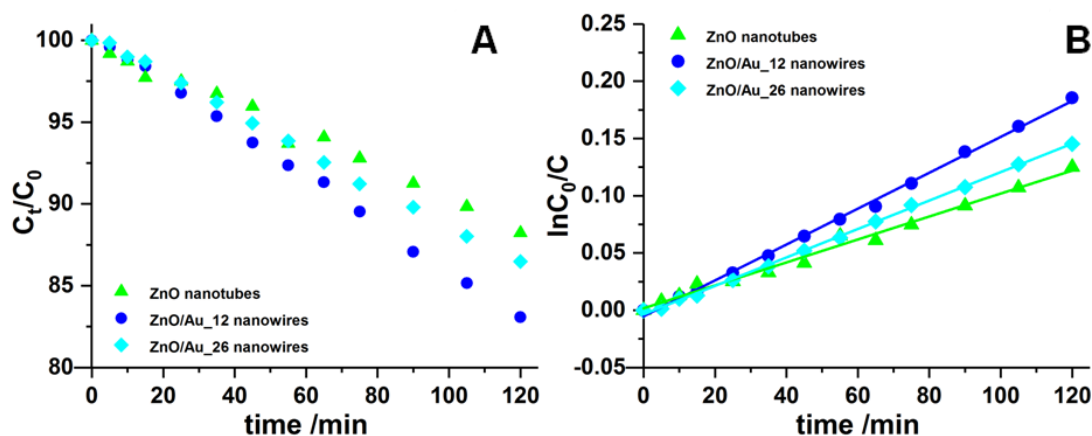
Fig. S7-8. Time-dependent decrease of levofloxacin during irradiation with terrestrial solar spectrum (A) and corresponding first-order kinetics plots (B) employing ZnO nanotubes, ZnO/Au_12 and ZnO/Au_26 nanowires as catalysts.

Table S7-10.

k' values for the different catalysts employed in the photocatalytic degradation of levofloxacin.

	ZnO nanotubes	ZnO/Au_12 nanowires	ZnO/Au_26 nanowires
k'/ min^{-1}	$1*10^{-3}$	$1.6*10^{-3}$	$1.2*10^{-3}$

References

[1]   C. Bojer, J. Schöbel, T. Martin, M. Ertl, H. Schmalz, J. Breu, Clinical Wastewater Treatment: Photochemical Removal of an Anionic Antibiotic (Ciprofloxacin) by Mesostructured High Aspect Ratio ZnO Nanotubes, Appl. Catal. B Environ. 204 (2017) 561–565.

8 Conclusion and Outlook

Two different concepts for the synthesis of highly active mesostructured catalysts were established in this thesis.

The first concept showed the versatility of worm-like crystalline-core micelles with a functional patchy corona as template materials for the efficient stabilization of different types of metal and metal oxide nanoparticles. The key parameter for successful hybrid material formation was a good solubility of the functionalized patches. For successful synthesis of a heterogeneous catalyst, these patchy micelles were supported on a polystyrene nonwoven and loaded with gold nanoparticles. In future, the impact of nanoparticle size on heterogeneous catalysis can be investigated. The modular design of this catalyst material allows for the incorporation of different types and shapes of nanoparticles, which enables the use in different catalytic reactions. Palladium nanoparticles, for example, can be used for the hydrogenation of alkenes or cross coupling reactions. Transition metal oxide nanoparticles like zinc oxide or copper oxide provide the accessibility to photocatalytic reactions. In addition to the type of nanoparticles, also the polymeric support can be tuned. By using polybutadiene-containing supports, the nonwoven exhibits elastic properties. Using a polyimide support, the temperature stability can be increased. Therefore, the patchy micelles can be heteroepitaxially grown on the surface of carbon nanotubes to further increase their thermal stability.

The second concept deals with the use of amorphous polymeric templates, which are removed by heat treatment after loading with nanoparticles. Here, the size of the different nanoparticles is a crucial parameter, which can be tuned in future to enhance the catalytic activity of these materials. Different types of nanoparticles like copper oxide, palladium, silver or platinum can be incorporated in the polymeric templates and a screening of synergistic effects depending on the composition of the hybrid materials should lead to highly technical relevant catalysts. The photocatalytic degradation of common antibiotics with a zinc oxide / gold catalyst already showed a superior performance in comparison with commercially available catalysts. In addition to these antibiotics, dyes and other active chemicals found in wastewater can be tested. As the mesostructured catalysts are temperature-stable, high-temperature catalysis, for example the hydrogenation of octene and propene can be tested. Here, the catalysts should provide the advantage that the surface remains active and accessible even after several cylces of catalysis.

List of Publications

1. Schieder, M.; Lunkenbein, T.; Bojer, C.; Dulle, M.; vom Stein, J.; Auffermann, G.; Löbling, T.I.; Schöbel, J.; Schmalz, H.; Breu, J.

   Selective Template Removal by Thermal Depolymerization to Obtain Mesostructured Oxycarbide

   Z. Anorg. Allg. Chem. **2015**, *641*, 1829-1834.

2. Gegenhuber, T.; Krekhova, M.; Schöbel, J.; Gröschel, A. H.; Schmalz, H.

   "Patchy" Carbon Nanotubes as Efficient Compatibilizers for Polymer Blends

   ACS Macro Lett. **2016**, *5*, 306-310.

3. Schöbel, J.; Karg, M.; Rosenbach, D.; Krauss, G.; Greiner, G.; Schmalz, H.

   Patchy Worm-Like Micelles with Tailored Functionality by Crystallization-Driven Self-Assembly: A Versatile Platform for Mesostructured Hybrid Materials

   Macromolecules **2016**, *49*, 2761-2771.

4. Schöbel, J., Burgard, M., Hils, C., Dersch, R., Dulle, M., Volk, K., Karg, M., Greiner, A., Schmalz, H.

   Bottom-Up Meets Top-Down: Patchy Hybrid Nonwovens as an Efficient Catalysis Platform

   Angew. Chem. Int. Ed., **2017**, *56*, 405-408.

5. Bojer, C., Schöbel, J., Martin, T., Ertl, M., Schmalz, H., Breu, J.

   Clinical Wastewater Treatment: Photochemical Removal of an Anionic Antibiotic (Ciprofloxacin) by Mesostructured High Aspect Ratio ZnO Nanotubes

   Appl. Catal. B, **2017**, *204*, 561-565.

6. Bojer, C., Schöbel, J., Martin, T., Lunkenbein, T., Wagner, D. R., Greiner, A., Breu, J., Schmalz, H.

Mesostructured ZnO/Au Nanoparticle Composites with Enhanced Photocatalytic Activity

Polymer, **2017**, *128*, 65-70.

Glossary

A	absorbance
α	polarizability
AFM	atomic force microscopy
AOP	advanced oxidation process
ATRP	atom transfer radical polymerization
BCPs	block copolymers
BET	Brunauer Emmett Teller
BV	polybutadiene-*block*-poly(2-vinylpyridine)
BVT	polybutadiene-*block*-poly(2-vinylpyridine)-*block*-poly(*tert*-butyl methacrylate)
°C	degree centigrade
c	concentration
$CDCl_3$	deuterated chloroform
CDSA	crystallization-driven self-assembly
cm	centimeter
CNTs	carbon nanotubes
CPBs	cylindrical polymer brushes
CTAB	cetyltrimethyl ammonium bromide
d	days
D	diameter
DCTB	*trans*-2-[3-(4-*tert*-butylphenyl)-2-methyl-2-propenylidene]malononitrile
DEEDA	*N,N*-diethylethylenediamine
D*i*PEDA	*N,N*-di*iso*propylethylenediamine
DLS	dynamic light scattering
$Đ_M$	molar mass dispersity
DMEDA	*N,N*-dimethylethylenediamine
DMF	*N,N*-dimethylformamide
DMSO	dimethylsulfoxide
ε	complex dielectric function of a metal
ε_m	dielectric constant of a medium
eq	eqivalents
f	degree of functionalization
^{1}H NMR	[1]H nuclear magnetic resonance spectroscopy

FT-IR	Fourier transform infrared
FWHM	full width at half maximum
g	gram
g mol^{-1}	gram per mol
g L^{-1}	gram per liter
GC-MS	gas chromatography coupled with mass spectrometry
h	hours
HFIP	hexafluoroisopropanol
ICP-OES	inductively coupled plasma optical emission spectrometry
IPEC	interpolyelectrolyte complex
IR	infrared
kDa	kilo Dalton
kV	kilo Volt
l	length
L	liter
L h^{-1}	liter per hour
LCST	lower critical solution temperature
LiEt$_3$BH	Superhydride
LSPR	localized surface plasmon resonance
MALDI-TOF MS	matrix-assisted laser desorption ionization time of flight mass spectrometry
μDSC	micro differential scanning calorimetry
μg	microgram
μL	microliter
μm	micrometer
mbar	millibar
MCMs	multicompartment micelles
meV	milli electron volt
mg	milligram
min	minute
mM	milli molar
M_n	number-weighted average molecular weight
n-BuLi	n-butyllithium
4-NiP	4-nitrophenol
nm	nanometer
NP	nanoparticle

P2VP	poly(2-vinylpyridine)
P3HT	poly(3-hexylthiophene)
P4VP	poly(4-vinylpyridine)
PAA	poly(acrylic acid)
PAN	polyacrylonitrile
PB	polybutadiene
PCL	poly(ε-caprolactone)
PDDF	pair distance distribution function
PDEA	poly(diethylaminoethyl methacrylamide)
PDEAMA	poly(diethylaminoethyl methacrylate)
PDI	polydispersity (changed to $Đ_M$)
PD*i*PA	poly(di*iso*propylaminoethyl methacrylamide)
PDLA	poly(*D*-lactide)
PDMA	poly(dimethylaminoethyl methacrylamide)
PDMAEMA	poly(dimethylaminoethyl methacrylate)
PDMS	polydimethylsiloxane
PE	polyethylene
PEI	polyethyleneimine
PEO	poly(ethylene oxide)
PEP	polyethylpropylene
PFS	polyferrocenylsilane
PI	polyisoprene
PLLA	poly(*L*-lactide)
PMAA	poly(methacrylic acid)
PMMA	poly(methyl methacrylate)
PP	polypropylene
ppm	parts per million
PS	polystyrene
PS-TTC	trithiocarbonate-terminated polystyrene
PXRD	powder X-ray diffraction
PZC	point of zero charge
RAFT	reversible addition fragmentation chain transfer
R	radius
*R*h	hydrodynamic radius
rpm	rounds per minute
RT	room temperature

SANS	small angle neutron scattering
SAXS	small angle X-ray scattering
SBM	polystyrene-*block*-polybutadiene-*block*-poly(methyl methacrylate)
sCCMs	spherical crystalline-core micelles
SEC	size exclusion chromatography
SEDEA	SEM amidated with DEEDA
SED*i*PA	SEM amidated with D*i*PEDA
SEDMA	SEM amidated with DMEDA
SEM	polystyrene-*block*-polyethylene-*block*-poly(methyl methacrylate)
SES	polystyrene-*block*-polyethylene-*block*-polystyrene
SLS	static ligth scattering
SPBs	spherical polymer brushes
T	temperature
T_c	crystallization temperature
TEG	triethylene glycol
TEM	transmission electron microscopy
TGA	thermal gravimetric analysis
THF	tetrahydrofuran
T_m	melting temperature
TOAB	tetraoctylammonium bromide
UV-Vis	ultraviolet - visible
V_E	elution volume
vol %	volume percent
wCCMs	worm-like crystalline-core micelles
wt %	weight percent
λ	wavelength

Acknowledgement

First, I want to thank Prof. Dr. Andreas Greiner and Dr. Holger Schmalz for the opportunity to work on this special topic. I appreciated all the scientific discussions and the help and support, which finally led to this thesis. Additionally, I want to thank them for letting me follow my ideas and inspirations and also giving me advice in the times, where I had to struggle with some parts of this work. Furthermore, I want to thank Prof. Dr. Seema Agarwal for continuous support and scientific discussions, which helped to improve my work. I acknowledge the financial support of the German Research Foundation in the framework of the Collaborative Research Center SFB840 (project A2).

Next, I want to thank Prof. Dr. Birgit Weber for being my mentor in the BayNat program and all cooperation partners. The most support, I gratefully received from Prof. Dr. Matthias Karg, who was involved in different publications of this thesis for DLS, supervising the master thesis of Anne Weckwerth, which led to a final manuscript and UV-Vis reflectance measurements. Furthermore, I want to thank Matthias Burgard, Carina Bojer and Anne Weckwerth for endless discussions, a lot of experiments we designed together and for writing manuscripts with me. I also thank Christian Hils for conducting many experiments and for always being motivated and happy with his work.

I want to thank the whole MC2 group for never ending support, scientific discussions, but also for very funny evening sessions and activities outside the university life. Especially, I want to thank Bianca, Rika, Julia, Marius (a.k.a. Samarius), Amanda and Paul, Matthias, Christian, Florian, Steffen, Viola, Tobi, Martin, Amir, Hadi and Liao who all gave me incredible support in every situation. I appreciated the nice atmosphere in lab 797 with Amanda, Fangyao (my kicker-partner!), Oli, Markus, Amir, Hui, Christian and lovely Linda, who all were addicted to music while working, just like me. Thank you for letting me be a part of this lab and for your support! Additionally, I want to thank all my students who did practical lab courses with me: Andreas, Gert, Dominic and Christian. Thank you for many experiments and discussions and for making my work better.

I want to emphasize the continuous support of Rika. I was always trusting her the most and I knew that things are going well if we worked together. Thank you for this and all the best in the future, Ms. Technician! I am proud to be part of your scientific carrier (although it was a small part…)!

For personal and scientific support, I want to acknowledge Bianca who always took care of me and remind me of the important things in life. Furthermore, I am deeply grateful for all the advices and support concerning all my little or sometimes bigger problems and for never loosing contact after our scientific carriers went in different directions!

I am also very grateful to Gaby Oliver and Niko Plocher, I really don't know if there is anything, these two can't handle in organizing and support!

Finally, I want to thank my family for amazing support in every part of my life, for giving me the chance to study and to do what I love. Special thanks to my sister who directly supported me in Bayreuth and who is always agreeing on my opinion. You are the best sister in the whole world!

(Eidesstattliche) Versicherungen und Erklärungen

(§ 9 Satz 2 Nr. 3 PromO BayNAT)

Hiermit versichere ich eidesstattlich, dass ich die Arbeit selbständig verfasst und keine anderen als die von mir angegebenen Quellen und Hilfsmittel benutzt habe (vgl. Art. 64 Abs. 1 Satz 6 BayHSchG).

(§ 9 Satz 2 Nr. 3 PromO BayNAT)

Hiermit erkläre ich, dass ich die Dissertation nicht bereits zur Erlangung eines akademischen Grades eingereicht habe und dass ich nicht bereits diese oder eine gleichartige Doktorprüfung endgültig nicht bestanden habe.

(§ 9 Satz 2 Nr. 4 PromO BayNAT)

Hiermit erkläre ich, dass ich Hilfe von gewerblichen Promotionsberatern bzw. -vermittlern oder ähnlichen Dienstleistern weder bisher in Anspruch genommen habe noch künftig in Anspruch nehmen werde.

(§ 9 Satz 2 Nr. 7 PromO BayNAT)

Hiermit erkläre ich mein Einverständnis, dass die elektronische Fassung meiner Dissertation unter Wahrung meiner Urheberrechte und des Datenschutzes einer gesonderten Überprüfung unterzogen werden kann.

(§ 9 Satz 2 Nr. 8 PromO BayNAT)

Hiermit erkläre ich mein Einverständnis, dass bei Verdacht wissenschaftlichen Fehlverhaltens Ermittlungen durch universitätsinterne Organe der wissenschaftlichen Selbstkontrolle stattfinden können.

……………………………………………………………………

Ort, Datum, Unterschrift